Chemical Design and Application of Organized Multicomponent Hybrid Nanostructures

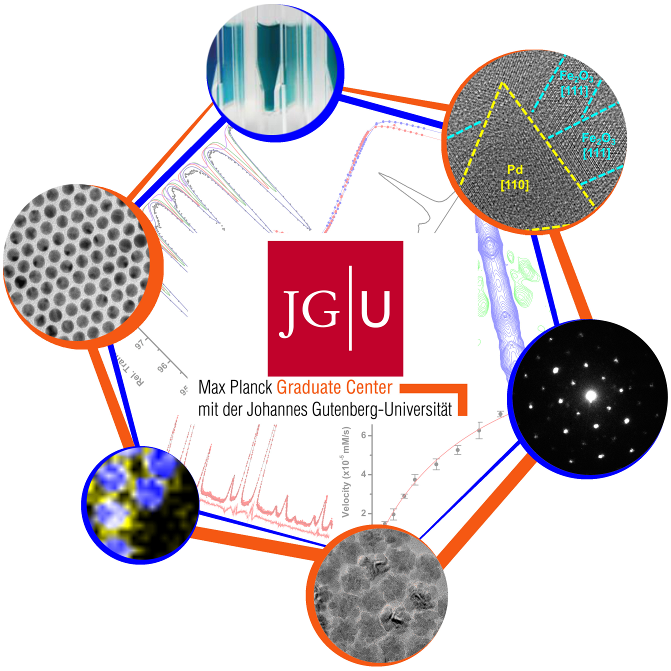

Dissertation

zur Erlangung des Grades eines
Doctor rerum naturalium (Dr. rer. nat.)

im Promotionsfach Chemie der Fachbereiche:
08 - Physik, Mathematik und Informatik,
09 - Chemie, Pharmazie und Geowissenschaften,
10 - Biologie,
und Universitätsmedizin der
Johannes Gutenberg-Universität Mainz

im Rahmen des **Max Planck Graduate Center** Promotionsprogrammes

vorgelegt von

Dipl.-Chem. Martin Klünker
geboren in Neuwied

Mainz, März 2018

Dekan: [redacted]
Erster Berichterstatter: [redacted]
Zweiter Berichterstatter: [redacted]
Datum der mündlichen Prüfung: 17. Mai 2018

Die vorliegende Arbeit wurde im Zeitraum vom Oktober 2014 bis März 2018 unter der Leitung von Prof. Dr. Wolfgang Tremel und Prof. Dr. Jürgen Brieger am Institut für Anorganische Chemie und Analytische Chemie der Johannes Gutenberg-Universität Mainz im Rahmen des Max Planck Graduate Center mit der Johannes Gutenberg-Universität (MPGC) Promotionsprogrammes angefertigt.

I hereby declare that I wrote the dissertation submitted without any unauthorized external assistance and used only sources acknowledged in the work. All textual passages which are appropriated verbatim or paraphrased from published and unpublished texts as well as all information obtained from oral sources are duly indicated and listed in accordance with bibliographical rules. In carrying out this research, I complied with the rules of standard scientific practice as formulated in the statutes of Johannes Gutenberg-University Mainz to insure standard scientific practice.

Mainz, March 2018

Martin Klünker

Für meine Familie

Abstract

Multicomponent inorganic nanostructures containing metal/metal oxide components connected through a solid interface are, unlike conventional single material nanoparticles, able to combine different or even incompatible properties within a single entity. They are multifunctional and resemble molecular amphiphiles, which makes them especially attractive for self-assembling complex structures, drug delivery, bioimaging or catalysis. The range of capabilities can be even advanced by selective surface functionalization. Three forms of heterodimeric nanoparticles are most intriguing: (i) two-domain systems with solid state interface, often also with different surface functionalization of the metal and the metal oxide domain, known as eponym Janus particles, (ii) colloidal superparticles, *i.e.* mesoscale particles defined as size- and shape-controlled assemblies from nanoscale building blocks, and (iii) core-shell nanoparticles, where a core material is covered by a shell of another material, often with variable shell thickness.

The present thesis focusses on these three types of multicomponent inorganic nanostructures and presents their enhanced performance in various applications. It combines the synthesis of complex nanoparticles, using the noble metals Pd and Au as well as the metal oxides from Fe and Zn, with their thorough characterization and selected applications ranging from catalysis and enzyme mimetic to imaging and biomedical application. The different nanoparticle types are analyzed by means of *i.a.* (aberration corrected) high resolution transmission electron microscopy (HR-TEM), powder X-Ray diffraction (XRD), UV-vis spectroscopy, Mössbauer spectroscopy, electron diffraction (ED), energy dispersive X-ray spectroscopy (EDX), nuclear magnetic resonance spectroscopy (NMR) and magnetic measurements (SQUID) to evaluate their chemical composition and physical properties.

Pd@γ-Fe_2O_3 superparticles and Fe_xO@Fe_xO superparticles of various morphologies are presented, where Pd or Fe_xO template nanoparticles are overgrown with iron oxide nanorods or nanodomains to yield highly organized nanostructures. This approach demonstrates the ability to obtain tailor-made nanostructures with well-defined size, morphology and chemical composition by systematic adjustment of reaction parameters and educt composition. Moreover, the synthesized superparticles display enhanced application properties compared to the respective seed particles. The Pd@γ-Fe_2O_3 superparticles exhibit superior peroxidase-like activity as enzyme mimetics compared to isolated iron oxide nanorods, whereas the Fe_xO@Fe_xO superparticles lead to a shortening of the longitudinal and transversal relaxation times in magnetic resonance imaging (MRI). This is attributed to a synergistic effect through the interface of the different materials based on the unique structure of the superparticles, whose components are interfaced *via* shared crystals faces compared to superstructures from self-assembled small nanoparticles stabilized by van der Waals interactions. Advantages such as electronic communication, due to the absence of separating organic surface layers, and increased physical stability make the super-

particles promising candidates for catalytic, biomedical, or nanodevice applications.

Pd@Fe$_x$O heterodimer nanoparticles are presented as hybrid nanostructures with separated metal and metal oxide domains in order to use the surface availability of both components as well as their distinct properties to establish a novel template-free synthesis of a nanocomposite material. The Pd@Fe$_x$O heterodimer nanoparticles are adopted to fabricate a macroporous, hydrophobic, magnetically active and three-dimensional (3D) hybrid foam, capable of repeatedly separating oil contaminants from water. The Pd domains in the Pd@Fe$_x$O heterodimers act as nanocatalyst for a hydrosilylation reaction, while the Fe$_x$O component confers magnetic properties to the final functional material. The nanocomposite material finally consists of a polysiloxane foam with embedded Pd@Fe$_x$O heterodimer nanoparticles. Additionally, the Pd@Fe$_x$O heterodimer nanoparticles also display advanced peroxidase-like activity as enzyme mimetics, which is compared to the Pd@γ-Fe$_2$O$_3$ superparticles.

ZnO nanoparticles of different morphologies are presented for the evaluation of their cell uptake and toxicity mechanisms. ZnO, especially in nano-dimensions, is subject to increased environmental release due to its use in sunscreens, paints and pharmaceutical products, while toxic effects to human health have been reported, but are poorly understood so far. ZnO nanoparticles functionalized with a silica shell and fluorescein dye are taken up into various cancer cell types and demonstrate gradual dissolution and successive increase in cytotoxicity. ZnO nanoparticles without silica coating are used to explore the mechanisms of ZnO mediated toxicity, unveiling that nanoparticle cell adhesion and uptake are crucial for the toxicity after the first hours of application, while the amount, biochemical character and properties of the released Zn^{2+} ions determine the toxicity in the following hours.

Finally, Au@Pd and Pd@Au heterodimer nanostructures, designed for a catalytic application and synthesized by a seed mediated growth in organic media, are shown. *Ex situ* surface modification of the Au and Pd seed nanoparticles with the long chain organic thiol 1-octadecanethiol allow to control and tune the morphology and catalytic activity of the heterodimers. For unraveling the influence of the thiol coating on the surface dynamics and reaction process detailed ^{1}H- and ^{19}F-NMR studies on 1-octadecanethiol functionalized Au nanoparticles are used, unveiling that ligand exchange is an equilibrium reaction associated with a Nernst distribution. Efficient surface coverage is found to depend on repeated exchange reactions with large ligand excess. In addition, the size of the nanoparticles, *i.e.* the surface curvature, surface defects and reactivity has a contribution as well as the size of the ligand.

Zusammenfassung

Anorganische Multikomponenten-Nanostrukturen mit Metall/Metalloxid Komponenten, die durch eine Festkörpergrenzfläche verbunden sind, können, im Gegensatz zu konventionellen Nanopartikeln aus nur einem Material, verschiedene oder sogar gegensätzliche Eigenschaften innerhalb eines einzelnen Partikels kombinieren. Sie sind multifunktional und ähneln molekularen Amphiphilen. Dies macht sie besonders attraktiv für die Darstellung komplexer, selbstgeordneter Strukturen, den Einsatz in der gezielten Wirkstofffreisetzung, biomedizinischen Bildgebung oder Katalyse. Darüber hinaus kann die Anwendungsbreite durch selektive Oberflächenfunktionalisierung noch erweitert werden. Drei Formen von Heterodimer-Nanopartikeln faszinieren am meisten: (i) Zwei-Domänen Syteme mit Festkörpergrenzfläche, in den meisten Fällen mit unterschiedlicher Oberflächenfunktionalisierung der Metall und Metalloxid Domäne, auch bekannt als Janus-Partikel. (ii) Kolloidale Superpartikel, auch Meso-Partikel genannt, definiert als größen- und formkontrollierte Anordnungen nanoskaliger Bausteine, und (iii) Kern-Schale Nanopartikel, in denen ein Kernmaterial mit einer Hülle eines weiteren Materials bedeckt ist. Die Hüllendicke kann dabei variiert werden.

Die vorliegende Arbeit beschäftigt sich mit diesen drei Arten von anorganischen Multikomponenten-Nanostrukturen und zeigt ihre gesteigerte Leistungfähigkeit in vielseitigen Anwendungen. Vorgestellt wird die Synthese komplexer Nanopartikel mit den Edelmetallen Pd und Au sowie den Metalloxiden von Fe und Zn, gefolgt von einer ausführlichen Charakterisierung ihrer chemischen und physikalischen Eigenschaften sowie ausgewählten Anwendungen. Die in dieser Arbeit untersuchten Anwendungen reichen von Katalyse und Enzym-Mimetik bis zu Bildgebung und biomedizinischen Anwendungen. Die verschiedenen Nanopartikelarten werden unter anderem mittels (aberrationskorrigierter) hochauflösender Transmissionselektronenmikroskopie (HR-TEM), Pulver-Röntgendiffraktometrie (XRD), UV-vis Spektroskopie, Mössbauer Spektroskopie, Elektronendiffraktion (ED), energiedispersiver Röntgenspektroskopie (EDX), Kernspinresonanzspektroskopie (NMR) und magnetischer Messungen (SQUID) charakterisiert.

Es werden Pd@γ-Fe_2O_3 Superpartikel und Fe_xO@Fe_xO Superpartikel unterschiedlicher Morphologien vorgestellt, für deren Synthese Pd oder Fe_xO Templat-Nanopartikel mit Eisenoxid Nanostäbchen oder Nanodomänen überwachsen werden um hochorganisierte Nanostrukturen zu erhalten. Dieser Ansatz demonstriert die Möglichkeit maßgeschneiderte Nanostrukturen mit wohldefinierter Größe, Morphologie und chemischer Zusammensetzung durch systematische Einstellung von Reaktionsparametern und Eduktzusammensetzung zu erhalten. Daneben zeigen diese Superpartikel verbesserte Leistungen in Anwendungen im Vergleich zu den jeweiligen Saatpartikeln. Die Pd@γ-Fe_2O_3 Superpartikel zeigen eine verbesserte katalytische Aktivität als Peroxidase Enzym-Mimetika im Vergleich zu isolierten Eisenoxid Nanostäbchen. Die Fe_xO@Fe_xO Superpartikel führen zu einer Reduktion der longitudinalen

und transversalen Relaxationszeiten in der Magnetresonanztomographie (MRT). Diese erhöhte Leistungsfähigkeit wird einem synergistischen Effekt, vermittelt durch die Festkörpergrenzfläche der verschiedenen Materialien, zugeschrieben. Die verschiedenen Materialien/Komponenten der einzigartigen Nanostrukturen sind durch diese Festkörpergrenzfläche miteinander in direktem Kontakt und teilen gemeinsame Kristallflächen im Gegensatz zu selbstgeordneten Strukturen aus kleinen Nanopartikeln, die nur über van der Waals-Wechselwirkungen stabilisiert werden. Die Vorteile, wie zum Beispiel elektronische Kommunikation durch die Abwesenheit von trennenden organischen Oberflächenbeschichtungen sowie eine verbesserte physikalische Stabilität, machen die Superpartikel zu aussichtsreichen Strukturen für katalytische oder biomedizinische Anwendungen oder Nanobauteile.

Pd@Fe_xO Heterodimer-Nanopartikel werden als hybride Nanostrukturen mit getrennten Metall und Metalloxid Domänen vorgestellt, wobei die Oberflächenverfügbarkeit beider Komponenten sowie deren verschiedene Eigenschaften zur Synthese eines neuen templatfreien Nanokomposit-Materials genutzt werden. Die Pd@Fe_xO Heterodimer-Nanopartikel sind Teil der Synthese eines makroporösen, hydrophoben, magnetischen und dreidimensionalen (3D) Hybrid-Schwammes, welcher in der Lage ist wiederholt Ölverschmutzungen von Wasser abzutrennen. Die Pd Domänen in den Pd@Fe_xO Heterodimeren fungieren dabei als Nanokatalysator für eine Hydrosilylierungsreaktion, während die Fe_xO Komponente dem fertigen Funktionsmaterial magnetische Eigenschaften verleiht. Das Nanokomposit-Material besteht schließlich aus einem Polysiloxan Schwamm mit eingebetteten Pd@Fe_xO Heterodimer-Nanopartikeln. Die Pd@Fe_xO Heterodimer-Nanopartikel zeigen zusätzlich eine verbesserte katalytische Aktivität als Peroxidase Enzym-Mimetika, welche mit der katalytischen Aktivität der Pd@γ-Fe_2O_3 Superpartikel verglichen wird.

Außerdem werden ZnO Nanopartikel mit unterschiedlicher Morphologie für die Untersuchung von Zellaufnahme und Toxizität verwendet. ZnO, speziell in Form von Nanopartikeln, wird aufgrund der verbreiteten Nutzung in Sonnencreme, Farben und pharmazeutischen Produkten vermehrt in die Umwelt freigesetzt. Toxische Effekte auf die menschliche Gesundheit wurden dabei bereits festgestellt, sind jedoch zur Zeit in ihrer Entstehung und Wirkung kaum verstanden. ZnO Nanopartikel, die mit einer Silicahülle und Fluorescein-Farbstoff versehen wurden, werden in verschiedene Typen von Krebszellen aufgenommen und zeigen eine sukzessive Freisetzung von Zinkionen durch Auflösung und einen damit verbundenen Anstieg der Zytotoxizität. ZnO Nanopartikel ohne Silicahülle werden verwendet um die Mechanismen der ZnO-vermittelten Toxizität zu untersuchen. Dabei wird offengelegt, dass die Adhäsion der Nanopartikel an die Zellen sowie die Zellaufnahme entscheidend sind für die toxische Wirkung der Nanopartikel in den ersten Stunden nach der Applikation. Die Menge, der biochemische Charakter und die Eigenschaften der freigesetzten Zn^{2+}-Ionen hingegen sind maßgeblich für die Toxizität in den darauffolgenden Stunden.

Schließlich wird die Entwicklung von Au@Pd sowie Pd@Au Heterodimer-Nanostrukturen für die katalytische Anwendung und deren Synthese mittels partikelvermitteltem Wachstum in organischem Medium gezeigt. *Ex situ* Oberflächenfunktionalisierung der Au und Pd Saatpartikel mit dem langkettigen organischen Thiol

1-Octadecanthiol ermöglicht die Kontrolle und Einstellung der Morphologie und katalytischen Aktivität der Heterodimere. Zur Aufklärung des Einflusses der Thiol-Funktionalisierung auf die Oberflächendynamik und den Reaktionsablauf werden detaillierte ^{1}H- und ^{19}F-NMR Analysen genutzt. Diese zeigen, dass der Ligandenaustausch eine Gleichgewichtsreaktion darstellt assoziiert mit einer Nernst-Verteilung. Eine effiziente Oberflächenbelegung mit dem neuen Liganden ist demnach nur mit einem wiederholten Ligandenaustausch mit großem Ligandenüberschuss möglich. Daneben sind Einflüsse der Nanopartikelgröße, also der Oberflächenkrümmung, von Oberflächendefekten und -reaktivität sowie der Ligandengröße zu beachten.

Acknowledgment

First of all, I particularly like to thank my supervisor [redacted] for giving me the opportunity to work on these excellent and fascinating projects, for his input and support, as well as for many fruitful discussions. I sincerely thank my co-supervisor [redacted] for inspiring visits, helpful conversations, and the good collaboration.

I want to express my very special gratitude to [redacted] for the exceptional support. It was always a great pleasure to work with you. Thank you for all the rewarding discussions and the scientific input.

I acknowledge the Max Planck Graduate Center for financial support in the course of my doctoral thesis, which further enabled me to attend several seminars and conferences all around the world.

Throughout my doctoral thesis, I was fortunate to have congenial cooperation partner to work with on these diversified projects:

Being part of the Max Planck Graduate Center was a great opportunity for me, as I was able to work with [redacted]. Thank you for adding the biomedical aspect to my work and the inspiring as well as pleasant cooperation.

Thank you, [redacted] and [redacted], not only for participating actively in the Au-Pd project and your untiring work, but even more for the wonderful time during your stay in our group.

I am thankful to [redacted] and [redacted] for being so motivated and eager bachelor students. I also thank all of the other bachelor students, which I supervised together with Nawaz, for the very good collaboration.

Special gratitude goes to [redacted] and [redacted] for the good collaboration.

I am indebted to [redacted] for the great collaboration and the readiness to support our work at any time. Thank you for the scientific input and the discussions.

Special gratitude also goes to [redacted] for introducing me into the world of Magnetic Resonance Imaging and the support throughout all the experiments.

I am thankful for collective efforts, good collaboration, and a supportive atmosphere to [redacted] and [redacted].

I acknowledge [redacted], [redacted], [redacted] and [redacted] for their support and time-consuming HR-TEM analysis. Moreover, I like to thank [redacted] for the pleasant cooperation and the brilliant HR-TEM data.

I am thankful to [redacted] for his assistance on refinement of X-ray diffraction data and numerous helpful discussions.

I thank [redacted], [redacted] and [redacted] for the close collaboration.

During my time in the group, I enjoyed working with [redacted] and [redacted]. Thank you for your efforts in managing our group.

I like to thank our Bio-Nano and TEM Crew as well as the whole AK Tremel Research Group for the cooperative work, the inspiring discussions, the creative and pleasant working atmosphere as well as the fun time during group activities and BBQ events.

Finally, I am most grateful to my great and exceptional parents [redacted] and [redacted] for their loving support as long as I can remember. Thank you for being always there when I needed you. I am also profoundly grateful to my aunt [redacted] for every kind of encouragement and to my grandfather [redacted] who would have loved to see this achievement accomplished.

Contents

1 Bio-Nano: Theranostic At Cellular Level - An Introduction 1

1

Bio-Nano: Theranostic At Cellular Level - An Introduction

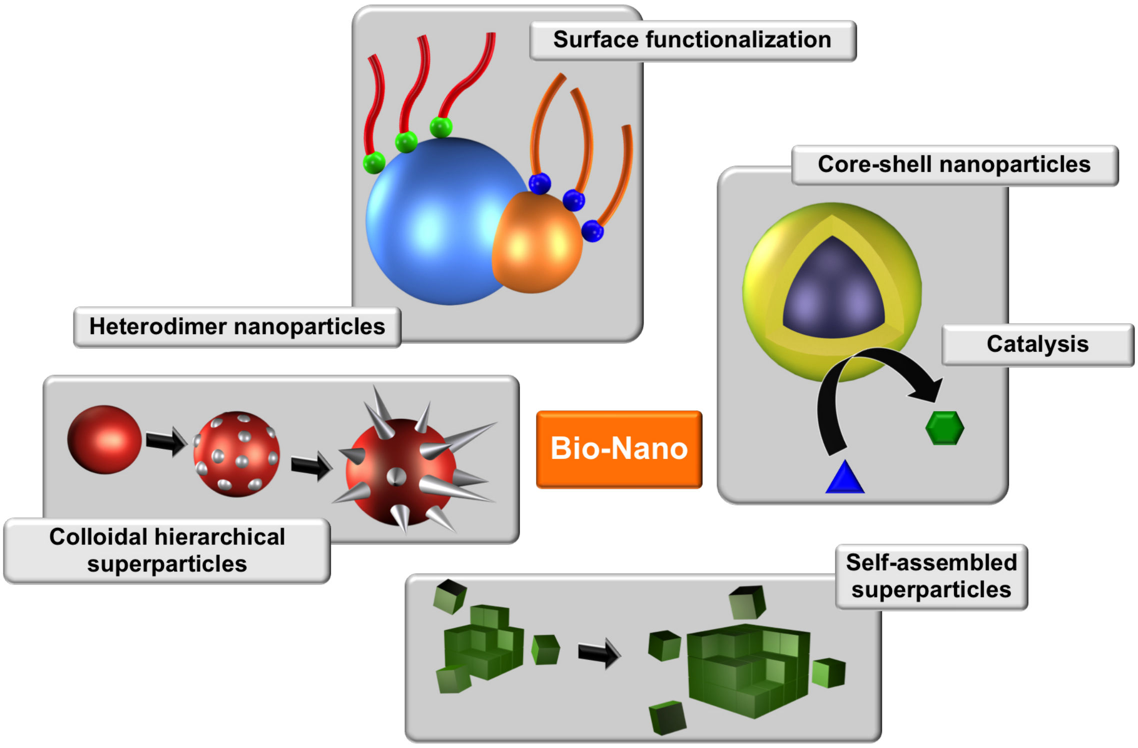

This chapter contains parts of an adapted reproduction of the book chapter "Bio-Nano: Theranostic At Cellular Level" in the book "The Role of Particulate Nature in Pharmaceuticals" by Editor Henk Merkus to be published in the Springer Series "Advances in the Pharmaceutical Sciences". A detailed Authorship Statement of the publication is attached in the Appendix of this dissertation. The following introduction chapter accommodates the part written by Martin Klünker.

1.1 Abstract

Functionalized nanoparticles (NPs) are important platforms for targeted drug delivery and multimodal imaging. Materials scientists provide tailor-made tools for medical research, diagnosis and treatment. These tools are rationally designed to have defined functions. Still, the value of these tools can only be determined by the users in medical sciences that develop assays for applying these tools. Until now, little is known about the impact of multifunctional particles that display intrinsic chemical and physical asymmetry which poses new challenges for cells associated with the amphiphilicity, dipole moments and chemical diversity/patchiness of the functionalized nanoparticles. Why is it important to study the impact of anisotropic multifunctional particles on biological cells extending the intricacy of the problem even further? Current nanotechnology projects that started during the past few years focus on the "supramolecular" weak binding of functionalized particles with the goal to form larger ensembles with new functionalities. Thus, one may anticipate new phenomena associated with the exposure of human tissue to the primary building blocks of these new materials. Despite the challenges that still have to be met, multifunctional nanoparticles provide fascinating opportunities for tailoring properties that are not possible with other types of therapeutics. As more clinical data become available, the nanoparticle strategy will improve to such an extent that more sophisticated tools actually reach the clinic.

Nanoscopic structures exhibit exceptional properties and characteristics and differentiate noticeably from their bulk counterparts. The origin of most new properties in multicomponent nanoparticles is related to their small size and special morphology. Their size significantly increases the number of surface atoms by increasing the surface-to-volume ratio, which leads to new chemical and physical properties. At the same time, the surface structure, determined by the shape and morphology of the nanoparticles, plays a pronounced role for the chemical and physical behavior of the nanostructures.

One of the first examples for the use of colloidal nanoparticles is an ancient Roman glass cup called "Lycurgus Cup" which contains gold nanoparticles causing a change of the glass color from red to green depending on the direction of illumination.[1] It was until the 19th century before Michael Faraday conducted breakthrough experiments on colloidal gold nanoparticles by reducing tetrachloroaurate with white phosphorus.[2] Since these experiments, important progress has been made in nanoscience: Father and son Ostwald studied the influence of particle size on the growth process *via* ripening,[3] further synthetic procedures were devised such as the trisodium citrate reduction established by Turkevich,[4] and a nucleation model, adapted later for nanoparticles, was proposed by LaMer and Dinegar.[5, 6] This knowledge led to a better understanding of nanomaterials and assisted to tune them towards specific applications. Nowadays the focus of researchers working in the area of nanoscience has stretched to demanding topics such as human health care, catalysis, renewable energy and nano-intelligence. Consequently, the diversity of nanostructures has reached a climax.

1.2 Janus Particles, Superparticles and Core-Shell Particles

Along with (spherical) monodisperse metal, metal oxide and semiconductor nanoparticles[7, 8] and nanoalloys,[9] three forms of heterodimeric nanoparticles are most intriguing: Metal-metal oxide heterodimers synthesized as (i) two-domain systems with solid state interface, often also with different surface functionalization of the metal and the metal oxide domain, known as eponym Janus particles (from the Roman god of beginnings and gates, Janus, who has two distinctive and opposite faces),[10] as (ii) colloidal superparticles, *i.e.* mesoscale particles defined as size- and shape-controlled assemblies from nanoscale building blocks,[11, 12] and as (iii) core-shell nanoparticles, where a core material is covered by a shell of another material often with variable shell thickness, including mesoporous core-systems for drug load and shells as gate system.[13, 14] We will discuss the role of these three morphologies in more detail starting with Janus-type particles.

1.2.1 Janus Particles

A key factor for the synthesis of monodisperse nanocrystals is the control of thermodynamics and kinetics by separating a short burst-nucleation stage from subsequent size-focusing by a diffusion-controlled growth process. Size-tuning can then be obtained by harmonizing the monomer consumption between the nucleation and growth stage. Generally, two methodologies are used to initiate a burst-nucleation process by oversaturation of monomers in the reaction mixture. In the heat-up approach active monomers are formed gradually from precursor molecules until a critical supersaturation is reached leading to burst nucleation. The hot-injection approach creates the critical supersaturation instantaneous by injecting the precursor solution into a hot reaction mixture. This also lowers the reaction temperature and prevents additional nucleation processes after burst nucleation.[17–19] Surfactants can stabilize the highly reactive surfaces and prevent agglomeration during the size focusing growth process.[20, 21] A critical supersaturation level of the monomer is required because of the large energy barrier of homogeneous nucleation. In classical nucleation theory (CNT) the positive surface energy term increases because of the formation of new surface and exceeds the negative volume energy term of newly generated volume. This results in an overall positive Gibbs free energy term until a critical radius of the nucleus is reached.[17, 18, 22] In recent years much progress was made to carefully evaluate these parameters and control the growth of monodisperse particles.[7] However, to obtain anisotropic structures[23] with cubic,[24] truncated[25] or rod-like morphologies, it is crucial to induce the symmetry break required for promoting anisotropy and to control the reaction kinetics and the facet specific adsorption of organic stabilizing ligands[20, 26] with dynamic temperature-dependent adhesion and diffusion rates,[21] twinning defects,[17, 27, 28] oriented attachment,[29, 30] chemical etching/galvanic displacement,[31, 32] or template assisted growth.[14, 33]

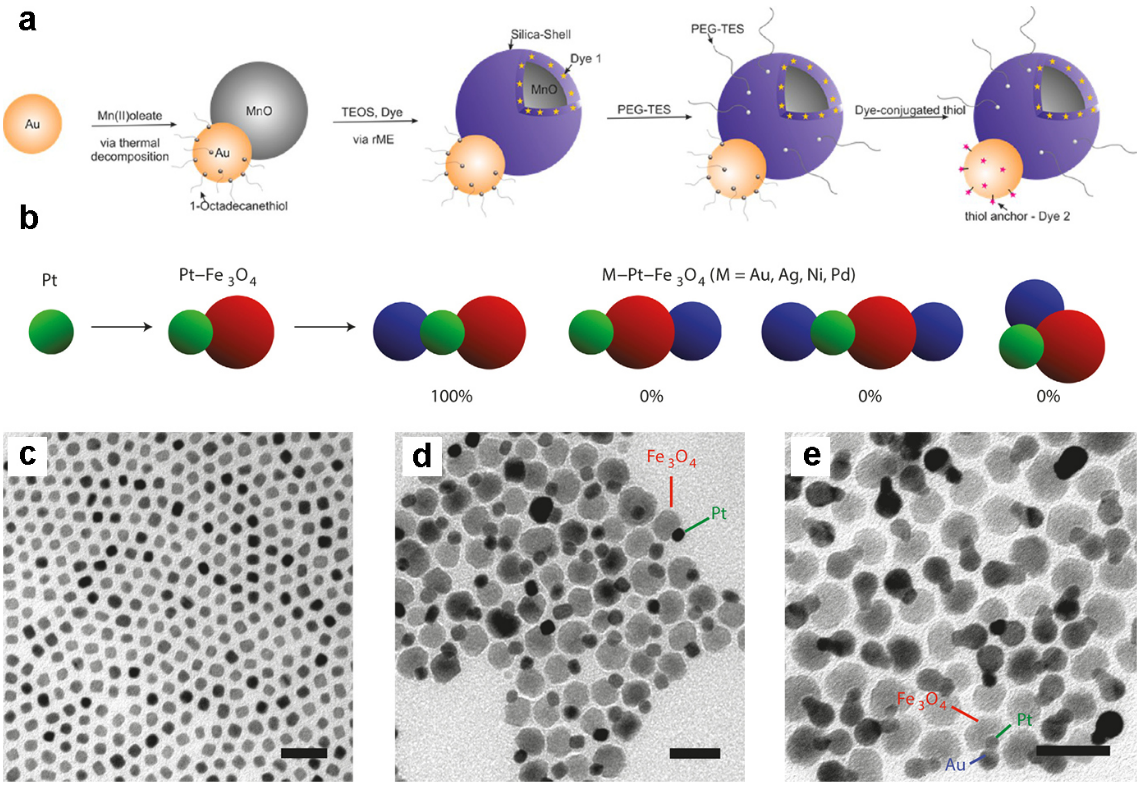

Figure 1.1: (a) Seed-mediated synthesis of Au@MnO heterodimers, subsequent encapsulation with silica and functionalization of the SiO_2-shell as well as the Au domain. Adapted with permission from ref.[15]. (b) Schematic showing the multistep synthesis of M–Pt–Fe_3O_4 heterotrimers, along with the most significant possible products and their observed frequencies (expressed as the percentage of observed heterotrimers, not total yield). Representative TEM images show (c) Pt nanoparticle seeds, (d) Pt–Fe_3O_4 heterodimers and (e) Au–Pt–Fe_3O_4 heterotrimers. All scale bars are 25 nm. Adapted with permission from ref.[16].

Moving to heterodimer structures, the interplay of energy and structural effects becomes more complex as more interaction factors occur simultaneously. One widely employed technique for the synthesis of heterodimeric nanoparticles, containing at least two different materials, is the seed mediated growth approach where preformed seed nanoparticles are used to grow one or more domains of a second material onto it.[20, 25] According to CNT, heterogeneous nucleation is favored compared to homogeneous nucleation because of a lower energy barrier which results in a lower Gibbs free energy and a lower chemical potential.[17, 18, 22] The reaction takes place at a critical thermodynamic-kinetic crossover. In addition, atomic diffusion, facet specific reactivity, surface wetting properties as well as interfacial stress and strain play major roles. Epitaxial growth, where the crystallographic orientation of the seed particle is preserved during addition of a second material, is important for tuning the properties of the different domains after they have merged.[34–36] As an interface between two materials is formed, several synergistic effects can be observed. In typical solid-state vapor deposition techniques a lattice mismatch of 1-3% is tolerated for epitaxial growth.[37] In solution-phase or beaker epitaxy a lattice mismatch of 7-12% can be surmounted when chemical match, temperature, solvents and surfactants are chosen carefully.[38, 39]

For controlling the formation of heterodimers two factors are important: (i) The amount of seed particles and the amount of precursor for the second domain determines the size ratio between the seed and second domain. (ii) The polarity of the solvent regulates the quantity of second domains. As shown for Au@Fe_3O_4[40] and Au@MnO[15, 41, 42] (Figure 1.1a), the nucleation of the metal oxide domain onto Au seeds in an apolar solvent leads to a withdrawal of electron density from Au and transfer to iron oxide through the interface and subsequent electron deficiency of Au, which prevents the nucleation of more than one iron oxide domain. When a polar solvent is used instead, electron density can be provided to the Au seed by the solvent, allowing the formation of multiple nucleation sites. For heterogeneous nucleation, the change of the Gibbs free surface energy is associated with the difference between the surface energies of both materials and a positive solid-solid interface term. Heterogeneous nucleation with layer-by-layer deposition for epitaxial growth is typically related to the Frank – van der Merwe mechanism where the overall Gibbs free surface energy is positive because the surface energy of the second material is lower than that of the first material, and the interface term is small.[37, 43] The surface energy is influenced by the exposed surface and the stabilizing ligands, whereas the interface term is controlled by binding strength and lattice mismatch. For tuning the chemical and physical properties of heterodimeric Janus particles interfacial electronic communication is essential. Direct contact of a noble metal and a semiconductor leads to the formation of a Schottky barrier.[44, 45] Electrons from the Fermi level of the noble metal are transferred to the semiconductor conduction band which causes a downwards bending of the conduction band. The Fermi levels of both materials are equilibrated. This leads to a charge accumulation at the interface and blocks electron transfer from the noble metal to the semiconductor. First observed for Au@CdS, the Schottky barrier blocks the electron-hole recombination after photo excitation of the semiconductor and therefore quenches photoluminescence.[46] This is especially relevant for (photo)catalysis.[38, 47–50] The electronic interplay is also reflected in altered surface plasmon resonance (SPR) and magnetic properties of Au@Fe_3O_4. The SPR is red-shifted compared to that of pure Au nanoparticles because of the change in the local dielectric environment caused by the high refractive index of iron oxide.[44, 46, 51, 52] The magnetic coercivity is higher and the remanence is lower for heterodimeric Au@Fe_3O_4 compared to Fe_3O_4 owing to a decreased number of nearest Fe neighbors at the interface. This leads to a smaller interatomic exchange coupling and larger spin canting effects.[53] As a result of the anisotropy, higher magnetic fields are needed to align the spins.[44, 46, 52] The electronic communication can also be influenced by surface chemistry; *e.g.* by functionalizing Ag in Ag@Fe_3O_4 with thiols the red shift of the SPR can be suppressed.[44, 54] A broad variety of heterodimers such as Au@TiO_2,[55–57] Pt@Fe_3O_4[58] or Au@ZnO[56, 59] with different morphologies have been reported. Similarly, trimer systems pointing towards multifunctional

lab-on-a-particle chemistry have been demonstrated.[46, 60] Schaak and coworkers combined Au, Ag, Ni or Pd with Pt@Fe_3O_4, but those structures are still challenging due to the complex reaction framework (Figure 1.1b-e).[16]
The ability to functionalize the different domains of heterodimeric nanoparticles individually and generating Janus particles (Figure 1.1a) makes them promising candidates for multiple applications reaching from catalysis[48, 61, 62] to biomedical applications[63, 64] in theranostics.[65] Amphiphilic Janus particles can be self-assembled for nanocapsules and –membranes.[66]

1.2.2 Superparticles

Superparticles are size- and shape-controlled nanoparticle assemblies in the form of colloidal particles.[69, 70] The individual nanoparticles can be viewed conceptually as artificial atoms, organized in an ordered superlattice structure, in order to generate new collective properties.[71, 72] This has been valuable for various applications in optoelectronics,[73] biochemistry,[74] plasmonics,[75] or storage devices.[76] Typically, solvophobic interactions are used to assemble the superparticles from their nanoparticle building blocks (Figure 1.2a-e).[11, 77] The nucleation of superparticles does not have a characteristic free-energy barrier like that of nanocrystals. The molecular or ionic precursors of nanocrystals are in true solutions and therefore have very different surface properties (no surface) from those of nuclei (solid nanophase, large surface area) that are formed during nucleation. Nanocrystal nucleation is accompanied by an increase in the volume and surface of the nuclei. The change of the total Gibbs free energy during nucleation is a balance between the energy gain due to the new volume (lattice energy) and the energy loss invested to generate the new surface (surface energy). The nucleation energy barrier ΔG^* needed to form a spherical nucleus is important for the separation of the nucleation and growth steps in nanocrystal synthesis, which is relevant for the synthesis of monodisperse nanocrystals. In contrast, the precursors for superparticle growth are nanocrystals retaining their own surface boundary and thus form a separate phase in the dispersion solution. The chemical and physical properties of the nanoparticle precursors are very similar to those of the resulting nuclei and/or superparticles. The free energy to form the surface of superparticle nuclei will be small. The decrease of the surface area will lead to a decrease in surface energy due to the surface binding between nanocrystals. In addition, the release of solvent molecules will add a large entropic contribution to the Gibbs free energy. Superparticle nucleation does not exhibit a characteristic free energy barrier as observed in nanocrystal nucleation.[21] The lack of a thermodynamic nucleation energy barrier makes it difficult to achieve the separation of nucleation and growth in superparticle synthesis, which leads to concurrent nucleation and growth, thus resulting in particles with a poor size distribution.
The Gibbs–Thomson equation does not apply to superparticle growth systems. Superparticles do not exhibit size-dependent "solubility" in their dispersion media because their surface properties are very close to those of their nanocrystal building blocks. In contrast, colloidal nanocrystals can be dissolved into atomic or molecular species

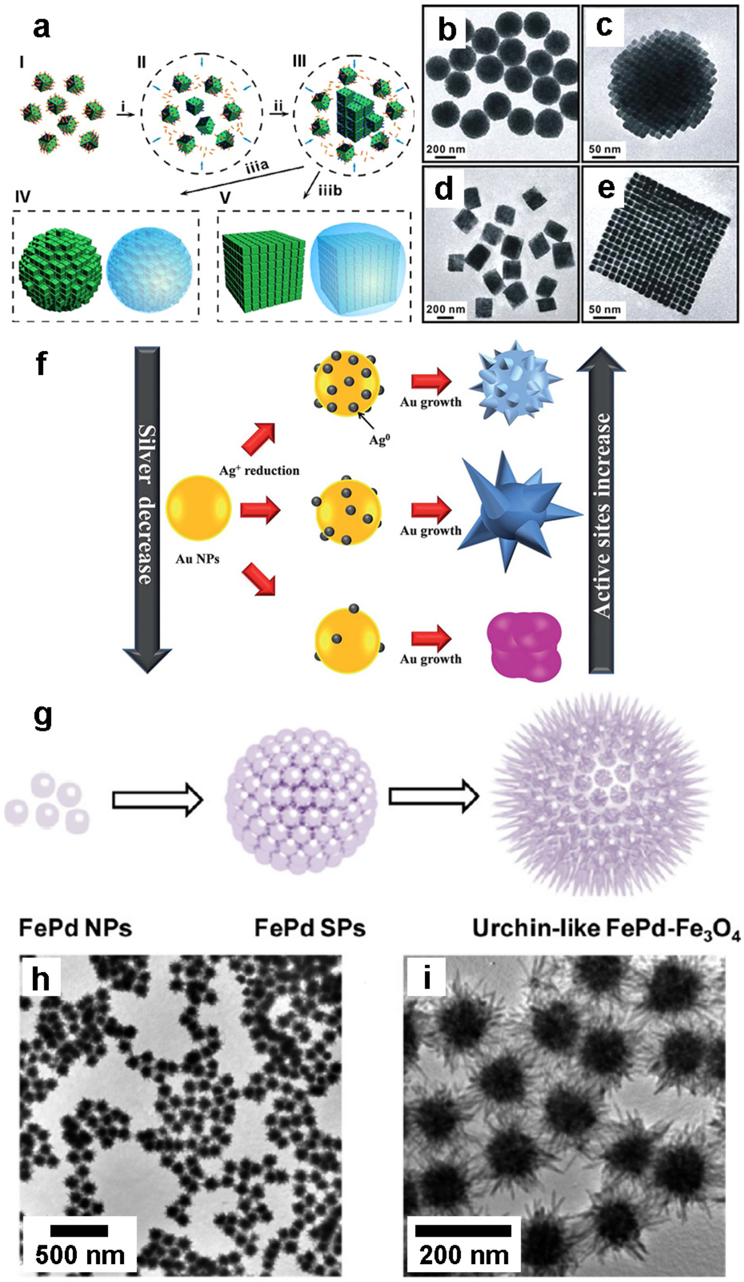

Figure 1.2: (a) Formation of colloidal superparticles from iron oxide nanocubes. Nanocube micelles (I), superparticles embryo (II, III), spherical (IV) and cube-shaped superparticles (V). Embryo formation (i), nanocube crystallization (ii) and superparticle formation (iii). (b) TEM images of sphere-shaped superparticles, (c) a spherical superparticle viewed along the [001] zone axis, (d) cube-shaped superparticles and (e) a cubic superparticle viewed along the [001] zone axis. Adapted with permission from ref.[11]. (f) Reduction of Ag^+-ions on the surface of Au nanoparticles to obtain star-shaped Au/Ag bimetallic superparticles. Decrease of $AgNO_3$ precursor leads to less formation of active Ag^0 sites resulting in the formation of fewer spikes. Adapted with permission from ref.[67]. (g) Schematic illustration of self-aggregation of FePd NPs into FePd superparticles and the formation of urchin-like FePd-Fe_3O_4 composite superparticles. (h, i) TEM images of the urchin-like FePd-Fe_3O_4 composite superparticles with an overall Fe/Pd ratio of 74/26. Adapted with permission from ref.[68].

in growth solution, and exhibit size-dependent solubility owing to a surface effect governed by the Gibbs–Thomson equation.[18, 78] The solubility of the nanocrystals increases as their size decreases. This size-dependent property is the thermodynamic basis of the Ostwald ripening process: Smaller nanocrystals redissolve and redeposit onto larger particles.

Another point is the surface functionalization itself. The surface ligands protecting colloidal particles allow for numerous particle interactions with multiple assembly geometries.[79] The identical surface functionalization can be a disadvantage in the organization of the colloidal particles to superparticles as well.[80] Their dispersions are typically not stable against aggregation or agglomeration. The forces responsible for the assembly of superparticles are long-range van der Waals/London forces based on induced dipole[80] along with solvophobic interactions.[69, 77, 81] Upon addition of a poor solvent for the colloidal nanoparticles the surface tension at the interface rises, and the solvent shell is minimized. As a result, colliding particles reduce their surface area and surface energy by aggregation and superparticle formation. Electrostatically charged surfaces should be avoided because of high-range electrostatic repulsion forces. Steric interactions from uncharged organic ligands can be both, attractive and repulsive. When such modified colloidal nanoparticles come into close proximity in a poor solvent, the solvent shell is reduced and solvent molecules are released. The concomitant entropy gain forms an attractive force. When the organic ligands come into contact by virtue of nanoparticle assembly, attractive van der Waals forces can arise but also steric hindrance may lead to repulsive forces.[81]

Nevertheless, superparticles by nanoparticle assembly lack a direct connection of the building blocks and therefore a direct electronic communication as heteroparticles obtained by epitaxial growth. This may be a disadvantage for applications where electronic or magnetic interfacial crosstalk combined with large surface areas is necessary (*e.g.* biomedical theranostic,[67, 82] (photo)catalysis,[83] enzyme mimetics[84]). Here, the concept of heterodimers with the benefits of Schottky junctions, diversive functionalization possibilities and reaction control can be extended to multidomain systems on a single seed particle, *i.e.* colloidal superparticles. Anisotropic and branched structures can be designed and synthesized using colloidal chemistry protocols.[32] However, it is worth mentioning that in order to achieve such epitaxially grown superparticles, one needs some intelligently designed synthetic protocols. As an example, when seedless growth is desired, the high symmetry of the closed-packed fcc-type structures must be broken. Strategies include axial growth along five-fold twin defects as observed in the early stages of noble metal nanocrystals,[25, 85] or initial stage surface protection of thermodynamically stable Wulff polyhedra by chemisorption of capping agents to control the growth rate of different surface facets.[20, 86] Superparticle-like branched and anisotropic structures can also be realized through ion assistance or chemical etching. Urchin-like growth of Au nanoparticles can be induced through the deposition of Ag nuclei on spherical Au nanoparticles (Figure 1.2f).[67] Anisotropic Pd nanoparticles can be synthesized with the aid of copper(II)-ions,[83] whereas nitrate anions can promote anisotropic growth of Pt nanoparticles.[87] The difference in the chemical potential of various noble metals and associated redox reactions can be used to reshape nanocrystals *via* a seed mediated growth process[88] or to generate branched Au structures by a Fe nanoparticle assisted templated growth.[89] Typical oxidative etching by addition of facet-specific etching agents like H_2O_2 or chlorine ions can also transform isotropic structures.[90, 91] Hedgehog-like particles can be designed by the growth of iron oxide nanorods on preformed seed particles with iron pentacarbonyl (Figure 1.2g-i)[68] Recently our group demonstrated that this synthetic approach can be extended on different seed particle materials (Ni, Pd) and different seed particle morphologies (nanotetrahedra and nanoplates) with epitaxial growth of the nanorods. The superparticles exhibit enhanced catalytic activity compared to their seed particles.[92, 93]

1.2.3 Core-Shell Particles

Core-shell particles are another type of heteroparticles where the second domain is present as a shell around a core material *e.g.* through multiple nucleation spots in a polar solvent (*vide supra*). Similarly, any organic or silica coating of inorganic nanoparticles is a wide synthetic field for core-shell nanoparticles.[94] Therefore core-shell nanoparticles can be divided into many categories based on their composition. A few important types will be discussed here. A widely used type of core-shell particles includes an inorganic core combined with an inorganic shell material, with silica as the most common example. Advantages of silica coatings on inorganic nanoparticles include extended suspension stability in aqueous media, various surface functionalization possibilities as well as improved biocompatibility.[95–97] Especially for plasmon active noble metals like Au, a silica shell has been shown to strongly influence the surface plasmon properties as a function of the shell thickness.[98] A typical synthesis of silica uses a modified sol-gel processing (Stöber process) based on hydrolysis and polycondensation of metal/silicon alkoxides under specific pH, temperature and alkoxide concentration conditions.[99] Particularly the pH value plays an important role for the hydrolysis of tetraalkoxy silanes under acidic as well as basic conditions. Usually a basic catalysis is used to increase the rate of condensation and to control the particle morphology by inhibiting a strong gelation to network structures.[100, 101]

Another possibility to obtain monodisperse and small silica particles/coatings is the reverse microemulsion technique. By applying surfactants, a water in oil microemulsion in form of aqueous nanodroplets is generated. These droplets are used subsequently as reaction containment for the formation of silica particles/coatings. The size of the micelles determines the particle size and morphology.[96, 97] The shell thickness can be controlled by the ratio of base/tetraalkoxy silane/number of seed particles. A template chemistry serves also for the formation of mesoporous silica structures for drug loading and triggered payload release.[102] Apart from silica coatings, inorganic core materials can be coated with other inorganic materials to form core-shell structures mainly to alter the chemical and physical properties of the core material. An Au coating is frequently used to provide chemical stabilization from oxidation/corrosion and add surface functionality by introducing the opportunity to apply amine and thiol functionalization. For catalytic applications, surface-enhanced Raman scattering (SERS) of Pd is low compared to that of Au or Ag due to the red-shifted SPR and strong morphology dependence.[103–105] By coating Au nanoparticles with Pd the SERS activity can be increased and fine-tuned owing to the electromagnetic communication.[103] Au coatings on silica core particles also exhibit an excellent tunability of the optical properties, suitable for optical imaging strategies and photothermal therapy.[106] Here the properties depend on the size of the core and the shell thickness. Further attention has been given to core-shell structures where both components are magnetic[107] or one component is a semiconductor and the second one the magnetic domain. This is particularly useful for bio-imaging,[108] catalysis,[109] and energy applications.[110] Other valuable systems contain one or both components of the core-shell structure from organic/polymeric nature. Often an organic shell is used to protect the core material or to create biocompatibility and surface functionality. Common strategies include the coating of inorganic core materials with hydrophilic polymers such as polyethylene glycol (PEG)[111–114] or polysaccharides such as dextran.[115] Further details on nanomaterial functionalization and surface modification strategies will be given in the section surface modification (*vide infra*). Full organic core-shell structures mainly use polymers on the basis of their glass transition temperature to prepare biodegradable drug encapsulation carriers for biomedical applications.[116]

1.3 Surface Modification

Surface modification is a *conditio sine qua non* for nanoparticle synthesis to be eligible for biomedical application. The nanoparticles are prepared either in aqueous solution or in organic solvents. In both cases, a suitable application of surfactants is required to prevent agglomeration and to provide colloidal stability. These surfactants also protect pure metal nanoparticles whose surfaces are highly reactive for oxidation. When the nanoparticles, prepared in apolar solvents, are dispersible only in organic non-polar media because of their long aliphatic chain surfactants,[117, 118] a ligand exchange is mandatory for biomedical applications to achieve water solubility and physiological compatibility. Furthermore, surface functionalization can provide a control on the intrinsic chemical reactivity of the particles, which may unintentionally affect reaction pathways at the cellular level, and can protect from opsonization, because the nanoparticles are recognized by the immune system and subsequently covered with serum proteins and surrendered to phagocytosis.[119] The latter is often referred to as the stealth effect.[120–122] Besides silica functionalization there are a number of strategies for surface modification based on polymers available resulting in core-shell-like structures. The most important ones will now be discussed.

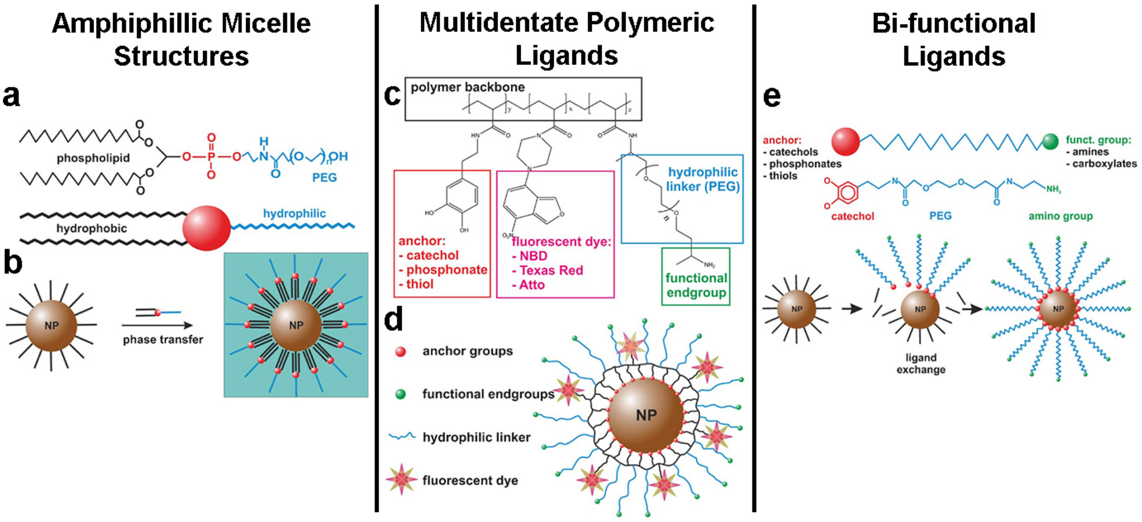

Figure 1.3: (a) Chemical structure of a PEG-phospholipid. (b) Coating procedure: The hydrophobic lipid tails are incorporated between the alkyl chains of the capping molecules on the nanoparticle surface, whereas the hydrophilic PEG chains point to the outside creating a hydrophilic shell. (c) Chemical structure of a typical multifunctional polymeric ligand. The co-polymer contains 3-hydroxytyramine (dopamine) as anchor group, a fluorescent dye, PEG chains and free amino groups for further functionalization. (d) Illustration of a magnetic NP modified with a multifunctional polymer. (e) Surface modification of magnetic nanoparticles using bi-functional ligands. These ligands consist of an anchor group conjugated to a hydrophilic linker carrying a functional end group. A key requirement for a successful exchange of the hydrophobic capping agents is the complete dispersability of the nanoparticles and the ligand molecules in the same solvent. Adapted with permission from ref.[123].

1.3.1 Amphiphillic Micelle Structures

This strategy does not change the initial apolar surfactant coating. Instead, a layer of amphiphilic surface active molecules like cetyltrimethylammonium bromide (CTAB) is assembled on the nanoparticles. The long hydrophobic alkyl chains of CTAB interact with the initial apolar surfactant on the surface (*e.g.* oleylamine, oleic acid) through van der Waals forces. The polar ammonium moiety enables water dispersability and stabilization through electrostatic repulsion by forming a micelle-like structure.[124, 125] This strategy is often applied for stabilizing Au colloids,[126] but it lacks long-term stability and robustness against shear forces.[125] Further evolution of this strategy includes amphiphilic polymer structures where the apolar part consist of phospholipids and the polar part is comprised of polyethylene glycol (PEG) which can also serve as an anchor for additional cell targeting moieties (Figure 1.3a, b).[127, 128] Thermoresponsive polymers are also available for temperature dependent drug release mechanisms as demonstrated by Qin *et al.* who combined thermosensitive poly(*N*-isopropylacrylamide) (PNIPAAm) with a hydrophobic poly(maleic anhydride-*alt*-1-octadecene) backbone to coat Fe_3O_4 nanoparticles.[129] Amphiphilic saccharide structures[130] and amphiphilic triblock copolymer structures were used as well.[128] Nevertheless, the hydrodynamic radius is increased due to the micellar structures,[131] which can affect the *in vivo* application. Due to the dynamic equilibrium a ligand exchange by washing or diluting is possible.

1.3.2 Multidentate Polymeric Ligands

Another strategy involves the replacement of the original apolar surfactant coating through a multifunctional polymeric ligand (Figure 1.3c, d). Here PEG is commonly used because of its antifouling, low polydispersity, non-ionic and non-toxic character.[132] For nanoparticle attachment the PEG chains are equipped with a functional anchor group. Most suitable is a chemisorption of the anchoring group on the nanoparticle based on Pearson's HSAB principle,[133] where Pearson-soft materials like Au show high affinity towards thiol groups, and Pearson-hard materials like transition metal oxides (*e.g.* iron oxides, manganese oxides) show high affinity towards oxygen groups. A variety of polymers like poly(ethyleneimine)[134] or poly(amidoamine)[135] and anchoring groups like phosphine oxide,[136] amines,[137] or carboxylates[138] have been used. When these anchoring ligands are executed as chelating ligands like catechols[139] or bidentate thiols,[140] the binding affinity is reinforced. Accordingly, a large variety of polymer-anchor combinations have been explored covering cross-linked polymers,[141] which provide more mechanical stability, and the introduction of terminal functional groups for attachment of dyes or targeting ligands through click chemistry.[142] Nevertheless, a drawback is that the nanoparticles can be linked through one polymer chain resulting in aggregates disadvantageous for biomedical application.

1.3.3 Bi-functional Ligands

Bi-functional ligands are used to replace the surface active capping agents from the particles. Those ligands contain an anchor group (catechol,[143, 144] thiol,[145] phosphonate,[146] or carboxylate[147]), a spacer (typically alkyl chain or PEG) and a reactive head group to bind functional molecules like dyes, targeting ligands or drug molecules (Figure 1.3e). Advantages of bi-functional ligands compared to the multidentate polymeric ligands are: i) a more compact structure, ii) precise adaptability of the spacer chain length to obtain the best colloidal stability and iii) independent functionalization possibility. Different polymer moieties can be used for functionalization of the same particle: A fluorescence dye can be attached to the nanoparticle *via* a short polymer chain, which is independent of a functional amine group connected *via* a second, long chain polymer, making the amine group easily accessible for subsequent drug coupling without interfering with the dye. As described above, catechol ligands are the most common anchor groups[114] because of their excellent binding affinity (also to HSAB ambivalent materials like transition metals[148]) and superior chelating effect by improved orbital overlap, reduced steric hindrance through generation of five-membered rings and stabilization through

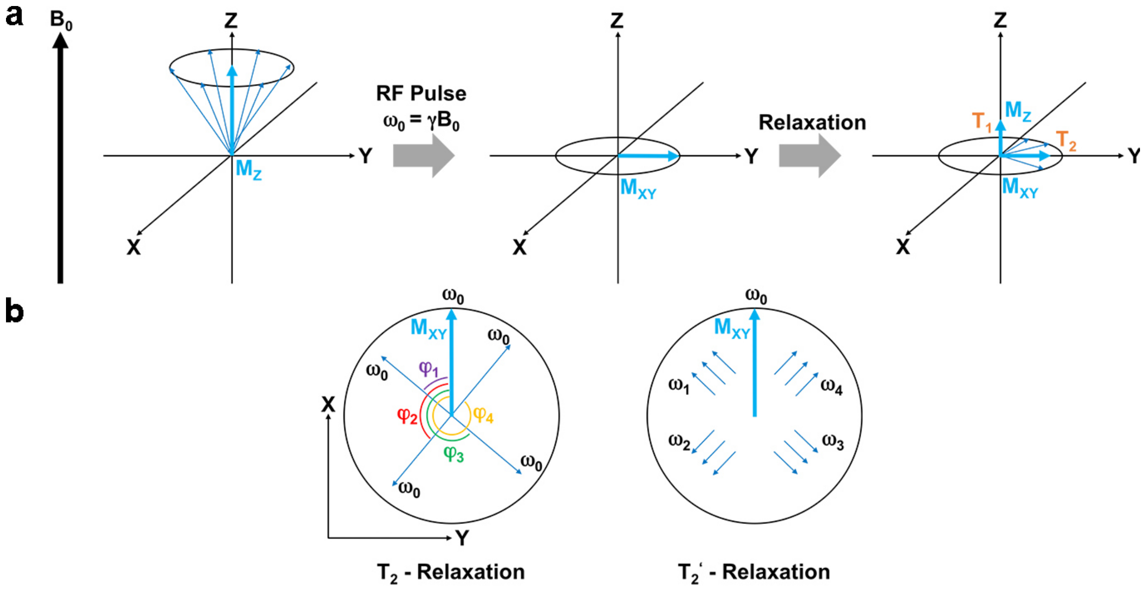

Figure 1.4: (a) Simplified nuclear magnetic resonance experiment. After application of the 90° excitation pulse with larmor frequency two different relaxation processes take place, restoring of the M_z magnetization (T_1-relaxation) and dephasation of the deflected spins reducing M_{xy} (T_2-relaxation). (b) T_2-relaxation with spontaneous phase differences and identical lamor frequency due to Brown- and Nèel-relaxation and T_2'-relaxation due to stationary local inhomogeneity of B_0 which additionally alters the Larmor frequency of several spin bundles. Idea for graphics from ref.[151].

electron delocalization.[149] However, catechols are prone to oxidation and subsequent polymerization resulting in insoluble polymers.[150]

1.4 Biomedical Application – Diagnostics and Therapy

Engineered multifunctional nanoparticles cover a wide range of applications in biomedicine and material science. They can easily be adjusted for specific use in diagnostics, therapy or materials science. Synthetic control combined with multiple surface functionalization strategies make them useful for multipurpose applications towards lab-on-a-particle structures.

1.4.1 Magnetic Resonance Imaging (MRI)

First theranostic approaches using magnetic iron oxide nanoparticles were made in the 1970's.[155] Since then, magnetic iron oxide nanoparticles have proven valuable for clinical use as MRI contrast agents.[156] However, first formulations of dextran coated superparamagnetic iron oxide nanoparticles (SPION) in clinical use (*e.g.* AMI-25[157]) showed poor monodispersity and increasable relaxation performance.[125] Until now

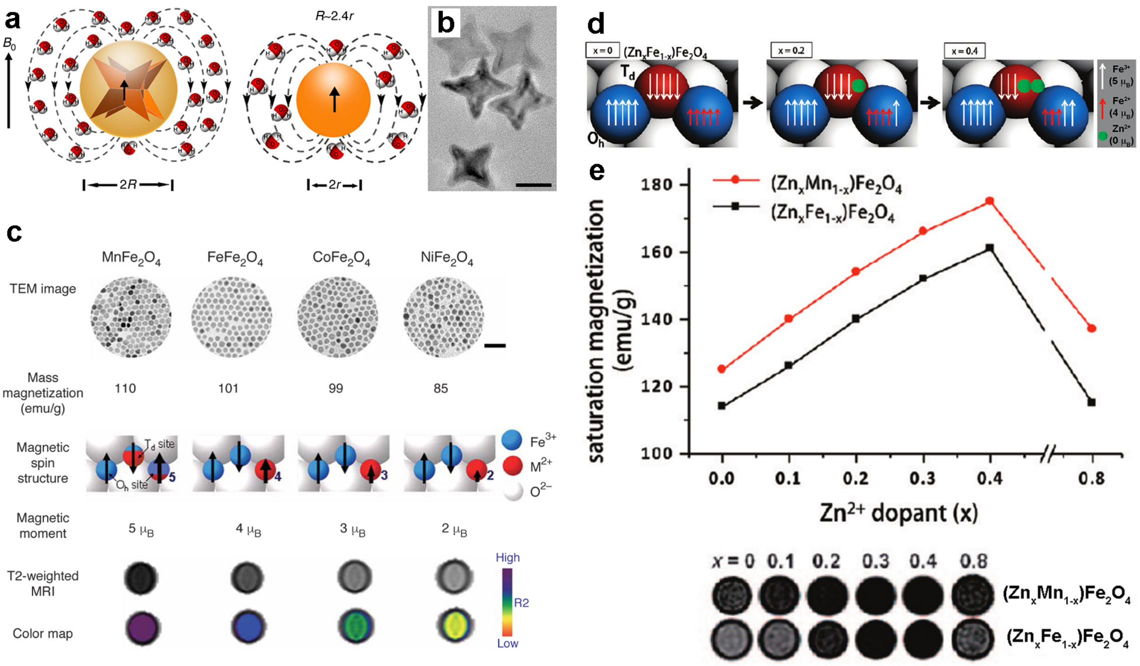

Figure 1.5: (a) Schematic cartoons showing the ball models of octapod and spherical iron oxide nanoparticles with the same geometric volume. The black dotted lines represent the magnetic field of the octapod and spherical iron oxide nanoparticles. The same length of black arrow means the same saturation magnetization (M_s) of octapod and spherical iron oxide nanoparticles. With the same geometric core volume, the octapod nanoparticles have much larger effective volume (radius, R) than the spherical nanoparticles (radius, r). (b) TEM image of octapod with average edge lengths of 30 nm. Scale bar 20 nm. Adapted with permission from ref.[152]. (c) Magnetism-engineered iron oxide nanoparticles and effects of their magnetic spin on MRI. TEM images show $MnFe_2O_4$, Fe_3O_4, $CoFe_2O_4$ and $NiFe_2O_4$ nanoparticles. Scale bar 50 nm. Additional data of mass magnetization values, magnetic spin structure, magnetic spin moment and T_2-weighted spin echo MR images with color map of R_2 relaxivity. Adapted with permission from ref.[153]. (d) Zn-doped magnetic nanoparticles for strong MRI contrast effect. Undoped ($x = 0$) and Zn^{2+} doped ($x = 0.2, 0.4$) magnetic spin alignment diagrams of inverse spinel-structured nanoparticles under magnetic field. (e) Graphs of M_s versus Zn^{2+} dopant moiety including T_2-weighted MR images of $(Zn_xM_{1-x})Fe_2O_4$. Adapted with permission from ref.[154].

many efforts have been made to understand the physical processes associated with magnetic relaxation and nanodimensional size as well as *in vivo* behavior of nanoparticles to improve their biocompatibility and performance. When protons are exposed in nuclear magnetic resonance (NMR) spectroscopy to an external homogeneous magnetic field (B_0) their nuclear spins start precessing with specific larmor frequencies along the direction of applied magnetic field (z-axis). Due to the two possible orientations of the nuclear spin of the protons and the resulting spin (dictated by the Boltzmann distribution) oriented along the direction of field, a small but detectable magnetization $M_z = M_0$ results along B_0. When a 90° radiofrequency pulse (P90) with larmor frequency is applied, the spins change their orientation with respect to the field and M_z decreases to zero. Additionally, the applied radiofrequency pulse bears a circular polarization perpendicular to B_0, which induces a rotation of the deflected magnetization vector in the *xy* plane where a detector coil is able to pick up the magnetization signal. Directly after the pulse $M_{xy} = M_0$,[158, 159] and two relaxation processes occur, which can be influenced by magnetic nanoparticles.

The longitudinal, positive or spin-lattice relaxation T_1 is associated with the return of the spins to the Boltzmann equilibrium and the concomitant restoration of M_z (Figure 1.4a). This arises from the realignment of the spins which were oriented perpendicular to the field B_0. The excess energy released through this process can be transferred to the water protons present in immediate vicinity (the "lattice", enthalpic process), and a T_1 enhancement or bright field imaging can be applied. The corresponding nanomaterials and their molecular counterparts (*e.g.* paramagnetic f^7-Gd^{3+} complexes) are strongly paramagnetic substances which can generate a fluctuating interference of the magnetic environment and additionally take over the excess relaxation energy through water adsorbance. A typical nanomaterial for T_1 contrast enhancement are MnO nanoparticles due to their antiferromagnetism. The T_1 activity results from the size of the particles and a magnetically disordered spin-glass-like surface layer, exhibiting spin-canting.[53, 160, 161] Here the surface spins are mostly uncompensated and not antiferromagnetically ordered. Additionally, the spins are canted and cannot fully align with the imposed magnetic field. The effect becomes more distinct with smaller particle size and larger surface area.[162].

The transversal, negative or spin-spin relaxation T_2 is coupled to the magnetization in the *xy* plane and occurs without energy transfer (entropic process, no effect on Boltzmann distribution, Figure 1.4a). It is based on the dephasing of the deflected spins which precess in the *xy* plane upon excitation through the radiofrequency pulse. Directly after the pulse they are all in phase, and therefore M_{xy} is maximized. The phase shift is induced by two factors: (i) fluctuating inhomogeneity of the microscopic environment based on Brownian relaxation (rotational external orientational fluctuations at the boundary to the solvent due to diffusion processes, *i.e.* particle rotation) and Néel-relaxation (internal rotation of the magnetic moments in the tissue due to thermal energy, *i.e.* spin rotation),[163] known as T_2 and (ii) stationary local inhomogeneity of B_0, which additionally alters the Larmor frequency of several spin bundles, known as T_2' (Figure 1.4b). Both processes ($T_2^* = T_2 + T_2'$) induce a drop of the free induction decay (FID) signal in the detector coil, but only T_2 is the desired relaxation time linked with the information about the microscopic environment. The T_2' part can be compensated by a 180° refocusing pulse (P180) in a spin-echo pulse sequence which brings the spins back to their original Larmor frequency. Thus, T_2 is accessible, which leads to less artifacts and higher resolution compared to T_2^* measurements (gradient-echo pulsing sequence).

The prerequisite for a good T_2 contrast agent is a high magnetic moment which supports the inhomogeneity of the microscopic environment by building an own magnetic field interfering with the detection field and therefore leading to a darkening of the MR image by fast reduction of the M_{xy} magnetization.[158, 159] Accordingly,

one-domain superparamagnetic nanoparticles are good candidates because of their large magnetic moment.
Tailoring magnetic nanoparticles for application in MRI diagnostics requires engineering of their magnetic characteristics. To achieve the best results one needs to adjust both, magnetic and physical properties of nanomaterials. For tuning the MRI relaxivities, magnetic properties such as saturation magnetization, coercivity and magnetocrystalline anisotropy as well as physical properties such as particle size, dispersity and surface stability must be evaluated and tuned.[154] For enhanceing the r_2 relaxivity ($r_2 = 1/T_2$) the quadratic dependency of the particle size and saturation magnetization should be considered, which leads to enhanced transversal contrast, if the effective radius of the superparamagnetic core and the saturation magnetization is increased.[164] This was demonstrated by Zhao *et al.* who synthesized iron oxide octapods as transversal contrast agent (Figure 1.5a, b).[152] They combined iron oxide with a saturation magnetization (M_s) up to 71 emu/g and a star-like octapod morphology which doubled the effective radius of the superparamagnetic core compared to a spherical iron oxide nanoparticle with same geometric core volume. Additionally, the anisotropy supports a more inhomogeneous local magnetic field compared to spherical nanoparticles resulting in better proton dephasing and reduced T_2 relaxation time. Nevertheless, enhancing the saturation magnetization might be a challenge due to spin canting effects, that lower the maximum saturation magnetization of the nanoparticles compared to their bulk counterparts,[165] and agglomeration phenomena even in the absence of an external magnetic field due to strong internal magnetization.[166] Lee *et al.* demonstrated a large saturation magnetization for manganese doped magnetite nanoparticles (Figure 1.5c).[153] Owing to the inverse spinel structure of magnetite, where a cubic face centered structure of oxide anions is combined with Fe^{3+} in tetrahedral (T_d) and octahedral sites (O_h) and Fe^{2+} in O_h sites, a total magnetic moment of 4 μB is expected.[167] Under an external magnetic field the ions in the octahedral site align parallel to the magnetic field delivering 5 μB from Fe^{3+} (d^5) and 4 μB from Fe^{2+} in high spin (d^6 hs) state. The Fe^{3+} ions in the tetrahedral sites align antiparallel to the magnetic field reducing the magnetic moment by 5 μB, leaving the 4 μB from Fe^{2+} as overall magnetic moment per unit. If Fe^{2+} is replaced by Ni^{2+} (d^8), Co^{2+} (d^7 hs) or Mn^{2+} (d^5) the magnetic moment is reduced to 2 μB, 3 μB or increased to 5 μB. The saturation magnetization is increased as well. In a consecutive work Jang *et al.* investigated the effect of non-magnetic Zn^{2+} on those iron and manganese spinels (Figure 1.5d, e).[168] They showed that Fe^{2+} in O_h sites is exchanged with Zn^{2+} which is located in T_d sites instead. Accordingly, Fe^{3+} from the T_d site moves to the O_h site and the antiparallel compensation of T_d and O_h sites is less, which in turn increases the overall magnetic moment.

1.4.2 Hyperthermia

A therapeutic approach based on the magnetic properties is hyperthermia treatment.[170, 171] Physically, magnetic nanoparticles can serve for energy dissipation and

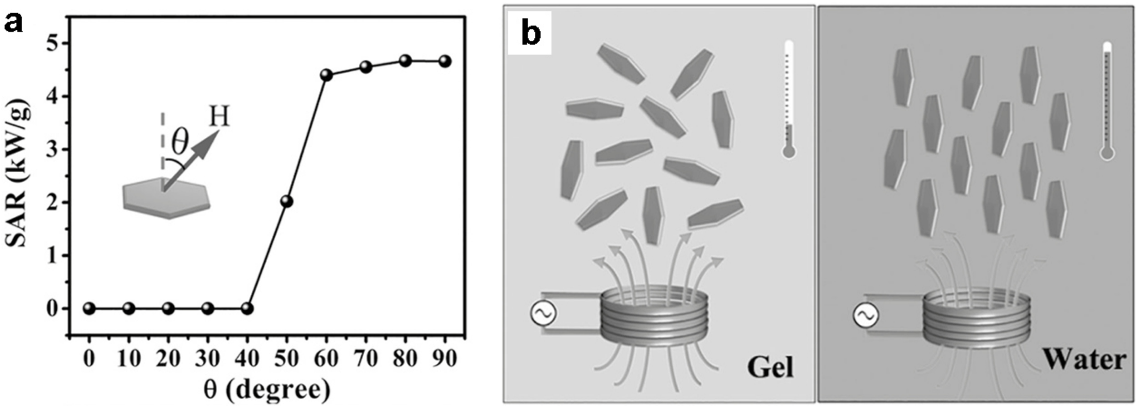

Figure 1.6: (a) Calculated SAR values of Fe_3O_4 nanodiscs when field is applied along different directions. (b) Illustration of orientations related magnetic hyperthermia of nanodiscs in different suspensions. Adapted with permission from ref.[169].

as heat generator. In an alternating current (AC) field heat emission *via* induction can be generated through repeated Néel- and Brownian-relaxation.[154] As a result of the thermal motion of the magnetic moments, the magnetization M is not in phase with the magnetic field (H) varying with time. This leads to a conversion of magnetic energy into heat.[171, 172] The heat emission, defined as specific loss power (SLP), is proportional to the saturation magnetization and reaches a maximum for a certain particle size and magnetic anisotropy.[173] It is also dependent on the heat capacity of the solvent and the mass of the magnetic material.[174, 175] Iron oxide nanocubes have been shown to exhibit higher specific absorption rates (SAR *i.e.* SLP) than their isotropic counterparts.[175] Additionally, dipolar effects depending on anisotropy can occur leading either to nanomaterial agglomeration or alignment in chains, which can reduce or increase the heating properties, respectively.[176] Iron oxide nanodiscs can be used to double the SAR values of oriented nanodiscs with respect to random orientation (Figure 1.6).[169] The nanodiscs align parallel to the AC field generating a maximum SAR of 4.66 kW/g. Zn substituted magnetite nanoparticles show potential for hyperthermia treatment owing to their high saturation magnetization.[168]

1.4.3 Computed Tomography (CT)

CT diagnostics measures the X-ray attenuation of X-ray photons penetrating tissue. The attenuation is linked to the mass attenuation coefficient (μ). Different tissues can be differentiated by differences in their mass attenuation. However, the difference in the μ values across the human soft tissue is not very substantial which makes application of contrast agents with distinct uptake in different tissue mandatory.[179] Two main processes are responsible for X-ray attenuation: Compton scattering and the photoelectric effect. Whereas a low X-ray energy results in a high exposure dose for the patient, because most X-rays are absorbed, a high X-ray energy lowers the patient's exposure and reduces the amount of Compton scattering through

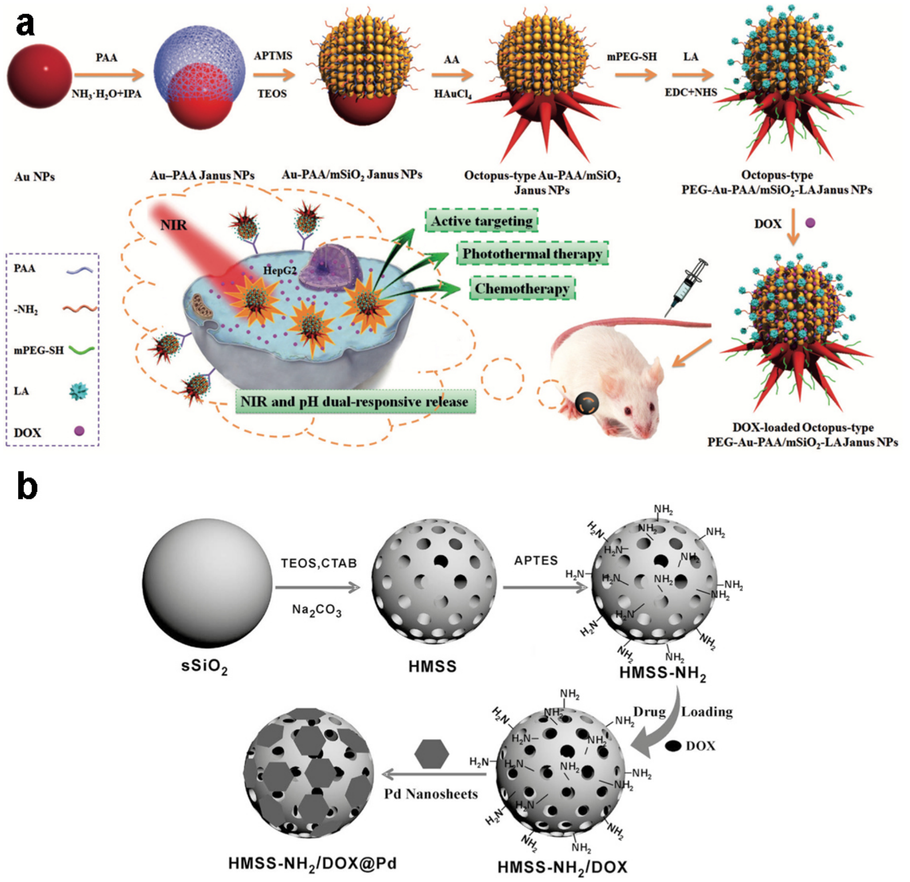

Figure 1.7: (a) Fabrication of octopus-type PEG-Au-PAA/mSiO_2-LA Janus nanoparticles with pH and NIR light dual-stimuli responsive properties for actively-targeted and chemo-photothermal cancer therapy *in vitro* and *in vivo*. IPA = isopropyl alcohol, PAA = poly(acrylic acid), mPEG-SH = methoxy-poly(ethylene glycol)-thiol, LA = lactobionic acid, DOX = doxorubicin. Adapted with permission from ref.[177]. (b) Schematic procedure for the preparation of HMSS–NH_2/DOX@Pd nanoparticles. HMSS = hollow mesoporous silica spheres, DOX = doxorubicin. Adapted with permission from ref.[178].

elastic impact. Consequently, the photoelectric effect dominates the attenuation which also leads to a strong increase of μ at the K-shell electron binding energy (K-edge).[180, 181] Typical X-ray spectra are taken between 57 and 69 keV with contrast agents exhibiting high atomic numbers for a good mass attenuation and K-edge values within the spectral boundaries.[180] A typical candidate for CT-contrast agents is Au because of its non-toxic and chemical inert behavior as well as morphologic and synthetic diversity combined with a high atomic mass for X-ray attenuation.[8, 182, 183] Combined with magnetic materials like Fe[145] or Gd chelates an application for dual mode imaging is possible.[184] Bi_2S_3 with an even higher relative atomic mass of Bi can serve as CT-contrast agent when the Bi^{3+} ions are sufficient stabilized by oleic acid or poly(vinylpyrrolidone) (PVP) to prevent reduction to chemically active Bi^0.[185] Recently, an Yb based CT-contrast agent was developed with improved

X-ray attenuation because the Yb K-edge energy of 61 keV is located within the typical energy range for CT spectra.[186]

1.4.4 Photothermal and Photodynamic Therapy

Visible or near infrared (NIR) light in combination with plasmon active metal nanoparticles can be used as an alternative heat or radical generating treatment, called phototherapy. Photothermal therapy is based on irradiation of plasmonic or photocatalytically active nanoparticles which transform the radiation into thermal energy.[187] Photodynamic therapy differs in the way the radiation energy is converted into chemically reactive species such as reactive oxygen species (ROS) *via* photosensitizers that subsequently initiate apoptosis of malignant tissue.[188] Especially Au,[82] Au/ZnO hybrids,[189] and Pd[190, 191] nanoparticles have gained interest for these applications since they exhibit a broad visible and tunable NIR SPR. The Zink group reported the use of octopus-type Janus nanoparticles for simultaneous photothermal and chemotherapy (Figure 1.7a).[177] They equipped Au nanoparticles with a poly(acrylic acid) (PAA) domain to form Janus particles. Subsequently, the PAA domain was used as template to grow mesoporous silica. Additional decoration of the Au domain with spikes lead to improved SPR. Finally, the particles were functionalized with methoxy-poly(ethylene glycol)-thiol (mPEG-SH) on the Au domain and lactobionic acid for active cell targeting on the mesoporous silica domain, carrying doxorubicin hydrochloride as chemotherapeutic agent. These designed multifunctional Janus particles were then used in an *in vivo* mouse model for photothermal therapy and NIR responsive drug release for chemotherapy. Similar dual therapeutic systems, where NIR irradiation is used both as photothermal therapy source and drug release, have been also established for Pd nanosheets in combination with mesoporous silica nanoparticles (MSNs, Figure 1.7b).[178] Tang *et al.* presented Pd nanosheets for NIR photothermal therapy and doxorubicin drug release.[192]

1.5 Electronic Properties of Nanomaterials

In recent years researchers have paid attention to explore the new electronic processes originating in artificial nanomaterial structures. Starting from luminescence in quantum dots (QDs),[193] complex interfacial electronic communication in heterodimers resulted in a variety of new applications. Owing to their fluorescent properties the heterodimers were utilized for biological detection and diagnostics.[122, 194, 195] The wide area of photocatalysis with nanomaterials mainly focuses on catalytic applications such as photovoltaics,[47] photodegradation,[196] and photogeneration.[49] Still, heterodimers containing noble metals and semiconductors are also of interest for many biochemical applications like photodynamic therapy or biomolecular detection/reaction[197] and diagnostics towards lab-on-a-particle architecture.[198] We will now take a closer look on the physical processes linked with QDs and their application in the area.[199]

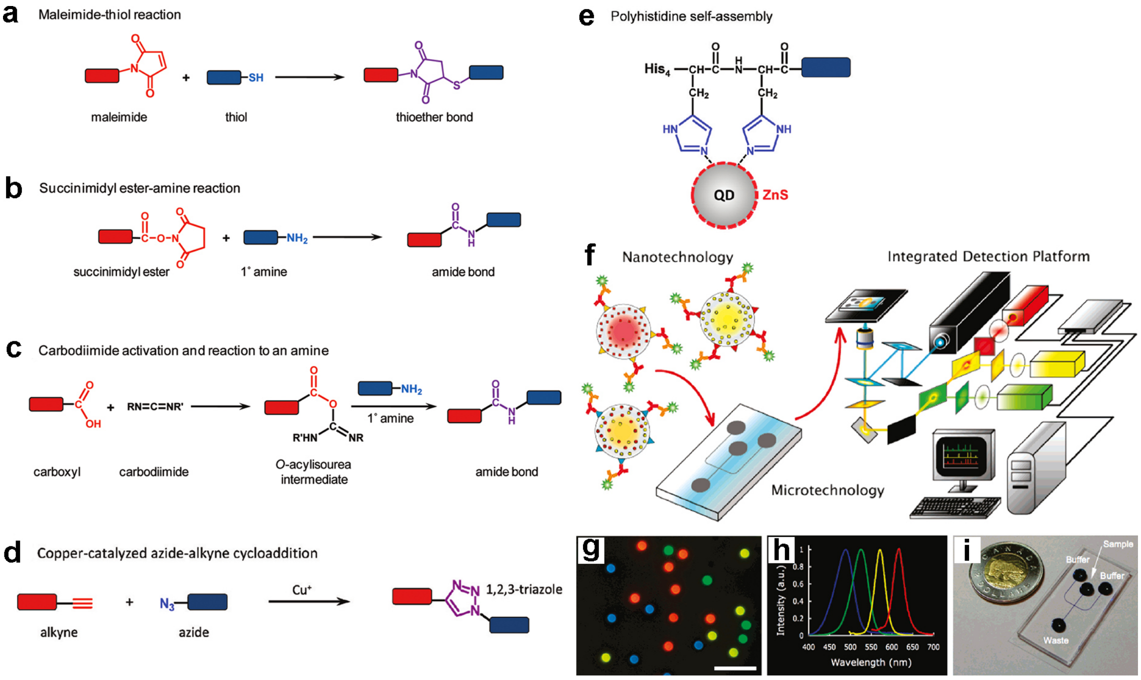

Figure 1.8: Bioconjugation reactions for QDs, including (a) maleimide-thiol, (b) succinimidyl ester-amine, (c) carbodiimide-mediated coupling between carboxyls and amines, (d) copper-catalyzed azide-alkyne cycloaddition and (e) self-assembly of polyhistidine to the inorganic ZnS surface of a QD *via* direct coordination of the imidazole moieties. Adapted with permission from ref.[200]. (f) Diagram illustrating the integration of QDs, solution-based sandwich assay, microfluidics and fluorescence detection with custom software for high throughput, multiplexed blood-borne pathogen detection. (g) Fluorescence image of a collection of different color emitting, 5.0 μm diameter polystyrene QDs suitable for proteomic or genomic assays (scale bar 20 μm). (h) Normalized QD emission profiles corresponding to the QDs used for the barcodes in (g), all excited using 365 nm light. (i) Sample microfluidic chip, fabricated in polydimethylsiloxane with wells labeled. Channel dimensions are 100 μm wide by 15 μm high. Blue dye was used to visualize the channel intersection for electrokinetic focusing. Adapted with permission from ref.[201].

1.5.1 Luminescence of Quantum Dots

Semiconductor QDs absorb photons with energies larger than their band gap. This results in the generation of electron-hole pairs (excitons) by promotion of electrons from the valence band (VB) to the conduction band (CB). Light is emitted when electron-hole recombination takes place. The emitted photons belong to a narrow emission window due to the quantum confinement of the QDs. This results from the spatial confinement of the wave function of QDs which is localized in a quantum well. It can be observed for nanomaterials with a smaller radius than the Bohr exciton radius.[195] These materials exhibit quantized energy states because they are in an intermediate size between an atom/molecule with defined molecular orbitals and orbital energies and a bulk solid with continuous electron bands. They can be referred as artificial molecules and described by the "particle in a box" model. Resulting from this model, the energy of the exciton is inversely proportional to the size of the particle and an increase in particle size leads to a red shift in the absorption spectrum.[199] Therefore tuning the QD size and material allows a precise adjustment of the emission wavelength.[202, 203] The QDs show remarkable properties in biochemical imaging applications. They exhibit high brightness due to a high quantum yield in combination with large molecular extinction coefficients and a broad absorption spectrum.[204] Additionally they possess a high two-photon conversion cross section[205] for two-photon spectroscopy with NIR radiation. Photobleaching is usually negligible.[202, 206] In contrast, organic dye molecules for bioimaging usually have a narrow excitation, but a broad emission range, and they are prone to photobleaching.[207] Compared to QDs they are less toxic and easy to conjugate to biomolecules without changing their biological function. In recent years surface functionalized QDs have been utilized for biomedical detection and labeling.[194, 208]

Normally, the as-synthesized QDs are not water dispersable and need additional surface functionalization. The functionalization strategies are comparable to those mentioned *vide supra* for metal and metal oxide nanoparticles. They are mainly based on chemisorption using the HSAB principle and tailored polymeric ligands. Because of the Pearson soft elements in QDs chemisorption typically relies on Pearson soft linkers like phosphines, phospholipids or thiols.[209] Dihydrolipoic acid with two sulfur anchor groups is a widely used bidentate linker which can be tailored subsequently with different PEG oligomers to achieve stability in aqueous dispersion independent of the pH or the ionic strength.[210] For the preparation of their nanobioconjugates, thiols, amines and carboxylate groups are used together with malimide, succinimidyl ester (NHS-ester) or carbodiimide activation for amide bonding (Figure 1.8a-c).[200] Click-chemistry like alkyne-azide cycloaddition to form 1,2,3-triazoles and self-assembly of polyhistidine ligands due to chemisorption of the imidazole side chains are also used on ZnS QDs (Figure 1.8d, e).[200] Biochemical applications are divided in many *in vitro* and some *in vivo* applications. Due to their excellent fluorescence properties QDs have been utilized for fast and highly sensitive diagnostic assays as biomarkers for infectious diseases which can be performed in microfluidic setups (lab-on-a-chip).[211] The Chan group developed a QD based barcode assay for the detection of the hepatitis B, hepatitis C and HI viruses (Figure 1.8f-i). The corresponding antigens are coupled to different fluorescent QDs and incubated with human serum containing the corresponding antibodies for viral antigens. A sandwich assay complex is formed by incubation with fluorophore-antibody conjugates. The QDs can now be traced with a microfluidic system on different emission wavelengths to target different viruses and antibody conjugations by the signal peak of the fluorophore. With this technique a 50 times higher sensitivity compared to FDA-approved methods was achieved for sample volumes less than 100 μL within a time span of less than one hour.[201, 212] *In vitro* drug targeting and bioimaging techniques have been developed, *e.g.* QD-aptamer-doxorubicin conjugates which simultaneously target prostate cancer and image the drug delivery process by activating the QD fluorescence when doxorubicin is released.[213] Further applications include the measurement of cell motility to evaluate the correlation between cell migration and their metastatic potential,[214] detection and imaging of apoptotic cells upon binding of annexin V functionalized QDs on phosphatidylserine[215] and visualization of folic receptors overexpressed in many types of cancer cells by a fluorescence switch principle.[216] However, for *in vivo* applications the toxicity is mostly associated with the elements Cd and Se of the CdSe QDs, whereas coating, blood circulation, accumulation as well as degradation and clearance are equally important to estimate the potential for clinical use and the risks for the patients.[217] In a mouse model five different NIR-QDs were used for lymphangiography[218] and NIR-QDs were applied for multimodal NIR and positron emission tomography (PET) studies, where the QDs were functionalized with a ^{64}Cu-DOTA ligand for PET to enhance the quantitative tomographic image of PET by qualitative information of QD fluorescence.[219] Ding *et al.* utilized QDs for improving CT diagnostics by forming nanoemulsions of QDs and iodinated oil.[220] This dual contrast agent was subsequently used to visualize atherosclerosis in rabbits by macrophage uptake.

1.6 Photocatalysis

The combination of a noble metal such as Pt or Au with the semiconductor TiO_2 enables enhanced photocatalytic properties, both when irradiated with UV-light or visible light. Under both circumstances the photocatalytic properties are enhanced because of better charge separation and reduced electron-hole recombination in the semiconductor.[45] Typically, a semiconductor is able to catalyze redox reactions upon absorption of UV-light and subsequent excitation of electrons from the VB to the CB. The electron-hole pairs can then be used for redox reactions. If nanoparticulate TiO_2 is in direct electronic contact with a noble metal exhibiting a larger work function and consequently a lower Fermi energy level (E_F) than TiO_2 (*e.g.* Au), it's VB and CB experience an upward bending upon equilibration of the Fermi levels.[55, 221] After UV-light irradiation the excited electrons in the semiconductor CB are charge transferred trough the interface to the noble metal E_F which acts as charge reservoir with higher reductive power to adhered molecules (Figure 1.9a).[222]

When such nanoparticles are exposed to visible light the SPR of the noble metal is excited.[223, 224] If the plasmon band is overlapping with the band gap of the semiconductor, the electrons can cross the Schottky barrier.[225] Excited electrons in the noble metal with higher energy than the CB of the semiconductor fall into the upwards bended CB of the semiconductor and are trapped there and available for reduction of molecules.[45] Due to the electron deficiency at the noble metal, oxidations preferentially take place there (Figure 1.9b).[226]

Another mechanism can occur when noble metal and semiconductor are separated by organic spacer molecules and don't have an electronic interface. Here the SPR can enhance the environmental electromagnetic field around the noble metal.[226] When the semiconductor is in close proximity, the excited plasmonic nanoparticles act as light intensifier for the semiconductor excitation, thus building a hot spot region.[45]

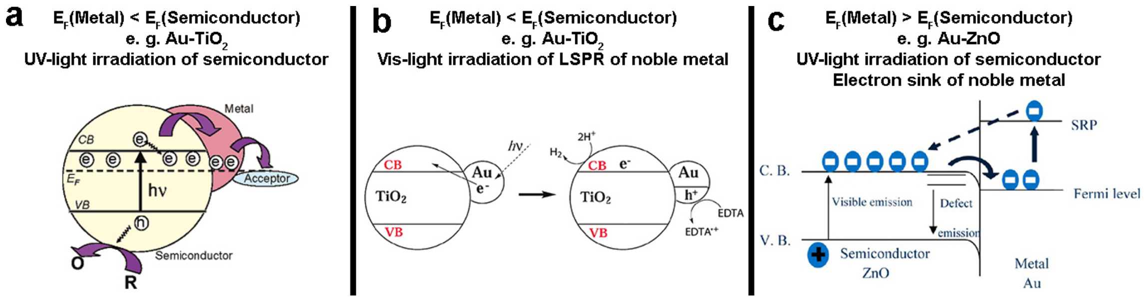

Figure 1.9: (a) Fermi level equilibration in a metal-semiconductor nanocomposite system under UV-light irradiation. Oxidation of substrate can take place next to the semiconductor and reduction can take place next to the noble metal. Adapted with permission from ref.[55]. (b) Proposed mechanism of hydrogen generation with Au-TiO_2 nanocomposite upon excitation of Au LSPR under visible light irradiation. EDTA serves as sacrificial reducing agent. Adapted with permission from ref.[224]. (c) Schematic band diagram of Au-ZnO nanocomposite upon UV-light irradiation. Au domain serves as electron sink for conduction band electrons of semiconductor and excited LSPR of Au get back to the Fermi level of Au *via* ZnO semiconductor. Adapted with permission from ref.[228].

In the vicinity of hot spots charge carrier can easily interact with chemisorbed reactants.[227]
A difference in the electronic structure occurs when *e.g.* Au is combined with ZnO as semiconductor (Figure 1.9c).[38] Owing to the high working function of ZnO its E_F is lower than the E_F of Au. As equilibration of the Fermi levels occurs, the E_F from Au is lowered and CB as well as VB of ZnO undergo a downwards bending. Upon excitation with UV-light, easy transfer of the generated CB electrons from ZnO to Au, which acts as electron sink, is possible.[56] Also excited plasmonic Au electrons will take their way back to the Au Fermi level *via* the ZnO CB.[228, 229] For a Ag-ZnO interface it was found that also the oxygen vacancies, typically present in ZnO, can influence the photocatalysis by trapping electrons but also reducing their availability for redox reactions.[230] In an aqueous environment the electron holes can oxidize chemisorbed OH^--ions or water to $OH^{\cdot}$-radicals. The excited electrons are further able to reduce dissolved oxygen to superoxide radials ($O_2^{\cdot-}$), which are highly active radicals for degradation reactions.[231]

1.7 Nanoparticles as Enzyme Mimetics

Enzymes are known to catalyze different biochemical reactions with extraordinary high efficiency, velocity and specificity due to the induced-fit adaptability of the enzyme pocket with respect to the structure of the applied substrate.[232, 233] These catalytic properties have been applied *e.g.* for cellular imaging and H_2O_2 detection based on horse radish peroxidase- (HRP) functionalized TiO_2 nanorods.[234] However, when functionalized with a natural enzyme those nanomaterials still show the intrinsic disadvantages of enzymes, like low stability and specific pH, temperature and substrate requirements.[232] Although alternative solutions for natural enzymes with higher stability were pursued by combining a metal atom as catalytic center with an artificial enzyme-like binding environment, it is still challenging to mimic enzymatic reactions while facing concomitant biochemical reactions *in vitro*.[233, 235] Important progress was made since 2007, when Gao *et al.* showed that Fe_3O_4 nanoparticles exhibit an intrinsic peroxidase-like activity.[236] Driven by the hypothesis that chemical redox processes occurring in natural peroxidases such as HRP,[237] which contains a Fe^{2+} (haem co-factor) in the active center,[238, 239] can be related to Fe^{2+}-Fe^{3+} oxidation state transitions in Fe_3O_4, other materials were tested and found to mimic natural enzymes. The following section discusses nanoparticle enzyme mimics and highlights possible applications ranging from biochemistry to materials science.

Since the detection of peroxidase-like activity of iron oxide nanoparticles many other nanomaterials with peroxidase-like activity such as MnO_2[240] Ag/Pt,[241] or V_2O_5[242] have been reported. In general, peroxidases decompose H_2O_2 by reduction to H_2O while oxidizing at the same time another substrate.[237] Peroxidases are especially valuable in the respiratory chain of cells because incomplete reduction of O_2 in the mitochondria leads to the formation of reactive oxygen species (ROS) such as H_2O_2, hydroxide radicals ($OH^{\cdot}$) and superoxides ($O_2^{\cdot-}$) which are potentially harmful.[243] Most peroxidases contain Fe, Mn or V in their active sites.[244] One of the oldest known examples of peroxidase activity is the Fenton reaction.[245] The iron oxide nanoparticles have advantages in pH (0-12) and temperature stability (4-90 °C) compared to HRP.[236] They also show higher catalytic activity than HRP with 7.5-24.5 times higher catalytic turnover numbers (k_{cat}) for the TMB (3,3',5,5'-tetramethylbenzidine) and H_2O_2 substrates, respectively.[236] Similarly important is the surface area of the nanoparticles as the smallest particles have the highest catalytic activity.[236] Also presented by the Yan group were applications for peroxidase mimicking nanoparticles by encapsulating iron oxide nanoparticles into a heavy-chain ferritin protein for targeting the transferrin receptor and visualizing the tumor tissue by the peroxidase-like activity of iron oxide[246] and the strip-based detection of the Ebola virus by conjugating anti-EBOV antibodies to iron oxide nanoparticles (Figure 1.10a). These particles subsequently recognize the EBOV-glycoproteins bound on the antibody functionalized test-strip to form a sandwich complex. After oxidation of 3,3'-diaminobenzidine (DAB) through the enzyme mimicking activity of the iron oxide nanoparticles the naked-eye detection limit was increased by two orders of magnitude compared to standard colloidal Au-strips.[247] Another application exploring nanoparticles as enzyme mimic is the glucose detection for food analysis or clinical purposes. Glucose can be oxidized to gluconic acid *via* glucose oxidase. O_2 is subsequently reduced to H_2O_2 (Figure 1.10b). Thus, the glucose detection can be coupled to peroxidase mimicking nanoparticles for colorimetric detection.[233, 248] It was also demonstrated that both activities can be exploited by nanomaterials where Au nanoparticles are used as glucose oxidase and V_2O_5 nanowires as peroxidase mimic.[249]

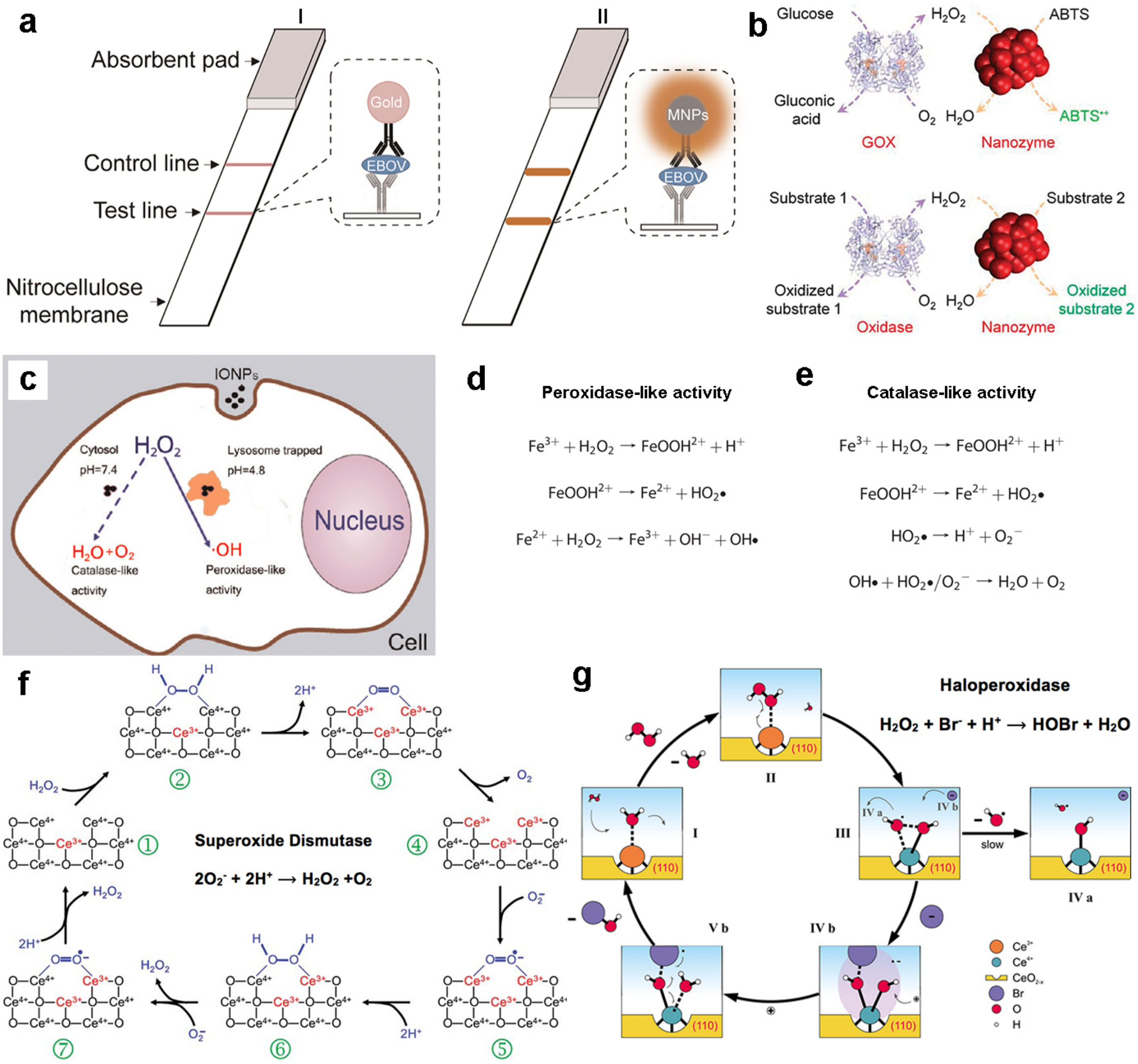

Figure 1.10: (a) Strip based detection of Ebola virus with (I) standard colloidal gold strip and (II) nanozyme-strip employing iron oxide nanoparticles in place of colloidal gold to form a novel nanozyme probe. The probe with nanozyme activity generates a color reaction with substrates, which significantly enhances the signal so that it can be visualized by the naked-eye. Adapted with permission from ref.[247]. (b) Nanozyme as peroxidase mimic for colorimetric sensing of H_2O_2 and glucose when combined with glucose oxidase. The sensing format could be extended to other targets (substrate 1) when combined with a appropriate oxidase. Numerous transduction signals can be adopted for sensing (such as colorimetric, fluorometric and chemiluminescent signals when the corresponding substrates are used; and electrochemical signals when a nanozyme is immobilized on an electrode). Adapted with permission from ref.[233]. (c) Schematic illustration of peroxidase-like activity induced cytotoxicity by iron oxide nanoparticles (IONPs). IONPs are trapped in acidic lysosomes when internalized into cells, so they catalyze (d) H_2O_2 to produce hydroxyl radicals through peroxidase-like activity. However, in neutral cytosol, IONPs would decompose (e) H_2O_2 through catalase-like activity. Adapted with permission from ref.[250].

Figure 1.10: (f) A model of the reaction mechanism for the oxidation of hydrogen peroxide by nanoceria and the regeneration *via* reduction by superoxide. An oxygen vacancy site on the nanoceria surface (1) presents a 2 Ce^{4+} binding site for H_2O_2 (2). After the release of protons and two-electron transfer to the two cerium ions (3) oxygen is released from the now fully reduced oxygen vacancy site (4). Subsequently superoxide can bind to this site (5), and after the transfer of a single electron from one Ce^{3+}, and uptake of two protons from the solution, H_2O_2 is formed (6) and can be released. After repeating this reaction with a second superoxide molecule (7) the oxygen vacancy site returns to the initial 2 Ce^{4+} state (1). It is also possible that the third Ce^{3+} indicated, which gives rise to the oxygen vacancy, could participate directly in the reaction mechanism. The square Ce-O matrix is shown here only to illustrate the model and does not correspond to the actual spatial arrangement of the atoms in the crystal structure. Adapted with permission from ref.[251]. (g) Proposed catalytic bromination mechanism of the CeO_{2-x} nanorods. On a (110) model surface (I), the H_2O ligand can be exchanged against H_2O_2 (II). An oxidation of the Ce^{3+} site with OH^- anion and $OH^{\cdot}$ radical ligands (III) takes place. These two groups are bound to each other through a weak two-center three-electron bond. A release of an $OH^{\cdot}$ radical from this species into solution may occur, but it represents a step "uphill" in Gibbs free energy and is therefore slow (IVa). A Br^- anion can add to one of the O atoms to form a species which is best described as an anionic surface site (with two hydroxide ligands) where one of the OH^- anions interacts with a $Br^{\cdot}$ radical (IVb). The other, noninteracting OH^- anion is protonated to restore a neutral surface site (Vb). Dissociation of the HOBr product finally regenerates the initial Ce^{3+} site (I). Adapted with permission from ref.[252].

In addition to their peroxidase-like activity some nanoparticles also exhibit catalase-like activity. This was demonstrated by Chen *et al.* for magnetite (Fe_3O_4) and maghemite (γ-Fe_2O_3) nanoparticles (Figure 1.10c-e).[250] Catalase not only reduces H_2O_2 to H_2O but also oxidizes H_2O_2 to O_2.[253] They reported a pH dependent enzyme mimicking function of the particles: (i) At a physiological pH of 7.4 where the particles are in cytosolic environment the decomposition of H_2O_2 produces $OH^{\cdot}$ and $O_2^{-\cdot}$, which quickly react with each other to form O_2 and H_2O as required for a catalase-like activity, and (ii) At lysosomal pH of 4.8 the formation of $HO_2^{\cdot}$ as preliminary step for the production of superoxide is slower resulting in a more pronounced Fenton reaction and peroxidase-like activity. The generated $OH^{\cdot}$ species have cellular toxicity which is more prominent for magnetite than for maghemite particles in harmony with their peroxidase-like activities.[250]

Superoxide radicals as part of ROS are also responsible for oxidative stress under aerobic conditions. As a defense mechanism the enzyme superoxide dismutase (SOD) terminates $O_2^{-\cdot}$ to H_2O_2 to O_2.[254] Natural SOD contains Fe/Mn[255] or Cu/Zn[256] as co-factor and Mn^{2+} ions have been shown to exhibit protection against oxygen radical induced damage[257] which is associated with the formation of a Mn^{4+} species (MnO^{2+}) disproportionating in a follow-up reaction to Mn^{2+}, O_2 and H_2O_2.[258] Therefore it is self-evident that materials that can reversibly switch oxidation states and display oxygen affinity are candidates for SOD mimetics. Nanoceria can switch easily between Ce^{3+} and Ce^{4+}. Oxygen vacancies compensate the reduced positive charge of Ce^{3+} and therefore stabilize the trivalent state.[259] The Seal group reported that normal cells can be protected from radiation induced radical mediated damage by a Ce^{3+}/Ce^{4+} catalytic process.[260] Self and coworkers afterwards demonstrated SOD activity of vacancy engineered nanoceria.[261] The Ce^{3+}/Ce^{4+} ratio is important for the SOD activity. A higher Ce^{3+} content supports enhanced SOD activity,[261] whereas a higher Ce^{4+} content supports the catalase reaction.[262] A mechanism was proposed that links H_2O_2 to two Ce^{4+} surface sites with subsequent reduction to Ce^{3+} and a release of O_2 (Figure 1.10f). Now the Ce^{3+} sites can coordinate superoxide and reduce it to H_2O_2. After one repeat cycle both Ce^{3+} sites are reoxidized for the next catalytic cycle.[251] Hyeon and co-workers presented an *in vivo* application of ceria particles with diameters of 3 nm for ROS reduction after stroke. The antioxidant properties of the nanoceria were used to reduce the infarct volume and oxidative induced apoptosis as a neuroprotective effect.[263]

In 2012 we presented the haloperoxidase-like activity of V_2O_5 nanowires which is suitable for marine paints with anti-biofouling properties.[264] Generally, haloperoxidases oxidize H_2O_2 in the presence of halides (Cl^-, Br^-, I^-) to form hypohalous acids (HOCl, HOBr, HOI).[265] The hypohalous acid in turn acts as halogenation reagent for nucleophilic acceptor molecules involved in the intracellular communication of bacteria and therefore exhibit biocidal activity.[266, 267] We showed under laboratory and under seawater conditions (60 days in Atlantic Ocean as marine paint containing V_2O_5) that V_2O_5 nanowires follow a similar mechanism of forming HOBr and singlet oxygen as naturally occurring vanadium haloperoxidases. They are at the same time less toxic for marine biota than currently approved antifouling coatings.[264]

Recently we showed that oxygen deficient ceria nanorods (dimensions 20-100 nm) also exhibited haloperoxidase-like activity suitable for antifouling applications (Figure 1.10g).[252] To evaluate the mechanism of HOBr formation, quantum chemical calculations were performed on the basis of X-ray photoemission spectroscopy to locate the Ce^{3+} surface sites. The results of the calculations suggest a mechanism of H_2O_2 adsorption on one Ce^{3+} (110) surface atom and a subsequent two-center three-electron bonding of OH^- and $OH^\cdot$ species at oxidized Ce^{4+} sites. Upon addition of Br^-, a radical anionic surface site with two hydroxide ligands is formed which is degraded to water in the next step. HOBr, that is formed simultaneously, restores the Ce^{3+} surface site for the next catalytic cycle.[252] These examples highlight the importance of enzyme mimics and nanomaterials for catalysis and material science because recombinant haloperoxidases have been proposed as additives for marine paints.[268] However, the lack of long-term stability and high production costs have prevented its use so far.[269]

The hypothesis that nanomaterials containing the transition atoms in the same oxidation state as the active center of enzymes has served as a useful guide to identify other new enzymes mimics. Ragg *et al.* demonstrated that MoO_3 nanoparticles with diameters of approx. 2 nm mimics the reaction of sulfite oxidase and can be used to treat sulfite oxidase deficiency.[143] Patients suffering from this disease lack an adequate sulfite oxidase enzyme in the intermembrane space of liver and kidney cells which plays a major role in cellular detoxification and catabolism of sulfur containing amino acids.[270] Typically, sulfite oxidase catalyzes the oxidation of sulfite to sulfate which otherwise would cause severe neurological damage and early childhood death of patients.[271, 272] It has been shown that MoO_3 nanoparticles, functionalized with triphenylphosphonium units for mitochondria targeting,[273] possess *in vitro* activity towards sulfite oxidase deficient cells. The functionalized MoO_3 nanoparticles were successfully internalized in the mitochondria and the sulfite oxidase activity could be fully recovered.[143]

2

Pd@Fe_2O_3 Superparticles with Enhanced Peroxidase Activity by Solution Phase Epitaxial Growth

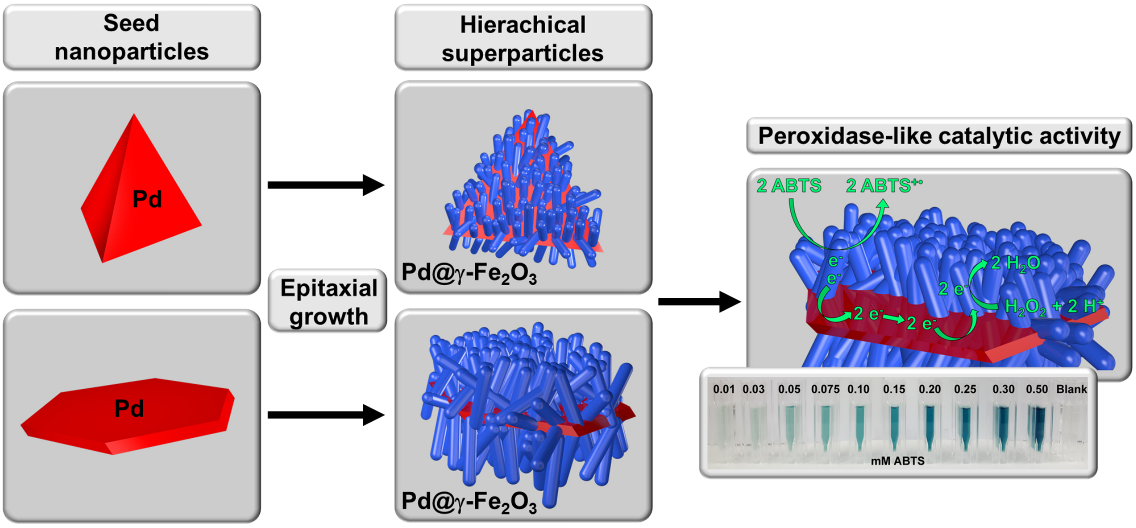

This chapter contains an adapted reproduction of Chemistry of Materials 2017, 29 (3), 1134-1146,[93] *reproduced with permission of the American Chemical Society. A detailed Authorship Statement of the publication is attached in the Appendix of this dissertation.*

2.1 Abstract

Compared to conventional deposition techniques for the epitaxial growth of metal oxide structures on a bulk metal substrate, wet-chemical synthesis based on a dispersible template offers advantages such as low cost, high throughput, and the capability to prepare metal/metal oxide nanostructures with controllable size and morphology. However, the synthesis of such organized multicomponent architectures is difficult because the size and morphology of the components are dictated by the interplay of interfacial strain and facet-specific reactivity. Here we show that solution-processable two-dimensional Pd nanotetrahedra and nanoplates can be used to direct the epitaxial growth of γ-Fe_2O_3 nanorods. The interfacial strain at the Pd-γ-Fe_2O_3 interface is minimized by the formation of an Fe_xPd "buffer phase" facilitating the growth of the nanorods. The γ-Fe_2O_3 nanorods show a (111) orientation on the Pd(111) surface. Importantly, the Pd@γ-Fe_2O_3 hybrid nanomaterials exhibit enhanced peroxidase activity compared to that of isolated Fe_2O_3 nanorods with comparable surface area because of a synergistic effect for the charge separation and electron transport. The metal-templated epitaxial growth of nanostructures *via* wet-chemical reactions appears to be a promising strategy for the facile and high-yield synthesis of novel functional materials.

2.2 Introduction

Epitaxial growth is a promising strategy for the controlled growth of one-dimensional nanostructures with a preferred orientation and alignment on substrate layers, which may lead to advances in areas such as energy harvesting or conversion, sensing, catalysis, optical, electrical, optoelectronic, and magnetic applications.[58, 274–280] Vapor deposition (PVD, CVD, and ALD) approaches, often relying on the vapor-liquid-solid (VLS) technique, electrochemical deposition, or laser ablation, have been widely used to induce the epitaxial growth of metal oxide semiconductors.[40, 281–283] Major disadvantages of these deposition techniques requiring ultra-high-vacuum conditions or special equipment are low throughput and high cost. Therefore, wet-chemical approaches are an attractive alternative because of their versatility, easy implementation, and low cost. The epitaxial growth of metal oxides has been demonstrated previously in the synthesis of ferroelectric perovskite films (*e.g.*, lead zirconate titanate, $Pb(Zr,Ti)O_3$ (PZT)) on oxide substrates, which can be achieved because of a tolerable lattice mismatch ($< 5\%$) and sufficient wetting of the substrate.[283, 284] However, despite the previous demonstration of substrate-seeded epitaxial growth of "complex" metal oxides (or metals[16, 40, 285–287]) from solution,[58, 278, 279, 284] the wet-chemical growth of metal oxide nanocrystals with a preferred orientation and alignment (besides inorganic Janus particles[78, 288–290]) on planar metal templates has rarely been reported,[92, 291, 292] because the nucleation of metal oxide domains on metal supports mostly occurs on surfaces with a high curvature[280, 293] or at defect sites,[294] whereas planar templates with atomically flat surfaces would be more suitable for achieving solution phase epitaxy under mild experimental conditions.

Metals exhibit three-dimensional bonding and are therefore more difficult to prepare as two-dimensional substrates (nanoplates and -sheets) than layered materials that have an inherent propensity to occur as nanosheets. Several methods have been used for the synthesis of metal (mostly Au and Ag) nanoplates and -sheets starting from metal salts or small metal nanoparticles (NPs). The majority of them rely on a surfactant-mediated[295, 296] or template-assisted synthesis,[72, 297, 298] polyol reduction,[299–302] seeded[105, 303–305] or carbon monoxide and halide ion confined growth,[306, 307] and bioinspired synthesis.[308–311] For Pd nanocrystals, a shape-controlled synthesis (cubes/octahedra) has been reported using HCl as the oxidative etchant.[312] Pd nanosheets were prepared using carbon monoxide as the surface active agent.[313] CO is known to strongly adsorb on the Pd$\{111\}$ surface leading to the growth of ultrathin nanosheets as well as tetrahedral nanocrystals with exposed $\{111\}$ surfaces,[105, 314, 315] and halide ions can control the $\langle 100\rangle$ growth rate to maintain the hexagonal shape of the nanoplates.[105, 311, 316]

Recently, we have devised a wet-chemical approach to Ni@γ-Fe_2O_3 superparticles containing Ni nanoplates densely decorated with highly oriented γ-Fe_2O_3 (maghemite) nanorods (NRs) by controlled reduction/decomposition of nickel acetate ($Ni(ac)_2$) and $Fe(CO)_5$.[92] Electron crystallography revealed that a buffer layer at the interface between the metal "support" and the metal oxide nanorods could be fine-tuned by "alloying" the metal components to achieve a match between the lattice parameters of the metal substrate and the metal oxide nanorods. Here we report a two-step seed-mediated growth synthesis for Pd@γ-Fe_2O_3 superparticles containing (planar or tetrahedral) Pd substrates densely covered with highly oriented, epitaxially grown maghemite nanorods.[68]

The key idea underlying the synthesis of epitaxially grown and three-dimensionally organized nanostructures is enhancement of interfacial electronic communication between the metal and metal oxide building blocks. This may increase the efficiency of heteroparticle devices.[34–36] As a proof of concept, we have demonstrated the *in situ* growth of iron oxide nanorods onto Ni nanoplates. Here we extend this approach to Pd, a more reactive metal that is used in many catalytic processes and in bioapplications to mimic intracellular chemistry.[105, 178, 317, 318] Additionally, the chemical properties of Pd for the heterogeneous nucleation and growth of a second domain are challenging to control and may lead to new insight into seed-mediated particle growth.

The first reaction step of superparticle synthesis involves the shape-controlled formation of Pd nanoparticles by thermal decomposition of $Pd(ac)_2$ in the presence of $Fe(CO)_5$ in a high-boiling point organic solvent (1-octadecene). *Via* variation of the solvent polarity and the amount of surfactant and $Fe(CO)_5$, the morphology of the Pd nanoparticles could be fine-tuned to obtain specifically tetrahedral or hexagonal Pd morphologies with {111} surface facets as analyzed by high-resolution and scanning transmission electron microscopy (HR-TEM and STEM, respectively). Mössbauer spectroscopy revealed the presence of iron traces (Fe_xPd alloy) facilitating the growth of the γ-Fe_2O_3 nanorods by the oxidation of $Fe(CO)_5$ using trimethylamine *N*-oxide (TMAO) in the subsequent reaction step. The γ-Fe_2O_3 phase was identified by Mössbauer spectroscopy. HR-TEM showed an epitaxial relationship between Pd{111} and the γ-Fe_2O_3 nanorods with a lattice mismatch of approximately 7%.

Importantly, the Pd@γ-Fe_2O_3 hybrid superparticles showed a 10-fold enhanced catalytic (peroxidase) activity for the decomposition of peroxides compared to that of isolated Fe_2O_3 nanorods with a comparable surface area. Our results indicate that the solution synthesis of γ-Fe_2O_3 nanorods with a preferred orientation and alignment on dispersible Pd metal nanoplates provides a new strategy for the facile and high-yield preparation of novel functional materials.

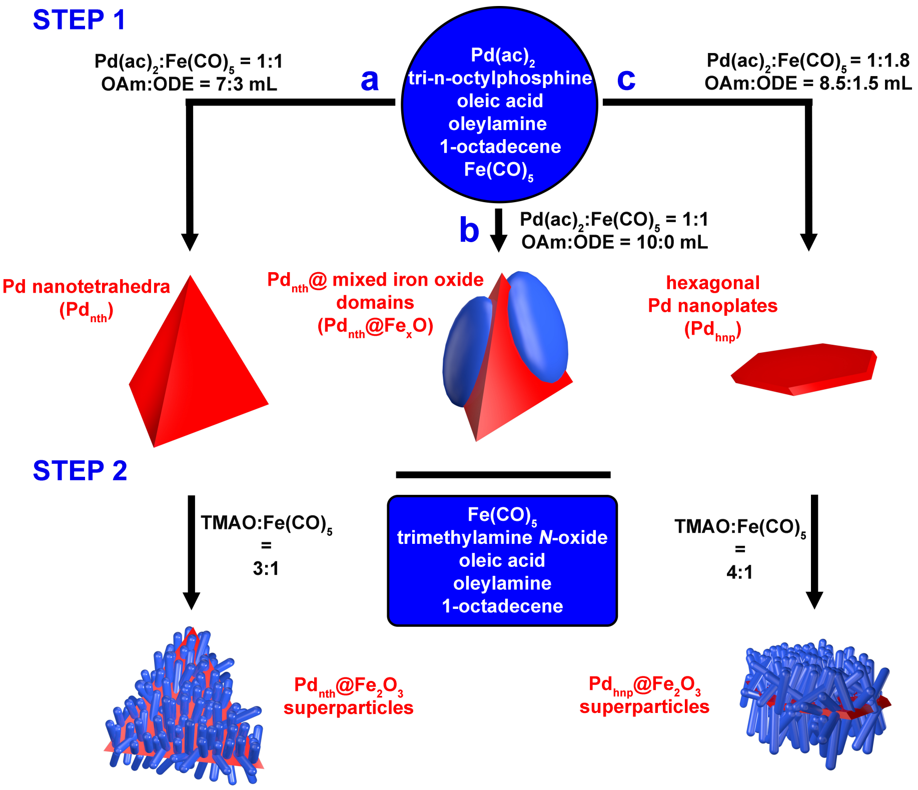

Figure 2.1: Synthesis of Pd NPs and Pd@γ-Fe_2O_3 superparticles. Reaction pathways to Pd@γ-Fe_2O_3 superparticles using (a) Pd nanotetrahedra and (c) hexagonal Pd nanoplates as seeds. (b) Formation of Pd nanotetrahedra with mixed iron oxide (Fe_3O_4/Fe_2O_3) domains.

2.3 Results and Discussion

Syntheses of (111) faceted Pd seed particle Pd nanotetrahedra (Pd_{nth}), hexagonal Pd nanoplates (Pd_{hnp}), and Pd@γ-Fe_2O_3 superparticles were performed using 1-octadecene as the high-boiling point organic solvent and oleylamine, oleic acid, and tri-n-octylphosphine as surfactants. Oleylamine is known to form complexes with $Fe(CO)_5$, thereby increasing its decomposition temperature from 100 to 180 °C.[319] The presence of a preformed oleylamine-$Fe(CO)_5$ complex acting as a co-reductant allows improved control of the nucleation and growth of the Pd NPs. The change from tetrahedral to hexagonal morphology (Figure 2.1) is likely to be induced by a selective passivation of a parallel pair of (111) facets, with subsequent Pd growth along the perimeter of the particle intermediate, resulting from an increased level of CO (1:1.8 $Pd(ac)_2$:$Fe(CO)_5$). No evidence of stacking faults within the Pd hexagons (which could promote particle growth along the perimeter) was observed in the HR-TEM analysis.[314]

The synthesis of the Pd@γ-Fe_2O_3 superparticles is illustrated in Figure 2.1. In the first step, Pd nanotetrahedra or Pd nanoplates were synthesized selectively by reduction of $Pd(ac)_2$ in the presence of $Fe(CO)_5$ and oleylamine at 120 °C. The

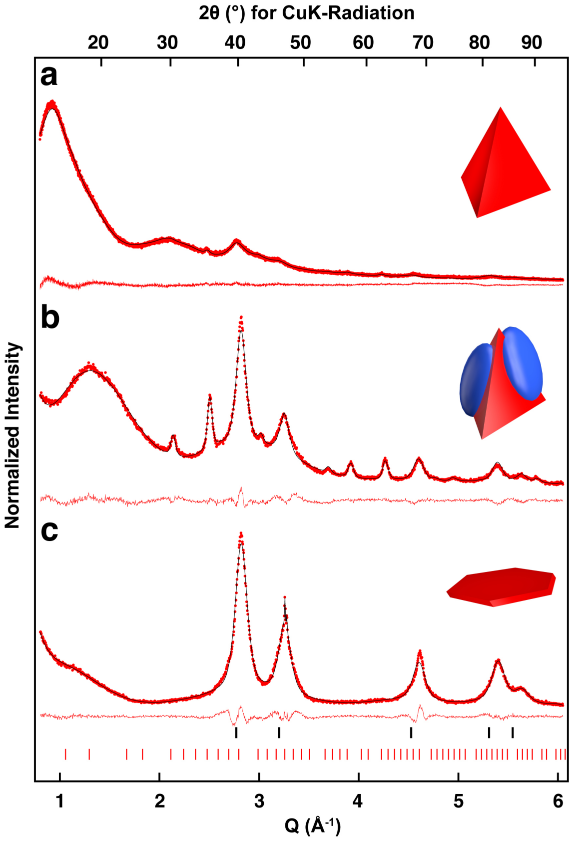

Figure 2.2: Rietveld refinements of powder XRD data for (a) Pd nanotetrahedra, (b) Pd_{nth}@Fe_xO, and (c) hexagonal Pd nanoplates. Red dots mark the experimental data, the black line corresponds to the calculated pattern, and the red line shows the difference between the experimental and calculated data. Black ticks mark reflections of Pd. $Q = [4\pi \sin(\Theta)]/\lambda$ is the scattering vector.

growth of the Pd nuclei could be tailored for the formation of the Pd nanotetrahedra or the Pd nanoplates depending on the ratio of the surfactant (oleylamine), the solvent (1-octadecene), and the amount of $Fe(CO)_5$ co-reductant (Figure 2.1a,c). By performing the Pd NP synthesis only in polar oleylamine (used as a solvent and a surfactant) for a 1:1 ratio of the $Pd(ac)_2$ precursor and the $Fe(CO)_5$ co-reductant, we believe that mixed iron oxide (magnetite/maghemite) domains form epitaxially on the (111) Pd facets of the Pd nanotetrahedra in a one-pot synthesis (Pd_{nth}@Fe_xO, Figure 2.1b). Because of the higher polarity of the reaction mixture in this case, enough electron density is provided to the Pd seed to facilitate a heteroepitaxial nucleation of the iron oxide. To facilitate the growth process, the final temperature was increased to 180 °C and held for 30 min. γ-Fe_2O_3 superparticles were formed in the second reaction step by seed-mediated growth using the preformed Pd NPs as seeds (Figure 2.1, step 2) and utilized for peroxidase-like enzyme mimetics (see Table 2.1).

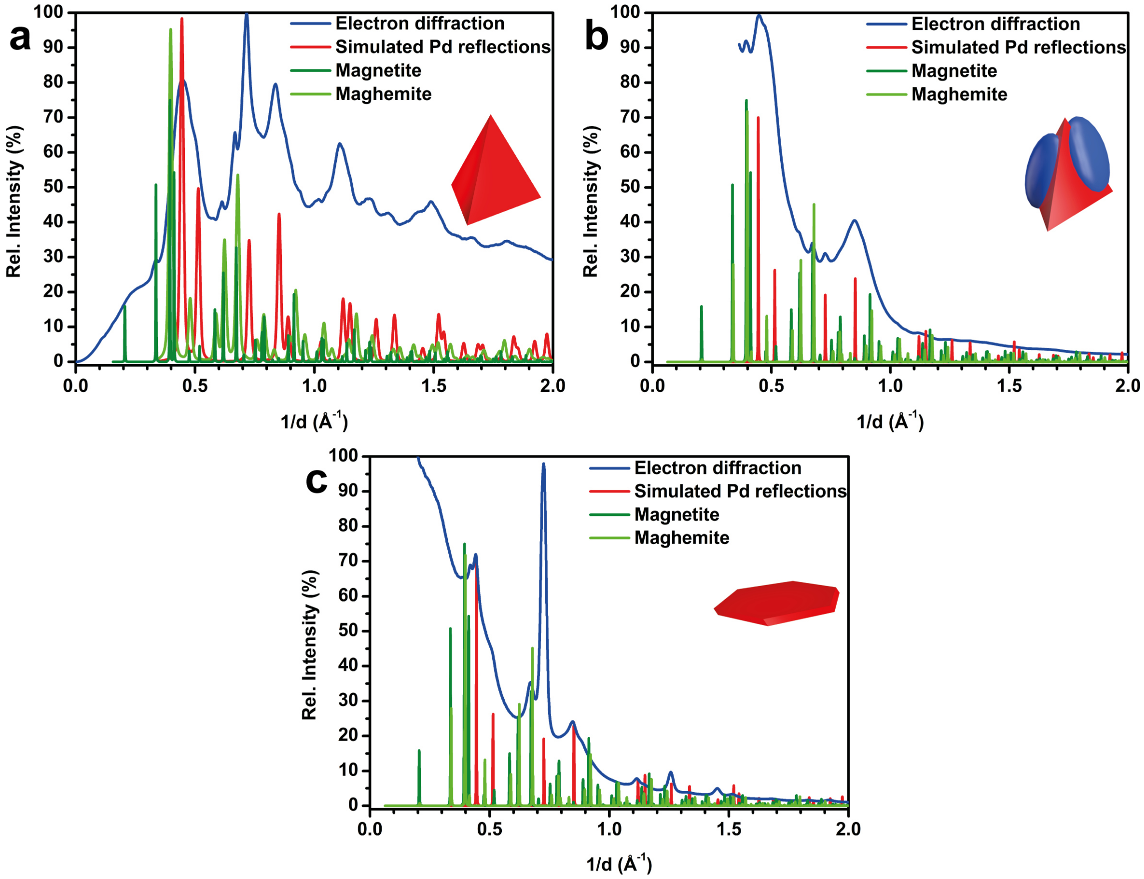

Figure 2.3: Electron diffraction (ED) of (a) Pd nanotetrahedra, (b) $Pd_{nth}@Fe_xO$ and (c) hexagonal Pd nanoplates. ED cannot distinguish between magnetite and maghemite.

2.3.1 Pd Nanotetrahedra

Figure 2.2a displays the results of a Rietveld refinement for the Pd nanotetrahedra. According to the diffractometric results, the sample contains two crystalline phases, the Pd main phase and the reflections of an iron oxide side phase (approximately 31 wt%, $Fe_{0.67(2)}O$, Table 2.2). The distinction between γ-Fe_2O_3 and Fe_3O_4 is difficult to determine on the basis of diffraction (XRD or electron diffraction) because of the structural and chemical similarity of both compounds. In addition, it is complicated by reflection broadening for nanocrystalline materials.[320] Maghemite (γ-Fe_2O_3) is an iron deficient defect variant of magnetite (Fe_3O_4). It also has a cubic structure with a slightly smaller lattice parameter.[321] The refined lattice parameter of 8.406(4) *Å* compared to those of γ-Fe_2O_3 (8.352 *Å*) and Fe_3O_4 (8.397 *Å*) has a slight tendency toward magnetite but cannot be considered as sufficient evidence given the peak broadening by the fine crystal size. Finally, electron diffraction of this sample also showed a mixture of the Pd and iron oxide phase (Figure 2.3a).

The other uncertainty lies in the assignment of the Pd phase. Pd and Fe form several ordered intermetallic phases with distinct crystal structures. A non-ordered

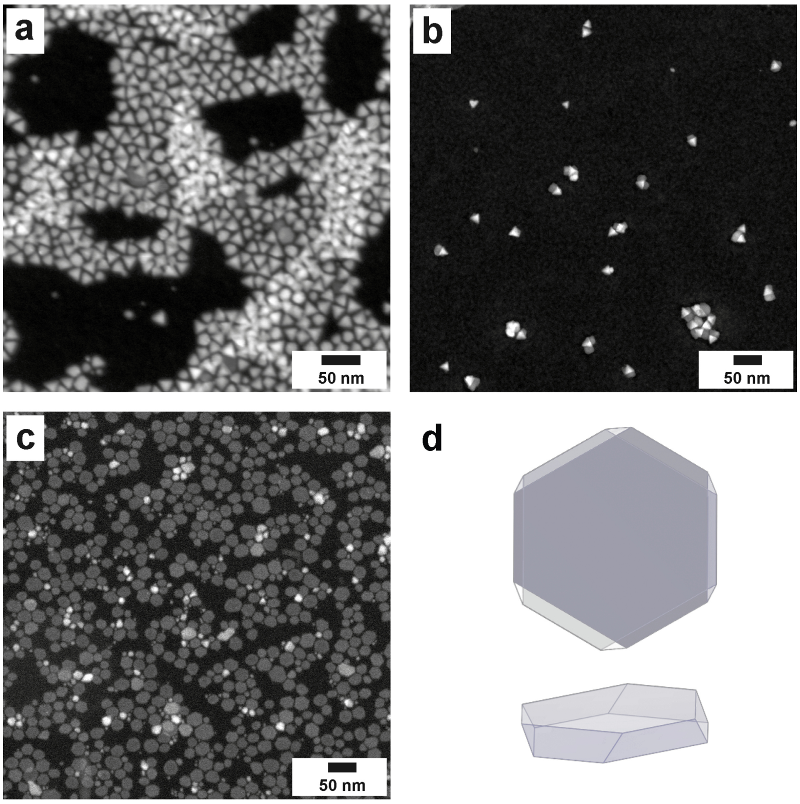

Figure 2.4: STEM images of (a) Pd nanotetrahedra, (b) Pd_{nth}@Fe_xO and (c) hexagonal Pd nanoplates and (d) their schematic representation.

structure with a small amount of Fe atoms dissolved in the Pd structure would not produce a diffraction pattern significantly different from that of pure Pd. Taking into account again the difficulties associated with the small crystal domain size, we find it is difficult to distinguish these two cases because of technical limitations. The tetrahedral morphology of the particles was confirmed by tilting in STEM mode (STEM images in Figure 2.4).

The Fe distribution in the sample could be clarified using Mössbauer spectroscopy. The ^{57}Fe Mössbauer spectrum of the Pd nanotetrahedra at 5.5 K (Figure 2.5a) can be simulated with four sextets with relative line intensities of 3:2:1:1:2:3 pointing to four different Fe sites that are magnetically ordered. Two outer sextets with high hyperfine fields of 529 and 512 kOe correspond to the Fe^{3+} sites in γ-Fe_2O_3 (Table 2.3).[322–324] Fe_3O_4 corresponds to the inner single fit with a small hyperfine field of 456 kOe and broad absorption lines, which is typical for magnetite accompanying maghemite.[325] In total, both oxides contribute to approximately 89% of the iron content in the sample. The remaining sextet with 11% fraction and a still smaller hyperfine field of 307 kOe corresponds to an Fe_xPd mixed phase.[326] A TEM image of the nanotetrahedra is shown in Figure 2.6a. The sample consists of particles with a homogeneous size distribution. A high-resolution aberration-corrected TEM image of the particles (Figure 2.6b) shows a homogeneous crystalline lattice with {111}

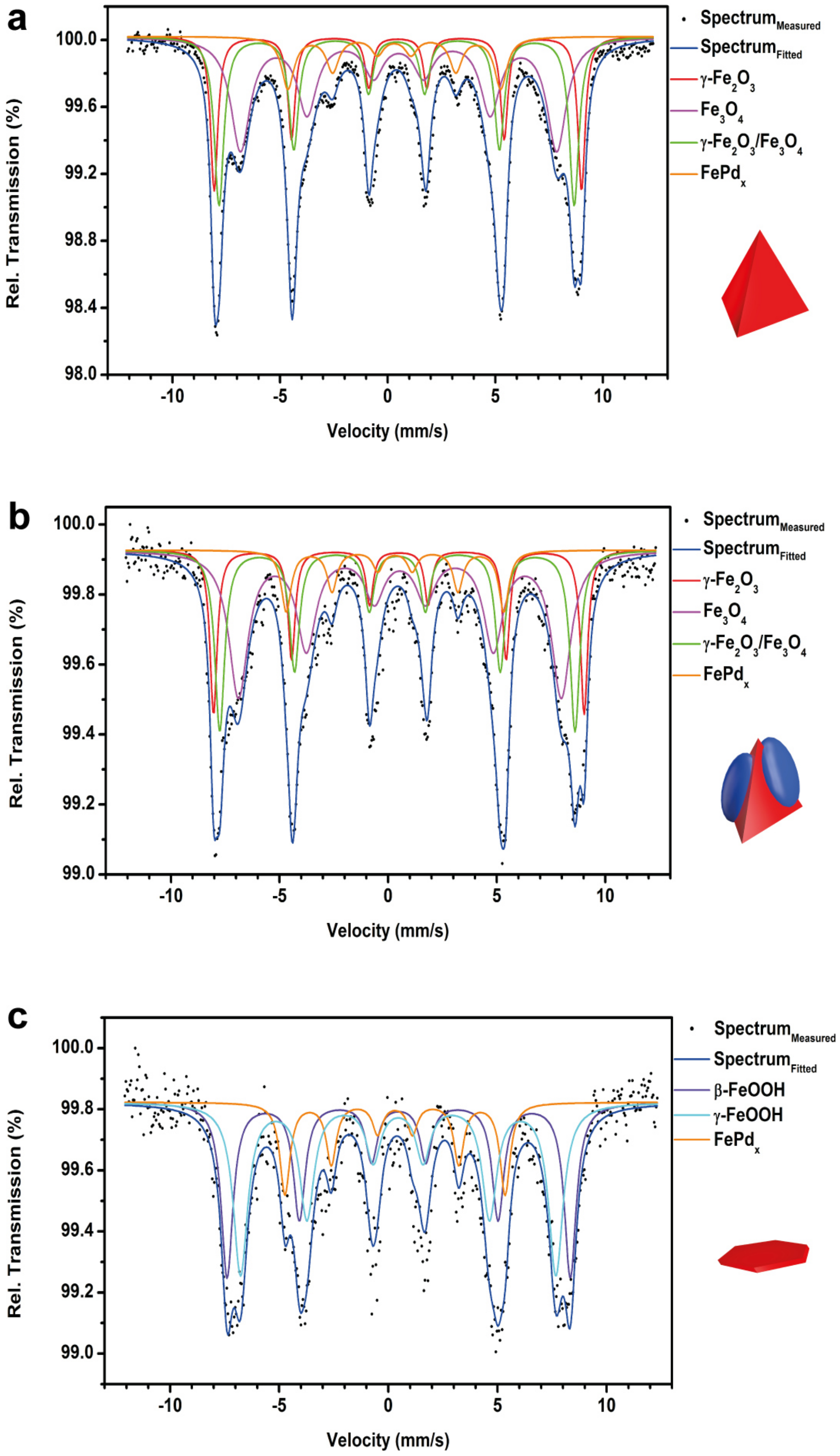

Figure 2.5: ^{57}Fe-Mössbauer spectra at 5.5 K of (a) Pd nanotetrahedra, (b) Pd$_{nth}$@Fe$_x$O, and (c) Pd nanoplates. The sextets in (a) and (b) correspond to γ-Fe$_2$O$_3$ (red, green), Fe$_3$O$_4$ (magenta, green) and FePd$_x$ (orange). The sextets in (c) correspond to β-FeOOH (purple), γ-FeOOH (cyan) and FePd$_x$ (orange).

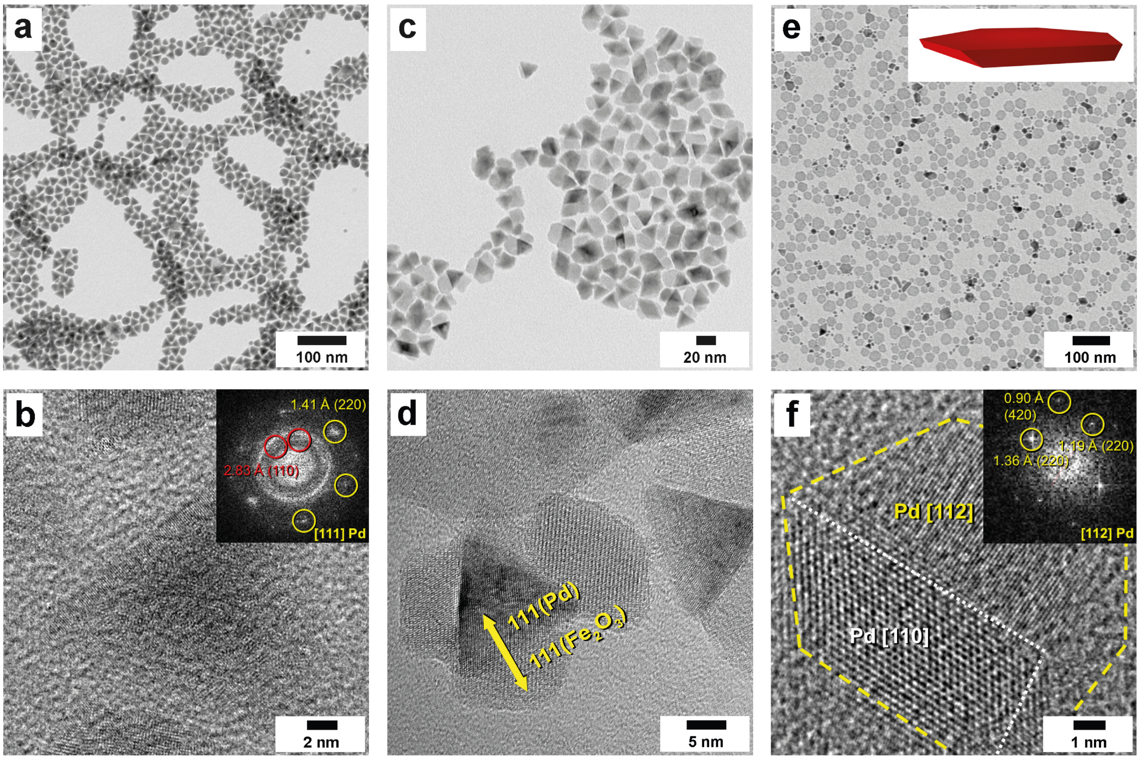

Figure 2.6: (a, c, and e) TEM overview images and (b (aberration-corrected), d, and f (aberration-corrected)) HR-TEM images of particles obtained after step 1 of the synthesis pathway. (a and b) Images of Pd nanotetrahedra (inset of power spectrum of Pd[111] zone axis showing Pd (yellow) and $FePd_3$ (red) reflections), (c and d) images of Pd_{nth}@Fe_xO showing epitaxial growth, and (e and f) images of hexagonal Pd nanoplates with a schematic representation of a hexagonal Pd metaprism with (111) facets (inset in panel e) and power spectrum of Pd[112] zone axis showing Pd (yellow) reflections (inset in panel f).

facets. Occasionally, iron oxide nanocrystals were detected (Figure 2.7). The power spectrum of the Pd[111] zone axis shows mainly reflections of Pd. Additionally, two (110) $FePd_3$ reflections were observed (Figure 2.6b, inset, marked in red). Because the additional (110) reflection is forbidden in the Pd structure, we assign this reflection to $FePd_3$. However, in most cases, we did not observe $FePd_3$. Thus, we conclude that $FePd_3$ may exist only as a thin layer on the Pd surface, which may become observable when a thicker layer of $FePd_3$ is formed. Generally, the weak individual reflections, which distinguish $FePd_3$ unambiguously from Pd, are not detected *via* HR-TEM or ED because of particle aggregation and the polycrystalline distribution interfering with these weak reflections. For the tetrahedral particles, EDX (Figure 2.8a, from a set of particles depicted in Figure 2.6a) revealed the presence of iron in the nanotetrahedra in harmony with the Mössbauer results, suggesting the presence of an Fe_xPd phase. EDX of a set of homogeneous Pd nanotetrahedra and single Pd nanotetrahedra (Figure 2.9) showed an iron content of approximately 25 at% in both cases, suggesting an iron distribution throughout the bulk Pd NP. In essence, the

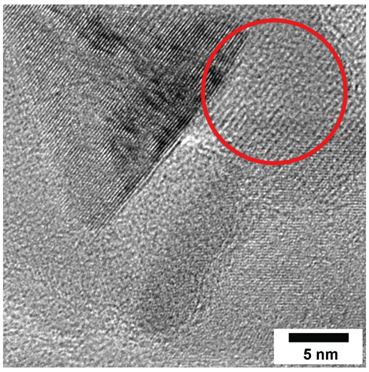

Figure 2.7: HR-TEM image of Pd nanotetrahedra showing some iron oxide (red circle).

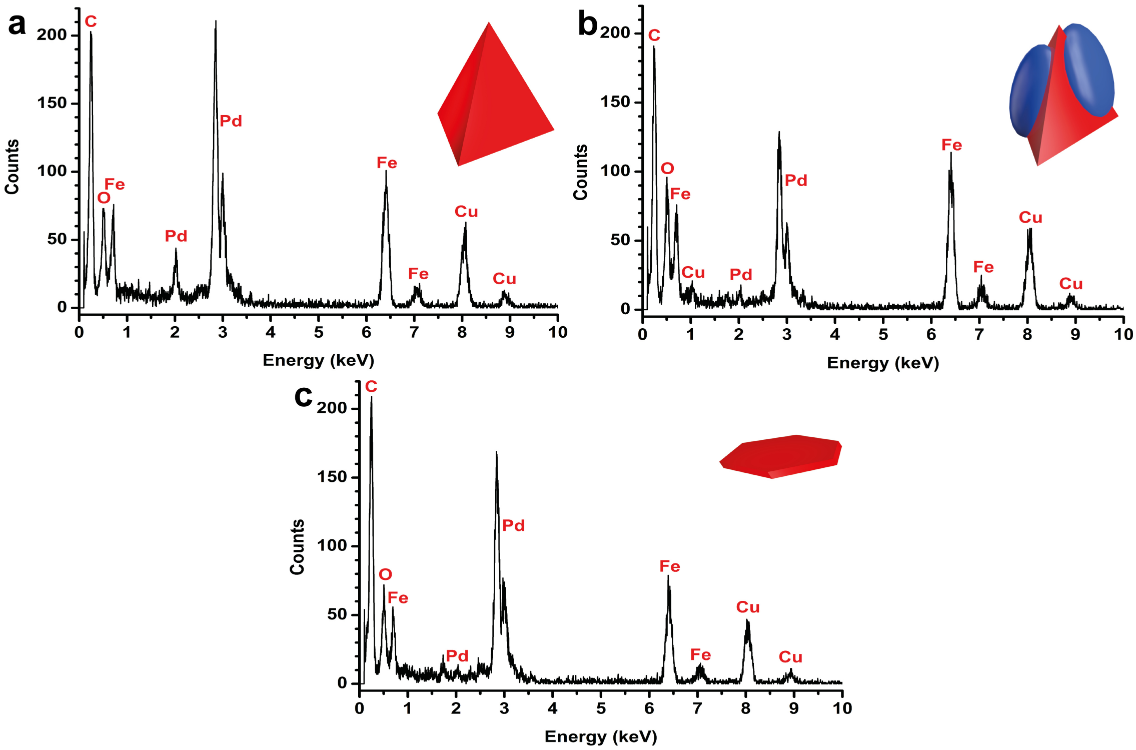

Figure 2.8: EDX spectra of (a) Pd nanotetrahedra, (b) Pd_{nth}@Fe_xO, and (c) hexagonal Pd nanoplates.

sample consists of heterocrystals containing a Pd core with Fe_xPd admixtures.

2.3.2 Pd_{nth}@Fe_xO

For the Pd_{nth}@Fe_xO domain NPs, the refinement of the XRD profile (Figure 2.2b) shows the presence of ≈ 53(2) wt% of the Pd phase (Table 2.2). The refined lattice parameter of 3.876(1) Å is close to that of Pd (3.890 Å).[327] From the Rietveld

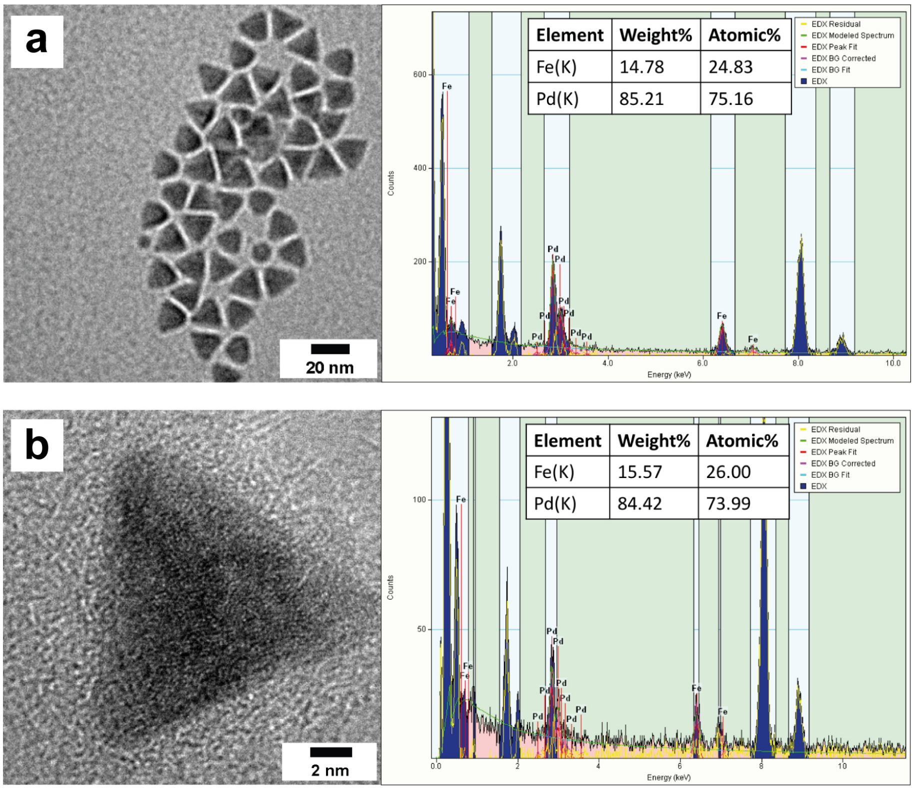

Figure 2.9: TEM/HR-TEM images and EDX of Pd nanotetrahedra. (a) EDX of a set of homogeneous Pd nanotetrahedra showing 25 at% Fe and 75 at% Pd. (b) EDX of single Pd nanotetrahedra showing 26 at% Fe and 74 at% Pd.

refinement, a Pd crystallite size of ≈ 13(1) nm could be derived (edge-sphere diameter of the nanotetrahedra), which is comparable with the Pd particle size extracted from the TEM images (17 nm ± 8%, edge length) indicating the single-crystalline nature of the nanotetrahedra. The crystalline iron oxide phase with an approximate composition of $Fe_{0.62(5)}O$ constitutes ≈ 47(2) wt% of the sample. As in the case of the nanotetrahedra, the nature of the Pd and iron oxide phases could not be determined unambiguously by powder X-ray diffraction. Again, the tetrahedral morphology of the particles was confirmed by tilting in STEM mode (see Figure 2.4 for STEM images).

The Mössbauer spectrum for $Pd_{nth}@Fe_xO$ domain NPs (Figure 2.5b) is nearly identical to the spectrum of the Pd nanotetrahedra (Table 2.3). A mixed magnetite:maghemite phase with an estimated 40:60 composition could be identified on the basis of the hyperfine magnetic field and the chemical shift. The appearance of maghemite and magnetite in the iron oxide domains of $Pd_{nth}@Fe_xO$ can be explained by the reduction of Pd^{2+} (in the $Pd(ac)_2$ precursor) to Pd^0, which requires an oxidation of $Fe(CO)_5$ (to Fe^{2+} and Fe^{3+} present in magnetite and maghemite). Evidence of Fe_xPd phase formation was also found in the form of a small sextet in the Mössbauer spectrum with approximately 10% spectral fraction. The EDX spectrum reflects

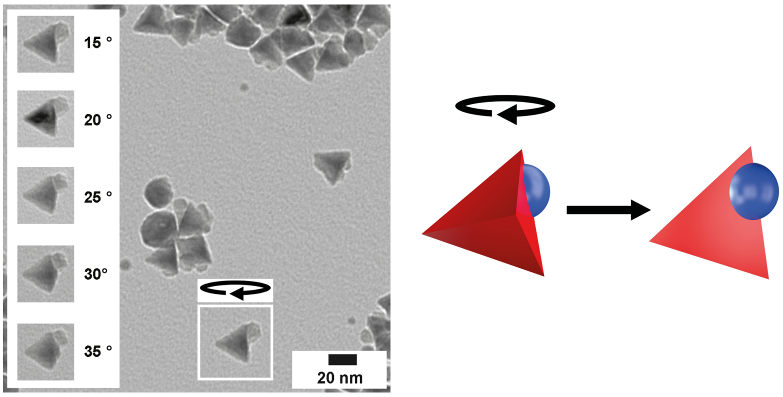

Figure 2.10: Tilted TEM image of $Pd_{nth}@Fe_xO$ (15°-35°) to confirm their tetrahedral shape and schematic representation of the tilting results.

the high iron content, which is in agreement with the iron oxide domains observed (Figure 2.8b, from a set of particles depicted in Figure 2.6c).

(HR)-TEM images of the $Pd_{nth}@Fe_xO$ domains (Figure 2.6c,d) show that the Pd cores are decorated with iron oxide blocks attached to the {111} facets of the Pd core. A variable portion of tetrahedra faces contained iron oxide blocks; occasionally, all four faces were decorated with iron oxide. All Pd-iron oxide aggregates were crystallographically coherent; all iron oxide blocks were aligned with the Pd core. The orientational relationship at the interface is given by $\{111\}\ Fe_2O_3 \| \{111\}$ Pd (Figure 2.6d). The misfit of the lattice parameters at the interface is ≈ 7%, which should cause significant strain at the interface extending up to ≈ 10 nm, the size of the tetrahedral face. Nevertheless, no misfit dislocations were seen in the core or in the iron oxide blocks.

Noticeably, HR-TEM as well as STEM imaging (Figure 2.6a,b, Figure 2.4a) showed that only the reaction in pure (polar) oleylamine (Figure 2.1b, $Pd_{nth}@Fe_xO$, Figure 2.10) leads to the formation of iron oxide domains on the faces of the Pd nanotetrahedra. Particles synthesized in a solvent mixture (Figure 2.1a, Pd_{nth}) did not show the presence of iron oxide domains.

2.3.3 Pd Nanoplates

No iron oxide phase was detected in the powder X-ray profile of the hexagonal Pd nanoplates (Figure 2.2c). The refined lattice parameter of the Pd phase was 3.867(1) *Å*, only slightly smaller than the pure Pd phase parameter. From the Rietveld refinement, a Pd crystallite size of ≈ 7(1) nm could be derived. The ED pattern (Figure 2.3c) contains mainly Pd reflections. Interestingly, the electron diffraction profile shows an inverse ratio between the intensities of the 111 and 220 reflections, the intensity of the 111 reflection being strongly suppressed. This points to a preferred orientation along [111], the most developed faces of the Pd particles. For Pd with a ccp structure, a hexagonal particle with (111) facets has the shape of

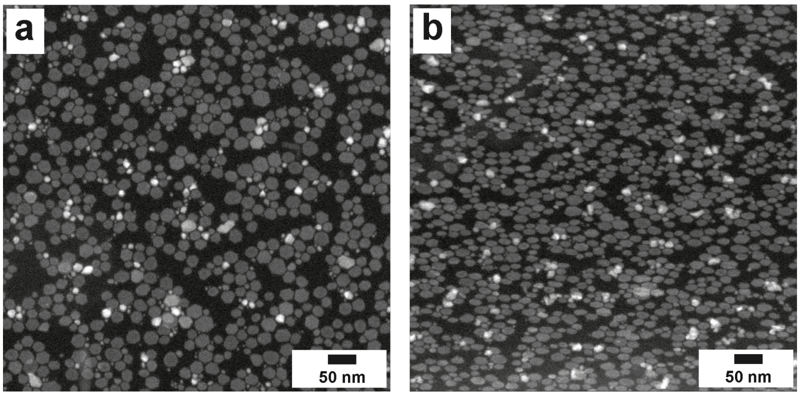

Figure 2.11: STEM images of hexagonal Pd nanoplates tilted at (a) 30° and (b) 60° to verify their flat appearance.

a hexagonal metaprism with inclined sides where all faces are of (111) type (Figure 2.6e, inset). A diffraction pattern of particles oriented in the [111] direction showed the increased intensity of the 220 reflection and a relatively weak 111 reflection. Indeed, STEM tilting experiments showed that most hexagonal Pd nanoplates were flat (Figure 2.11), which can explain the preferred orientation observed in the electron diffraction pattern. The EDX spectrum (Figure 2.8c, from a set of particles depicted in Figure 2.6e) shows the presence of Fe, although in smaller amounts than in the Pd_{nth}@Fe_xO sample.

The Mössbauer spectrum of the Pd nanoplates (Figure 2.5c) shows an Fe_xPd content of $\approx$ 17%. One single fit was compatible with the presence of β-FeOOH and the other with γ-FeOOH based on their hyperfine parameters (Table 2.3). The presence of hydroxylated iron oxide species might be rationalized by the formation of iron carboxylate intermediates and their subsequent decomposition.[328]

Although these oxyhydroxides cannot be detected by X-ray powder diffraction because of their noncrystallinity (Figure 2.2c), Mössbauer spectroscopy can provide useful clues about the hexagonal Pd nanoplates. The passivation of the (111) facet by CO prevents the formation of crystalline iron oxides. Still, iron oxides on the other Pd seed particles may hide oxyhydroxide Mössbauer signals because of their signal intensity (Figure 2.5a, b). ED data (Figure 2.3) unambiguously show the presence of iron oxide. A tentative explanation might be a transformation of FeOOH into iron oxide under TEM conditions. In addition, HR-TEM images of Pd nanoplates revealed a distinct bending of particles with a thickness of < 5 nm.

High-resolution aberration-corrected TEM of a nanoplate (Figure 2.6f) revealed the polycrystalline nature of the plates and showed Pd reflections of the Pd[112] and [110] zone axis. A HR-TEM image of a nanoplate in a "side view" along (110) obtained from a TEM focal series reconstruction at 300 kV (Figure 2.12c) shows (111) lattice planes of Pd. No twinning or stacking faultlike defects were observed for the Pd particles, which are typically associated with a two-dimensional growth of the nanoplates. The aspect ratio of the Pd nanoplates was $\approx$ 10:1 (Figure 2.13).

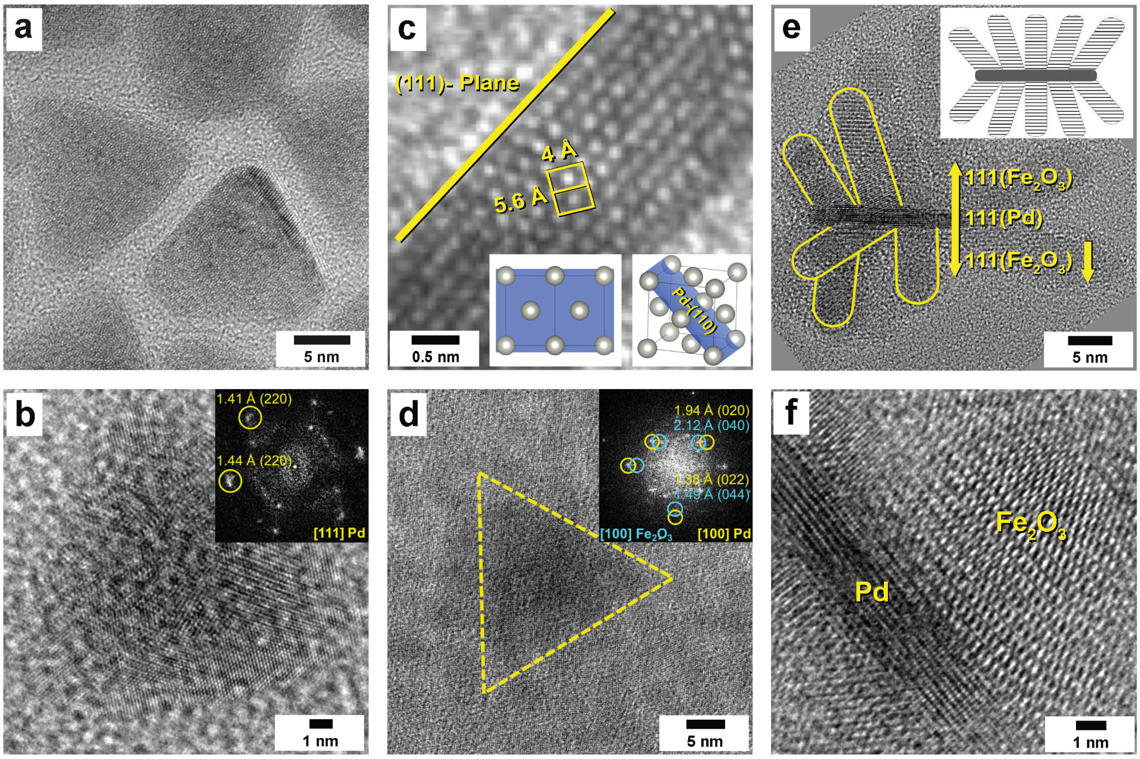

Figure 2.12: HR-TEM images of particles obtained after step 1 of the synthesis pathway (a-c) and after step 2 of the synthesis pathway (d-f). (a) HR-TEM image of Pd nanotetrahedra. (b) HR-TEM (aberration corrected and noise filtered) image of Pd nanotetrahedra showing reflections of Pd[111] zone axis in the power spectrum (insert). (c) HR-TEM image of hexagonal Pd nanoplates projection in [110]-direction showing stacking fault free Pd lattice structure. (d) HR-TEM (aberration corrected) image of $Pd_{nth}@Fe_2O_3$ superparticles showing reflections of Pd[100] and Fe_2O_3[100] zone axis in the power spectrum (insert, Pd yellow and Fe_2O_3 blue). (e) HR-TEM of $Pd_{hnp}@Fe_2O_3$ superparticles showing epitaxial growth and particle modeling (insert). (f) HR-TEM (aberration corrected and noise filtered) image of $Pd_{hnp}@Fe_2O_3$ superparticles.

2.3.4 Kinetic Control of γ-Fe_2O_3 Nanorod Formation

The seed-mediated growth of the Pd@γ-Fe_2O_3 superparticles was performed with TMAO as the oxidizing agent for $Fe(CO)_5$. To study the effect of the TMAO oxidant, the reactions were performed with different amounts of TMAO while keeping the amount of $Fe(CO)_5$ constant (Figure 2.14). Well-defined products were found for $Fe(CO)_5$:TMAO ratios of 1:3 and 1:4. For a $Fe(CO)_5$:TMAO ratio of 1:3, urchin-like structures with sizes between 50 and 100 nm were formed containing a tetrahedral Pd core decorated with γ-Fe_2O_3 nanorods with a maximal length of 20-30 nm and a lateral diameter of $\approx$ 8 nm (Figure 2.15). The nanorods were arranged statistically around the Pd seeds. Reducing the amount of TMAO led to the formation of larger superparticles with a rounded shape caused by iron oxide particles with a less pronounced rod morphology. This resulted eventually in the formation of a

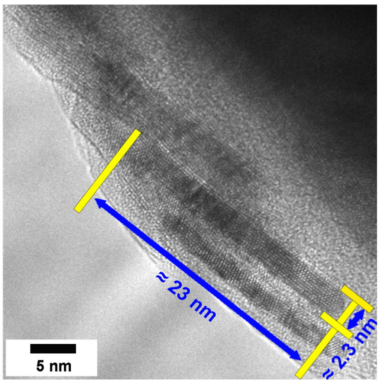

Figure 2.13: HR-TEM image of hexagonal Pd nanoplates representing an aspect ratio of 10:1 (average of > 20 particles).

dense coating around the seeds and rounded superparticles. Figure 2.14a shows the product distribution when an excess of Fe(CO)$_5$ was used, and spherical iron oxide particles with diameters of ≈ 8 nm (often also not connected to the seed particles) were formed. For a Fe(CO)$_5$:TMAO ratio of 1:3 or 1:4 (*i.e.* an excess of the oxidant), iron oxide nanorods were formed in a fast reaction, indicating kinetic control of the reaction. For a very large excess of TMAO, the formation of iron oxide nanorods proceeded so fast that epitaxial growth seems no longer possible and phase-separated Pd and iron oxide particles appeared. As a result, the superparticles became much smaller (Figure 2.14f).

2.3.5 Synthesis of Pd@γ-Fe$_2$O$_3$ Superparticles

The seed-mediated growth of Pd@γ-Fe$_2$O$_3$ superparticles was performed with TMAO as the oxidizing agent for Fe(CO)$_5$. The Pd nanotetrahedra and hexagonal nanoplates were used as seeds for the epitaxial growth of γ-Fe$_2$O$_3$ nanorods (Figure 2.15). Although we could find evidence of only an Fe$_x$Pd phase in Mössbauer spectroscopy and HR-TEM analysis, we verified the importance of an iron admixture in the Pd seed particles by preparing Pd nanoplates without Fe(CO)$_5$ using a method reported by Trinh *et al.*[329] Under a similar set of conditions, we could not grow iron oxide nanorods onto these nanoplates (Figure 2.16). This control experiment highlights the importance of Fe$_x$Pd as a "buffer layer" to overcome the interfacial strain. Although the lattice mismatch of Pd and maghemite is 7% (which is high assuming solid-state epitaxial growth), it can be surmounted in solution or beaker epitaxy by proper reaction design and chemical matching. Other parameters such as solvent, stabilizing ligand, and temperature are equally important for achieving heterogeneous nucleation, as we showed for the synthesis of Au@ZnO heterodimeric particles with 12% lattice mismatch.[38, 39]

Figure 2.17a shows the X-ray diffractogram of the Pd$_{\mathrm{nth}}$@Fe$_2$O$_3$ superparticles. The reflections can be assigned to Pd as well as γ-Fe$_2$O$_3$. The intensity of the Pd reflections is much lower than that of the corresponding reflections for the Pd

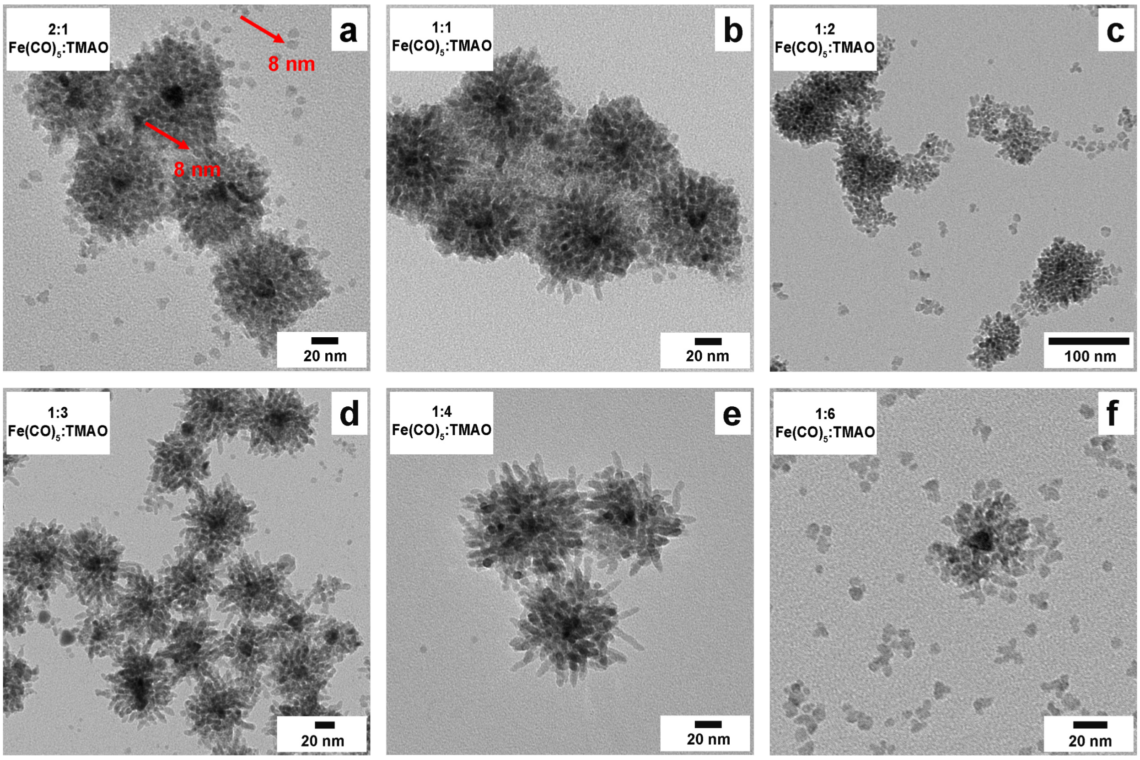

Figure 2.14: TEM images of Pd_{nth}@Fe_2O_3 superparticles synthesized with different ratios of $Fe(CO)_5$:TMAO, (a) 2:1, (b) 1:1, (c) 1:2, (d) 1:3, (e) 1:4 and (f) 1:6. Arrows in (a) highlight spherical iron oxide particles with 8 nm diameter formed under thermodynamic reaction control.

nanotetrahedra because of the absorption by the surrounding γ-Fe_2O_3 nanorods (Figure 2.17a, Figure 2.18a). Hence, only the maghemite ($Fe_{0.67(1)}O$) content with a crystallite size of 13(1) nm could be refined; the X-ray data do not give information concerning the composition of a bulk sample of the superparticles.

For Pd_{hnp}@Fe_2O_3 superparticles (Figure 2.17b, Figure 2.18b), a Pd content of 11(1) wt% could be extracted from the Rietveld refinement. The remaining portion of the superparticles consists of maghemite (Table 2.2). Here the presence of a Pd core, selectively overgrown with maghemite nanorods, could be demonstrated for a bulk sample. Figure 2.19 shows ^{57}Fe Mössbauer spectra of the two types of Pd@γ-Fe_2O_3 superparticles at 5.5 K. Both spectra contain two magnetic sextets with high hyperfine fields (Table 2.3) characteristic of γ-Fe_2O_3. The absence of an electric quadrupole splitting (black arrows) supports the formation of γ-Fe_2O_3 due to full oxidation of Fe by excess TMAO.

Panels c and d of Figure 2.15 show aberration-corrected and noise-filtered HR-TEM images of Pd_{nth}@Fe_2O_3 superparticles. The maghemite nanorods appear to grow epitaxially on the Pd seeds, and they are statistically distributed. The power spectra of the Pd[101] and Fe_2O_3[111] zone axis show reflections of Pd and Fe_2O_3, respectively. The images of the interface do not show remarkable strain or misfits

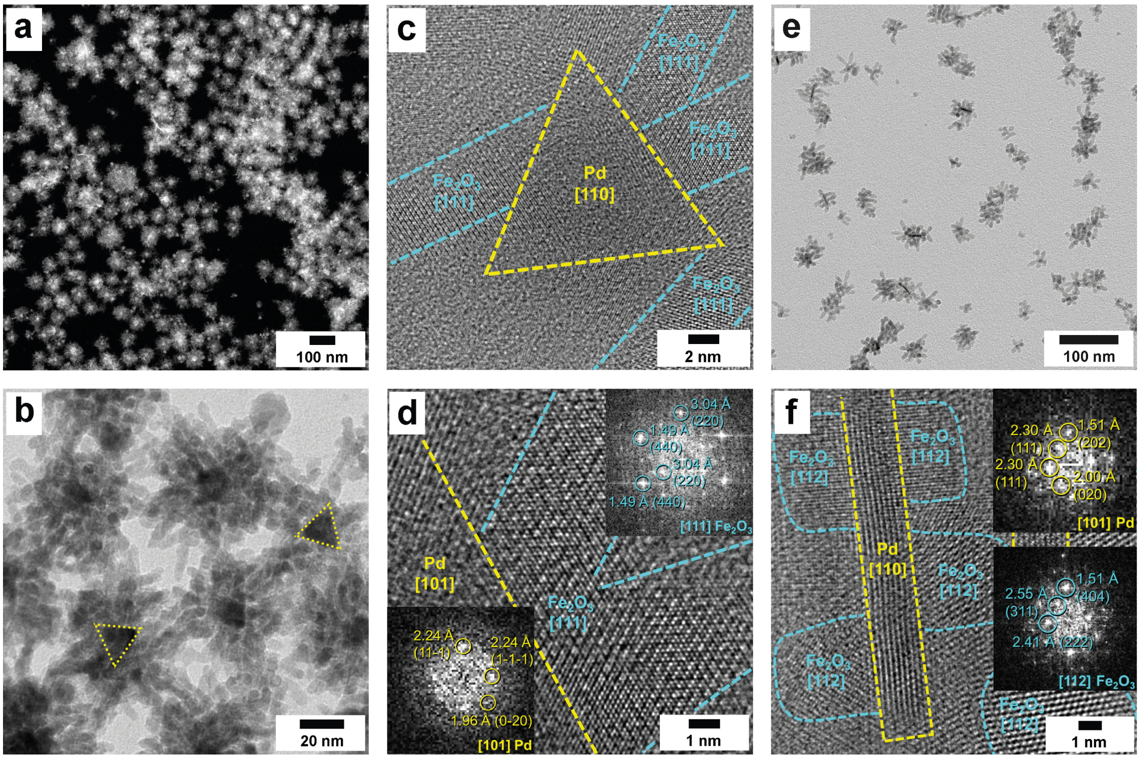

Figure 2.15: TEM images of superparticles obtained after step 2 of the synthesis pathway. (a) STEM and (b) TEM images of Pd_{nth}@Fe_2O_3 superparticles. (c and d) HR-TEM (aberration-corrected and noise-filtered) images of Pd_{nth}@Fe_2O_3 superparticles showing the Pd and Fe_2O_3 zone axis, epitaxial growth, and Pd (yellow) and Fe_2O_3 (blue) reflections in the power spectra (insets in panel d). (e) TEM and (f) HR-TEM (aberration-corrected and noise-filtered) images of PPd_{hnp}@Fe_2O_3 superparticles showing the Pd and Fe_2O_3 zone axis, epitaxial growth, and Pd (yellow) and Fe_2O_3 (blue) reflections in the corresponding power spectra (insets in panel f).

in the case of the Pd_{nth}@Fe_2O_3 superparticles or in the case of the Pd_{hnp}@Fe_2O_3 superparticles (*e.g.* Figure 2.12f or Figure 2.15f). The epitaxial relation for the Pd_{nth}@Fe_2O_3 superparticles is given by [110]Pd/[111]Fe_2O_3 (Figure 2.15c,d) and for the Pd_{hnp}@Fe_2O_3 superparticles by [110]Pd/[112]Fe_2O_3 (Figure 2.15f). For the Pd_{nth}@Fe_2O_3 superparticles, the observation of the interface proved to be difficult because the nanotetrahedron has a tilted facet in the view direction and thus the γ-Fe_2O_3 nanorod does not end just at the visible edge but seems to invade the nanotetrahedron. However, the nanorods are visible also "inside" the nanotetrahedron and do not cause an observable distortion of the Pd lattice. For the plate-like Pd core, a crystallographic alignment was also observed. Figure 2.15f shows an aberration-corrected noise-filtered HR-TEM image of a superparticle formed with Pd nanoplates (thickness of $\approx$ 2 nm, $\approx$ 10 atomic layers, Pd_{hnp}@Fe_2O_3). At the surface of the Pd nanoplate, the Pd core and the γ-Fe_2O_3 nanorods share a common (111) interface ((111) Fe_2O_3‖(111) Pd). The nanorods at the periphery of the Pd plate are inclined

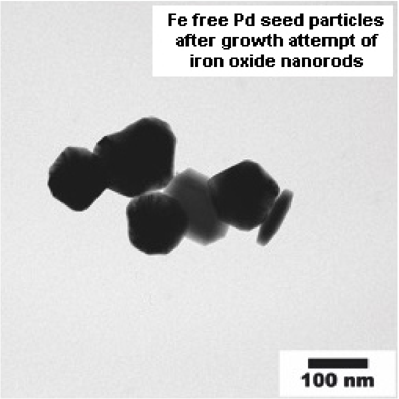

Figure 2.16: TEM image of iron free Pd nanoplates, prepared using a method reported by Trinh *et al.*, after growth attempt of iron oxide nanorods. No maghemite nanorods on the preformed Pd nanoplate seeds could be obtained.[329]

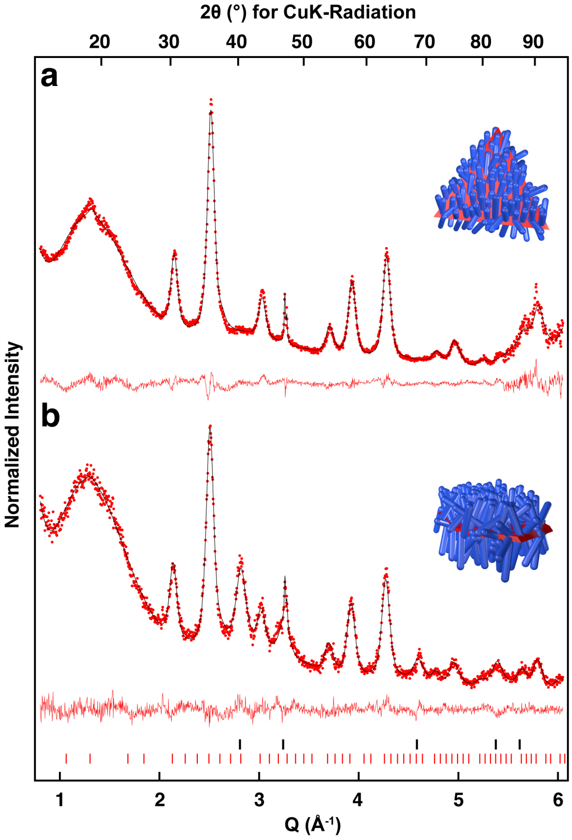

Figure 2.17: Rietveld refinements of powder XRD data for (a) $Pd_{nth}@Fe_2O_3$ superparticles and (b) $Pd_{hnp}@Fe_2O_3$ superparticles. Red dots mark the experimental data, the black line corresponds to the calculated pattern, and the red line shows the difference between the experimental and calculated data. Black ticks mark reflections of Pd. $Q = [4\pi \sin(\Theta)]/\lambda$ is the scattering vector.

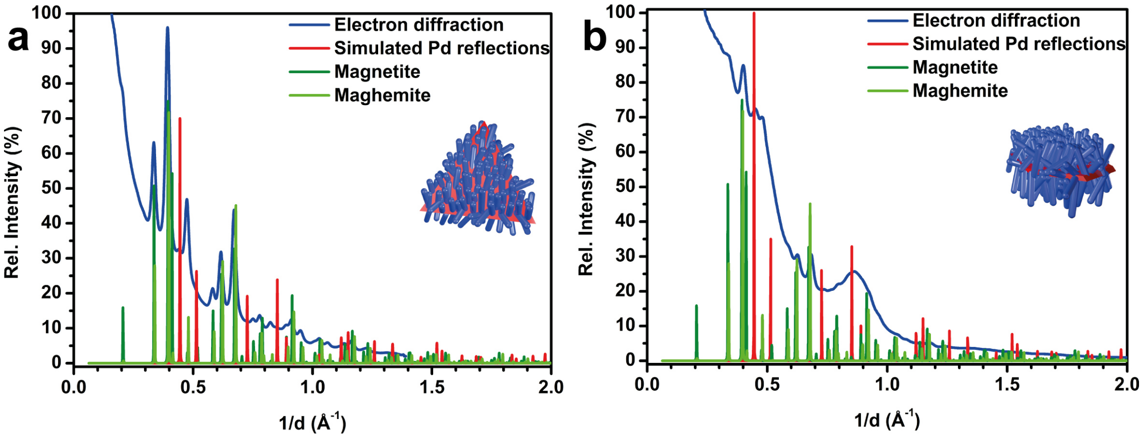

Figure 2.18: Electron diffraction of (a) Pd$_{nth}$@Fe$_2$O$_3$ superparticles and (b) Pd$_{hnp}$@Fe$_2$O$_3$ superparticles. ED cannot distinguish between magnetite and maghemite.

to the Pd core, probably because of spatial demands during growth (Figure 2.12e). The γ-Fe$_2$O$_3$ rods still follow the epitaxial relationship at the interface, but because of the inclination, they do not grow exactly along [111] anymore. EDX spectra of the superparticles (Pd$_{nth}$@Fe$_2$O$_3$) show an Fe content of $\approx$ 95% (Figure 2.20), and the total composition does not change significantly for superparticles containing Pd nanoplates as seeds.

2.3.6 Magnetic Properties of Pd@γ-Fe$_2$O$_3$ Superparticles

The Pd@γ-Fe$_2$O$_3$ superparticles are ferromagnetic at 5 K and superparamagnetic at room temperature, as extracted from temperature-dependent magnetization and hysteresis curves (Figure 2.21a and c). The blocking temperatures of 260 K (Pd$_{nth}$@Fe$_2$O$_3$, Figure 2.21b) and 210 K (Pd$_{hnp}$@Fe$_2$O$_3$, Figure 2.21d), are relatively high because of the particle sizes. These results indicate that all γ-Fe$_2$O$_3$ nanorods are magnetically decoupled, *i.e.* there is no magnetic communication between individual nanorods. The larger volume and the size distribution of the superparticles are responsible for the broad maxima of the ZFC and FC curves. The saturation magnetizations (summation of the magnetic moments of all individual γ-Fe$_2$O$_3$ nanorods) at 5 K and 300 K for both superparticle types are $>$ 40 emu/g (Table 2.4). The maximum value of 66.4 emu/g was observed for the Pd$_{hnp}$@Fe$_2$O$_3$ superparticles (Figure 2.21c), which is slightly lower than the saturation magnetization of bulk maghemite (80 emu/g).[330]

2.3.7 Catalysis

In recent years, metal oxide and also noble metal nanoparticles were shown to be functional enzyme mimics. In particular, iron oxides, which are robust and low-cost materials compared to natural enzymes,[242, 250, 265, 332] were reported to exhibit peroxidase and catalase activity. For small molecules with little space demand, the

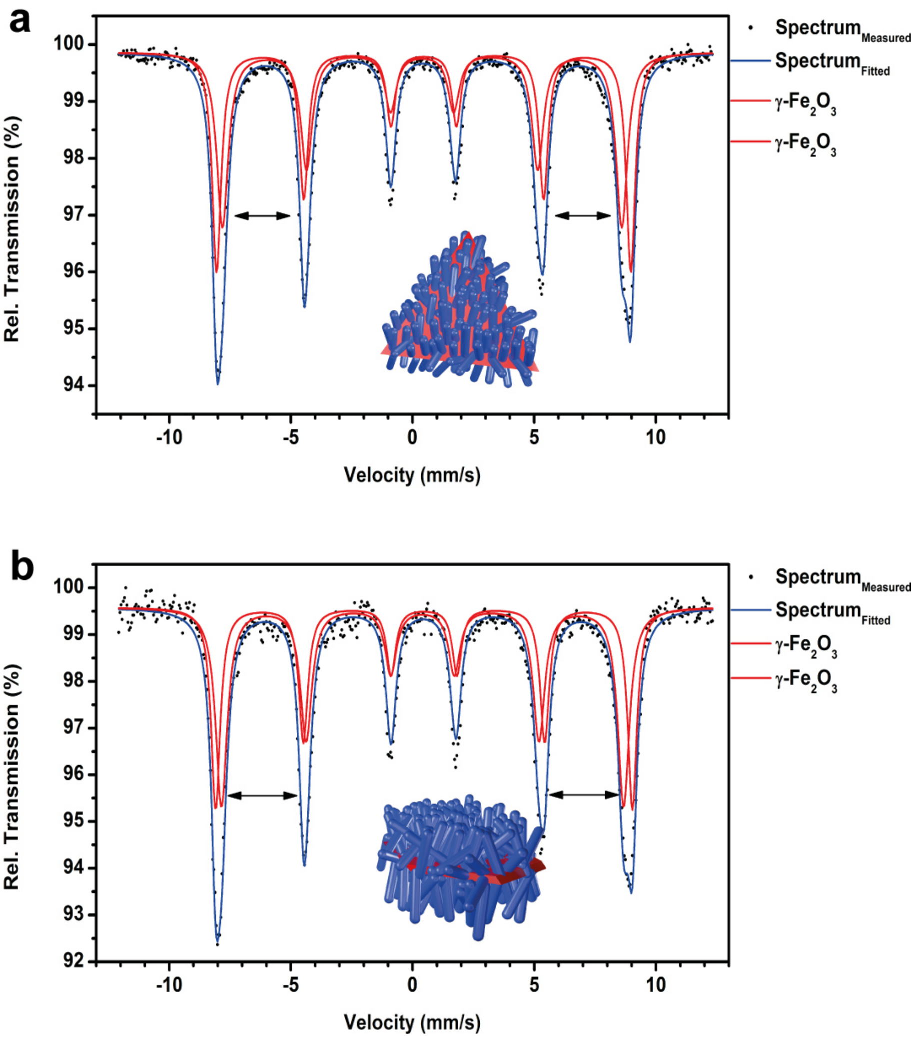

Figure 2.19: ^{57}Fe-Mössbauer spectra at 5.5 K of (a) $Pd_{nth}@Fe_2O_3$ superparticles and (b) $Pd_{hnp}@Fe_2O_3$ superparticles. Both sextets in panels a and b correspond to γ-Fe_2O_3 (red line).

essentials of the active sites of metalloproteins are sufficiently well modeled by the surface of oxide particles containing the respective metal atoms in the appropriate oxidation states. An important question in this context is whether heteroparticles show enhanced catalytic activity due to (i) electron transport across the metal-metal oxide interface and (ii) the increased surface area. As the peroxidase-like activity of iron oxide nanoparticles is well documented,[233, 250] we have selected the peroxidase system to probe these questions for Pd@γ-Fe_2O_3 superparticles.

To disperse the Pd@γ-Fe_2O_3 superparticles in water, the superparticles were surface functionalized with a catechol-PEG polymer (Figure 2.22) as described previously.[92, 114] Briefly, the C-PEG was synthesized using anionic ring opening polymerization of ethylene oxide (EO) starting from a protected catechol-initiator (Figure

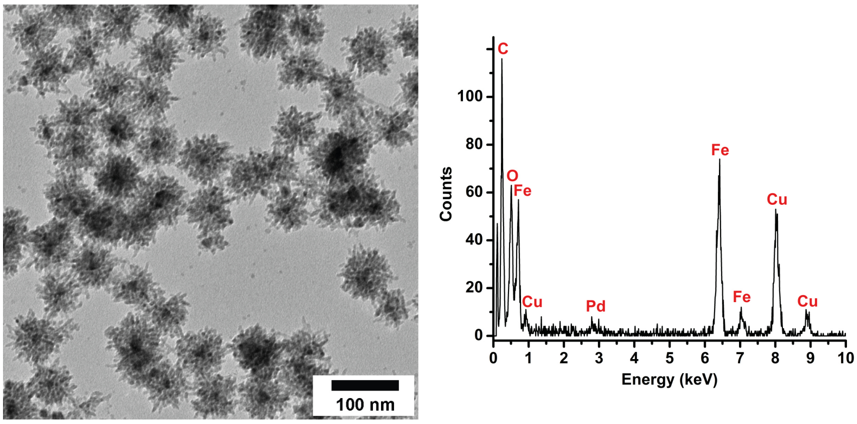

Figure 2.20: TEM image and EDX spectrum of Pd$_{nth}$@Fe$_2$O$_3$ superparticles.

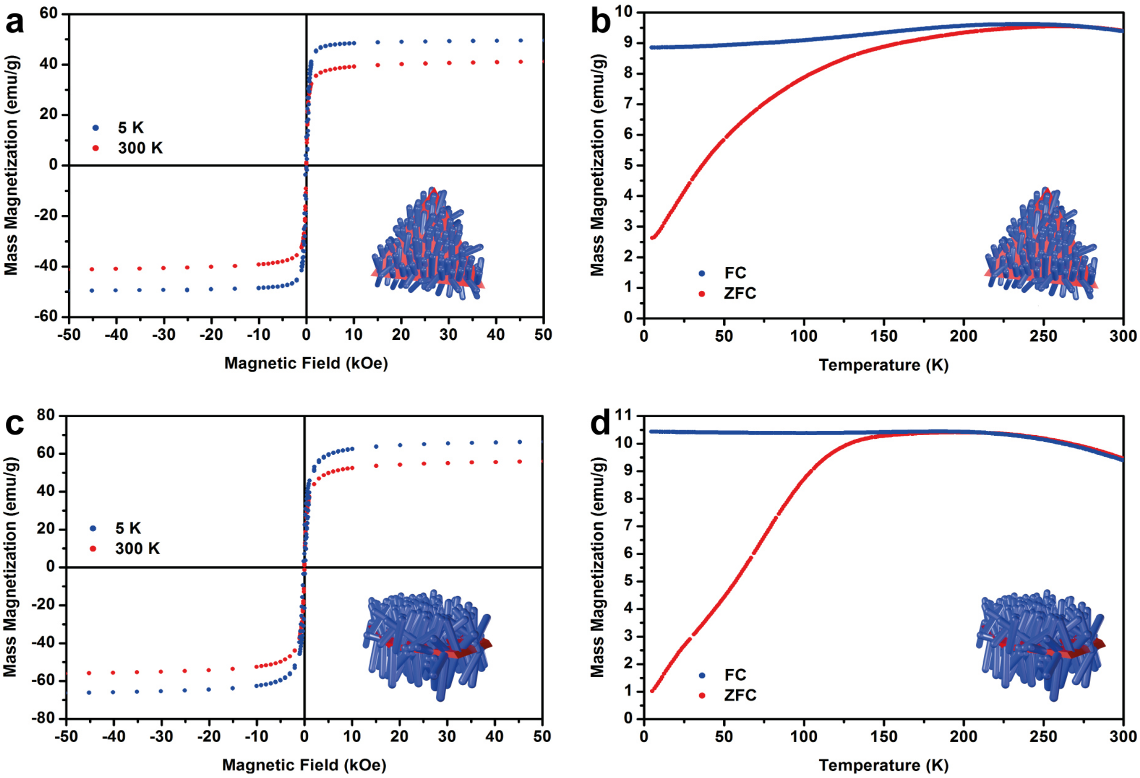

Figure 2.21: Magnetic hysteresis and blocking temperature measurements with field cooled (FC) and zero field cooled (ZFC) magnetic field for Pd@γ-Fe$_2$O$_3$ superparticles: (a, b) Pd$_{nth}$@Fe$_2$O$_3$ superparticles, (c, d) Pd$_{hnp}$@Fe$_2$O$_3$ superparticles.

2.22). The living character of this polymerization strategy allows the synthesis of well-defined PEGs with tailored molecular weights, which provide sufficient stabilization of superparticles with sizes up to 100 nm. The applied C-PEG possesses 67 ethylene oxide repeating units (M_n = 2450 g/mol, PDI = 1.07, from SEC (DMF, RI signal, PEG standard)). After functionalization the Pd@γ-Fe$_2$O$_3$ superparticles were

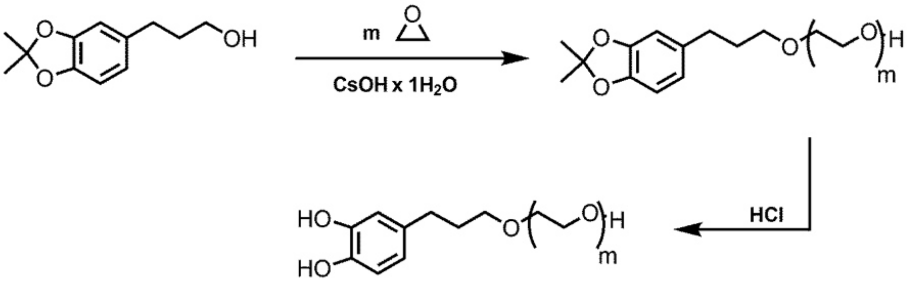

Figure 2.22: Synthesis scheme of catechol-PEG. Polymerization of ethylene oxide (EO) starting from an acetonide-protected catechol initiator, followed by deprotection of CA-PEG with an aqueous solution of hydrochloric acid resulting in hydrophilic C-PEG.

easily dispersible in water. Despite the size of the superparticles, the dispersions were stable for several weeks.

The peroxidase-like activity was investigated using a colorimetric assay based on the catalytic oxidation of 2,2'-azinobis(3-ethylbenzothiazoline-6-sulfonic acid) (ABTS) with H_2O_2.[333] The catalytic efficiency of the superparticles was monitored by oxidation of the ABTS dye, which leads to the formation of a radical absorbing at 405 nm and yielding a green solution. In a first step, the concentration of the Pd@γ-Fe_2O_3 superparticles was varied. An increase of the superparticle concentration from 0.12 to 3.6 µg/mL showed a linear trend with higher reaction rates as a result of increasing NP concentrations (Figure 2.23a).

2.3.8 Calculation of Kinetic Parameters

In the next step, the concentration of the ABTS substrate was varied from 0.01 to 0.5 mM, where a Michaelis-Menten-like saturation curve, as typically observed for enzyme reactions, was found (Figure 2.23b). The data points were fitted to the Michaelis-Menten equation to yield the maximal reaction rate (v_{max}) and Michaelis-Menten substrate binding constant (k_m) as kinetic parameters. The small Michaelis-Menten constant of 0.049 mM, indicating a high affinity of the substrate for the catalyst, and a large maximal reaction rate of 1.02 x 10^{-7} Ms^{-1} (Table 2.1) is comparable to values reported for other iron oxide nanoparticles, but significantly higher than that for natural horseradish peroxidase (HRP).[334–338] To calculate the catalytic constant k_{cat}, defined as the maximal catalytic turnover per active catalytic site per second, the number of active sites had to be evaluated.[339] A surface:volume ratio for the iron atoms was calculated through a calibration factor that allowed conversion of the total molar iron concentration (determined by AAS) to the surface iron concentration. To do this, the superparticle Fe_2O_3 nanorods were modeled by nanocylinders with an average length of 27 nm and an average radius of 4 nm (obtained as average dimensions from TEM images). HR-TEM indicated the (111) epitaxial growth of the γ-Fe_2O_3 nanorods on the Pd seeds (Figure 2.15d) with an exposed (100) side surface.

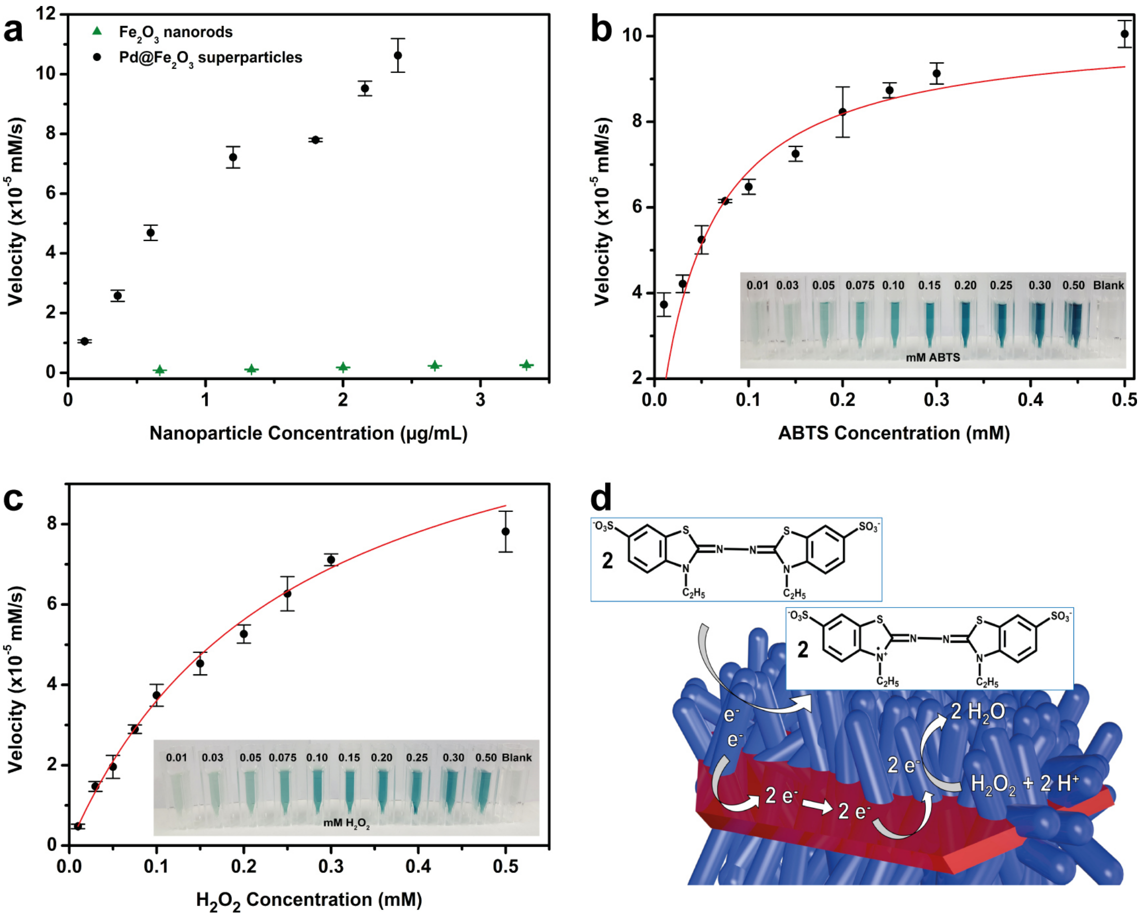

Figure 2.23: Peroxidase-like activity of $Pd_{hnp}@Fe_2O_3$. (a) Variation of the NP concentration using 0.5 mM ABTS and 0.2 mM H_2O_2 showing linear behavior for $Pd_{hnp}@Fe_2O_3$ superparticles and isolated Fe_2O_3 nanorods. (b) Variation of the ABTS concentration using 1.8 µg/mL NP and 0.2 mM H_2O_2 showing Michaelis-Menten-like behavior. (c) Variation of the H_2O_2 concentration using 1.8 µg/mL NP and 0.15 mM ABTS showing Michaelis-Menten-like behavior. (d) Schematic representation of the synergistic effect of electron transport through the Pd-γ-Fe_2O_3 interface. All experiments were performed in a 1 mL reaction volume at 37 °C (23 °C for isolated Fe_2O_3 nanorods) in acetic acid buffer at pH 3.62.

The number of Fe atoms present on the (100) surface of the unit cell of an inverse spinel structure was calculated and related to the total number of surface atoms of the nanocylinder (approximately 2100 Fe surface atoms, *vide infra* Experimental Section).[321] From the ratio of the cylinder volume and the volume of the maghemite unit cell, the total number of Fe atoms (approximately 50000) within the volume of a single γ-Fe_2O_3 nanorod was approximated.[340] The ratio of 2100 surface Fe atoms to 50000 Fe atoms in a single γ-Fe_2O_3 nanorod was used as a calibration factor (0.0420) to derive the number of active Fe surface sites in a sample from the total Fe concentration (determined by AAS).

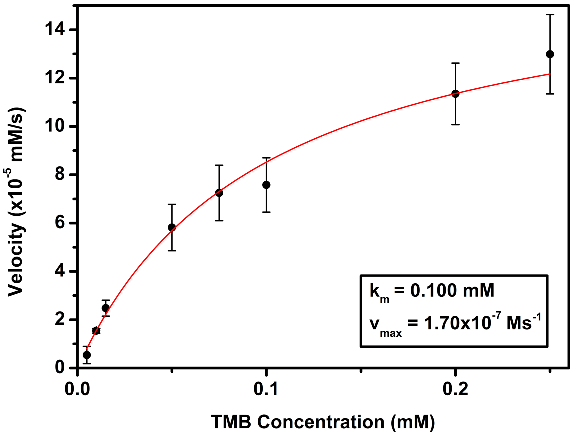

Figure 2.24: Peroxidase-like activity of Pd@γ-Fe_2O_3 superparticles. Variation of TMB (3,3',5,5'-tetramethylbenzidine) concentration using 3 µg/mL NP and 25 mM H_2O_2 showing Michaelis-Menten-like behavior. All experiments were carried out in 1 mL reaction volume at 37 °C in acetic acid buffer at pH 3.62.

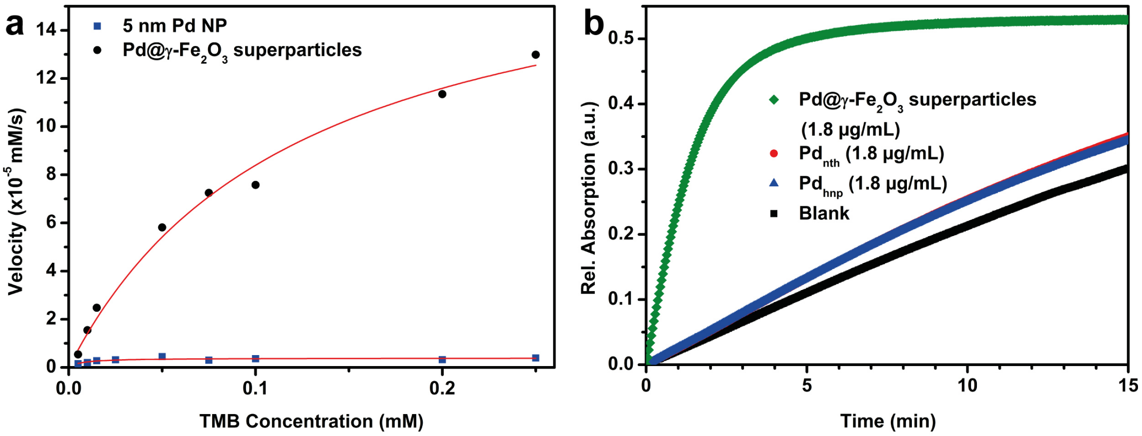

Figure 2.25: (a)Peroxidase-like activity of 5 nm Pd NPs compared to Pd@γ-Fe_2O_3 superparticles. Variation of TMB (3,3',5,5'-tetramethylbenzidine) concentration using 3 µg/mL Pd@γ-Fe_2O_3 superparticles, 30 µg/mL 5 nm Pd NPs and 25 mM H_2O_2 showing Michaelis-Menten-like behavior. The 5 nm Pd NP were synthesized according to Kim *et al.* and functionalized using 11-mercaptoundecanoic acid.[331] (b) Enhanced peroxidase-like activity of Pd@γ-Fe_2O_3 superparticles compared to Pd nanotetrahedra (Pd_{nth}) and hexagonal Pd nanoplate (Pd_{hnp}) seeds. Time dependent relative absorption of ABTS (2,2'-azino-bis(3-ethylbenzothiazoline-6- sulphonic acid)) using equal NP concentrations of 1.8 µg/mL, 0.5 mM ABTS and 0.2 mM H_2O_2. All experiments were carried out in 1 mL reaction volume at 37 °C in acetic acid buffer at pH 3.62.

Using this model, turnover values (k_{cat}) of 0.075 s^{-1} (ABTS) and 0.094 s^{-1} (H_2O_2) were calculated, which are significantly lower than those reported in the literature,[236] which appear to be based on the assumption that each nanoparticle (with a size compatible to the diameter of a single enzyme molecule) typically has only one

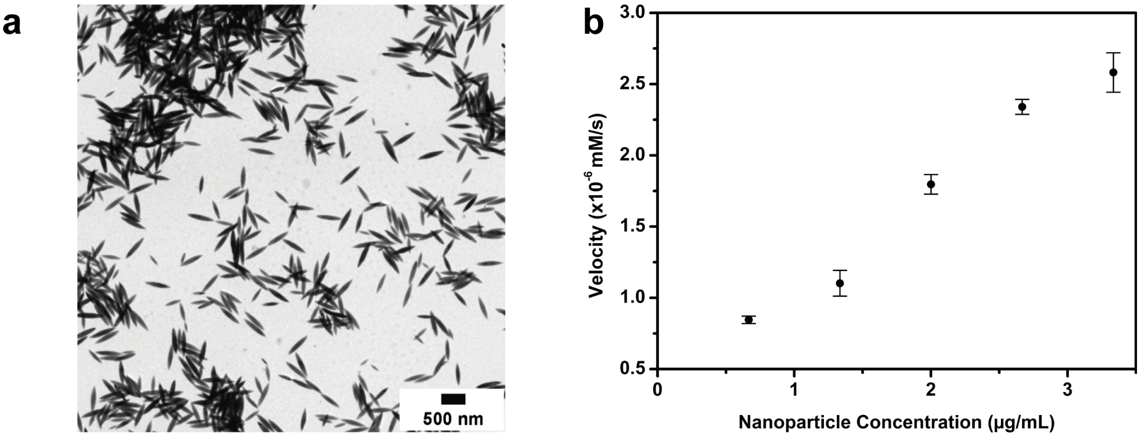

Figure 2.26: (a) TEM image of isolated Fe_2O_3 nanorods. (b) Peroxidase-like activity of isolated Fe_2O_3 nanorods at different NP concentrations using 0.5 mM ABTS and 0.2 mM H_2O_2 showing linear behavior. All experiments were carried out in 1 mL reaction volume at 23 °C in acetic acid buffer at pH 3.62.

active site. These assumptions lead to low nanoparticle concentrations and very large turnover values. However, on the basis of the assumption that every Fe surface atom may act as an active site, nanoparticles - and also the superparticles described here - exhibit many binding sites and therefore a high reactivity compared to that of enzymes, which on the other hand have a highly specific binding site with exceptional complexity. Therefore, enzyme mimetic catalysis with nanoparticles is successful, especially in those cases in which small molecular species like peroxides, superoxides, or sulfites are involved and steric demands play an only minor role in the specificity of the reaction.[143]

Finally, the H_2O_2 concentration was varied from 0.01 to 0.5 mM, resulting in similar v_{max} and k_{cat} values (Figure 2.23c). The lower affinity of H_2O_2 for the particles compared to that of ABTS may be caused by the weakened Coulomb interaction between the Pd@γ-Fe_2O_3 superparticles and H_2O_2 leading to higher k_m values (Table 2.1). These Coulomb forces are also evident upon comparison of the k_m for ABTS with the k_m for TMB (Figure 2.24), showing a lower value for ABTS because of the negative overall charge of the radical interacting with the positively charged nanoparticles (ζ potential of 15.7 mV), whereas the positively charged TMB may suffer from repulsion forces.[341]

Still, the high catalytic activity of the Pd@γ-Fe_2O_3 superparticles with respect to that of other iron oxide nanoparticles can be conceived by comparing the k_m and v_{max} values of similar magnitude with the much lower NP mass concentration used in the assay here.[236] A peroxidase-like activity of Pd combined with metals Au and Ir has been reported.[342, 343] To estimate the effect of Pd, single 5 nm Pd particles as well as Pd nanotetrahedra and Pd nanoplate seeds were tested and showed a negligible peroxidase-like activity (Figure 2.25).[331]

The synergistic effect becomes especially apparent when the reaction rates for the

Table 2.1: Calculated kinetic parameters. [NP] is the NP concentration. k_m is the Michaelis-Menten constant. v_{max} is the maximal reaction rate. k_{cat} is the catalytic constant given by $k_{cat} = v_{max}/[NP]$.

	[NP] (M)	substrate	k_m (mM)	v_{max} (Ms^{-1})	k_{cat} (s^{-1})
Pd@γ-Fe_2O_3 SPs	1.35 x 10^{-6}	ABTS	0.049	1.02 x 10^{-7}	0.075
Pd@γ-Fe_2O_3 SPs	1.35 x 10^{-6}	H_2O_2	0.254	1.28 x 10^{-7}	0.094

superparticles are compared with those of isolated iron oxide (Fe_2O_3) nanorods at otherwise identical concentrations. Thus, for a comparison of the peroxidase-like activity of Pd@γ-Fe_2O_3 superparticles and isolated Fe_2O_3 nanorods, isolated Fe_2O_3 nanorods (Figure 2.26a) were synthesized according to Ishikawa *et al.*, functionalized with the same PEG-polymer as used for the superparticles and measured at 23 °C (Figure 2.26b).[92, 344] According to the RGT-rule, which relates the reaction velocity with the reaction temperature, the nanorod activity should be approximately three times higher at 37 °C. This corresponds to a maximum reaction velocity of 9.0 x 10^{-6} mM/s, which is still lower than the activity of the smallest NP concentration of superparticles (Figure 2.23a).

In summary, Pd@γ-Fe_2O_3 superparticles show a 10-fold increase in the reaction rate (Figure 2.23a and Figure 2.26b). We attribute this increase in peroxidase-like activity to a synergistic effect for the charge separation and the resulting electron transfer between the palladium core and the iron oxide nanorod "antennae" (Figure 2.23d).[40, 44, 45, 58, 289, 345]

2.4 Conclusion

We have demonstrated a two-step synthesis for Pd@γ-Fe_2O_3 superparticles by seed-mediated growth of γ-Fe_2O_3 nanorods on Pd nanotetrahedra and hexagonal Pd nanoplates. *Via* adjustment of the ratios of solvent, the amount of surfactant, and the co-reductant $Fe(CO)_5$, the morphology of the Pd seed particles could be varied systematically. The γ-Fe_2O_3 nanorods were grown on the preformed Pd seeds by oxidizing $Fe(CO)_5$ with TMAO. Mössbauer measurements revealed the nanorods to consist exclusively of maghemite, and a HR-TEM analysis supported their epitaxial growth on the Pd(111) surface.

In addition, Pd@γ-Fe_2O_3 superparticles have an enhanced peroxidase-like catalytic activity (compared to that of isolated Fe_2O_3 nanorods) because of synergistic effects of electron transport through the Pd-γ-Fe_2O_3 interface between the Pd metal core and the γ-Fe_2O_3 nanorods. This leads to a 10-fold higher activity of Pd@γ-Fe_2O_3 superparticles compared to that of pure iron oxide nanorods.

The advantages of superparticles, whose components are interfaced *via* shared crystals faces compared to superstructures from self-assembled small nanoparticles stabilized by van der Waals interactions,[77, 346] are electronic communication due to the absence of separating organic surface layers and physical stability, which make superparticles promising candidates for catalytic, biomedical, or nanodevice application.

2.5 Experimental Section

Materials

Palladium(II) acetate ($Pd(ac)_2$, Sigma-Aldrich, 98%), oleylamine (OAm, Acros Organics, 80-90%), 1-octadecene (ODE, Acros Organics, 90%), oleic acid (OAc, Fisher Scientific, reagent grade), tri-n-octylphosphine (TOP, abcr, 97%), iron(0) pentacarbonyl ($Fe(CO)_5$, Aldrich), trimethylamine *N*-oxide (TMAO, Aldrich), cyclohexane (Fisher Scientific, analytical reagent grade), ethanol (techn.), chloroform (Aldrich, 99-99.4%), hydrogen peroxide (H_2O_2, Aldrich, $\geq$ 34%), 2,2'-azinobis(3-ethylbenzothiazoline-6-sulfonic acid) diammonium salt (ABTS, Aldrich, $\geq$ 98%), 11-mercaptoundecanoic acid (Sigma-Aldrich, 99%) and 3,3',5,5'-tetramethylbenzidine (TMB, Sigma-Aldrich, $\geq$ 99%) were used in this work.

Synthesis of Pd Nanoparticles

Tetrahedral Pd NPs (Pd_{nth}) were prepared by mixing 56.5 mg of $Pd(ac)_2$ (0.25 mmol), 7 mL of oleylamine, 3 mL of 1-octadecene, 670 µL of oleic acid, and 0.56 mL of tri-n-octylphosphine under inert gas (Ar) conditions in a 100 mL threeneck round-bottom flask. Subsequently, 30 µL of $Fe(CO)_5$ were added. Before the heating program was started, the mixture was stirred for 10 min under a gentle Ar flow. The mixture was heated to 120 °C at a rate of 2 °C/min and held at this temperature for 20 min. The heating proceeded to 180 °C at a rate of 2 °C/min, and the temperature was kept at 180 °C for 30 min. Afterward, the solution was cooled slowly to room temperature. A black product was precipitated from the solution by adding 15 mL of ethanol. The precipitate was separated by centrifugation (9000 rpm, 10 min, RT), dissolved in cyclohexane, washed twice with ethanol (cyclohexane:ethanol = 1:2), and centrifuged again (9000 rpm, 5 min, RT). Finally, the product was dissolved in cyclohexane, flushed with Ar, and stored at room temperature.

Hexagonal Pd nanoplates (Pd_{hnp}) were prepared by changing the amounts of oleylamine (8.5 mL), 1-octadecene (1.5 mL), and $Fe(CO)_5$ (60 µL).

Pd nanotetrahedra with mixed iron oxide surface domains ($Pd_{nth}@Fe_xO$) were synthesized by changing the amount of oleylamine to 10 mL and adding no 1-octadecene.

Synthesis of Pd@γ-Fe_2O_3 Superparticles

The synthesis of the maghemite nanorods was adapted from ref.[68] with some modifications. The superparticles containing tetrahedral Pd substrates were prepared by mixing 1.38 mmol of trimethylamine *N*-oxide (TMAO) with 12 mL of oleylamine under Ar in a 100 mL three-neck round-bottom flask. 10 mg of Pd seed particles dispersed in 1 mL of 1-octadecene was added. Subsequently, an additional 7 mL of 1-octadecene and 1.5 mL of oleic acid were added. The solution was stirred for 5 min at room temperature and then heated to 90 °C at a rate of 10 °C/min. The temperature was maintained for 5 min, and 60 µL of $Fe(CO)_5$ was added with a syringe. Afterward, the mixture was heated to 200 °C at a rate of 5 °C/min and held at this temperature for 1 h. The precipitation and purification were identical as described above for Pd NPs.

Surface Functionalization of Pd@γ-Fe$_2$O$_3$ Superparticles with C-PEG

The catechol-PEG polymer (C-PEG$_{67}$; M_n = 2450 g/ mol; PDI = 1.07, from SEC (DMF, RI signal, PEG standard)) was synthesized as described elsewhere.[92, 114] A 1 mg/mL solution of Pd@γ-Fe$_2$O$_3$ superparticles dispersed in chloroform was mixed with a 1 mg/mL solution of C-PEG in chloroform. The reaction mixture was stirred with a mechanical stirrer for 6 h at 40 °C under a gentle Ar flow. 6 mL of hexane per milligram of Pd@γ-Fe$_2$O$_3$ superparticles was added, and the superparticles were extracted into 1 mL of Milli-Q water per milligram of Pd@γ-Fe$_2$O$_3$ superparticles using a separating funnel.

Kinetic Analysis

Steady-state kinetic measurements were taken by measuring the absorbance of the oxidized ABTS radical at 405 nm and 37 °C in an acetic acid buffer solution with a pH of 3.62 on an UV-vis spectrophotometer.[333] The NP concentrations (Pd$_{\mathrm{hnp}}$@Fe$_2$O$_3$) were varied using 0.5 mM ABTS and 0.2 mM H_2O_2. For the variation of ABTS, 1.8 µg/mL NPs with 0.2 mM H_2O_2 and for the variation of H_2O_2, 1.8 µg/mL NPs and 0.15 mM ABTS were used. All experiments were performed in a 1 mL reaction volume. The initial rate values were adjusted to the Michaelis-Menten model by applying the Michaelis-Menten equation. Calculated kinetic parameters were k_m (Michaelis-Menten constant), v_{max} (maximal reaction rate), and k_{cat} (catalytic constant given by $k_{cat} = v_{max}/[NP]$). The molar NP concentration ([NP]) was calculated according to a model (*vide infra*) that accounts for the number of available catalytically active Fe surface sites. In a first step, superparticle γ-Fe$_2$O$_3$ nanorods, with an average length of 27 nm and an average radius of 4 nm, were approximated by a cylinder. The nanorods have a (100) side surface. Accordingly, two Fe atoms were assumed to be present on the (100) surface of a unit cell of an inverse spinel structure. The total (100) surface area of the approximated nanocylinder contains approximately 2100 Fe atoms (representing the surface of a single γ-Fe$_2$O$_3$ nanorod).[321] In the next step, the ratio of the cylinder volume to the volume of the maghemite unit cell was calculated and multiplied by the total amount of approximately 21 Fe atoms present in a single γ-Fe$_2$O$_3$ unit cell, which corresponds to approximately 50000 Fe atoms within the volume of a single γ-Fe$_2$O$_3$ nanorod.[340] The ratio of 2100 surface Fe atoms to 50000 Fe atoms in a single γ-Fe$_2$O$_3$ nanorod was used as a calibration factor of 0.0420 to convert the total Fe concentration determined by atomic absorption spectroscopy (AAS) to the number of active Fe surface sites. On the basis of this approach, an iron concentration of 1.35 x 10^{-6} M was calculated for evaluating k_{cat}.

Nanoparticle Characterization

Samples for *transmission electron microscopy (TEM)* were prepared by placing a drop of a dilute NP solution in cyclohexane on a carbon coated copper grid. TEM images for the characterization of size and morphology were obtained with a Philips EM-420 instrument operated at 120 kV. Aberration-corrected high-resolution TEM was performed on a JEM-ARM300F instrument (Grand ARM, JEOL Co.) with double correction. The spherical aberration of the condenser and the objective lens are corrected by dodecapole correctors in the beam and the image-forming system. The TEM resolution is 0.5-0.7 $\mathring{A}$ depending on the resolution criterion applied. TEM images were recorded on a 4K x 4K pixel CCD array (Gatan US4000). EDX analysis was performed with the FEI Tecnai F30-G2 instrument with a Super-Twin lens (FEI) with a field emission gun at an acceleration voltage of 300 kV. The point resolution amounted to 2.0 $\mathring{A}$, and the information limit amounted to $\sim$ 1.2 $\mathring{A}$. The microscope was equipped with a wide angle slow scan CCD camera (MultiScan, 2K x 2K pixels; Gatan Inc., Pleasanton, CA). High-resolution TEM, STEM, EDX, and ED data were also obtained on a FEI Tecnai F30 S-TWIN TEM instrument equipped with a field emission gun and operated at 300 kV.
X-ray diffraction (XRD) patterns were recorded on a Bruker AXS D8 Advance diffractometer equipped with a SolX energy dispersive detector in reflection mode using unfiltered Mo Kα radiation. Crystalline phases were identified according to the PDF-2 database using Bruker AXS EVA version 10.0. Full profile fits (Le Bail/Pawley/ Rietveld) were performed with TOPAS Academic version 4.1 by applying the fundamental parameter approach.[347, 348]
^{57}Fe Mössbauer spectra of powdered samples were recorded in transmission mode with a ^{57}Co source embedded in a rhodium matrix using a conventional constant-acceleration Mössbauer spectrometer equipped with a helium cryostat at 5.5 K. Isomer shifts are given with respect to iron metal at ambient temperature. Simulations of the experimental data were performed with the Recoil software.[349]
Magnetic susceptibility measurements were performed on a Quantum Design MPMS-XL superconducting quantum interference device (SQUID) magnetometer. Field-cooled (FC) and zero-field-cooled (ZFC) data were obtained in a temperature range between 5 and 300 K at 100 Oe. Hysteresis measurements were taken at 5 and 300 K.
UV-vis spectra were recorded on a Cary 5G UV-vis-NIR spectrophotometer in a range from 200 to 600 nm.
The ζ *potential* was recorded on a Malvern Zetasizer Nano ZS instrument; 1 μL of an aqueous solution was placed in Malvern cuvettes (disposable capillary cell) and measured at 25 °C.

Calculation of Fe-atoms Surface to Volume Ratio

To perform a model calculating, yielding a ratio of Fe-atoms present at the surface of the nanorods to the total amount of Fe-atoms in the nanorods, an average length (l) and radius (r) of the nanorods was measured using transmission electron microscopy data:

$$\mathrm{l = 27\,nm} \tag{2.1}$$

$$\mathrm{r = 4\,nm} \tag{2.2}$$

In the next step the nanorods were modeled by a cylinder (Figure 2.27) having a total volume (V_C) and surface (S_C) of:

$$\mathrm{V_C = \pi \times r^2 \times l} \tag{2.3}$$

$$\mathrm{S_C = \pi \times r^2 + 2 \times \pi \times r \times l} \tag{2.4}$$

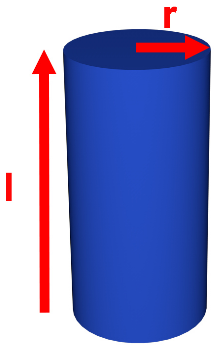

Figure 2.27: Cylinder model for nanorods.

The formula of S_C taking into consideration that only one of the two top sites of the cylinder is available to the substrate because the other site is grown onto the Pd core. This leads to the total cylinder volume and surface values of:

$$\mathrm{V_C = 1357\,nm^3} \tag{2.5}$$

$$\mathrm{S_C = 729\,nm^2} \tag{2.6}$$

Next, the surface of a cubic maghemite (100) plane ($S_{(100)}$) and the volume of one unit cell (V_{UC}) is calculated using the lattice constant of a = 0.833 nm.[321]

$$\mathrm{S_{(100)} = a^2 = 0.694\,nm^2} \tag{2.7}$$

$$\mathrm{V_{UC} = a^3 = 0.578\,nm^3} \tag{2.8}$$

Now an amount of unit cells present on the surface of one nanorod can be calculated according to:

$$\frac{\mathrm{S_C}}{\mathrm{S_{(100)}}} = \frac{729\,\mathrm{nm}^2}{0.694\,\mathrm{nm}^2} = 1050 \tag{2.9}$$

This value can be multiplied by 2 Fe-atoms per unit cell which are present on the (100) plane to give a total amount of 2100 Fe-atoms at the surface of an iron oxide nanorod.[340] Further, the quantity of unit cells present in one nanorod can be calculated similarly:

$$\frac{\mathrm{V_C}}{\mathrm{V_{UC}}} = \frac{1357\,\mathrm{nm}^3}{0.578\,\mathrm{nm}^3} = 2348 \tag{2.10}$$

According to the structure of maghemite (Fe_2O_3 = "Fe_8O_{12}") as Fe^{2+} deficient structure of magnetite (Fe_3O_4 = "Fe_9O_{12}") one needs to pay attention on a correction factor of 8/9 for the 24 Fe-atoms per unit cell of magnetite because of only partially occupied octahedral and tetrahedral holes.[321] This leads to approximately 21 Fe-atoms in one unit cell of maghemite, resulting in 50012 Fe-atoms in one nanorod. Finally an iron surface to volume ratio can be calculated, which can be used as a correction factor for Fe-concentration determined by AAS:

$$\frac{\mathrm{S_{Fe}}}{\mathrm{V_{Fe}}} = \frac{2100}{50012} = 0.0420 \tag{2.11}$$

Eventually a Pd@γ-Fe_2O_3 superparticle concentration can be calculated:

$$[\mathrm{NP}] = 1.35 \times 10^{-6}\,\frac{\mathrm{mol}}{\mathrm{L}} \tag{2.12}$$

2.6 Appendix

Table 2.2: Additional data to the Rietveld refinement of powder XRD data. Measurement conditions: $5 \leq 2\Theta/° \leq 41.4$; $\Delta\Theta = 0.0065°$; $\Delta t = 5.14$ sec.* Due to the low signal to background ratio of the data the refinement leads to a too high value for the lattice parameter of the Pd-phase. Even upon consideration of the slight increase of lattice parameters of nanoparticular materials in comparison to the corresponding bulk materials this value has to be classified as an artifact of the data quality.

		Pd nano-tetrahedra (Pd_{nth})	**Pd_{nth}@Fe_xO**	**Hexagonal Pd nanoplates (Pd_{hnp})**	**Pd_{nth}@Fe_2O_3 superparticles**	**Pd_{hnp}@Fe_2O_3 superparticles**
Pd-Phase						
Cell parameter	*Å*	3.925(1)*	3.876(1)	3.867(1)	-	3.876(1)
Crystallite size	nm	-	13(1)	7(1)	-	9(1)
Fraction	%wt	69(5)	53(2)	100	-	11(1)
Fe_xO-Phase						
Cell parameter	*Å*	8.406(4)	8.356(2)	-	8.350(2)	8.348(2)
Crystallite size	nm	-	20(1)	-	13(1)	12(1)
Fraction	%wt	31(5)	47(2)	-	100	89(1)
Approx. composition		$Fe_{0.67(2)}O$	$Fe_{0.62(5)}O$	-	$Fe_{0.67(1)}O$	$Fe_{0.65(2)}O$
R_{wp}		4.17	3.76	5.39	5.43	5.32
Goodness of fit (G)		2.36	2.08	2.09	3.10	1.34
Number of parameter/ background		15/3 + scaled model for sample holder material	29/15	23/15	25/15	28/15

Table 2.3: Additional data to the Mössbauer measurements.

	Chemical shift	Quadrupole shift	Magnetic field	Fraction	Substance
	mm/s	mm/s	kOe	%	
Pd nano-tetrahedra (Pd_{nth})					
Sextet 1	0.47(1)	0	529(1)	20(3)	γ-Fe_2O_3
Sextet 2	0.51(1)	0	456(1)	39(2)	Fe_3O_4
Sextet 3	0.42(1)	0	512(1)	29(4)	Fe_3O_4 + γ-Fe_2O_3
Sextet 4	0.31(1)	0	307(2)	12(1)	$FePd_x$
Pd_{nth}@Fe_xO					
Sextet 1	0.50(1)	0	529(1)	19(5)	γ-Fe_2O_3
Sextet 2	0.54(1)	0	461(3)	44(5)	Fe_3O_4
Sextet 3	0.43(1)	0	507(1)	28(7)	Fe_3O_4 + γ-Fe_2O_3
Sextet 4	0.32(1)	0	311(3)	10(2)	$FePd_x$
Hexagonal Pd nanoplates (Pd_{hnp})					
Sextet 1	0.48(2)	0	488(3)	38(9)	β-FeOOH
Sextet 2	0.31(1)	0	313(3)	17(3)	$FePd_x$
Sextet 3	0.45(2)	0	448(3)	45(1)	γ-FeOOH
Pd_{nth}@Fe_2O_3 superparticles					
Sextet 1	0.40(1)	0	509(1)	51(4)	γ-Fe_2O_3
Sextet 2	0.46(1)	0	528(1)	49(4)	γ-Fe_2O_3
Pd_{hnp}@Fe_2O_3 superparticles					
Sextet 1	0.47(1)	0	531(1)	45(8)	γ-Fe_2O_3
Sextet 2	0.41(1)	0	512(1)	55(8)	γ-Fe_2O_3

Table 2.4: Additional data to the SQUID magnetic measurements.

			Pd$_{nth}$@Fe$_2$O$_3$ superparticles	**Pd$_{hnp}$@Fe$_2$O$_3$ superparticles**
	Blocking temperature	K	260	210
	At mass magnetization	emu/g	9.6	10.4
5 K	Saturation magnetization at 50 kOe	emu/g	49.6	66.4
	Remanence	emu/g	12	21
	Coercivity	Oe	-160	-200
300 K	Saturation magnetization at 50 kOe	emu/g	41	56

3

Iron Oxide Superparticles with Enhanced MRI Performance by Solution Phase Epitaxial Growth

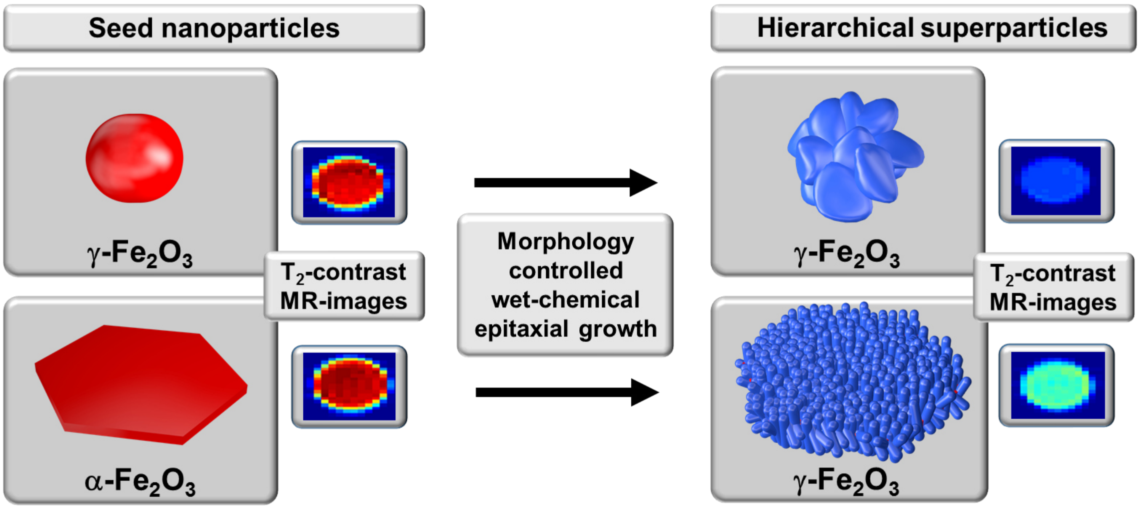

This chapter contains a manuscript for publication, submitted to the ACS Chemistry of Materials journal. A detailed Authorship Statement of the publication is attached in the Appendix of this dissertation. I thank [redacted]*,*[350] [redacted]*,*[351] *and* [redacted][352] *for their collaboration in this project during their bachelor thesis research.*

3.1 Abstract

Organized three-dimensional (3D) nanomaterial architectures are promising candidates for applications in optoelectronics, catalysis or theranostics owing to their anisotropy and advanced structural features that allow tailoring their physical and chemical properties. The synthesis of such complex, but well-organized nanomaterials is difficult because the interplay of interfacial strain and facet-specific reactivity must be considered. Especially the magnetic anisotropy with controlled size and morphology plays a decisive role for applications like magnetic resonance imaging (MRI) and advanced data storage. We present a solution phase seed mediated synthesis of colloidal, well dispersible iron oxide superparticles with flower- and hedgehog-like morphology starting from dispersible spherical maghemite (SPH) and nanoplate hematite (HEX) templates. In the superparticles the templates are epitaxially decorated with nanodomains and -rods as shown by (high-resolution) transmission electron microscopy (TEM), orientation mapping and electron diffraction (ED). While the templates determine the morphology of the superparticles, the chemistry determines the phase identity. Oxidation of $Fe(CO)_5$ during superparticle formation reaction leads to maghemite nanodomains and -rods decorating the templates, unveiled by a combination of X-ray diffraction (XRD) and Mössbauer spectroscopy (MS). After hydrophilic surface functionalization the superparticles are well dispersible. The cytotoxicity of templates and superparticles is low. The magnetic resonance imaging R_2-relaxivity of the flower-like superparticles could be increased by a factor 2.5 compared to its spherical nanoparticle template due to direct interfacial connection resulting from the unique nanoarchitecture.

3.2 Introduction

Uniform magnetic nanoparticles (NPs) with enhanced/improved magnetic properties have important applications in MRI, hyperthermia, targeted drug release or in theranostics.[123, 154, 353–356] Their properties may even be enhanced in hierarchically organized superparticles (SPs),[12, 69, 81] accessible by self-assembly of functionalized small NPs.[11, 77, 81, 357, 358] Here, the individual NPs are organized in ordered superlattices with new collective properties.[71, 72] Weak interactions like van-der-Waals forces between organic surface molecules or hydrogen bonding lead to particle alignment.[12] This has been proven valuable for applications in optoelectronics,[73] biochemistry,[74] plasmonics,[75] or in storage devices.[76] The drawbacks of particle assemblies for functional nanodevices by weak interactions are low mechanical stability, lack of interfacial electronic communication and poor processability.[359] Therefore, efforts have been made to synthesize multicomponent SPs using colloidal chemistry.[19, 38, 92, 93, 353, 360, 361] A bottom-up synthesis of uniform magnetic nanomaterials in high boiling point organic solvents requires an accurate control of the nucleation and growth steps. The fixed connection of the individual domains can lead to improved/enhanced optoelectronic and catalytic properties because the properties of the SPs are not a simple superposition of the individual properties of the constituents. New and unexpected properties may arise through interfacial electronic communication resulting from epitaxial particle growth,[20, 93, 202, 362, 363] which make these SPs valuable for technological applications.[15, 16, 73, 289] Such meso-scaled SPs, defined as size- and shape-controlled assemblies from nanoscale building blocks, where different domains are directly connected without any interfacial ligand layer, can be synthesized by heterogeneous nucleation and growth on pre-nucleated seeds. The SP architecture improves the particle stability and has shown merit in many applications for biomaterials,[70, 123] catalysis[291] or solar cells.[364]

We present a seed-mediated synthesis for flower- and hedgehog-like SPs from spherical and hexagonal iron oxide template seed particles by growing secondary iron oxide domains to achieve the next level of hierarchy in nanostructures. The seeds were synthesized either by thermal decomposition from an iron(III) oleate precursor or solvothermally, yielding spherical nanoparticles (SPH NPs) or hexagonal nanoplates (HEX NPs). MS revealed the presence of maghemite for the SPH NP seeds which was verified by XRD analysis. This demonstrates the variety of the iron oxide phases in typical "magnetite" particles.[365–367] The HEX NP seeds consist of hematite. Subsequent oxidation of $Fe(CO)_5$ with trimethylamine *N*-oxide (TMAO) led to the formation of SPs with maghemite nanodomains and -rods. Orientation mapping based on ED and HR-TEM showed an epitaxial relationship between the iron oxide templates and the overgrown secondary iron oxide nanostructures. During SP growth the hematite templates transformed to maghemite. This shows that the template particles not only control the morphology of the SPs by inducing epitaxial overgrowth, they actively participate[368] in the reactions associated with seed mediated growth. Both, templates and SPs are dispersible in aqueous media after surface functionalization with a tailor-made catechol-PEG. They show low cytotoxicity, good physiological compatibility, and enhanced T_2-weighted MRI contrast, which makes them promising new dark field imaging contrast agents.

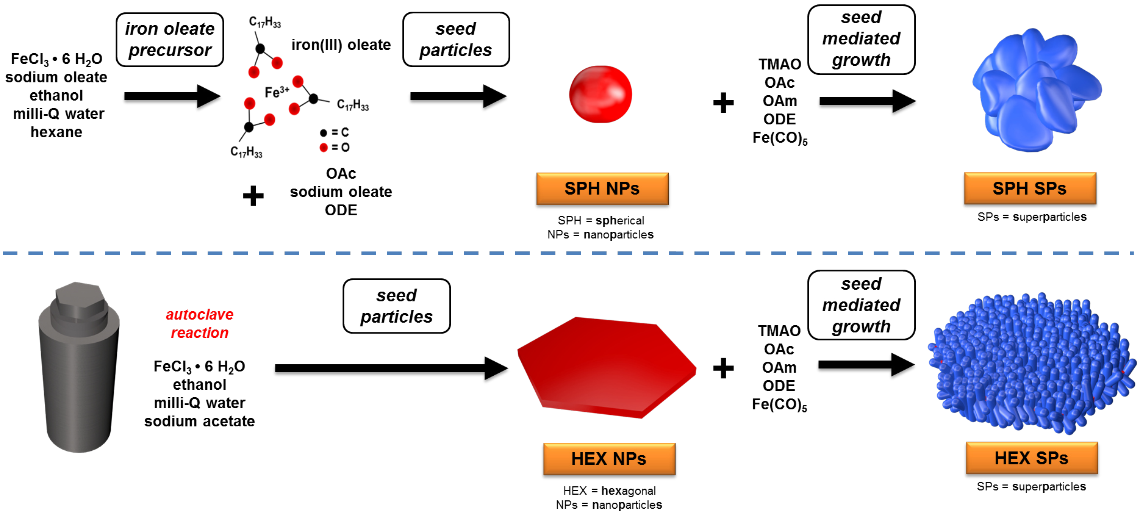

Figure 3.1: Flow-scheme of the synthesis of spherical and hexagonal nanoparticle seeds and the seed-mediated growth process for superparticles.

3.3 Results and Discussion

Figure 3.1 shows a schematic representation for the synthesis of the spherical (SPH) and hexagonal (HEX) seed NPs. The synthesis of the SPH seed NPs proceeds in two steps: (i) Synthesis of the iron(III) oleate precursor from $FeCl_3$ and sodium oleate, followed by purification and drying and (ii) thermal decomposition of iron(III) oleate in ODE at 330 °C to iron oxide NPs. OAc was used as surfactant and sodium oleate was used as facet stabilizer. The HEX seed NPs were obtained solvothermally. Iron oxide nanoplates were prepared from $FeCl_3$ in ethanol and water using sodium acetate as facet stabilizer. The iron oxide seeds were used as templates in ODE for superparticle (SP) formation. The $Fe(CO)_5$ precursor was decomposed in the presence of the TMAO oxidant to yield flower-like SPH SPs and hedgehog-like HEX SPs with OAc and OAm as surfactants, respectively.

3.3.1 Spherical Nanoparticles

The morphology of the SPH and HEX NPs was characterized by (HR)-TEM, STEM and SEM analysis as shown in Figure 3.2 which shows a STEM image of the SPH NPs with electron diffraction (ED) of selected single particles. The NPs are mostly spherical and facetted with a diameter of $\approx$ 18-20 nm (with some exceptions showing slight elongation of one axis (Figure 3.3)). The ED of two NPs (Figure 3.2a) shows reflections of the [-112] and [111] zone axis of magnetite (Fe_3O_4) and a chessboard-like reflection pattern due to extinctions of the cubic crystal system. For maghemite (γ-Fe_2O_3) additional weak reflections should appear due to the primitive cell of the maghemite structure. A clear distinction between magnetite and maghemite based on ED data is difficult because of the structural similarity of both compounds, the crystallinity and the particle size.[320, 369, 370] Typically, such facetted SPH NPs are

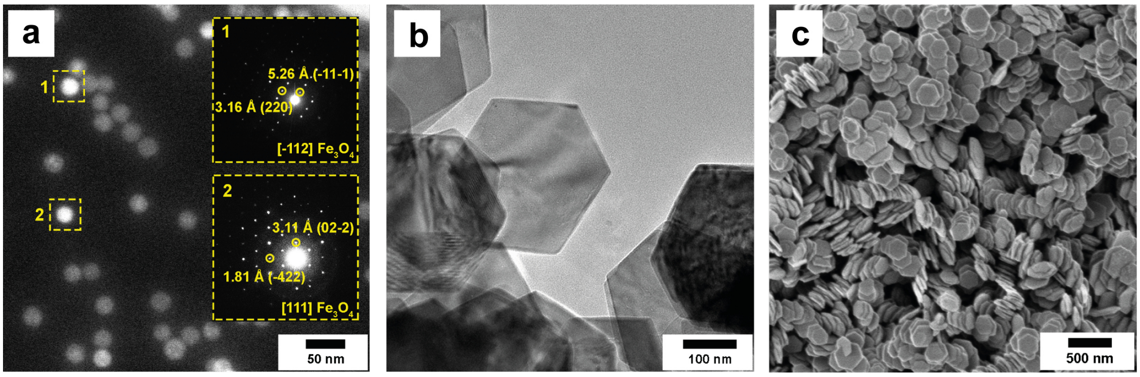

Figure 3.2: (a) HAADF-STEM image of SPH NPs with ED of two selected NPs. (b) TEM image of HEX NPs showing bending contrasts and Moirè pattern. (c) SEM image of HEX NPs.

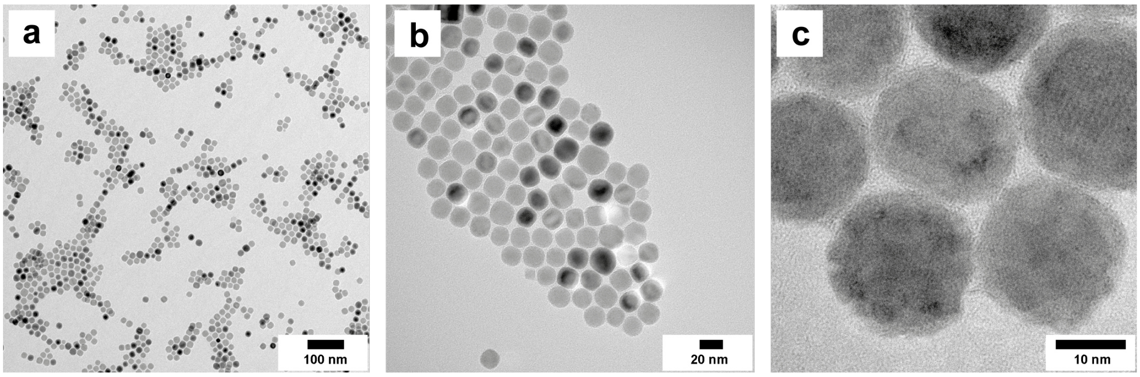

Figure 3.3: (a, b, c) TEM images of SPH NPs.

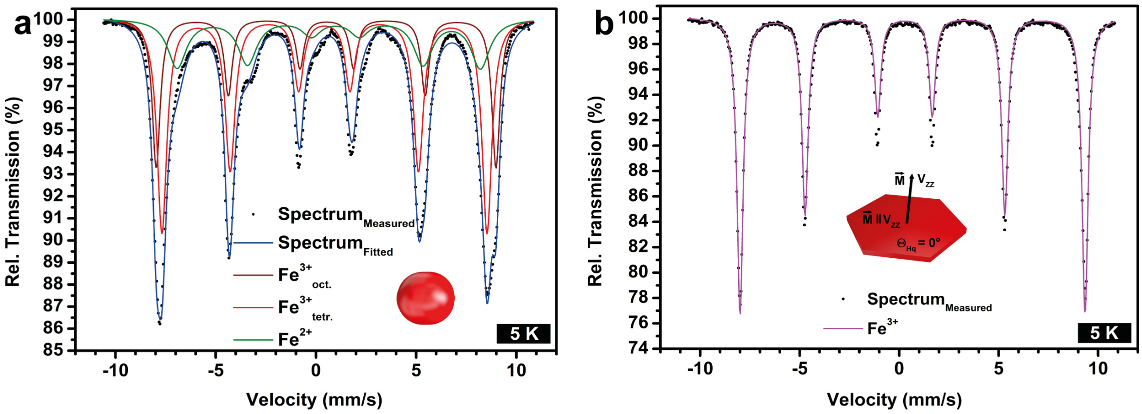

Figure 3.4: ^{57}Fe-Mössbauer spectra of (a) SPH NPs and (b) HEX NPs at 5 K.

formed from a polyhedral precursor structure with poly-facets as known for OAc-stabilized NPs of cubic symmetry.[371, 372] A low sodium oleate:iron(III) oleate ratio of 1:20 was used in this reaction. Thus, only a small amount of sodium oleate was available for stabilizing the Fe_3O_4 {111} facets with the highest density of iron ions,

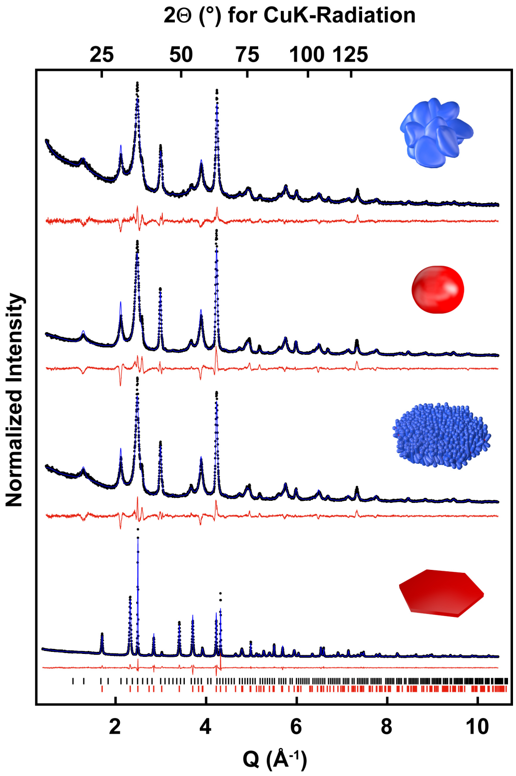

Figure 3.5: Refinements of powder XRD data for SPH SPs, SPH NPs, HEX SPs and HEX NPs (top to bottom). Black dots mark the experimental data, the blue line corresponds to the calculated pattern, and the red line shows the difference between the experimental and calculated data. Black and red ticks mark reflections of maghemite and hematite, respectively. $Q = [4\pi \sin(\Theta)]/\lambda$ is the scattering vector.

and only slight faceting and elongation was observed. Higher sodium oleate contents would lead to a complete preservation of the Fe_3O_4 {111} facet by stabilization through negative charged oleate ions, resulting in tetrahedral NP morphology.[373] Mössbauer spectroscopy (MS) is the most reliable and unique tool for identifying iron oxides. ED in TEM always represents a spot check in contrast to a bulk analysis in MS and X-ray diffraction (XRD). MS was performed at 5 K (Figure 3.4a), where all relaxation processes are frozen.[322, 374] This allows a distinction between Fe^{2+}/Fe^{3+} and octahedral (oct.)/tetrahedral (tetr.) sites based on chemical shifts and hyperfine magnetic field strength.[322, 323, 374] In Figure 3.4a the broad inner sextet (24% fraction, Table 3.1), with a comparatively high chemical shift of 0.80 mm/s and a comparatively low magnetic hyperfine field of 469 kOe, corresponds to Fe^{2+}, where a distinction between oct. and tetr. sites is not possible due to the width of the sextet. The outer sextets (26% and 50% fraction) have contributions from $Fe^{3+}{}_{oct.}$ and $Fe^{3+}{}_{tetr.}$.[322, 323, 374] The hyperfine magnetic field ≥ 500 kOe points towards maghemite.[322, 323, 374] The Fe^{2+} contribution in maghemite may result from Fe^{2+} surface (defect) sites. This partial reduction of the Fe^{3+} species in the iron(III) oleate precursor[375] might be possible due to thermal decomposition of *i.a.* ketonic

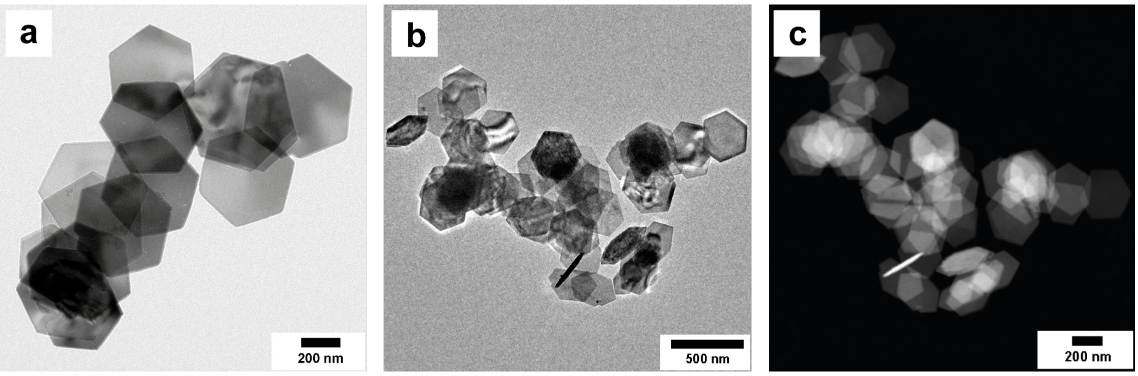

Figure 3.6: (a, b) TEM images and (c) HAADF-STEM image of HEX NPs.

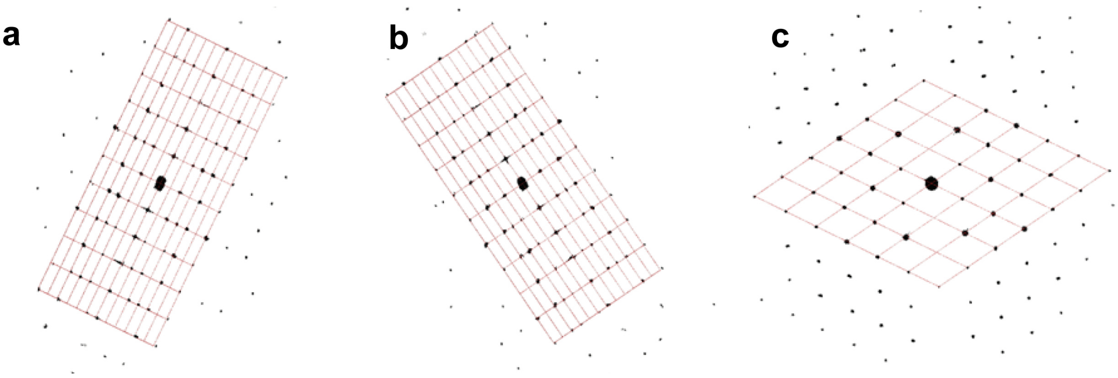

Figure 3.7: Projections of the reconstructed reciprocal space from eADT analysis of HEX NPs. (a) View down the a-axis. (b) View down the b-axis. (c) View down the c-axis. Unit cells from hematite phase overlaid in red.

byproducts resulting from a ketonic decarboxylation reaction, and the subsequent formation of thermal radicals, CO and H_2 after complete fragmentation.[376, 377] Different to a previous study using iron(III) oleate precursor only minor surface reduction was observed.[378]

XRD was used to verify the MS results. Maghemite with a refined composition of $Fe_{0.67(1)}O$ and a refined lattice parameter of 8.395(1) $\AA$ was found (Figure 3.5, Table 3.2) after Rietveld refinement.[340] This is in accordance with the MS analysis. The Fe^{2+} surface species cannot be detected in XRD due to crystallinity and reflection broadening of the nanomaterial.[320, 321]

3.3.2 Hexagonal Nanoparticles

Figure 3.2b and c show a TEM image and a SEM image of the HEX NPs used as template for the second type of SPs. The HEX NPs have a size of ≈ 480-520 nm and a thickness of ≈ 30 nm (Figure 3.6). Due to the small particle thickness, the TEM images show bending contrasts and Moiré patterns. An automated diffraction tomography (ADT) analysis (Figure 3.7, Table 3.3) revealed the NPs to be single

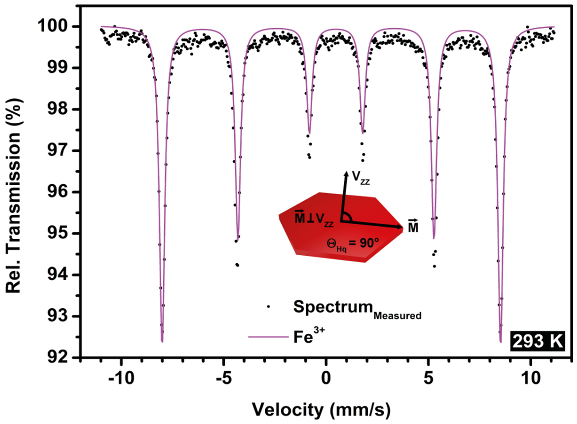

Figure 3.8: ^{57}Fe-Mössbauer spectra of HEX NPs obtained at RT.

phase hematite. The morphology of the HEX NPs in the solvothermal reaction was controlled by the contents of water, ethanol and sodium acetate. Water controls the transformation of amorphous iron oxyhydroxide precursors into hematite by promoting $FeCl_3$ hydrolysis. Ethanol and chelating acetate ions stabilize the polar $\{0001\}$ facets of hematite and eventually retard the growth along the *c*-axis. The growth in the *ab* plane leads to nanoplate formation.[169, 379]

The MS measurements of the HEX NPs are in accordance with the TEM analyses, confirming the phase identity of the hematite nanoplates.[322, 325, 380] Surprisingly, the magnetization vector of the HEX NPs changes its orientation upon cooling. This points to a second order phase transition related to the Morin transition of hematite at $\approx$ 260 K (*vide infra*).[370] The MS measurement at RT (Figure 3.8) shows that the hyperfine magnetic field and magnetization are in-plane and perpendicular to the electrical field gradient (EFG) V_{ZZ} and the 3-fold symmetry axis of the nanoplates ($\Theta_{Hq} = 90°$). The hyperfine magnetic field between the sextets one and six is 512 kOe at RT. At 5 K (Figure 3.4b) the hyperfine magnetic field increases to 538 kOe and the out-of-plane magnetization is oriented parallel to V_{ZZ} and the 3-fold symmetry axis of the nanoplates ($\Theta_{Hq} = 0°$).

Rietveld refinements of the XRD data yielded lattice parameters of a = 5.042(1) $\AA$ and c = 13.760(1) $\AA$ (Figure 3.5) compatible with hematite.[381] The reflections between Q = 2.3-2.5 $\AA^{-1}$ display the anisotropy of the nanoplates with a crystallite size ratio of $\approx$ 106/29 nm.

3.3.3 Spherical Superparticles

The SPH SPs have diameters between 25 and 35 nm as shown in the TEM image in Figure 3.9a. The seed particles are overgrown with iron oxide domains (length $\approx$ 10 nm). The flower-like morphology of the SPH SPs was confirmed by surface rendering 3D TEM tomography (Figure 3.9a, insets). A slice through the tomogram (Figure 3.9a inset) shows densely packed domains with parallel faces. Similarly, a gray value 3D surface plot (Figure 3.10) of Figure 3.9a shows the 3D structure of the

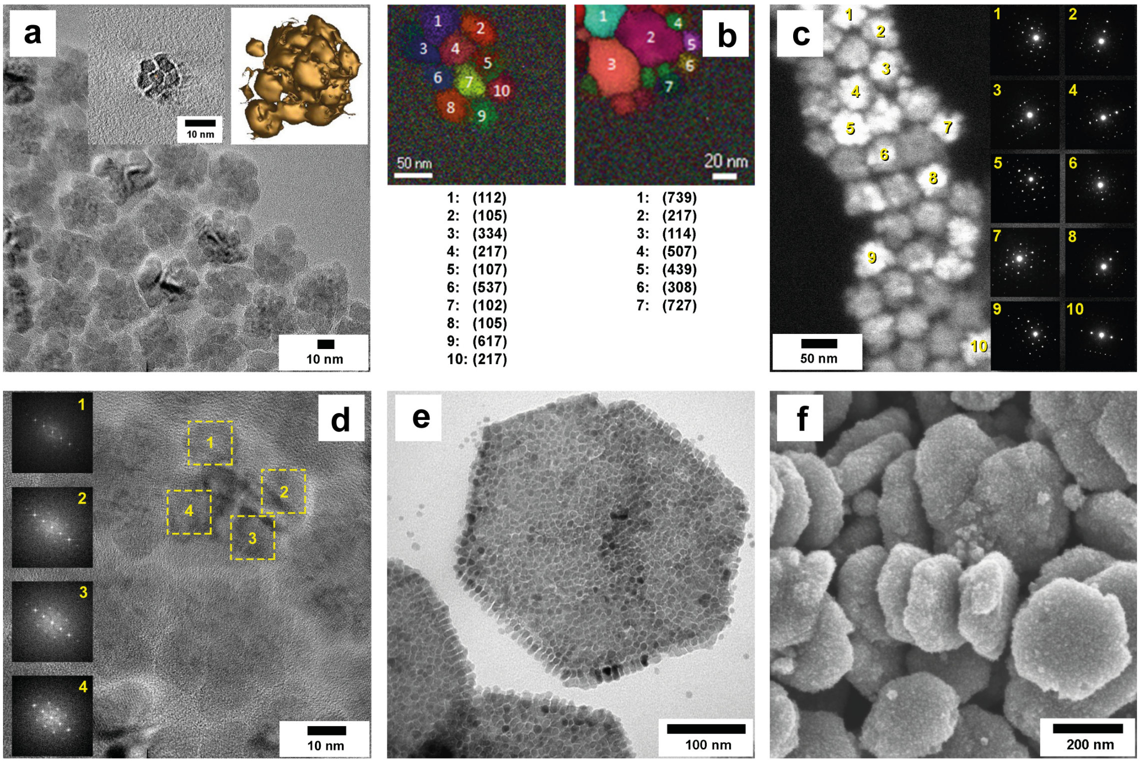

Figure 3.9: (a) TEM image of SPH SPs with surface rendering 3D tomography (inserts). (b) ASTAR orientation mapping of two SPH SP agglomerates. (c) HAADF-STEM image of SPH SPs with ED of selected SPs. (d) FFT analysis of four different overgrown domains of a single SPH SP. (e) TEM image of a HEX SP. (f) SEM image of HEX SPs.

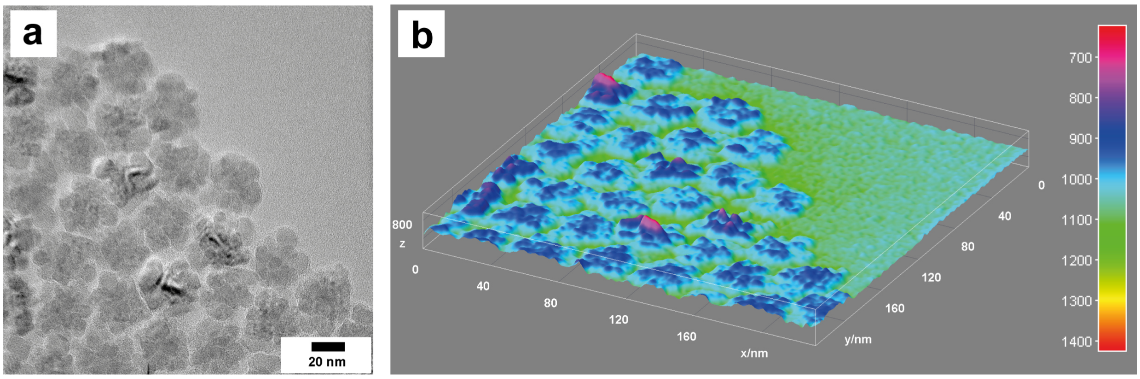

Figure 3.10: (a) TEM image of SPH SPs. (b) 3D surface plot based on gray value evaluation for the TEM image from (a).

SPH SPs. Figure 3.9b displays ASTAR orientation mappings of two different particle agglomerates. Based on ED and the maghemite structure the orientation of each SP was derived and color coded. In the left particle agglomerate, SPs number 2 and 8 have a (105) plane orientation whereas SPs number 4 and 10 have a (217) plane orientation. Hence, the overgrown iron oxide domains have a common orientation in

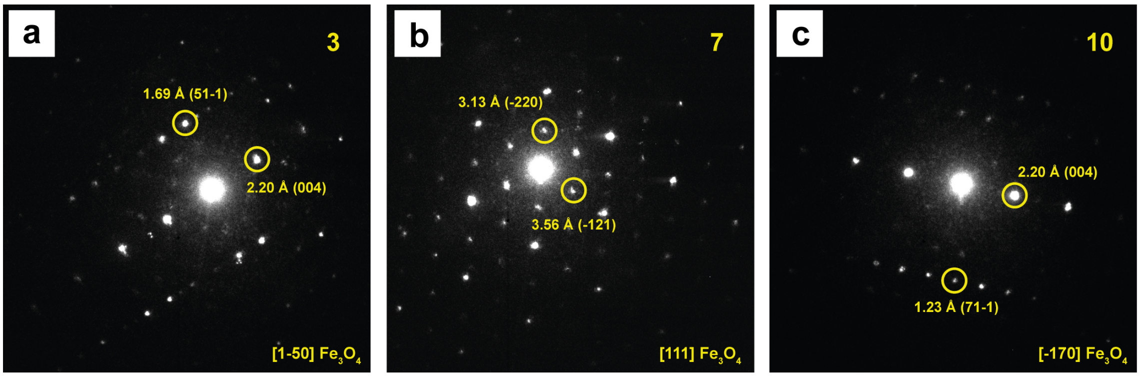

Figure 3.11: ED from SPH SPs number (a) 3, (b) 7 and (c) 10 presented in Figure 3.9c.

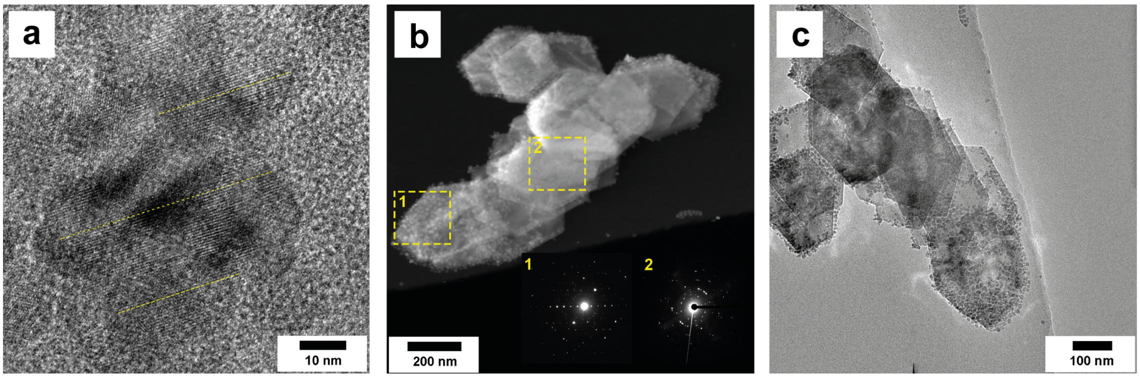

Figure 3.12: (a) HR-TEM of a SPH SP showing coherent net planes through the SP. (b) HAADF-STEM image of HEX SPs with less dense iron oxide nanorods covering revealing (1) magnetite phase of nanorods and (2) hematite phase of template particles based on ED. (c) TEM images of HEX SPs from (b).

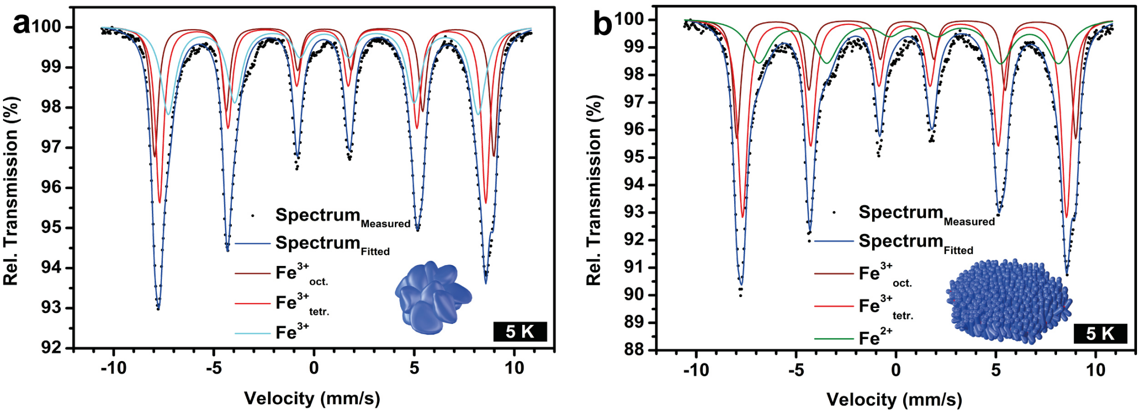

Figure 3.13: ^{57}Fe-Mössbauer spectra of (a) SPH SPs and (b) HEX SPs obtained at 5K.

an individual SP, as expected for an epitaxial growth on the template particle. Phase mapping to elucidate the iron oxide composition was carried out, but due to the data reliability and similarity of the magnetite and maghemite structure no conclusive statement could be given. ED of selected SPs (Figure 3.9c) showed well-resolved reflections of magnetite with a chessboard-like pattern and systematic extinctions. Reflection indexing (Figure 3.11) revealed recurring strong $d_{004} = 2.20$ $\AA$ reflections in diffraction pattern 3 and 10, which allowed an assignment to the [1-50] and [-170] zones of magnetite due to the systematic absence of additional weak maghemite reflections (*vide supra*). Epitaxial growth was examined by power spectra analysis of a single SP as well. Figure 3.9d displays the power spectra of four different overgrown domains of a single SP with the same reflection patterns. A HR-TEM image of a single SP (Figure 3.12a) shows coherent net planes through the full SP.

The iron oxide phase composition of the SPH SPs was unraveled by MS at 5 K (Figure 3.13a). The magnetic splitting of the two outer sextets with high hyperfine fields of 525 and 505 kOe suggests the presence of $Fe^{3+}{}_{oct.}$ (25% fraction) and $Fe^{3+}{}_{tetr.}$ (37% fraction). The inner sextet with the smallest hyperfine field of 480 kOe and narrow lines corresponds to a 38% fraction of Fe^{3+} with a typical chemical shift of 0.49 mm/s.[322, 323, 374] Hence, the SPH SPs also consist of a maghemite phase, but without surface Fe^{2+} admixture (due to sufficient amount of TMAO oxidant).

These findings are consistent with the XRD data which revealed the presence of maghemite with a refined composition of $Fe_{0.63(1)}O$ and a refined lattice parameter of 8.382(1) $\AA$ (Figure 3.5). The XRD data could be modeled with a Rietveld refinement on basis of the space group and metric data of maghemite.

3.3.4 Hexagonal Superparticles

A TEM image of a single HEX SP with a hedgehog-like structure is shown in Figure 3.9e. The hexagonal nanoplate template is densely overgrown with iron oxide nanorods, while the template morphology is completely preserved. The SEM image in Figure 3.9f shows the increased thickness of the particles, whose edges are covered with nanorods. ED on HEX SPs whose decoration with iron oxide nanorods is less dense (Figure 3.12b and c) clearly distinguishes the hematite template and magnetite nanorods. Figure 3.14a-c displays a TEM imaging series of a HEX SP twin. The TEM contrast demonstrates the agglomeration of two hexagonal nanoplate templates which are overgrown by the iron oxide nanorods (Figure 3.14a). Figure 3.14b shows the edge of the HEX SP in a zoom-in TEM image, covered with interconnected nanorods having a length of up to 20 nm. Epitaxial growth is evident from Figure 3.14c. The higher resolution shows the coherent net planes through the nanorods with distances of 0.564 and 0.540 nm equivalent to the (110) facet of maghemite/magnetite. Figure 3.14d displays another HEX SP twin with oriented nanorods at the SP edges. A gray value 3D surface plot (Figure 3.15) of Figure 3.14d demonstrates the overlap of the two template particles and highlights the surface and edge structures. The oriented nanorods at the edges are parallel to the long axis of the template (pointing away from the SP, Figure 3.14e). A 60-70 nm thickness of the SPs (Figure 3.14f) on the TEM grid was estimated from the decoration with nanorods (length 15-20 nm) and the thickness of the hexagonal template ($\approx$ 30 nm).

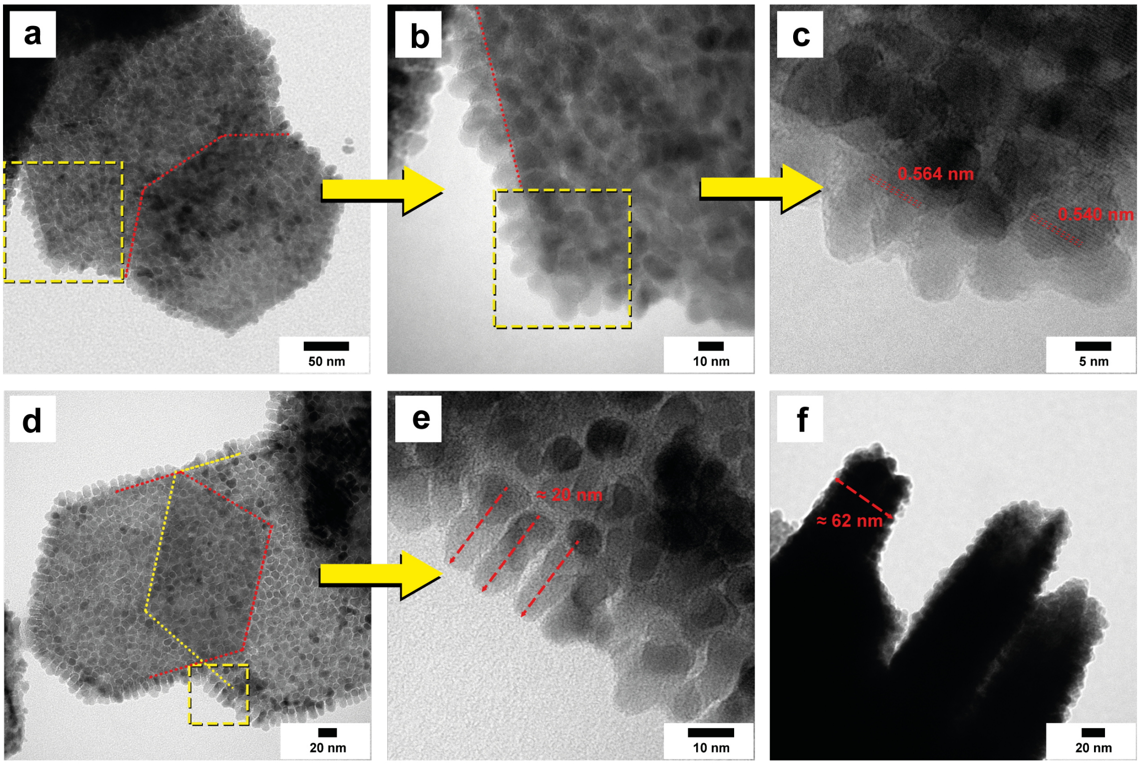

Figure 3.14: (a, b, c) and (d, e) TEM imaging series of HEX SPs showing epitaxial growth and nanorod structure. (f) TEM image of vertically aligned HEX SPs.

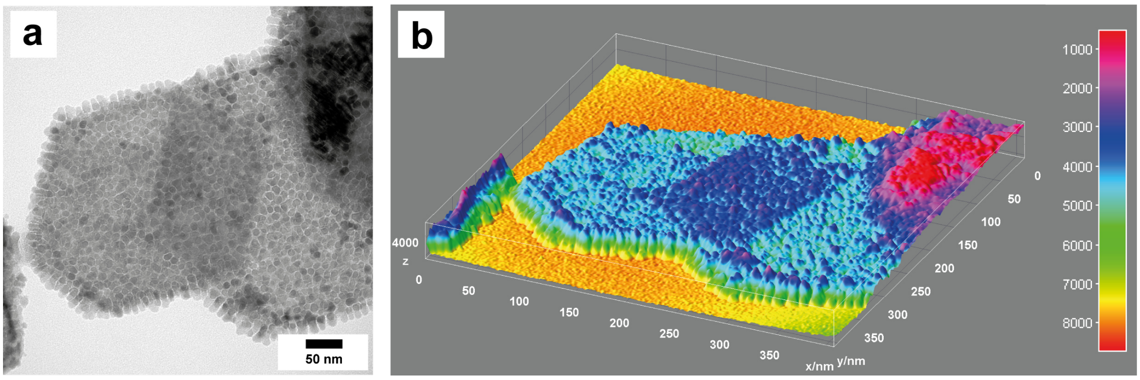

Figure 3.15: (a) TEM image of HEX SPs. (b) 3D surface plot based on gray value evaluation for the TEM image from (a).

MS spectroscopy revealed the overall iron oxide composition of the HEX SPs. A sextet (22% contribution) with a hyperfine field of 526 kOe in the spectrum at 5 K (Figure 3.13 b) was attributed to $Fe^{3+}{}_{\mathrm{oct.}}$. The remaining two sextets are assigned to $Fe^{3+}{}_{\mathrm{tetr.}}$ and Fe^{2+} with contributions of 49% and 29% and chemical shifts of 0.43 mm/s and 0.76 mm/s, respectively.[322, 323, 374] Accordingly, the HEX SPs are composed of maghemite (with some Fe^{2+} caused by incomplete oxidation of $Fe(CO)_5$ with TMAO).

The refined XRD data of the HEX SPs showed only maghemite with a lattice parameter of 8.396(1) $Å$ (Figure 3.5) and an approximate composition of $Fe_{0.67(1)}O$. As in MS, no hematite from the template HEX NPs was found. This shows the template NPs to serve as a feedstock for the SPs. During particle growth the hexagonal hematite transforms to cubic maghemite. This phase transformation may occur (i) *via* a solid state mechanism or (ii) through dissolution-recrystallization. A solid state transformation is more likely because of the solubility of the iron oxide phases involved. Since the conversion occurs only when the template NP is densely overgrown by nanorods, interface reorganization, resulting from the mobility of the involved metal ions, seems to be relevant for the conversion.
In essence, the templates for the SPH and HEX SPs determine the overall morphology of the SPs. They are not chemically inert in the SP formation step and participate either in the redox reaction (SPH NPs) or they are converted (HEX NPs) to maghemite as dominating iron oxide phase. Our findings have very fundamental implications in the context of "magnetite" NPs[365] (especially when made from iron(III) oleate),[366] because the composition of iron oxide NPs may be more complex and more variable than generally assumed. Unravelling this complexity is difficult both, in nano- and bulk-analysis. Possible reasons are (i) the structural similarity of different iron oxide phases such as wüstite, magnetite and maghemite, (ii) the redox equilibria involving metal species, organic precursors or surfactants, (iii) the dependence on the reaction conditions and (iv) the facile Fe^{2+}/Fe^{3+} conversion. The unique architecture and composition of the SPs in combination with direct lattice intergrowth and surface epitaxy are powerful tools for a targeted application design (*vide infra*).

3.3.5 Magnetic Properties

The SPH NPs are ferromagnetic at 5 K with a saturation magnetization of 41 emu/g at a magnetic field of 50 kOe (Figure 3.16a, Table 3.4). This is lower than the reported 80 emu/g saturation magnetization of bulk magnetite.[330] The reduced value is caused presumably by spin canting effects of the surface Fe ions or effects of non-magnetic surfactants.[370, 373, 382] Above the blocking temperature (T_B) the particles are superparamagnetic at 300 K. Figure 3.16b shows the affiliated FC-ZFC plot of the SPH NPs with a T_B of $\approx$ 300 K. The magnetic hysteresis of the HEX NPs (Figure 3.16c) reveals a low saturation magnetization due to the antiferromagnetic properties of hematite.[383–385] The moments within a layer are aligned parallel, but adjacent layers are aligned antiparallel to each other causing the antiferromagnetic behavior.[386, 387] Between the Neél temperature of 961 K and the Morin transition temperature (T_M) of 265 K, hematite still shows weak ferromagnetic behavior,[388, 389] as demonstrated by the weak hysteresis at 300 K in Figure 3.16c caused by a Dzyaloshinskii-Moriya interaction due to spin-orbit coupling.[390, 391] The magnetic moments in the layers are slightly canted leading to a net magnetization. Below T_M the magnetic moments rotate by 90 ° and align exactly (anti)parallel to the *c*-axis.[370, 392–394] This is evident in the FC-ZFC data (Figure 3.16d), where a

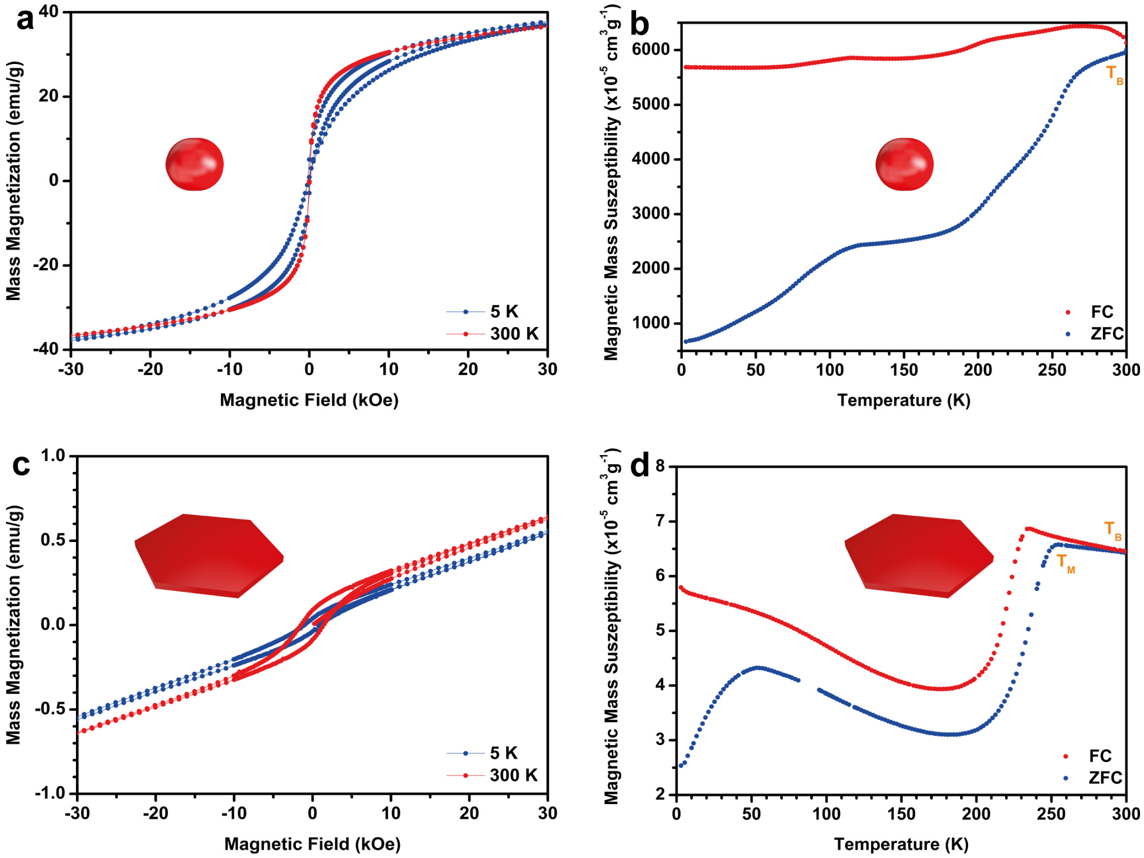

Figure 3.16: SQUID magnetic measurements of (a, c) hysteresis at 5 K and 300 K and (b, d) zero-field-cooled (ZFC) and field-cooled (FC) magnetization. (a, b) SPH NPs and (c, d) HEX NPs.

sharp drop in the mass magnetization appears below T_M (≈ 260 K).
The SPH SPs (Figure 3.17a and b) display a similar behavior as the seed particles with ferromagnetic properties below T_B of 287 K and superparamagnetic properties at 300 K. T_B of the resulting HEX SPs is 290 K. The increasing FC magnetization at lower temperature is due to magnetic interactions between the particles (Figure 3.17c and d). For both SP types the saturation magnetization at 50 kOe is ≈ 40 emu/g.

3.3.6 Cytotoxicity

The magnetic properties of the particles allow their use for MRI (*vide infra*). Therefore, the (potential) toxicity of the seed NPs and the SPs was checked using an Alamar Blue assay with A549 lung cancer cells. The as-synthesized SPs are covered with a hydrophobic oleic acid ligand shell and therefore insoluble in water. Therefore, they were re-functionalized with a hydrophilic polymer (PEG) ligand (M_W ≈ 4020 gmol^{-1}; PDI = 1.09) with catechol anchor group to establish solubility in aqueous solution, *i.e.*, Milli-Q water[92, 114] and to allow *in vitro* applications (Figure 3.18).

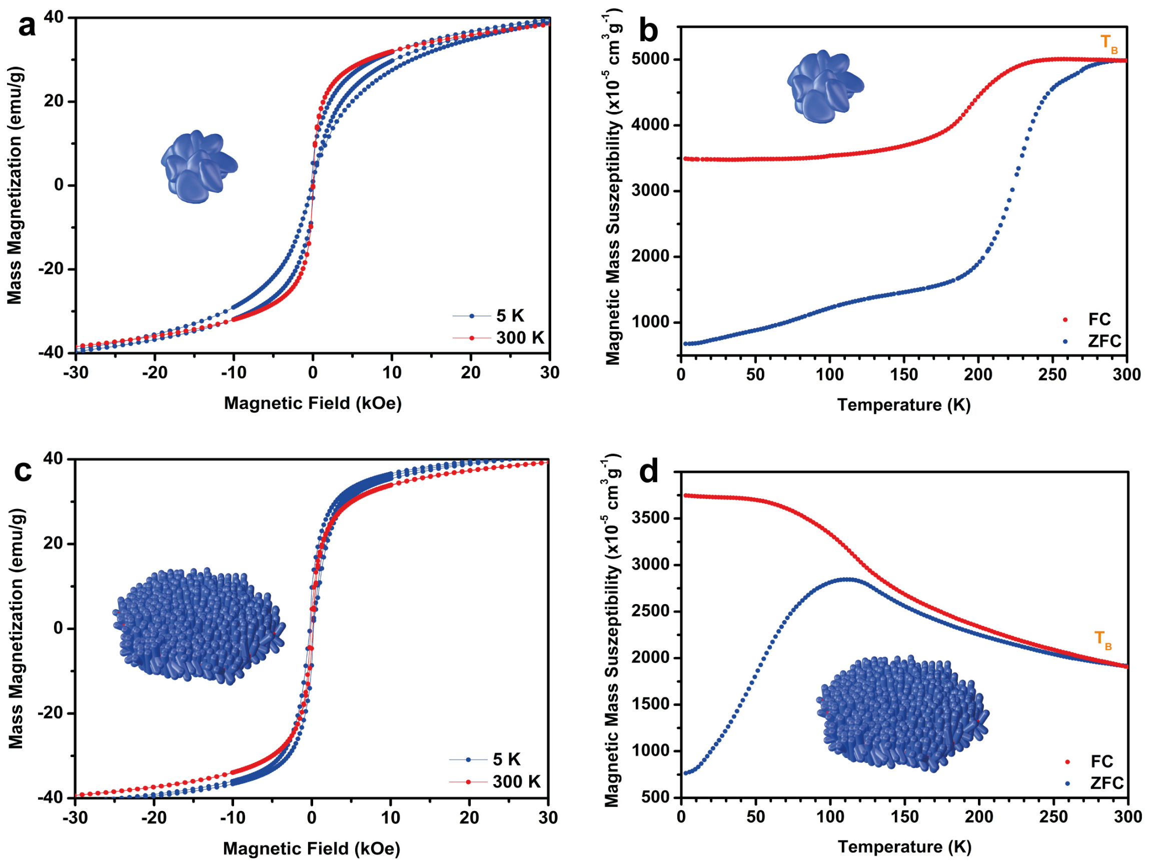

Figure 3.17: SQUID magnetic measurements of (a, c) hysteresis at 5 K and 300 K and (b, d) zero-field-cooled (ZFC) and field-cooled (FC) magnetization. (a, b) SPH SPs and (c, d) HEX SPs.

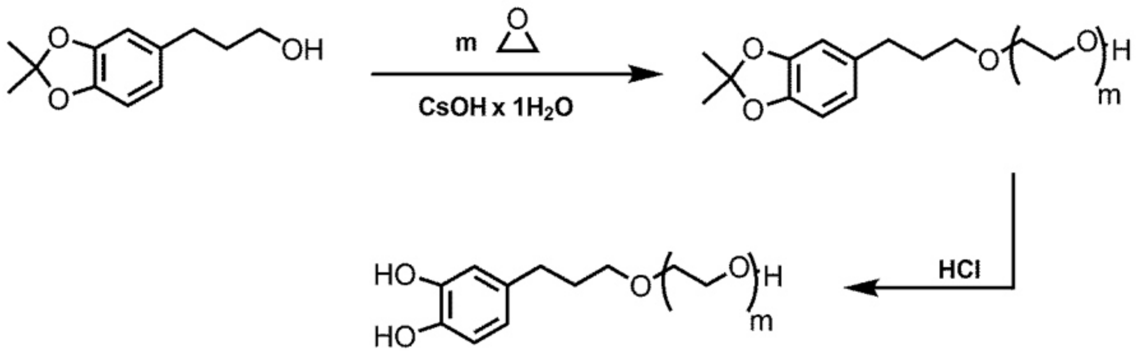

Figure 3.18: Synthesis scheme of catechol-PEG. Polymerization of ethylene oxide (EO) starting from an acetonide-protected catechol initiator, followed by deprotection of CA-PEG with an aqueous solution of hydrochloric acid resulting in hydrophilic C-PEG.

Dispersions of the particles in water or physiological media were stable for several weeks. Figure 3.19 shows the results of the cytotoxicity tests after 6 h and 27 h. The cellular viability for all particle types was comparable after 6 h and 27 h; no

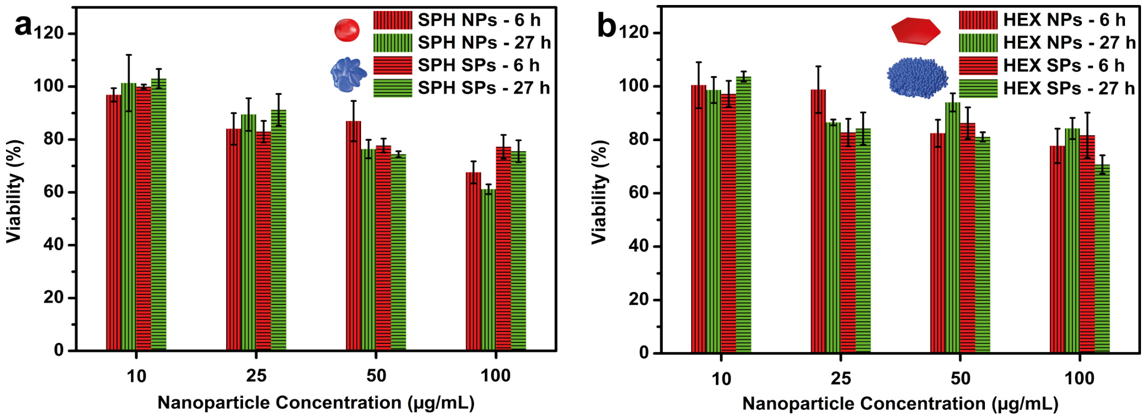

Figure 3.19: Cytotoxicity measurements of (a) SPH NPs and SPH SPs after 6 h and 27 h and (b) HEX NPs and HEX SPs after 6 h and 27 h.

significant increase in cytotoxicity was observed with time. Generally, the viability of the cells decreases with increasing particle concentration reaching a minimum of 70-80% cellular viability at 100 µg/mL NPs. The cytotoxicity between the SPH NPs and SPs as well as the HEX NPs and SPs differ up to 10%, resulting in suitable viability values for all potential applications.

3.3.7 Magnetic Resonance Imaging

Iron oxide NPs are well known for their T_2 signal enhancement properties in MRI and they are already in clinical use.[125, 154, 355] The prerequisite for a good transversal T_2 contrast agent is a high magnetic moment which supports the inhomogeneity of the microscopic environment. The magnetic field built by the NPs interferes with the detection field and leads to a darkening of the MR image by fast decay of the M_{xy} magnetization.[158, 159] Consequently, superparamagnetic iron oxide NPs are good candidates because of their large magnetic moment. Tailoring magnetic NPs for applications as MRI contrast agent requires engineering of their magnetic characteristics, adjusting both, magnetic and physical properties of the nanomaterials. For tuning the R_2-relaxivity of iron oxide NPs, magnetic properties such as saturation magnetization, coercivity and magnetocrystalline anisotropy as well as physical properties such as particle size, dispersity and surface stability must be evaluated and tuned.[154] The quadratic dependence of particle size and saturation magnetization must be considered, which leads to enhanced transversal contrast if the effective radius of the superparamagnetic core and the saturation magnetization is increased.[164] Magnetic resonance properties of the seed NPs and the SPs were characterized by measurements of the T_1 and T_2 relaxation times to evaluate the potential for signal enhancement. Figure 3.20a and b display the r_1- and r_2-relaxivities of SPH NPs and SPH SPs for three particle concentrations (1, 2 and 4 mM) in Milli-Q water. The r_1- and r_2-relaxivities were obtained by an exponential fit of the FID curves (Figure 3.21). For all concentrations an increase in r_1- and r_2-relaxivities of the SPH

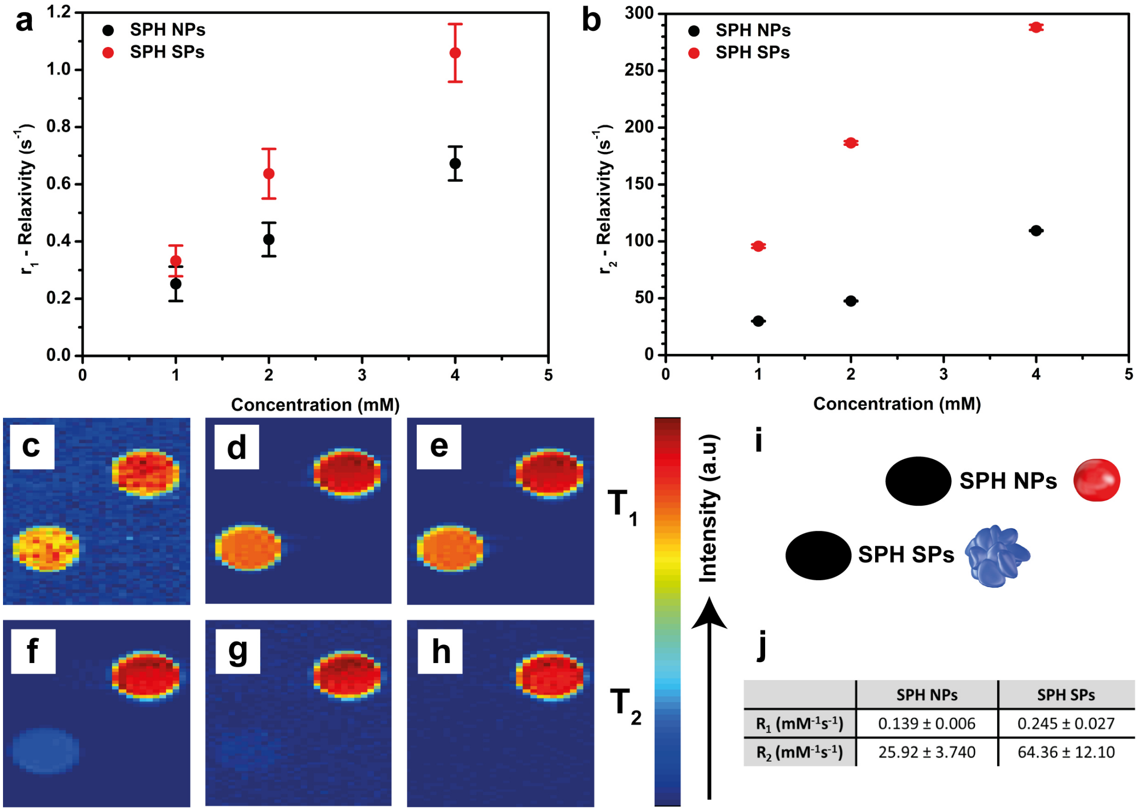

	SPH NPs	SPH SPs
R_1 ($mM^{-1}s^{-1}$)	0.139 ± 0.006	0.245 ± 0.027
R_2 ($mM^{-1}s^{-1}$)	25.92 ± 3.740	64.36 ± 12.10

Figure 3.20: (a) r_1-relaxivity and (b) r_2-relaxivity of SPH NPs and SPH SPs. (c, d, e) T_1-weighted MR images and (f, g, h) T_2-weighted MR images of (i) SPH NPs and SPH SPs with increasing RD values of 30000, 50000 and 2000000 µs for (c, d, e) and increasing TAU values of 5000, 10000 and 20000 µs for (f, g, h). (j) Concentration related R_1- and R_2-relaxivities for SPH NPs and SPH SPs.

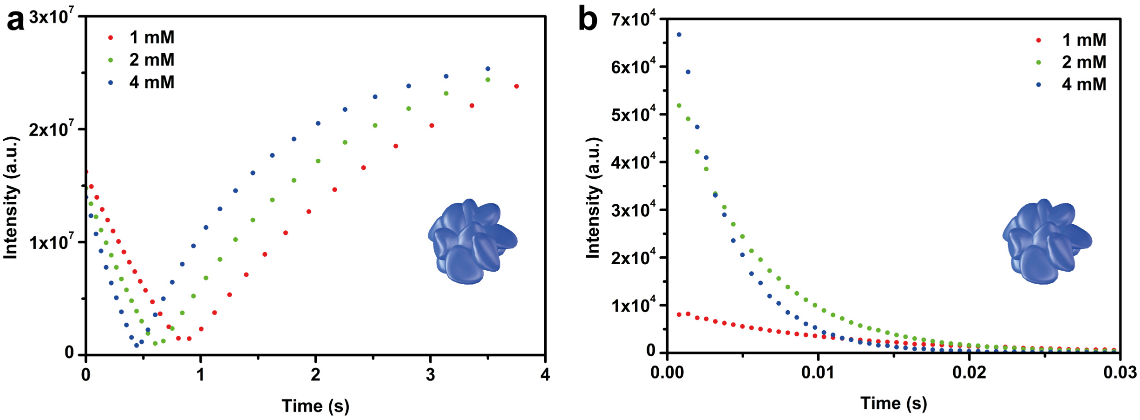

Figure 3.21: Measured FID signals of 1, 2 and 4 mM dispersions of SPH SPs to obtain (a) T_1 relaxation times and (b) T_2 relaxation times by fitting the FID signals with the appropriate exponential decay function (see Experimental Section *vide infra*).

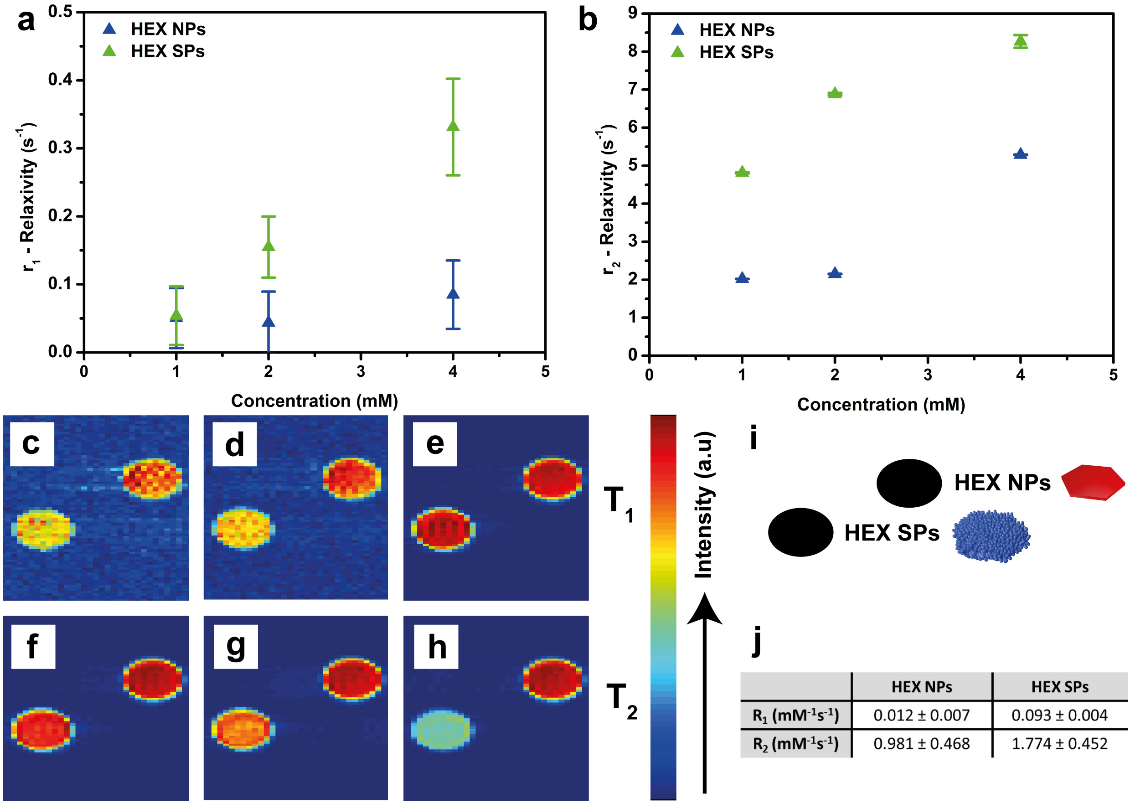

	HEX NPs	HEX SPs
R_1 ($mM^{-1}s^{-1}$)	0.012 ± 0.007	0.093 ± 0.004
R_2 ($mM^{-1}s^{-1}$)	0.981 ± 0.468	1.774 ± 0.452

Figure 3.22: (a) r_1-relaxivity and (b) r_2-relaxivity of HEX NPs and HEX SPs. (c, d, e) T_1-weighted MR images and (f, g, h) T_2-weighted MR images of (i) HEX NPs and HEX SPs with increasing RD values of 30000, 50000 and 2000000 µs for (c, d, e) and increasing TAU values of 5000, 10000 and 20000 µs for (f, g, h). (j) Concentration related R_1- and R_2-relaxivities for HEX NPs and HEX SPs.

SPs in relation to the SPH NPs was observed equivalent with decreased T_1 and T_2 relaxation times. Thus, the decoration of the seed NPs with iron oxide domains leads to a signal enhancement for both, longitudinal and transversal relaxation. Due to the only slight increase of the saturation magnetization upon formation of the SPH SPs (43 emu/g at 300 K for SPH SPs compared to 40 emu/g at 300 K for SPH NPs) we attribute the contrast enhancement to (i) the higher effective radius of the superparamagnetic core because of the increased particle size and epitaxial growth relationship of the domains[164] and (ii) the anisotropy and inhomogeneity of the particle-generated magnetic field because of the unique SP morphology.[152] Figure 3.20c-h show T_1-weighted and T_2-weighted MR images of 4 mM particle dispersions (see Figure 3.20i for image assignment). Figure 3.20c-e show only slight differences in the bright field contrast of the SPH NPs and SPs for increasing values of the repetition duration (RD). In contrast, Figure 3.20f-h display T_2-weighted images with a strongly reduced signal intensity of the SPH SPs leading to a completely darkened image at a TAU value of 20000 µs (Figure 3.20h). In summary, the concentration-related R_1-relaxivity could almost be doubled for the SPH SPs (Figure

3.20j). However, it is still relatively low because iron oxide is not a typical bright field imaging contrast agent. The R_2-relaxivity could be increased by a factor 2.5 to 64.36 $mM^{-1}s^{-1}$ (Figure 3.20j) showing the potential for an application as dark field imaging contrast agent.

Figure 3.22 displays the MRI measurement results of the HEX NPs and SPs. For all concentrations (Figure 3.22a and b) an increase in r_1- and r_2-relaxivities of the HEX SPs compared to the HEX NPs was observed. Hence, longitudinal and transversal relaxation performance was enhanced. The MR images (Figure 3.22c-i) also reveal low contrast enhancement for T_1-weighted images and stronger contrast enhancement for T_2-weighted images. In summary, the R_1- and R_2-relaxivities reached values of 0.093 $mM^{-1}s^{-1}$ and 1.774 $mM^{-1}s^{-1}$ for the HEX SPs (Figure 3.22j). It could be demonstrated that the decoration with iron oxide nanorods leads to a signal enhancement as well.

3.4 Conclusion

The synthesis of iron oxide flower- and hedgehog-like SPs starting from spherical and hexagonal seeds was achieved by oxidation of $Fe(CO)_5$ with TMAO. In a seed-mediated growth process maghemite (SPH NPs) and hematite (HEX NPs) seeds were decorated with maghemite domains (SPH SPs) and maghemite nanorods (HEX SPs) as revealed by MS and XRD analysis. The template particles determine the morphology of the SPs, but they were not inert to the chemical processes associated with the seed mediated growth, where the HEX hematite seed NPs were converted to maghemite. Epitaxial growth of the SPs was established by orientation mapping, ED and HR-TEM of the interfaces between the seeds and iron oxide domains and nanorods, respectively. All SPs showed low cytotoxicity in an Alamar Blue assay. They were tested subsequently for signal enhancement in magnetic resonance imaging. Both types of SPs displayed contrast enhancement by increased R_1- and R_2-relaxivities compared to the template particles due to (i) a higher effective superparamagnetic core radius because of the increased particle size by epitaxial growth and (ii) the anisotropy and inhomogeneity of the particle-generated magnetic field because of the unique SP morphology. Significant contrast enhancement was achieved for transversal relaxation making the SPs promising contrast agents for dark field imaging.

3.5 Experimental Section

Materials

Oleylamine (OAm, Acros Organics, 80-90%), 1-octadecene (ODE, Acros Organics, 90%), oleic acid (OAc, Fisher Scientific, Reagent Grade), iron(III) chloride hexahydrate ($FeCl_3{\cdot}6H_2O$, Sigma-Aldrich, 98%), sodium oleate ($C_{18}H_{33}O_2Na$, TCI, 97%), cyclohexane (Fisher Scientific, Analytical Reagent Grade), ethanol (Sigma-Aldrich, *p.a.*, > 99.8%), iron(0) pentacarbonyl ($Fe(CO)_5$, Sigma-Aldrich, 99.99%), trimethylamine *N*-oxide (TMAO, Sigma-Aldrich, 98%), sodium acetate (Acros Organics, 99%), n-hexane (Fisher Scientific, Analytical Grade), methanol (Sigma-Aldrich, 99.8%) and chloroform (Sigma-Aldrich, 99-99.4%) were used in this work.

Synthesis of Iron(III) Oleate

The iron(III) oleate as precursor was synthesized from 40 mmol of iron(III) chloride hexahydrate and 120 mmol of sodium oleate in 80 mL of ethanol, 60 mL of Milli-Q water and 140 mL of n-hexane and heated at 70 °C for 4 h (adapted from Park *et al.*[395]). Afterwards, the organic phase was removed with a separating funnel and washed three times with a 1:1 Milli-Q:methanol solution. The solvent was removed using a rotary evaporator, and the residue was dried with a Schlenk line under 10^{-3} mbar for 1 d at RT, followed by 1 d at 100 °C.

Synthesis of Spherical Nanoparticles (SPH NPs)

The synthesis of the spherical nanoparticles (SPH NPs) was adapted from Zhou *et al.* with some modifications.[373] 2 mmol of iron(III) oleate, 0.1 mmol of sodium oleate and 0.5 mmol of oleic acid were dissolved in 15 mL of 1-octadecene under inert (Ar) conditions. The flask was equipped with a mechanical stirrer and heated to 300 °C at a rate of 5 °C/min. This temperature was maintained for 2 h. Afterwards the flask was heated to 330 °C at a rate of 5 °C/min. This temperature was maintained for 30 min. The flask was slowly cooled to RT and the reaction product was precipitated with ca. 35 mL of ethanol and centrifuged for 10 min at 9000 U/min. The black product was washed three times through centrifugation (10 min, 9000 U/min, RT) with a 1:5 cyclohexane:ethanol solution, re-dispersed in cyclohexane and stored at RT.

Synthesis of Hexagonal Nanoplates (HEX NPs)

The synthesis of the hexagonal nanoparticles (HEX NPs) was adapted from Chen *et al.*[379] and Yang *et al.*[169] with some modifications. 2 mmol of iron(III) chloride hexahydrate were dissolved in 20 mL of ethanol and 1.4 mL of Milli-Q water. 2.5 g (30.48 mmol) of sodium acetate were added. The reaction mixture was transferred to a 25 mL teflon-lined stainless steel autoclave. The autoclave was placed in an oven and heated at 180 °C for 12 h. After cooling to RT the reaction product was precipitated with 25 mL of Milli-Q water and centrifuged for 10 min at 9000 U/min. The red product was washed through centrifugation (10 min, 9000 U/min, RT) with a 1:5 ethanol:Milli-Q water solution, re-dispersed in ca. 50 mL of ethanol using an ultrasonic bath and again centrifuged for 10 min at 9000 U/min. The precipitated product was dried in an oven at 60 °C and stored at RT.

Synthesis of Spherical Superparticles (SPH SPs)

The synthesis of the superparticles (SPs) starting from spherical nanoparticle seeds (SPH NPs) is an extension of our contribution towards the synthesis of colloidal Pd@Fe_2O_3 or Ni@Fe_2O_3 SPs.[92, 93] 1.38 mmol of trimethylamine *N*-oxide (TMAO) were dissolved in 12 mL of oleylamine under inert (Ar) conditions. 10 mg of the SPH NPs dissolved in 8 mL of 1-octadecene were added. Finally, 1.5 mL of oleic acid were added. The reaction mixture was stirred for 5 min at RT and subsequently heated to 90 °C at a rate of 10 °C/min. The temperature was maintained for 5 min, and 180 μL of $Fe(CO)_5$ were added using a syringe. Afterwards, the mixture was heated to 200 °C at a rate of 5 °C/min and held at this temperature for 1 h. The flask was slowly cooled to RT, and the reaction product was precipitated with ca. 30 mL of ethanol and centrifuged for 10 min at 9000 U/min. The black product was washed twice through centrifugation (10 min, 9000 U/min, RT) with a 1:5 cyclohexane:ethanol solution, re-dispersed in cyclohexane and stored at RT.

Synthesis of Hexagonal Superparticles (HEX SPs)

The synthesis of the superparticles (SPs) based on the hexagonal nanoplates as seeds (HEX NPs) was identical to the synthesis of the SPH SPs except for the amount of $Fe(CO)_5$, which was reduced to 120 μL.

Surface Functionalization of Nanoparticles and Superparticles with C-PEG

The catechol-PEG polymer (C-PEG_{120}, M_n = 4020 g/mol, PDI = 1.09, from SEC (DMF, RI signal, PEG standard)) was synthesized as described previously.[92, 114] A 1 mg/mL solution of the SPH NPs, HEX NPs, SPH SPs or HEX SPs was dispersed in chloroform and mixed with a 1 mg/mL solution of C-PEG in chloroform. The reaction mixture was stirred with a mechanical stirrer for 6 h at 40 °C under a gentle Ar flow. 6 mL of hexane per mg particles were added, and the particles were extracted into 1 mL of Milli-Q water per mg particles using a separating funnel.

Nanoparticle Characterization

Samples for *transmission electron microscopy (TEM)* were prepared by placing a drop of dilute NP dispersion in cyclohexane on a carbon coated copper grid. TEM images for the size and morphology characterization and surface rendering 3D tomography were obtained with a FEI Tecnai 12 TWIN LaB_6 at 120 kV together with a Gatan US1000 CCD-camera (16-bit, 2048 x 2048 pixels) using the Gatan Digital Micrograph software. High-resolution TEM, electron diffraction (ED) data and automated diffraction tomography (ADT) were obtained on a FEI Tecnai F30 S-TWIN transmission electron microscope at 300 kV equipped with a field emission gun. TEM images and electron diffraction patterns were acquired with a CCD camera (16-bit, 4096 x 4096 pixels) using the Gatan Digital Micrograph software. Scanning transmission electron microscopy (STEM) images were acquired using a Fischione high-angular annular dark field (HAADF) detector by means of the Emispec ES Vision software. The electron diffraction tomography measurements were carried out with a Fischione tomography holder and an automatic acquisition module developed for FEI microscopes.[396] Crystal position tracking was performed in microprobe STEM and nano-beam diffraction (NBD) patterns were sequentially acquired with a tilt step of 1 degree through an angular range of 91 degree. A 10 μm condenser aperture and mild illumination settings (spot size 6 and gun lens 8) were used to obtain a quasi-parallel beam of 50-100 nm in diameter (NBD setting). Atomic modeling and electron diffraction simulation were performed using the Crystal Maker software. The eADT software was used for three-dimensional electron diffraction data processing.[397] NanoMegas ASTAR software package was used to acquire and process the diffraction data for the orientation and phase mapping, which allows the indexation and orientation assignation by optimized matching to a template database using a cross-correlation approach.[398, 399] A 10 μm condenser aperture, spot size 7 and gun lens 1 were used to obtain a 5 nm beam for the 2D mapping. DigiStar generator unit provided by NanoMEGAS were used to generate a 1 degree precession and counter-precession signals.

X-ray diffraction (XRD) patterns were recorded on a STOE Stadi P diffractometer equipped with a Dectris Mythen 1k detector in transmission mode using unfiltered Mo $K\alpha_1$ radiation. Crystalline phases were identified according to the PDF-2 database using Bruker AXS EVA 10.0 software. Full pattern profile fits (Pawley/Rietveld) were performed with TOPAS Academic 6.0 applying the fundamental parameter approach.[348, 400]

^{57}Fe-Mössbauer spectra of powdered samples were recorded at 5.5 K in transmission geometry with a ^{57}Co source embedded in a rhodium matrix using a conventional constant-acceleration Mössbauer spectrometer equipped with a helium cryostat. Isomer shifts are given with respect to iron metal at ambient temperature. Simulations of the experimental data were performed with the Recoil software.[349]

Magnetic measurements were performed on a Quantum Design MPMS-XL superconducting quantum interference device (SQUID) magnetometer. Field-cooled (FC) and zero-field-cooled (ZFC) data were obtained in a temperature range between 5 and 300 K at 100 Oe. Hysteresis measurements were performed at 5 and 300 K.

Cytotoxicity tests were carried out with the non-small cell lung cancer (NSCLC) cell line A549 which was purchased from DSMZ (German collection of microorganisms and cell cultures, Braunschweig, Germany) and whose identity was verified *via* STR analysis. All cells used in the experiments directly originate from the stocks, which were verified. Cells were maintained in DMEM/Ham's F12 (Sigma-Aldrich, St. Louis, MO) supplemented with 10% FCS (fetal calf serum; Sigma-Aldrich, St. Louis, MO) and antibiotics (100 U/ml penicillin and 100 mg/ml streptomycin) at 37 °C in 5% CO_2. For the analysis of the cellular viability after treatment with the NPs, 10.000 cells per well were seeded in a 96 well plate and were cultivated overnight for adherence. The next day, cells received fresh cell culture medium and were treated with the NP dispersions in Milli-Q water. Cells treated only with the equivalent amount of water served as control. To all wells 10% Alamar Blue (Biozol Diagnostica, Eching, Germany) were added 3 h before the desired readout point and the samples were incubated for 3 h at 37 °C under cell culture conditions. The results were obtained using a plate reader (Fluoroskan Ascent Microplate reader, Thermo Fisher Scientific GmbH, Rockford, USA; ex: 540 nm, em: 600 nm) and normalized to control cells.

Magnetic resonance relaxation times and imaging measurements were performed with a Bruker/Oxford 7 T 150 mm super wide bore-system loaded to 4.7 T. A Resonance Instruments DRX spectrometer was used together with a Bruker Microimaging probe head at 199.876 MHz at ^{1}H-frequency. A Bruker BLAH and BLAX (1 kW) HF-amplifier and a Copley gradient amplifier were used. The user interface software was developed by Dr. Peter Blümler, Department of Physics, Johannes Gutenberg-University Mainz, Germany. Parameters for measuring the T_1 relaxation times were: P90 = 12 μs, P180 = 24 μs, STEPS = 30 and NS = 2. T_1 relaxation times were first obtained by fitting the FID signal with the exponential decay function $y = abs(A \cdot (1\text{-}2 \cdot exp(\text{-}x/T_1))+b)$ where T_1 is the desired relaxation time, A the amplitude and b the noise parameter. Data fitting led to an unrealistically high constant term, about 50 times larger than the integrated noise. Therefore the root of the function was used as a physical meaningful access to T_1 from the linear part around the zero-crossing ($y = 0$) of the measured data using a linear fit. Parameters for T_2 relaxation time measurements were: P90 = 12 μs, P180 = 24 μs, DW = 48 μs, NS = 64, NECH = 500 and SI = 1. T_2 relaxation times were obtained by fitting the FID signal with the exponential decay function $y = A \cdot exp(\text{-}x/T_2)+b$. NP dispersions of 1, 2 and 4 mM in Milli-Q water were degassed prior to the measurement to remove any dissolved oxygen. The T_1 relaxation times were corrected by the T_1 relaxation time of pure degassed Milli-Q water. The errors of T_1 and T_2 relaxation times were obtained by Gaussian error propagation calculation. R_1 and R_2 values were obtained by linear fitting of r_1 (= $1/T_1$) and r_2 (= $1/T_2$) in dependence of the NP concentration. For obtaining magnetic resonance images RD and TE = 2·TAU were varied according to $S (TE, RD) = S_0 \cdot exp(\text{-}TE/T_2) \cdot (1\text{-}exp(\text{-}RD/T_1))$ where S is the signal intensity, S_0 is the proton density, TAU is the time between P90 and P180 and RD is the repetition duration. T_1 weighted images were obtained by using a constant and short TAU value of 900 μs and increasing but short RD values of 30000, 50000 and 2000000 μs, respectively. T_2 weighted images were obtained by using a constant and long RD value of 5000000 μs and increasing but long TAU values of 5000, 10000 and 20000 μs, respectively.

Samples for *scanning electron microscopy (SEM)* were prepared with carbon film on aluminum holders. SEM images for the characterization of size and morphology were obtained using a HITACHI SU 8000 (Hitachi High-Technologies Europe GmbH, Krefeld, Germany).

3.6 Appendix

Table 3.1: Additional data to the Mössbauer measurements.

Chemical shift	Quadrupole shift	Magnetic field	Fraction	Substance
mm/s	mm/s	kOe	%	
SPH NPs 5 K				
0.52(1)	-0.01(1)	526(1)	26(1)	$Fe^{3+}{}_{oct.}$
0.42(1)	0	503(1)	50(2)	$Fe^{3+}{}_{tetr.}$
0.80(1)	-0.16(1)	469(1)	24(1)	Fe^{2+}
SPH SPs 5 K				
0.51(1)	0	525(1)	25(1)	$Fe^{3+}{}_{oct.}$
0.43(1)	0	505(1)	37(4)	$Fe^{3+}{}_{tetr.}$
0.49(1)	-0.03(1)	480(1)	38(3)	Fe^{3+}
HEX NPs 293 K				
0.37(1)	0.45(1)	512(1)	100	Fe^{3+}
HEX NPs 5 K				
0.48(1)	0.38(1)	538(1)	100	Fe^{3+}
HEX SPs 5 K				
0.53(1)	-0.02(1)	526(1)	22(2)	$Fe^{3+}{}_{oct.}$
0.43(1)	0	503(1)	49(3)	$Fe^{3+}{}_{tetr.}$
0.76(2)	-0.12(2)	465(3)	29(3)	Fe^{2+}

Table 3.2: Additional data to the Rietveld refinement of powder XRD data. Measurement conditions: $1.5 \leq 2\Theta/^\circ \leq 73.5$; 300 s/°; continuous scan.

	SPH NPs	**HEX NPs**	**SPH SPs**	**HEX SPs**
Cell parameter Å	8.395(1)	a = 5.042(1) (α-Fe_2O_3, lit.[381] 5.025) c = 13.760(1) (α-Fe_2O_3, lit.[381] 13.735)	8.382(1)	8.396(1)
Approx. composition	$Fe_{0.79(1)}Fe_{1.88(6)}O_4 = Fe_{0.67(1)}O$	Fe_2O_3	$Fe_{0.71(1)}Fe_{1.80(5)}O_4 = Fe_{0.63(1)}O$	$Fe_{0.78(1)}Fe_{1.88(6)}O_4 = Fe_{0.67(1)}O$
R_{wp}	10.70	7.88	6.28	7.96
Goodness of fit (G)	2.60	1.73	1.38	1.76
Number of parameter/ background	56/43	49/36	56/43	56/43

Table 3.3: Cell parameter obtained from eADT analysis of HEX NPs.

		Primitive cell	**Transformed cell**
a	Å	5.26	4.87
b	Å	4.93	4.86
c	Å	4.86	13.48
α	°	120.1	89.6
β	°	90.2	90.0
γ	°	117.6	119.4

Table 3.4: Additional data to the SQUID magnetic measurements.

			SPH NPs	**HEX NPs**
	Blocking temperature	K	300	290
5 K	Saturation magnetization at 50 kOe	emu/g	41	0.962
	Remanence	emu/g	5	0.040
	Coercivity	Oe	-200	-1020
300 K	Saturation magnetization at 50 kOe	emu/g	40	0.966

			SPH SPs	**HEX SPs**
	Blocking temperature	K	287	290
5 K	Saturation magnetization at 50 kOe	emu/g	42	44
	Remanence	emu/g	5	2
	Coercivity	Oe	-230	260
300 K	Saturation magnetization at 50 kOe	emu/g	43	42

4

From Single Molecules to Nanostructured Functional Materials: Formation of a Magnetic Foam Catalyzed by Pd@Fe$_x$O Heterodimers

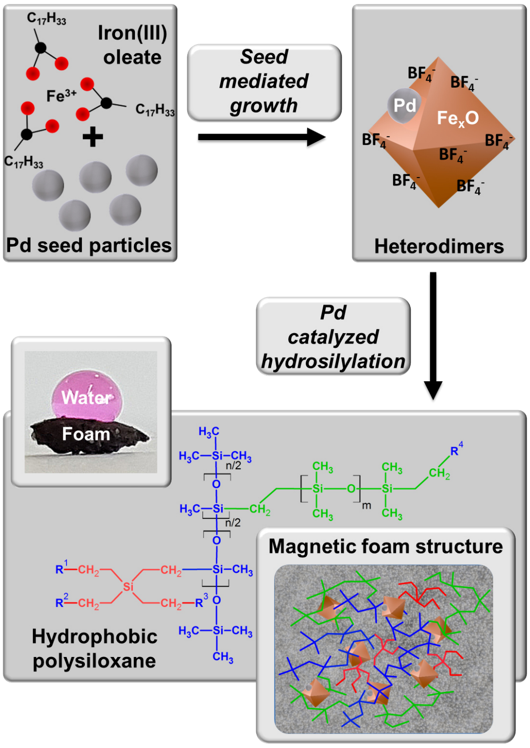

This chapter contains an adapted reproduction of Applied Nano Materials 2017, DOI: 10.1021/acsanm.7b00051,[378] *reproduced with permission of the American Chemical Society. A detailed Authorship Statement of the publication is attached in the Appendix of this dissertation. I acknowledge the collaboration of* [redacted].[401]

4.1 Abstract

Multicomponent nanostructures containing purely organic or inorganic as well as hybrid organic-inorganic components connected through a solid interface are, unlike conventional spherical particles, able to combine different or even incompatible properties within a single entity. They are multifunctional and resemble molecular amphiphiles, like surfactants or block copolymers, which makes them attractive for the self assembly of complex structures, drug delivery, bioimaging or catalysis. We have synthesized Pd@Fe$_x$O heterodimer nanoparticles (NPs) to fabricate a macroporous, hydrophobic, magnetically active, three-dimensional (3D) and template-free hybrid foam capable of repeatedly separating oil contaminants from water. The Pd domains in the Pd@Fe$_x$O heterodimers act as nanocatalyst for the hydrosilylation of polyhydrosiloxane and tetravinylsilane, while the Fe$_x$O component confers magnetic properties to the final functional material. Pd@Fe$_x$O heterodimers were synthesized by heterogeneous nucleation and growth of the iron oxide domain onto presynthesized Pd NPs at high temperatures in solution. The morphology, structure, and magnetic properties of the as-synthesized heterodimers were characterized by transmission electron microscopy (TEM), X-ray diffraction (XRD), Mössbauer spectroscopy, and a superconducting quantum interference device (SQUID). The epitaxial growth of the Fe$_x$O domain onto Pd was confirmed by high-resolution TEM. A potential application of the 3D hydrophobic magnetic foam was exploited by demonstrating its ability to soak oil beneath a water layer, envisioning its use in oil sampling during oil prospection drilling, or to remove oil films after oil spills.

4.2 Introduction

The use of nanomaterials as catalysts in organic synthesis has attracted interest in research and technology because they combine exceptionally high surface area and reactive surfaces.[402–404] Different types of nanoparticles (NPs) have been used as catalysts in organic reactions: *e.g.*, Cu NPs in "click" cycloaddition reactions,[405] two-dimensional Au nanostructures for the selective oxidation of C-H bonds,[406] Ru or Pt NPs for selective hydrogenation reactions,[407] and Pd NPs for C-C and Si-C (hydrosilylation)[408] coupling reactions under mild conditions.[402, 409–411] Nanocatalysts could be the best contenders for the development of green and sustainable industrial processes.[412] The prime interest in this area was so far to mimic molecular catalysts used in conventional organic synthesis with nanomaterials containing the respective metal atoms. Recent developments in colloidal synthesis allow for the synthesis of NPs by joining two or more than two domains at the same platform. The option to graft different functions to a single particle in an individual fashion allows one to make materials with enhanced optical, magnetic and catalytic properties.[42, 47, 413–415] In essence, the design and synthesis of multicomponent NPs with discrete domains that impart their functions in a synergistic manner may lead to new functional materials. Several multicomponent NPs with morphologies ranging from core-shell, dumbbell, to epitaxially grown colloidal superparticles have been reported.[38, 92, 93, 360, 416] Among these multicomponent NPs, heterodimers or Janus NPs have good prospects to perform complementary functions because their architecture offers a domain-specific surface chemistry.[289, 417] These heterodimers from metals and magnetic or semiconducting metal oxides and metal chalcogenides have a wide range of compositions to explore new chemical and physical properties.[418–420] Nanomaterials containing Pd have received immense attention because they may catalyze organic reactions including Heck, Sonogashira, Suzuki, Stille, Negishi, Hiyama, Corriu-Kumada, Tsuji-Trost, and Ullmann reactions,[105, 404, 409, 410, 421–423] while iron oxide NPs may serve as a tool for magnetic separation.[424–427] Here we report the synthesis of Pd@$\mathrm{Fe_xO}$ heterodimer NPs, where the very small ($\approx$ 5 nm) Pd domain catalyzes a hydrosilylation reaction. The surface availability of both components (metal and metal oxide) as well as their distinct properties offer a new route to a template-free synthesis of nanocomposite materials. With the proper choice of reactant structures we could synthesize a (poly)organosilicone-based three-dimensional (3D) hydrophobic, macroporous and magnetic composite with impregnated Pd@$\mathrm{Fe_xO}$ NPs that act as "magnetic foam". The potential application of the magnetic foam composite was demonstrated by removing oil contaminants from water. This magnetic foam could be manipulated with an external magnetic field. The strategy could easily be extended for oil sampling during oil prospection drilling or oil film removal after an oil spill.[428, 429]

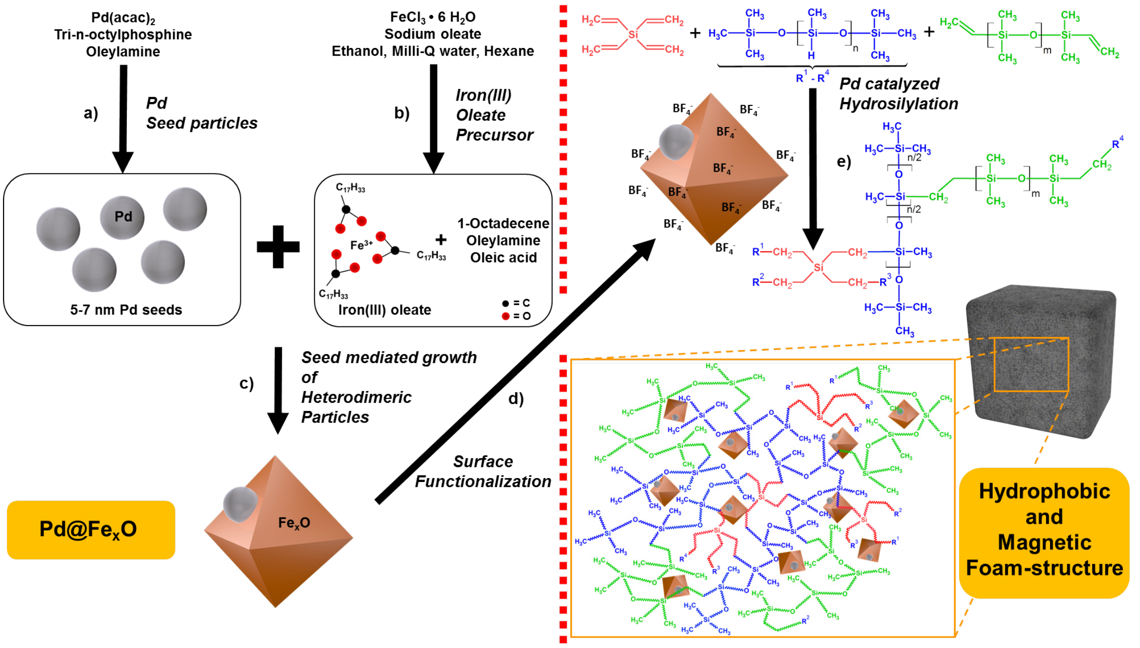

Figure 4.1: Synthesis of (a) Pd seed NPs, (b) the iron(III) oleate precursor, and (c) Pd@Fe$_x$O NPs. After functionalization with (d) NOBF$_4$, the Pd@Fe$_x$O NPs were used for a Pd catalyzed hydrosilylation reaction (e) of tetravinylsilane, poly(methylhydrosiloxane), and vinyl-terminated poly(dimethylsiloxane) to form a hydrophobic and magnetic foam-structure.

4.3 Results and Discussion

Figure 4.1 illustrates the synthesis of Pd@Fe$_x$O heterodimers using Pd NPs as seeds and an iron(III) oleate precursor for iron oxide. The Pd NPs used as seed particles were synthesized by the decomposition/reduction of Pd(acac)$_2$ using TOP (tri-n-octylphosphine) and OAm (oleylamine) at 250 °C (Figure 4.1a), whereas the Fe$_x$O domain was formed by the decomposition of iron(III) oleate and heterogeneous nucleation/growth onto the presynthesized Pd seed NPs at 310 °C (Figure 4.1b and c). Subsequent surface functionalization (Figure 4.1d) of the as-synthesized Pd@Fe$_x$O heterodimer NPs was mandatory to transfer them into a polar organic solvent (DMF) to catalyze the hydrosilylation reaction between unsaturated silane and polysiloxane (Figure 4.1e). The Pd domain acted as nanocatalyst, and iron oxide imparted the magnetic character. Through the choice of the proper silane and siloxanes in an appropriate ratio, a three-dimensionally organized network of polysiloxane with entrapped NPs was obtained. The final composite material was macroporous and could be manipulated with an external magnetic field.

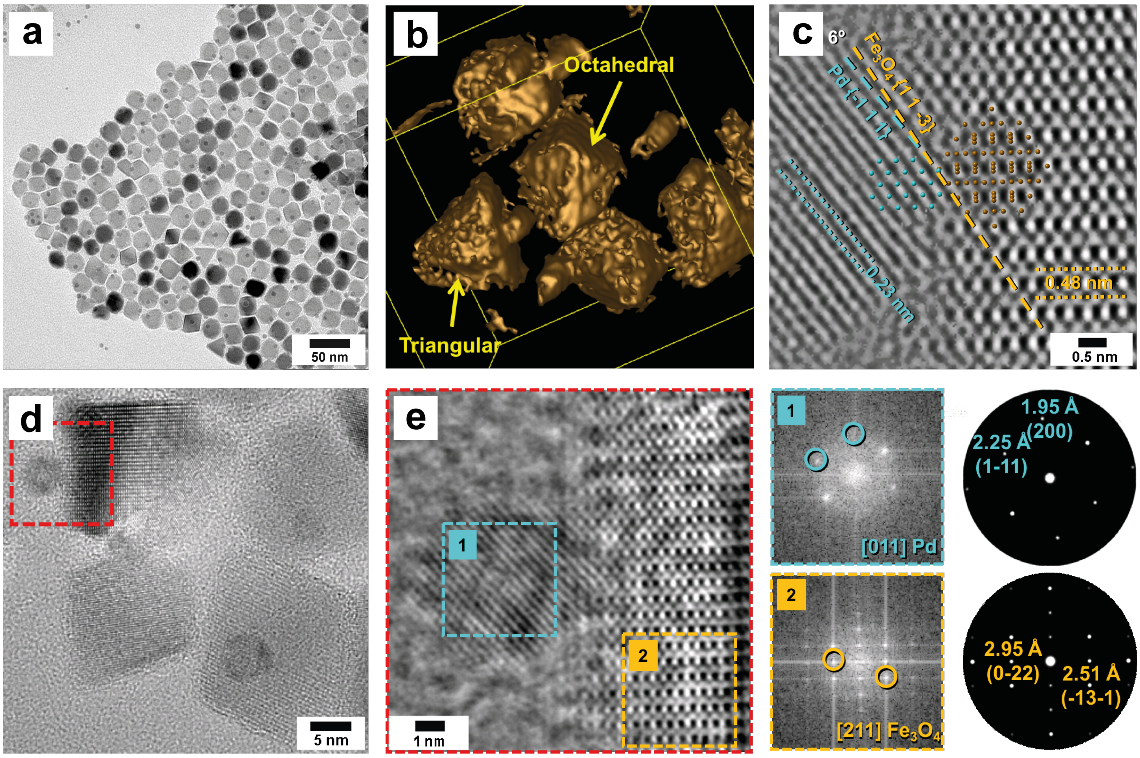

Figure 4.2: TEM images of Pd@Fe$_x$O NPs. (a) TEM image of Pd@Fe$_x$O heterodimer NPs. (b) Surface rendering 3D tomography of octahedral and triangular shaped Pd@Fe$_x$O NPs. (c) Holography phase image of the Pd[011] and Fe$_3$O$_4$[211] zone axes superimposed with a model of the atomic layers. (d) TEM image of Pd and Fe$_x$O interface in the red boxed region. (e) HR-TEM image of red boxed region from (d) with power spectra and simulated ED patterns of the Pd (1, cyan) and Fe$_x$O (2, orange) domains.

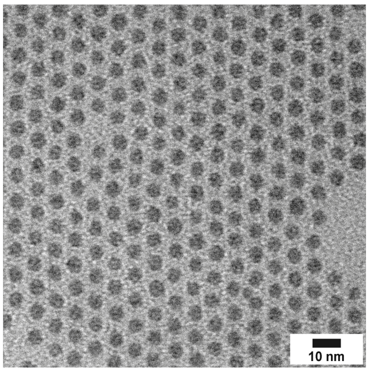

Figure 4.3: TEM image of 5.2 nm (± 10%) Pd seed NPs synthesized according to Kim *et al.*[331]

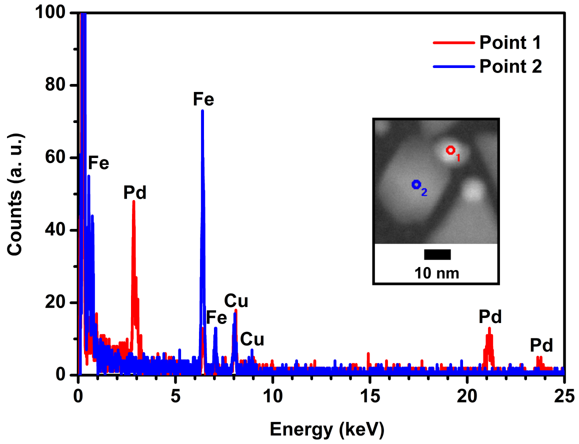

Figure 4.4: EDX spectrum of Pd@Fe$_x$O NPs with Pd signals for spot 1 on Pd domain and Fe signals for spot 2 on Fe$_x$O domain. Cu signals are due to the use of carbon coated copper grids.

4.3.1 Structure, Phase Composition and Morphology of Pd@Fe$_x$O Heterodimers

Figure 4.2 shows TEM and HR-TEM micrographs of Pd@Fe$_x$O heterodimer NPs. The Pd domain in the Pd@Fe$_x$O heterodimers is spherical with a diameter ≈ 5 nm (Figure 4.2a, Figure 4.3). The iron oxide domain is faceted (anisotropic) with octahedral morphology and a diameter ≈ 25 nm (along with a very small fraction of particles with triangular morphology) (Figure 4.2a). The faceted octahedral morphology of the iron oxide domains was confirmed by surface rendering 3D tomography (Figure 4.2b) and TEM tilting studies. For further examination of the domains and the interface, TEM holography from phase imaging was carried out (Figure 4.2c-e). Figure 4.2c shows an extended holography phase image of the Pd[011] and Fe_3O_4[211] zone axis superimposed with a model of the atomic layers to characterize the growth of the iron oxide on the Pd domain. The magnetite {11-3} layer with a d spacing of 0.48 nm grew on the Pd{-111} layer characterized by a d spacing of 0.23 nm. The lattice mismatch of approximately 7% caused a 6° tilted growth of the magnetite domain on Pd and enabled epitaxial growth of the Fe$_x$O domain on the Pd seed particles. Holography of HR-TEM (Figure 4.2d) was performed on the Pd (Figure 4.2e, boxed region 1) and the iron oxide domains (Figure 4.2e, boxed region 2) extracting the power spectra from the phase image. For the Pd domain, the simulated diffraction pattern of the Pd[011] zone axis matched well with the power spectrum. For the iron oxide domain, the simulated diffraction pattern of the magnetite [211] zone axis was also in agreement with the power spectrum. The chemical composition of both domains was confirmed by EDX analyses, which show Pd signals for the Pd domain and Fe signals for the Fe$_x$O domain of Pd@Fe$_x$O NPs (Figure 4.4).

Because the structure of iron(III) oleate plays a major role in defining the morphology of the iron oxide domain, the as-synthesized iron(III) oleate precursor was analyzed

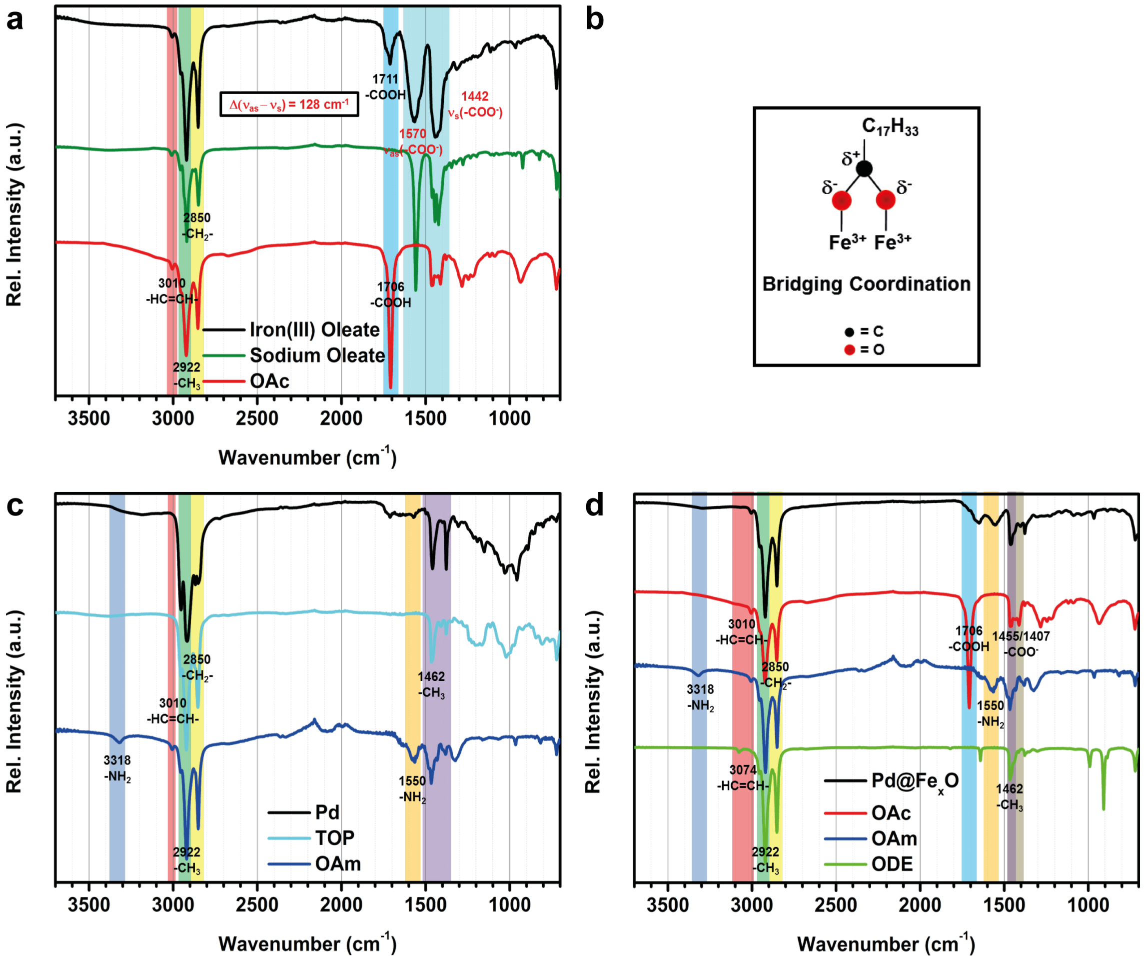

Figure 4.5: (a) IR spectra of iron(III) oleate with (b) schematic representation of bridging oleate coordination. (c) 5 nm Pd seed particles and (d) Pd@Fe$_x$O heterodimeric particles along with reference IR spectra of surfactant substances and solvent, *i.e.* OAc = oleic acid, TOP = tri-n-octylphosphine, OAm = oleylamine and ODE = 1-octadecene.

initially by FT-IR spectroscopy and TGA. The FT-IR spectra of the surfactants, iron(III) oleate and as-synthesized NPs are presented in Figure 4.5. The FT-IR spectrum of iron(III) oleate (Figure 4.5a) shows typical C-C and C-H vibrations in the region of 2800-3100 cm^{-1}. The bands corresponding to the COO$^-$ symmetric and asymmetric stretching vibrations at 1400-1600 cm^{-1} were used to characterize the binding and coordination modes of Fe^{3+} to the oleate moiety. The difference (Δ) between the two modes indicates the type of coordination. For Δ = 200-300 cm^{-1} a monodentate binding is likely. For Δ = 110-200 cm^{-1} ionic or bridging coordination and for $\Delta < 110$ cm^{-1} chelating bidentate coordination can be assumed.[430, 431] The reduced difference results from the group symmetry of the chelating bidentate and bridging coordination which is the same as that in the free ionic state. Accordingly, the frequency of the asymmetric vibration decreases and the frequency of the symmetric vibration increases relative to the monodentate binding mode.[430] Here, Δ = 128 cm^{-1}

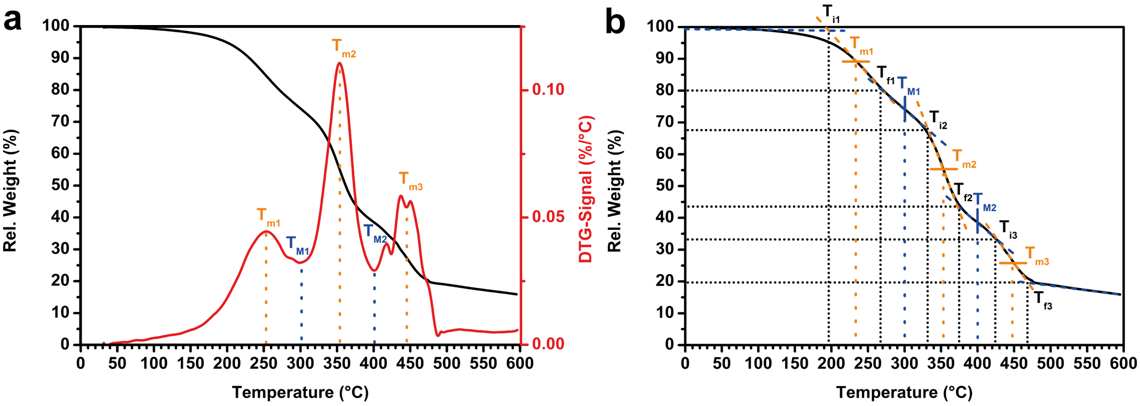

Figure 4.6: Thermogravimetric analysis of the iron(III) oleate precursor complex used for the synthesis of Pd@Fe$_x$O NPs and Fe$_x$O NPs. (a) Thermogravimetric analysis together with its first order derivation (DTG) signal. (b) Graphic analysis of thermogravimetric data. T$_i$, T$_m$ and T$_f$ describing the starting temperature, temperature at maximum slope and ending temperature of a clear weight loss step, respectively. T$_M$ marks midpoint temperature between two clear weight loss steps, where weight is not constant.

indicates a bridging coordination (Figure 4.5b).[376] This also explains the faceted morphology of the iron oxide domain formed in the Pd@Fe$_x$O heterodimer NPs. It has been reported that iron(III) oleate with bridging coordination leads to the formation of anisotropic iron oxide particles.[376, 432] The band at 1711 cm^{-1} can be assigned to the carbonyl vibration of free OAc.[433] The IR spectrum in Figure 4.5c shows that the 5 nm Pd seed particles are mainly functionalized with TOP, whereas the Pd@Fe$_x$O NPs display a surface functionalization of OAm and OAc (Figure 4.5d). The TGA data (Figure 4.6, Table 4.1) show the typical plot for iron(III) oleate synthesized in ethanol. In the temperature range from 196 °C to 267 °C, dissociation of the symmetric oleate ligands of the quasi-octahedral Fe^{3+}(oleate)$_3$ complex takes place (lower binding energies).[376] This step is attributed to the nucleation process.[375] The second smaller weight loss between 267 °C and 331 °C is attributed to the dissociation of the third asymmetric ligand and characterizes the particle growth.[434] These two weight losses are mainly due to the loss of CO$_2$ due to a ketonic decarboxylation reaction.[376] Because this is not a redox reaction and according to XPS measurements reported by Bronstein *et al.*,[375] as-synthesized iron(III) oleate shows only the presence of Fe^{3+}-species. The partial reduction to Fe^{2+}, which leads to the formation of magnetite and maghemite in the iron oxide domain (*vide infra*), is likely to occur during the thermal decomposition of the remaining, *i.a.* ketonic, byproducts. Kwon *et al.*[377] demonstrated by thermogravimetric mass spectrometry that CO$_2$ and H$_2$ can be detected during a second transition step at 320 °C, leading to the reduction of Fe^{3+} and the formation of a phase similar to magnetite. They assign this to the formation of thermal radicals resulting in the formation of CO and H$_2$ after complete fragmentation.[377] The differential thermogravimetric (DTG) data (Figure 4.6a) and highest TGA mass loss of 24%

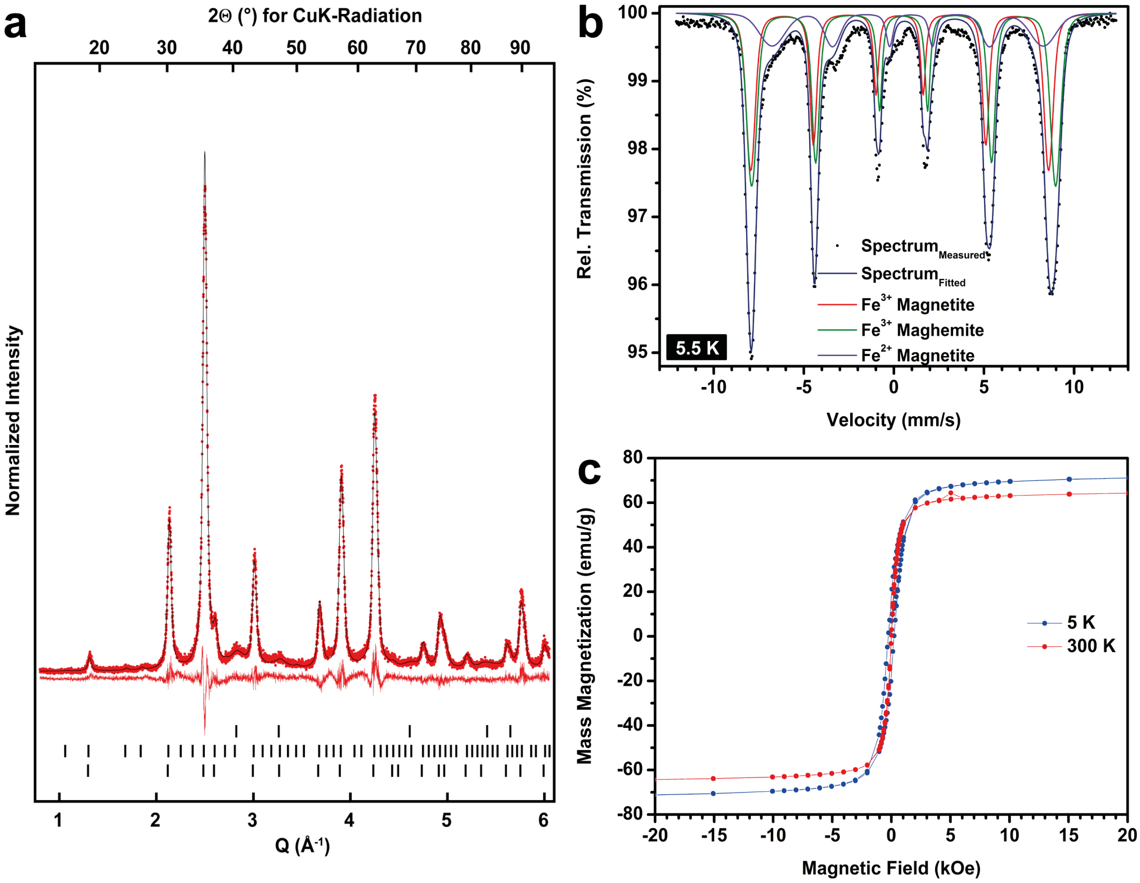

Figure 4.7: (a) Rietveld refinement to the powder XRD data of Pd@Fe$_x$O NPs. Red dots mark the experimental data, the black line corresponds to the calculated pattern, and the red line shows the difference between the experimental and calculated data. Black ticks mark reflections of Pd and iron oxide, respectively. $Q = [4\pi \sin(\Theta)]/\lambda$ is the scattering vector. (b) ^{57}Fe-Mössbauer spectrum of Pd@Fe$_x$O NPs at 5.5 K. (c) Hysteresis measurements at 5 K and 300 K for Pd@Fe$_x$O NPs.

(Figure 4.6b) reveal this decomposition step to take place between 331 °C and 374 °C with a maximum slope at 353 °C. Further smaller weight losses (11%, 374-424 °C and 13%, 424-468 °C) follow, describing the complete desorption of the decomposed ligands as well as the vaporization of the organics leaving a 20% portion of iron oxide NPs.[376]

4.3.2 Magnetite versus Maghemite in the Fe$_x$O Domains

Figure 4.7a displays the results of a Rietveld refinement for the as-synthesized Pd@Fe$_x$O heterodimer NPs. According to the XRD data, the sample contains three crystalline phases – a Pd side phase due to the presence of Pd domains and the reflections of two iron oxide main phases (Table 4.2). The Pd side phase with a weight fraction of 3.4% has a refined lattice parameter of 3.853(2) $\AA$, which is close to

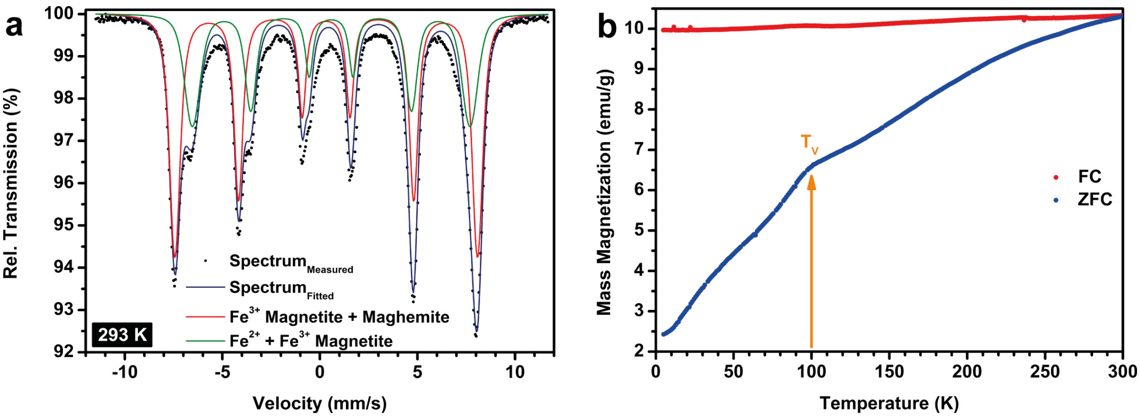

Figure 4.8: (a) ^{57}Fe-Mössbauer spectrum of Pd@Fe$_x$O NPs at 293 K. (b) Magnetic blocking temperature measurements with field cooled (FC) and zero field cooled (ZFC) magnetic field for Pd@Fe$_x$O NPs. T$_V$ marks the Verwey transition at approximately 100 K.

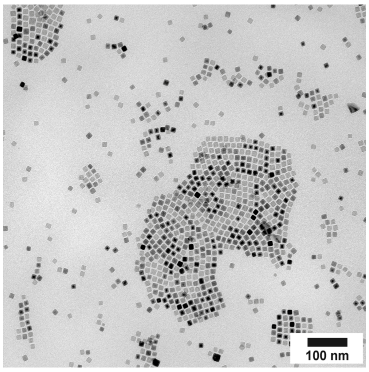

Figure 4.9: TEM image of Fe$_x$O NPs without Pd domain.

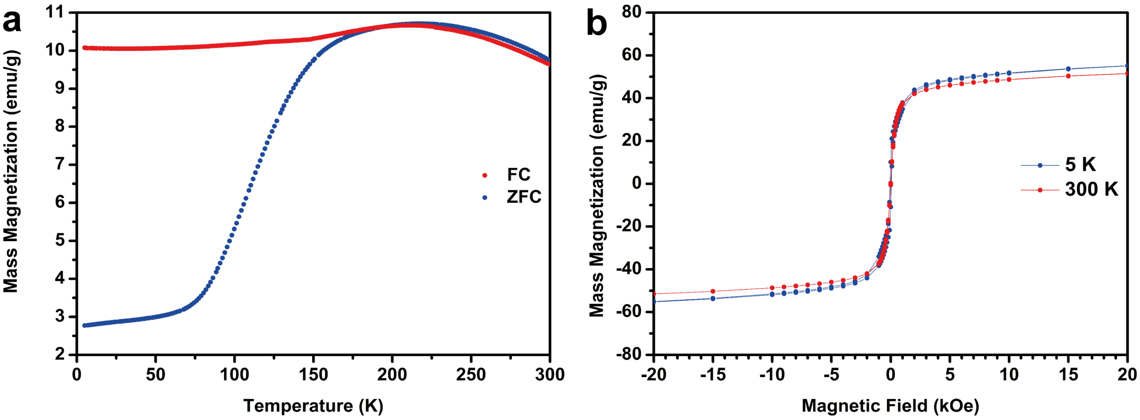

Figure 4.10: (a) Magnetic blocking temperature measurements with field cooled (FC) and zero field cooled (ZFC) magnetic field and (b) hysteresis measurements at 5 K and 300 K and for Fe$_x$O NPs.

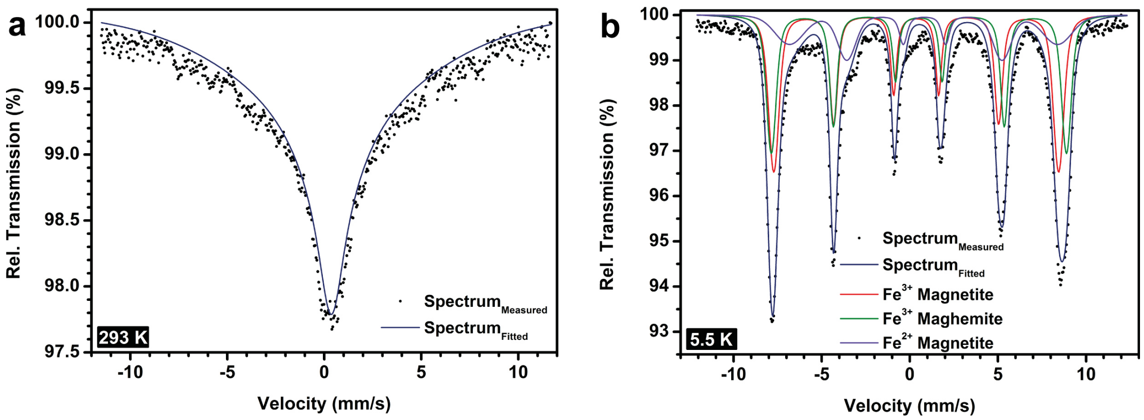

Figure 4.11: ^{57}Fe-Mössbauer spectra of Fe_xO NPs at (a) 293 K and (b) 5.5 K. At 5.5 K the two outer sextets of 41% and 37% fraction belong to Fe^{3+} of magnetite and Fe^{3+} of maghemite. At 5.5 K the inner broad sextet of 22% fraction belongs to Fe^{2+} of magnetite leading to an overall composition of ca. 60% magnetite and ca. 40% maghemite.

the reported lattice parameter of Pd (3.879 *Å*), and a crystallite size of 3.5 nm which is comparable to the crystallite size of the Pd domain obtained from TEM imaging (5.2 nm ± 10%, Figure 4.2a, Figure 4.3).[381] The distinction between γ-Fe_2O_3 and Fe_3O_4 based on XRD data is difficult because of the structural and chemical similarity of both compounds. Maghemite is an iron deficient defect variant of magnetite and has a cubic structure as well, but with a slightly smaller lattice parameter.[321] Additionally, reflection broadening for nanocrystalline materials occurs.[320] Nevertheless, maghemite (60 wt%) co-occurs with magnetite (37 wt%). The crystallite size of iron oxide was determined to be 16.6 nm, which is comparable to the iron oxide domain sizes extracted from the TEM images (Figure 4.2a).

4.3.3 Magnetite versus Maghemite in the Fe_xO Domains – Extended Mössbauer Spectroscopy and Magnetic Analysis

The distribution of Fe in the sample was clarified using Mössbauer spectroscopy at 5.5 K (Figure 4.7b) and 293 K (Figure 4.8a). The ^{57}Fe-Mössbauer spectrum of the Pd@Fe_xO NPs at 293 K allows to correlate the data to those of the SQUID magnetic measurements (Figure 4.7c, Figure 4.8b). The Pd@Fe_xO NPs showed a high blocking temperature (T_B) of ≈ 295 K (Figure 4.8b, Table 4.3). Thus, the blocking temperature is slightly above the measurement temperature, the easy axes are blocked and the magnetization is large enough to perform Mössbauer spectroscopy at 293 K.[322, 323] The spectrum (Figure 4.8a) could be simulated with 2 sextets having relative line intensities of 3:2:1:1:2:3 compatible with 4 different magnetically ordered Fe sites. The inner sextet with 40% fraction can be attributed to Fe^{2+} and Fe^{3+} in the octahedral positions of magnetite with a small hyperfine field of 442 kOe, typical for magnetite accompanied by maghemite (Table 4.4).[325] The

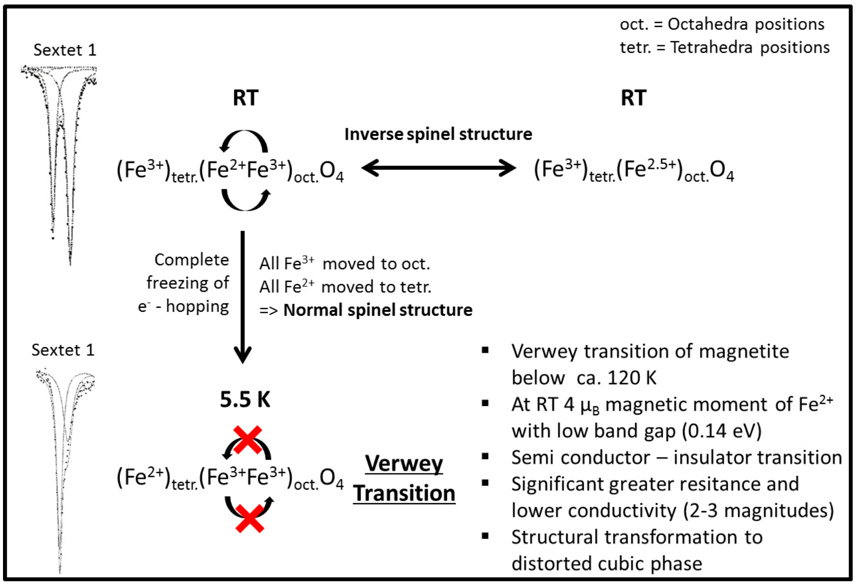

Figure 4.12: Schematic representation of the structural changes in magnetite caused by the Verwey transition at 120 K and impact on Mössbauer spectroscopy.[435–438]

outer sextet with 60% fraction corresponds to Fe^{3+} in maghemite and Fe^{3+} in the tetrahedral positions of magnetite showing a typical small hyperfine field of 481 kOe as well.[324, 439] A total magnetite content of 60% was calculated from a 40% fraction of the inner sextet and 20% of the outer sextet. The remaining 40% of the outer sextet correspond to the total maghemite content.

According to HR-TEM analysis (Figure 4.2) homogeneous Fe_xO domains are present, giving no indication of separated magnetite and maghemite phase domains in the NPs. Therefore, each NP is like to contain a variable magnetite/maghemite two-phase distribution due to the spinel structure of both phases, octahedral site vacancies and fluctuating Fe^{2+} ion content in the octahedral sites. Comparable Fe_xO NPs of similar particle size (Figure 4.9) exhibit a lower blocking temperature of $\approx$ 210 K (Figure 4.10a, Table 4.3). Thus, the magnetic moments exhibit fast fluctuation due to thermal energy and superparamagnetic relaxation leading to a collapse of the hyperfine splitting and no Mössbauer measurement at 293 K (Figure 4.11a).[322, 323] Hence, the Pd@Fe_xO NPs were measured at 5.5 K as well (Figure 4.7b). The broad inner sextet (19% fraction) corresponds to Fe^{2+} in magnetite. The outer sextet (37% and 44% fraction, Table 4.4) has contributions from Fe^{3+} in magnetite and Fe^{3+} in maghemite.[323, 324] This is compatible with a total of 55.5% magnetite and 44.5% maghemite. The different distribution of Fe^{2+} and Fe^{3+} at low temperature compared to 293 K arises from the Verwey phase transition of magnetite below 120 K. This semiconductor – insulator transition results in a significant higher resistance and lower conductivity accompanied by a structural transition to monoclinic symmetry (Figure 4.12).[435, 436] The electron-hopping of Fe^{2+} and Fe^{3+} ions in the octahedral sites of nano-magnetite is blocked and all Fe^{3+} ions move to the octahedral sites (outer sextet, Figure 4.7b) while all Fe^{2+} ions move to the tetrahedral sites (inner broad sextet, Figure 4.7b) forming a normal spinel structure.[435–438] The Mössbauer spectrum of the Fe_xO NPs at 5.5 K (Figure 4.11b, Table 4.4) shows a similar magnetite/maghemite distribution of 60/40 confirming that the iron oxide distribution does not depend on the heterodimeric nature of the NPs. In summary, an approximate 50/50 distribution of magnetite:maghemite can be derived from the Mössbauer data. The Pd@Fe_xO NPs show ferromagnetic behavior at 5 K and superparamagnetic behavior at room temperature, which was extracted from temperature-dependent magnetization and hysteresis curves (Figure 4.7c). The blocking temperature of $\approx$ 295 K at a mass magnetization of 10.3 emu/g (Figure 4.8b, Table 4.3) is relatively high because of bigger particle size, which is also responsible for the broad maxima of the ZFC and FC curves.[353, 440] The ZFC curve (Figure 4.8b) displays a kink at approximately 100 K that is due to the Verwey-transition of magnetite (T_V).[169, 435, 436] The trend of the FC curve provides useful information about the magnetic interactions between the magnetic nanoparticles. Typically, above the blocking temperature the FC magnetization is inversely related to the temperature due to decreased thermal fluctuations at lower temperature. This leads to an increased alignment of the moments with the applied magnetic field (visible here only for the Fe_xO NPs in Figure 4.10a).[441] The FC curves of both Pd@Fe_xO and Fe_xO NPs in Figure 4.8b and Figure 4.10a display a slight decrease in the magnetization for temperatures below T_B. This may be caused by dipolar interactions between the particles influencing an alignment of the moments to the magnetic field.[442–445] The saturation magnetization is a summation of the magnetic moments of all individual iron oxide domains; at 5 K and 300 K they are 72 emu/g and 65 emu/g, respectively for the Pd@Fe_xO NPs (Figure 4.7c). This is lower than the saturation magnetization of both bulk magnetite (92 emu/g) and bulk maghemite (80 emu/g).[330, 446] These reduced values can be caused by the presence of both iron oxide phases, spin canting effects of the surface Fe-ions or effects of the surfactants.[382]

4.3.4 Catalytic Activity for Hydrosilylation

The Pd@Fe_xO NPs were tested for their activity to catalyze hydrosilylation reactions to synthesize porous silicones. Hydrosilylation, an addition of a silane to a double bond, is catalyzed typically by noble metals like Pd or Pt and undergoes a Heck cyclic reaction of oxidative addition and reductive elimination.[447] We adopted this hydrosilylation for the reaction of a poly(methylhydrosiloxane) with double bond bearing vinyl terminated poly(dimethylsiloxane) and tetravinylsilane. This led to the formation of a hydrophobic foam-like structure with Pd@Fe_xO NPs entrapped inside the composite. The Si-C coupling reaction between alkene (C=C) and hydrosiloxane (Si-H) was confirmed by FT-IR spectroscopy (Figure 4.13). Tetravinylsilane showed a typical C-H stretching vibration associated with a double bond at 3049 cm^{-1} and a C=C stretching vibration at 1590 cm^{-1}. The asymmetric C-H bending vibration at 1399 cm^{-1} is strong as well. This confirms the presence of the vinyl groups. The vinyl-terminated poly(dimethylsiloxane) showed a strong band of the symmetric

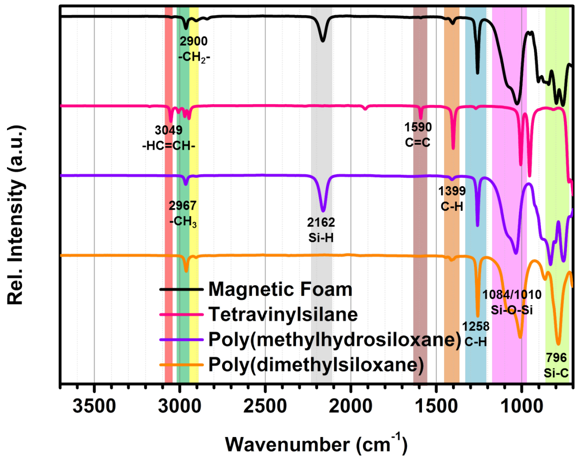

Figure 4.13: IR spectrum of magnetic foam along with reactants for hydrosilylation.

C-H bending vibration at 1258 cm^{-1} and a weak band of the asymmetric band. The asymmetric and symmetric Si-O-Si stretching vibrations (1084 cm^{-1} and 1010 cm^{-1}) merge into one broad band and the Si-C asymmetric stretching vibration appears as a strong band at 796 cm^{-1}. Because of the methyl groups, the CH$_3$ stretching vibration appears at 2967 cm^{-1}. The third silyl component, poly(methylhydrosiloxane), additionally has a Si-H functional group for hydrosilylation shown as stretching vibration at 2162 cm^{-1}.[448, 449] In summary, the IR spectrum of the final sponge product displays the Si-C, Si-O-Si and C-H vibrations. It also shows the Si-H vibration which is probably due to the excess of poly(methylhydrosiloxane) used. This is supported by the missing bands associated with double bounds. Accordingly, all double bonds must have reacted in the hydrosilylation reaction.

4.3.5 Surface Properties of "Magnetic" Silicone Foam Allowing the Collecting of Oil

The reactants designed for the hydrosilylation reaction were soluble in organic polar solvents like DMF. Therefore, the Pd@Fe$_x$O NPs were surface functionalized to tune their solubility in DMF. The particles were treated with a NOBF$_4$ solution to exchange the OAc and OAm surface ligands with BF$_4^-$. As shown in Figure 4.14a, this ligand exchange allowed one to transfer the Pd@Fe$_x$O NPs from cyclohexane to DMF. To start the reaction, the functionalized Pd@Fe$_x$O heterodimer NPs were mixed with the reactants and heated at 80 °C for 4 days. The extended reaction time was necessary to achieve a stable structure due to the very small active Pd next to a much larger iron oxide domain. Figure 4.14b shows the reaction mixture after heat treatment with and without NPs, verifying that the reaction was catalyzed by the NPs and not triggered by heating. The resulting foam-like structure was magnetic (Figure 4.14c) and hydrophobic (Figure 4.14d). As demonstrated in Figure 4.14d the foam is superhydrophob, exhibiting a contact angle of 125.8° (average from

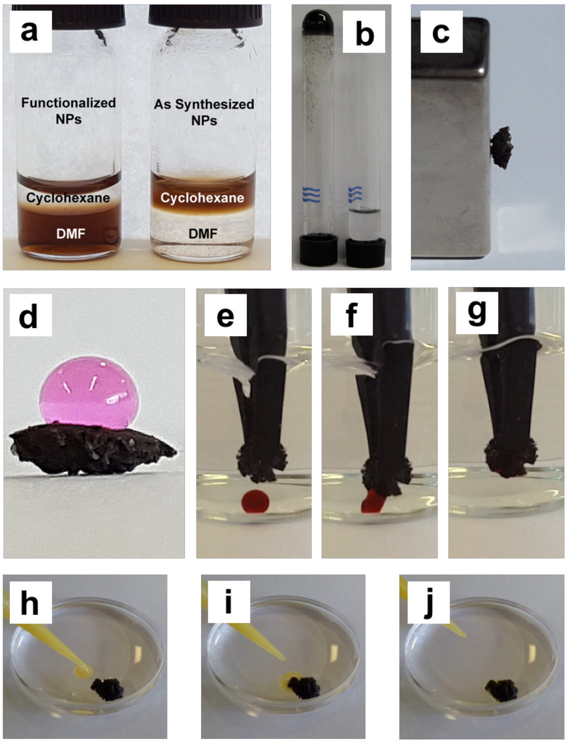

Figure 4.14: (a) Functionalized NPs dispersed in DMF compared to as-synthesized NPs in cyclohexane. (b) Reaction mixture for hydrosilylation with and without NPs after reaction. (c) Magnetic property of the NP foam. (d) Water drop on the NP foam. Adsorption of hydrophobic liquid by the NP foam (e-g) under water and (h-j) on the water surface.

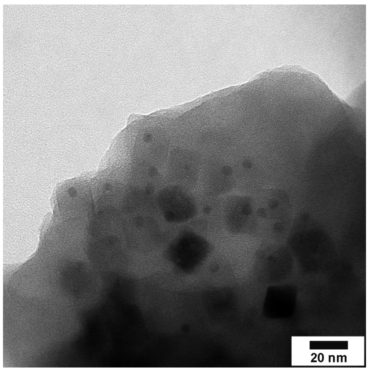

Figure 4.15: TEM image of Pd@Fe$_x$O NPs embedded into hydrophobic foam structure.

three measurements). The foam had a hard texture and was slightly brittle upon cutting. TEM analysis verified that the Pd@Fe$_x$O NPs were physically embedded in the hydrophobic foam, with the siloxane network acting as a "glue" (Figure 4.15). The hydrophobic magnetic foam floated on water and could be moved easily with a magnet. When a hydrophobic liquid (with high density) was dropped beneath water (Figure 4.14e-g) or made to float (with a low density such as oil) on the water surface (Figure 4.14h-j) near the magnetic foam, the foam could be directed towards the oil patch and used to selectively adsorb the oil. The oil-loaded foam could be removed from the water with a magnet, and the adsorbed oil could easily be expelled by rinsing the foam with a nonpolar solvent. Subsequently, the foam could be reused.

4.4 Conclusion

In summary, we have developed a protocol to synthesize Pd@Fe_xO heterodimer NPs with a spherical Pd component (5 nm) and faceted iron oxide domains (25 nm). Starting from an iron(III) oleate precursor we were able to obtain anisotropic iron oxide domains constituted of a $\approx$ 50/50 maghemite/magnetite with 65 emu/g saturation magnetization at 300 K. The Pd@Fe_xO heterodimer NPs were surface-functionalized to achieve a better dispersibility in polar organic media to perform catalysis. With a proper choice of reactants and by exploring the individual properties of both domains of the heterodimer NPs, we synthesized a template-free, hydrophobic, macroporous, and magnetic foam that could be used for a reversible adsorption of nonpolar liquids. Such magnetically triggered hydrophobic foams could be a potential adsorbent for oil sampling in oil wells or for separating oil from water.

4.5 Experimental Section

Materials

Palladium(II) acetylacetonate ($Pd(acac)_2$, Acros Organics), oleylamine (OAm, Acros Organics, 80-90%,), 1-octadecene (ODE, Acros Organics, 90%), oleic acid (OAc, Fisher Scientific, Reagent Grade), tri-n-octylphosphine (TOP, abcr, 97%), iron(III)-chloride hexahydrate ($FeCl_3{\cdot}6H_2O$, Chem Pur, 99+%), sodium oleate ($C_{18}H_{33}O_2Na$, Sigma-Aldrich, > 82% fatty acids (as oleic acid) basis, powder), nitrosonium tetrafluoroborate ($NOBF_4$, Acros Organics, 97%), poly(dimethylsiloxane) (Sigma-Aldrich, vinyl terminated, $M_w \approx 25000$), tetravinylsilane (abcr, 95%), poly(methylhydrosiloxane) (Sigma-Aldrich, trimethylsilyl terminated, $M_n \approx$ 1700-3200), cyclohexane (Fisher Scientific, Analytical Reagent Grade), ethanol (Aldrich, *p.a.*, > 99.8%), hexane (Fisher Scientific, Analytical Reagent Grade), methanol (Fisher Scientific, Analytical Reagent Grade), dimethylformamide (DMF, Sigma-Aldrich, 99.8%), dichloromethane (CH_2Cl_2, Sigma-Aldrich, *p.a.*, > 99.9%) and toluene (Sigma-Aldrich, *p.a.*, > 99.7%) were used in this work.

Synthesis of Pd Seed Nanoparticles

The synthesis of the Pd seed NPs was adapted from Kim *et al.*[331] In a 100 mL three-neck round bottom flask, 100 mg of $Pd(acac)_2$ were dissolved in 1 mL of tri-n-octylphosphine under inert gas (Ar) conditions and stirred for 10 min. Subsequently, 10 mL of oleylamine were added. The mixture was heated to 250 °C at a rate of 2 °C/min and held at this temperature for 30 min. Afterwards, the mixture was cooled slowly to room temperature (RT). A black product was precipitated from the mixture by adding 15 mL of ethanol. The precipitate was separated by centrifugation (9000 rpm, 10 min, RT), dispersed in cyclohexane and washed twice by adding ethanol (cyclohexane:ethanol = 1:2), followed by centrifugation (9000 rpm, 10 min, RT). Finally, the product was dispersed in cyclohexane, flushed with Ar, and stored at RT.

Synthesis of Iron(III) Oleate

For the synthesis of the iron(III) oleate as the precursor, 40 mmol of iron(III)chloride hexahydrate and 120 mmol of sodium oleate were dissolved in 80 mL of ethanol, 60 mL of Milli-Q water and 140 mL of hexane followed by heating at 70 °C for 4 h as adapted from Park *et al.*[395] Afterwards the organic phase was separated using a separating funnel and washed once with a 1:1 Milli-Q water:methanol solution. The solvent was removed using a rotary evaporator, and the residue was dried under Schlenk line conditions at 10^{-3} mbar for 24 h at RT and for 24 h at 100 °C.

Synthesis of Pd@Fe$_x$O Nanoparticles

The Pd@Fe$_x$O heterodimer NPs were synthesized by dissolving 900 mg (1 mmol) of the iron(III) oleate complex in 4 mL of 1-octadecene in a 100 mL three-neck round bottom flask under inert gas (Ar) conditions. Subsequently, 160 µL (0.5 mmol) of oleic acid and 160 µL (0.5 mmol) of oleylamine were added. After 10 min of stirring at RT, 10 mg of the prepared 5-7 nm Pd seed NPs dispersed in 1 mL of 1-octadecene were added to the reaction solution. The mixture was heated to 110 °C at a rate of 2 °C/min and held at this temperature for 20 min. The heating proceeded to 310 °C with 2 °C/min and kept for 30 min. Afterwards, the mixture was slowly cooled to RT. A black product was precipitated from the mixture by adding 15 mL of ethanol. The precipitate was separated by centrifugation (9000 rpm, 10 min, RT), dispersed in cyclohexane and washed twice by adding ethanol (cyclohexane:ethanol = 1:2) and centrifugation (9000 rpm, 10 min, RT). Finally, the product was dispersed in cyclohexane, flushed with Ar and stored at RT. The iron oxide NPs without Pd domains (Fe$_x$O NPs) were synthesized according to the heterodimer NPs without Pd seed particles.

Surface Functionalization of Pd@Fe$_x$O Nanoparticles

The hydrophilic surface functionalization of the as-synthesized Pd@Fe$_x$O heterodimer NPs was adapted from Dong *et al.*[450] First, 5 mL of a 1 mg/mL dispersion of the Pd@Fe$_x$O heterodimer NPs in hexane and a solution of $NOBF_4$ (5.8 mg, 0.01 M) in 5 mL of dichloromethane was prepared. For better solubility of $NOBF_4$, 2 mL of DMF were added. Both solutions were combined, and the resulting mixture was slowly shaken for 10 min at RT. The mixture was then centrifuged (9000 rpm, 10 min, RT) to precipitate the NPs. The precipitate was re-dispersed in DMF and washed twice by adding toluene and cyclohexane (DMF:toluene:cyclohexane = 1:2:2), followed by one additional centrifugation (9000 rpm, 10 min, RT). Finally, the product was redispersed in DMF and stored at 8 °C.

Preparation of Hydrophobic and Magnetic NP Foam Structure by Hydrosilylation

A 1 mg/mL dispersion of the hydrophilic functionalized Pd@Fe$_x$O NPs in DMF and a second solution containing 250 mg of tetravinylsilane, 440 mg of poly(methylhydrosiloxane) and 100 mg of vinyl-terminated poly(dimethylsiloxane) (equivalent to an 1:4:1 molar ratio with respect to the functional groups) were prepared. A total of 0.5 mL of the NP dispersion was added to the prepared silane/siloxane solution and the reaction mixture was placed in an oven at 80 °C for 96 h. Afterwards the resulting NP foam residue was washed with cyclohexane and dried at 100 °C for 30 min.

Nanoparticle Characterization

Samples for *transmission electron microscopy (TEM)* were prepared by placing a drop of dilute NP dispersion in cyclohexane on a carbon coated copper grid. TEM images for characterization of the size and morphology and the surface rendering 3D tomography were obtained using a FEI Tecnai 12 microscope equipped with a LaB_6 source at 120 kV and a twin-objective together with a Gatan US1000 CCD-camera (2K x 2K pixels). High-resolution TEM, scanning TEM and energy-dispersive X-ray (EDX) data were obtained on a FEI Tecnai F30 S-TWIN TEM equipped with a field emission gun and operated at 300 kV. Atomic modeling and electron diffraction (ED) simulation were performed by Crystal Maker software.

X-ray diffraction patterns (XRD) were recorded on a Bruker AXS D8 Advance diffractometer equipped with a SolX energy dispersive detector in reflection mode using unfiltered Mo Kα radiation. Crystalline phases were identified according to the PDF-2 database using Bruker AXS EVA 10.0 software. Full profile fits (Le Bail/Pawley/Rietveld) were performed with TOPAS Academic 4.1 by applying the fundamental parameter approach.[347, 348]

^{57}Fe-Mössbauer spectra of powdered samples were recorded in transmission geometry with a ^{57}Co source embedded in a rhodium matrix using a conventional constant-acceleration Mössbauer spectrometer equipped with a helium cryostat at 5.5 K. Isomer shifts are given with respect to iron metal at ambient temperature. Simulations of the experimental data were performed with the Recoil software.[349]

Magnetic susceptibility measurements were performed on a Quantum Design MPMS-XL superconducting quantum interference device (SQUID) magnetometer. Field-cooled (FC) and zero-field-cooled (ZFC) data were obtained in a temperature range between 5 and 300 K at 100 Oe. Hysteresis measurements were performed at 5 and 300 K.

Fourier transform (FT)-IR spectroscopy was carried out on a Thermo Scientific Nicolet iS10 FT-IR Smart iTR infrared spectroscope equipped with a Platinum-ATR (diamond crystal, one reflection) and OMNIC 8.1.210 software.

Thermogravimetric analysis (TGA) was performed on a Perkin Elmer Pyris 6 TGA instrument under nitrogen atmosphere (5 mL/min). The heat program was (i) 20 min at 30 °C and (ii) at a ramp-up of 10 °C/min from 30 to 600 °C.

4.6 Appendix

Table 4.1: Additional data to the thermogravimetric analysis. T_i, T_m and T_f describing the starting temperature, temperature at maximum slope and ending temperature of a clear weight loss step, respectively. T_M marks midpoint temperature between two clear weight loss steps, where weight is not constant. DTG temperature extracted from Figure 4.6a and TGA temperature extracted from Figure 4.6b.

	Temperature DTG	Temperature TGA	Mass TGA	Weight Loss
	°C	°C	%	%
T_{i1}	254	196	99	19
T_{m1}		233	89	
T_{f1}		267	80	
T_{M1}	302	301	74	12
T_{i2}	353	331	68	24
T_{m2}		353	56	
T_{f2}		374	44	
T_{M2}	401	400	39	11
T_{i3}	444	424	33	13
T_{m3}		449	26	
T_{f3}		468	20	

Table 4.2: Additional data to the Rietveld refinement of powder XRD data. Measurement conditions: $5 \leq 2\Theta/^\circ \leq 41.4$; $\Delta\Theta = 0.0065^\circ$; $\Delta t = 5.14$ sec.

		Pd@Fe$_x$O NPs
Pd-Phase		
Cell parameter	*Å*	3.853(2) (lit.[381] 3.879)
Crystallite size	nm	3.5(1)
Fraction	%wt	3.4(2)
γ-Fe$_2$O$_3$-Phase		
Cell parameter	*Å*	8.370(1) (lit.[381] 8.352)
Crystallite size	nm	16.6(1)
Fraction	%wt	60(3)
Fe$_3$O$_4$-Phase		
Cell parameter	*Å*	8.391(2) (lit.[381] 8.397)
Crystallite size	nm	16.6(1)
Fraction	%wt	37(3)
R_{wp}		10.63
Goodness of fit (G)		1.78
Number of parameter/background		15/2

Table 4.3: Additional data to the SQUID magnetic measurements.

			Pd@Fe_xO NPs	**Fe_xO NPs**
	Blocking temperature	K	295	210
	At mass magnetization	emu/g	10.3	10.7
5 K	Saturation magnetization at 50 kOe	emu/g	72	60
	Remanence	emu/g	18	10
	Coercivity	Oe	-250	-109
300 K	Saturation magnetization at 50 kOe	emu/g	65	55

Table 4.4: Additional data to the Mössbauer measurements.

Chemical shift	Quadrupole shift	Magnetic field	Fraction	Substance
mm/s	mm/s	kOe	%	
Pd@Fe$_x$O NPs 293 K				
0.32(1)	0	481(1)	60(3)	Fe^{3+}; Magnetite and Maghemite
0.58(1)	0	442(1)	40(3)	Fe^{2+} and Fe^{3+}; Magnetite
Pd@Fe$_x$O NPs 5.5 K				
0.32(1)	0	513(1)	37(1)	Fe^{3+}; Magnetite
0.54(1)	0	523(1)	44(1)	Fe^{3+}; Maghemite
0.86(2)	0	467(2)	19(1)	Fe^{2+}; Magnetite
Fe$_x$O NPs 5.5 K				
0.36(1)	0	501(1)	41(1)	Fe^{3+}; Magnetite
0.52(1)	0	519(1)	37(1)	Fe^{3+}; Maghemite
0.81(3)	0	472(4)	22(1)	Fe^{2+}; Magnetite

5

Enhanced Peroxidase Activity of Pd@Fe$_x$O Heterodimer Nanoparticles

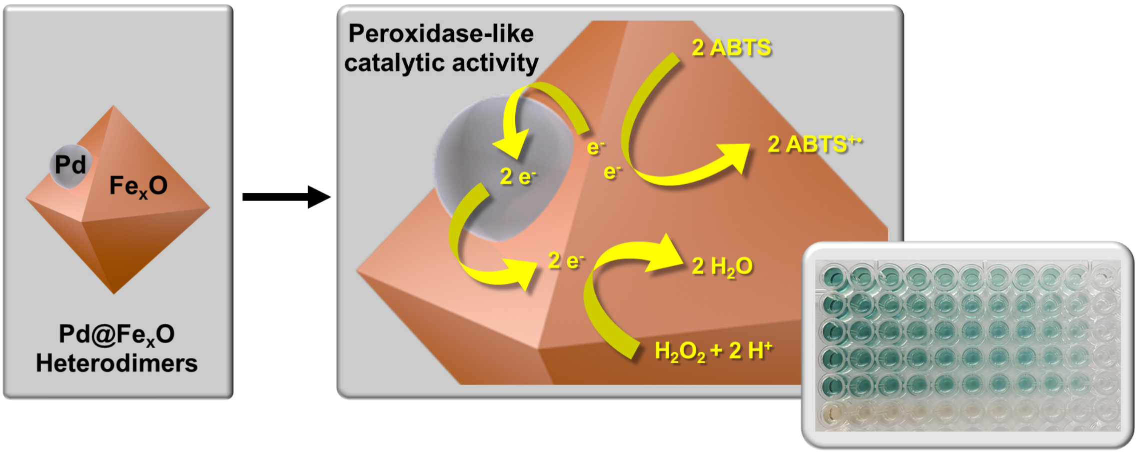

This chapter accommodates a second catalytic application for the Pd@Fe$_x$O NPs which were presented in Chapter 4. Special thanks goes to [redacted] *for assisting in performing the colorimetric assay measurements during her bachelor thesis research.*[351]

5.1 Abstract

The Pd@Fe_xO NPs, introduced in Chapter 4, were used in a colorimetric assay to evaluate their peroxidase-like activity compared to single Fe_xO NPs and single Pd NPs using ABTS as substrate. The main focus was to answer the question whether heteroparticles show enhanced catalytic activity compared to the single material NPs due to (i) electron transport across the metal-metal oxide interface and (ii) the increased surface area. It was found that the Pd@Fe_xO heterodimer NPs displayed higher kinetic parameters (v_{max} and k_{cat}) compared to single Fe_xO NPs demonstrating a synergistic effect, charge separation and resulting electron transfer through the Pd domain and the iron oxide domain. Additionally, a comparison of the kinetic parameters with those obtained for the Pd@γ-Fe_2O_3 superparticles presented in Chapter 2 was carried out. The concentration of surface available Fe-atoms of Pd@Fe_xO heterodimer NPs is approximately 2.5 times higher compared to the Pd@γ-Fe_2O_3 superparticles. Interestingly, the superparticles show the better catalytic performance, additionally supported by the lower amount of superparticles necessary to obtain this performance. The open structure with multiple nanorods available for a catalysis is probably more favorable for the substrate. This is also reflected in a higher atomic absorption spectroscopy (AAS) correction factor for the Pd@γ-Fe_2O_3 superparticles, representing more surface available Fe-atoms per single NP.

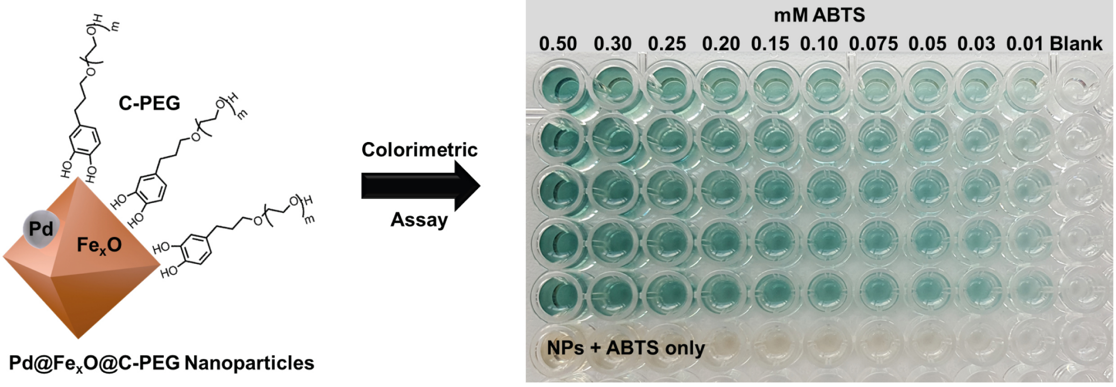

Figure 5.1: Water dispersable catechol-PEG (C-PEG) functionalized Pd@Fe$_x$O NPs were used in a colorimetric assay to reduce H_2O_2 to H_2O while oxidizing ABTS to the green ABTS$^{+\cdot}$ radical. Variation of the ABTS concentration from 0.50 mM to 0.01 mM using 8 µg/mL NPs and 0.5 mM H_2O_2 is shown.

5.2 Results and Discussion

Following up the enhanced peroxidase-like catalytic activity demonstrated for the Pd@γ-Fe_2O_3 superparticles in Chapter 2, the Pd@Fe$_x$O heterodimer NPs presented in Chapter 4 were also analyzed for their peroxidase-like catalytic activity due to the similar chemical composition, but different morphology.

The elevated amount of catalytically active metal atoms in the appropriate oxidation states at the surface of oxide particles compared to metalloproteins enables the possibility of improved catalytic reaction rates. This accounts most for small molecules with little space demand, as demonstrated here for the oxidation of 2,2’-azinobis(3-ethylbenzothiazoline-6-sulfonic acid) (ABTS) with H_2O_2 (Figure 5.1). In focus is the question whether heteroparticles show enhanced catalytic activity compared to single material NPs due to (i) electron transport across the metal-metal oxide interface and (ii) the increased surface area due to the anisotropic morphology. By comparing Pd@γ-Fe_2O_3 superparticles and Pd@Fe$_x$O heterodimer NPs, especially the latter point is addressed in this study.

To disperse the Pd@Fe$_x$O NPs in water, the NPs were surface-functionalized with a catechol-PEG polymer as shown in Figure 5.1.[92, 114] The peroxidase-like activity was investigated by a colorimetric assay based on the catalytic oxidation of ABTS with H_2O_2, which leads to the formation of an ABTS$^{+\cdot}$ radical absorbing at 405 nm and yielding a green solution.[333] In the first step, the concentration of the Pd@Fe$_x$O NPs was varied. An increase of the NP concentration from 1.25 to 12.5 µg/mL showed a linear trend with higher reaction rates as a result of the increasing NP concentrations (Figure 5.2a). With an optimized NP concentration of 8 µg/mL the concentration of the ABTS substrate was varied from 0.01 to 0.5 mM, where a Michaelis-Menten-like saturation curve was found, typically observed for enzyme reactions (Figure 5.2b). Next, the data points were fitted to the Michaelis-Menten equation to yield the maximal reaction rate (v_{max}) and Michaelis-Menten substrate binding constant

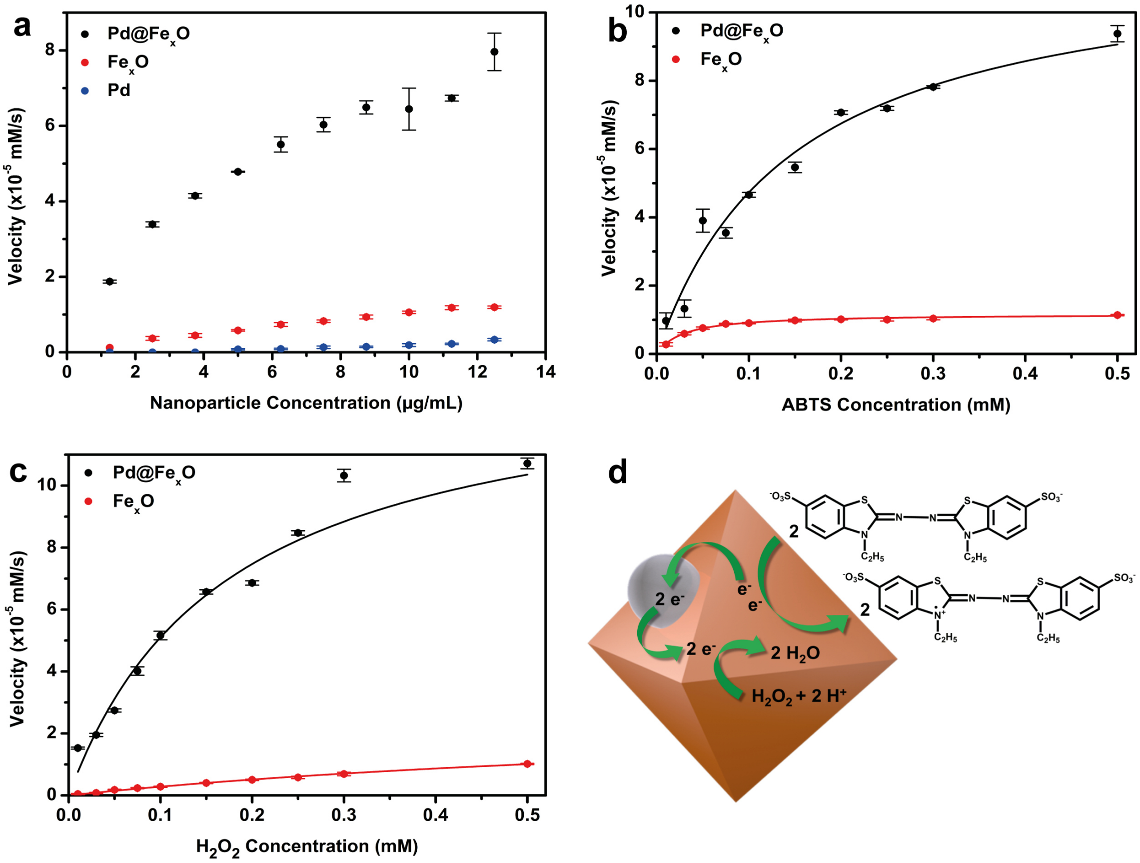

Figure 5.2: Peroxidase-like activity of Pd@Fe$_x$O NPs compared to Fe$_x$O NPs and Pd NPs. (a) Variation of the NP concentration using 0.2 mM ABTS and 0.5 mM H_2O_2 showing linear behavior for Pd@Fe$_x$O NPs, Fe$_x$O NPs and Pd NPs. (b) Variation of the ABTS concentration using 8 µg/mL Pd@Fe$_x$O NPs / 10 µg/mL Fe$_x$O NPs and 0.5 mM H_2O_2 showing Michaelis-Menten-like behavior. (c) Variation of the H_2O_2 concentration using 8 µg/mL Pd@Fe$_x$O NPs / 10 µg/mL Fe$_x$O NPs and 0.3 mM ABTS for Pd@Fe$_x$O NPs / 0.2 mM ABTS for Fe$_x$O NPs showing Michaelis-Menten-like behavior. (d) Schematic representation of the synergistic effect of electron transport through the Pd-Fe$_x$O interface. All experiments were performed in a 0.3 mL reaction volume at 37 °C in acetic acid buffer at pH 3.66. Parts of the kinetic measurements were performed by B.Sc. Mareike Deuker.[351]

(k_m) as kinetic parameters. The higher Michaelis-Menten constant of 0.148 mM compared to 0.049 mM for the Pd@γ-Fe_2O_3 superparticles, indicates a reduced affinity of the substrate for the catalyst and a comparable maximal reaction rate of 1.17 x 10^{-7} Ms^{-1} (Table 5.1, 1.02 x 10^{-7} Ms^{-1} for the Pd@γ-Fe_2O_3 superparticles) is significantly higher than that for natural horseradish peroxidase (HRP).[334–338] For calculating the catalytic constant k_{cat}, defined as the maximal catalytic turnover per active catalytic site per second, the number of active sites had to be evaluated.[339] A surface:volume ratio for the iron atoms was calculated similarly as presented in Chapter 2 through a calibration factor that allowed conversion of the total molar iron concentration (determined by AAS) to the surface iron concentration. Hence,

Table 5.1: Calculated kinetic parameters. [NP] is the NP concentration. k_m is the Michaelis-Menten constant. v_{max} is the maximal reaction rate. k_{cat} is the catalytic constant given by $k_{cat} = v_{max}/[NP]$.

	[NP] (M)	substrate	k_m (mM)	v_{max} (Ms^{-1})	k_{cat} (s^{-1})
Pd@Fe$_x$O NPs	3.35 x 10^{-6}	ABTS	0.148	1.17 x 10^{-7}	0.035
Pd@Fe$_x$O NPs	3.35 x 10^{-6}	H_2O_2	0.173	1.39 x 10^{-7}	0.041
Fe$_x$O NPs	5.25 x 10^{-6}	ABTS	0.028	1.17 x 10^{-8}	0.002
Fe$_x$O NPs	5.25 x 10^{-6}	H_2O_2	0.910	2.84 x 10^{-8}	0.005

the Pd@Fe$_x$O NPs were modeled, considering the octahedral morphology with an average edge length of 25 nm (obtained as average dimensions and morphology from TEM images). The facets of an octahedron are defined by {111} planes.[20] Accordingly, the number of Fe atoms present on the (111) surface of the unit cell of an inverse spinel structure was calculated and related to the total number of surface atoms of the octahedron (yielding approximately 6700 Fe surface atoms per NP).[321] From the ratio of the octahedron volume and the volume of the maghemite unit cell, the total number of Fe-atoms (approximately 289000) within the volume of a single Pd@Fe$_x$O NP was approximated.[340] The ratio of 6700 surface Fe atoms to 289000 Fe atoms in a single Pd@Fe$_x$O NP was used as a calibration factor (0.0234) to derive the number of active Fe surface sites in a sample from the total Fe concentration (determined by AAS). Eventually, turnover values (k_{cat}) of 0.035 s^{-1} (ABTS) and 0.041 s^{-1} (H_2O_2) were calculated (Table 5.1), which are lower than those reported for the Pd@γ-Fe_2O_3 superparticles (0.075 s^{-1} (ABTS) and 0.094 s^{-1} (H_2O_2)). This demonstrates the importance of the NP morphology. The concentration of surface available Fe-atoms of Pd@Fe$_x$O heterodimer NPs is approximately 2.5 times higher compared to the Pd@γ-Fe_2O_3 superparticles (1.35 x 10^{-6} M). Accordingly, the superparticles show the better catalytic performance. The amount of NPs necessary to obtain these values was significantly higher for the heterodimer NPs compared to the superparticles (8 μg/mL to 1.8 μg/mL) being one of the reasons for the higher concentration of surface available Fe-atoms. The open structure with multiple nanorods available for a catalysis is probably more accessible for the substrate which is also reflected in the higher correction factor of 0.0420 for the Pd@γ-Fe_2O_3 superparticles, representing more surface available Fe-atoms per single NP. In contrast, Pd@Fe$_x$O NPs demonstrate less surface available Fe-atoms per single NP (0.00234) and a higher NP concentration of 8 μg/mL.

Finally, the H_2O_2 concentration was varied from 0.01 to 0.5 mM, resulting in similar v_{max} and k_{cat} values (Figure 5.2c). The lower affinity of H_2O_2 for the particles compared to that of ABTS was also found for the Pd@γ-Fe_2O_3 superparticles and may be caused by the weakened Coulomb interaction between the superparticles and H_2O_2 leading to higher k_m values (Table 5.1).

Like for the Pd@γ-Fe_2O_3 superparticles, the catalytic activity of the heterodimer NPs compared to their single material counterparts (*i.e.* Pd and iron oxide NPs) was evaluated (Table 5.1). For the Fe_xO NPs, the correction factor obtained a slightly higher value of 0.0293 compared to the heterodimer NPs resulting in a higher NP concentration of 5.25 x 10^{-6} M considering 10 μg/mL NP concentration in the assay. However, all kinetic parameters are lower. For the Pd NPs only a variation of the NP concentration could be carried out (Figure 5.2a) due to the negligible activity being in the error range of the measurement. This unveils the synergistic effect between the Pd domain and the iron oxide domain which we attribute to a charge separation and the resulting electron transfer through the Pd domain and the iron oxide domain (Figure 5.2d).[40, 44, 45, 58, 289, 345]

5.3 Conclusion

It was demonstrated that Pd@Fe_xO heterodimer NPs show enhanced peroxidase-like activity compared to their single material NPs (*i.e.* Pd and iron oxide NPs) due to (i) electron transport across the metal-metal oxide interface and (ii) the increased surface area. The former statement could be addressed by a colorimetric assay based on the catalytic oxidation of ABTS with H_2O_2, which leads to the formation of an $ABTS^{+\cdot}$ radical yielding a green solution. The Pd@Fe_xO heterodimer NPs obtained higher kinetic parameters (v_{max} and k_{cat}) compared to single Fe_xO NPs demonstrating a synergistic effect, charge separation and resulting electron transfer through the Pd domain and the iron oxide domain. The latter statement could be addressed by a comparison of the kinetic parameters with those obtained for the Pd@γ-Fe_2O_3 superparticles presented in Chapter 2. The concentration of surface available Fe-atoms for the Pd@Fe_xO heterodimer NPs is approximately 2.5 times higher compared to the Pd@γ-Fe_2O_3 superparticles, while v_{max} is comparable. Accordingly, the superparticles show the better catalytic performance, additionally supported by the lower amount of superparticles necessary to obtain these values. The open structure of the superparticles with multiple nanorods available for a catalysis is probably more favorable for the substrate which is also reflected in a higher AAS correction factor for the Pd@γ-Fe_2O_3 superparticles compared to the Pd@Fe_xO heterodimer NPs, representing more surface available Fe-atoms per individual NP.

5.4 Experimental Section

Materials

O-[2-(3-mercaptopropionylamino)ethyl]-O-methylpolyethyleneglycol (S-PEG, Sigma-Aldrich, 5000), chloroform (Aldrich, 99-99.4%), hexane (Fisher Scientific, Analytical Reagent Grade), hydrogen peroxide (H_2O_2, Aldrich, $\geq$ 34%) and 2,2'-azinobis(3-ethyl-benzothiazoline-6-sulfonic acid) diammonium salt (ABTS, Aldrich, $\geq$ 98%) were used in this work.

Surface Functionalization of Pd Nanoparticles with S-PEG

A 1 mg/mL solution of Pd NPs dispersed in chloroform was mixed with a 1 mg/mL solution of S-PEG in chloroform. The reaction mixture was stirred with a mechanical stirrer for 6 h at 40 °C under a gentle Ar flow. 6 mL of hexane per milligram of NPs was added, and the NPs were extracted into 1 mL of Milli-Q water per milligram of NPs using a separating funnel.

Surface Functionalization of Pd@Fe$_x$O and Fe$_x$O Nanoparticles with C-PEG

The catechol-PEG polymer (C-PEG$_{120}$, M_n = 4020 g/mol, PDI = 1.09, from SEC (DMF, RI signal, PEG standard)) was synthesized as described elsewhere.[92, 114] A 1 mg/mL solution of the Pd@Fe$_x$O NPs or Fe$_x$O NPs was dispersed in chloroform and was mixed with a 1 mg/mL solution of C-PEG in chloroform. The reaction mixture was stirred with a mechanical stirrer for 6 h at 40 °C under a gentle Ar flow. 6 mL hexane per mg particles was added and the particles were extracted into 1 mL of Milli-Q water per mg particles using a separating funnel.

Kinetic Analysis

Steady-state kinetic measurements of the catalytic oxidation of ABTS were performed on a Tecan Infinite M Pro 200 Plate Reader equipped with a UV Xenon Flash lamp. 300 µL Greiner UV-Star transparent 96 well plates were used to monitor the absorbance of the oxidized ABTS radical at 405 nm and 37 °C in an acetic acid buffer solution with a pH of 3.66.[333] The NP concentrations (Pd@Fe$_x$O NPs, Fe$_x$O NPs, Pd NPs) were varied using 0.2 amM ABTS and 0.5 mM H_2O_2. For the variation of ABTS, 8 µg/mL Pd@Fe$_x$O NPs / 10 µg/mL Fe$_x$O NPs with 0.5 mM H_2O_2 and for the variation of H_2O_2, 8 µg/mL Pd@Fe$_x$O NPs / 10 µg/mL Fe$_x$O NPs with 0.3 mM ABTS for Pd@Fe$_x$O NPs / 0.2 mM ABTS for Fe$_x$O NPs were used. All experiments were performed in a 0.3 mL reaction volume. The initial rate values were adjusted to the Michaelis-Menten model by applying the Michaelis-Menten equation. Calculated kinetic parameters were k_m (Michaelis-Menten constant), v_{max} (maximal reaction rate) and k_{cat} (catalytic constant given by $k_{cat} = v_{max}/[NP]$).

The molar NP concentration ([NP]) was calculated according to a model (details *vide infra*) that accounts for the number of available catalytically active Fe surface sites. In a first step, Pd@Fe$_x$O NPs, with an average edge length of 25 nm were approximated by an octahedron. The octahedron has a (111) side surface. Accordingly, 1.875 Fe-atoms were assumed to be present on the (111) surface of a unit cell of an inverse spinel structure. The total (111) surface area of the approximated octahedron contains approximately 6754 Fe-atoms (representing the surface of a single Pd@Fe$_x$O NP).[321] In the next step, the ratio of the octahedron volume to the volume of the maghemite unit cell was calculated and multiplied by the total amount of approximately 22.65 Fe-atoms present in a single maghemite unit cell, which corresponds to approximately 288652 Fe-atoms within the volume of a single Pd@Fe$_x$O NP.[340] The ratio of 6754 surface Fe-atoms to 288652 Fe-atoms in a single Pd@Fe$_x$O NP was used as a calibration factor of 0.0234 to convert the total Fe concentration determined by atomic absorption spectroscopy (AAS) to the number of active Fe surface sites. On the basis of this approach, an iron concentration of 3.35 x 10^{-6} M was calculated for evaluating k_{cat}.

An analogous calculation for the Fe$_x$O NPs resulted in an NP concentration of 5.25 x 10^{-6} M.

Calculation of Fe-atoms Surface to Volume Ratio

The molar NP concentration ([NP]) for the Pd@Fe$_x$O NPs and Fe$_x$O NPs was calculated according to a model that accounts for the number of available catalytically active Fe surface sites.

Pd@Fe$_x$O Nanoparticles

To perform a model calculating, yielding a ratio of Fe-atoms present at the surface of the Pd@Fe$_x$O NPs to the total amount of Fe-atoms in the Pd@Fe$_x$O NPs, an average edge length (l) of the NPs was measured using transmission electron microscopy data:

$$\mathrm{l} = 25\,\mathrm{nm} \tag{5.1}$$

In the next step the Pd@Fe$_x$O NPs were modeled by an octahedron having a total volume ($\mathrm{V_O}$) and surface ($\mathrm{S_O}$) of:

$$\mathrm{V_O} = \frac{\mathrm{l}^3}{3} \times \sqrt{2} \tag{5.2}$$

$$\mathrm{S_O} = 2 \times \mathrm{l}^2 \times \sqrt{3} \tag{5.3}$$

This leads to the total octahedron volume and surface values of:

$$\mathrm{V_O} = 7366\,\mathrm{nm}^3 \tag{5.4}$$

$$\mathrm{S_O} = 2165\,\mathrm{nm}^2 \tag{5.5}$$

Next, the surface of a cubic maghemite (111) plane ($\mathrm{S_{(111)}}$) and the volume of one unit cell ($\mathrm{V_{UC}}$) is calculated using the lattice constant of a = 0.833 nm.[321]
With the (111) facet being an equilateral triangle in the cubic maghemite unit cell with face diagonal $\mathrm{d} = \mathrm{a}\sqrt{2}$, the value of $\mathrm{S_{(111)}}$ is calculated according to:

$$\mathrm{S_{(111)}} = \frac{1}{2} \times \mathrm{d} \times \frac{\mathrm{d} \times \sqrt{3}}{2} \tag{5.6}$$

$$\mathrm{S_{(111)}} = 0.601\,\mathrm{nm}^2 \tag{5.7}$$

And $\mathrm{V_{UC}}$ is:

$$\mathrm{V_{UC}} = \mathrm{a}^3 = 0.578\,\mathrm{nm}^3 \tag{5.8}$$

Now an amount of unit cells present on the surface of one Pd@Fe$_x$O NP can be calculated according to:

$$\frac{\mathrm{S_O}}{\mathrm{S_{(111)}}} = \frac{2165\,\mathrm{nm}^2}{0.601\,\mathrm{nm}^2} = 3602 \tag{5.9}$$

This value can be multiplied by 1.875 Fe-atoms per unit cell which are present on the (111) plane (3x1/2 + 3x1/8) to give a total amount of 6754 Fe-atoms at the surface of a Pd@Fe$_x$O NP.[340] Further, the quantity of unit cells present in one Pd@Fe$_x$O NP can be calculated similarly:

$$\frac{\mathrm{V_O}}{\mathrm{V_{UC}}} = \frac{7366\,\mathrm{nm}^3}{0.578\,\mathrm{nm}^3} = 12744 \tag{5.10}$$

According to the 50% magnetite (Fe_3O_4) and 50% maghemite (Fe_2O_3) mixture present in the Pd@Fe$_x$O NPs one needs to take into account the different amounts of Fe-atoms in the unit cells.[374] One unit cell of magnetite contains 24 Fe-atoms and one unit cell of maghemite contains 21.3 Fe-atoms. This leads to 22.65 Fe-atoms in one unit cell for a 50/50 magnetite/maghemite mixture, resulting in 288652 Fe-atoms in one Pd@Fe$_x$O NP. Finally an iron surface to volume ratio can be calculated, which can be used as a correction factor for the Fe-concentration determined by AAS:

$$\frac{\mathrm{S_{Fe}}}{\mathrm{V_{Fe}}} = \frac{6754}{288652} = 0.0234 \tag{5.11}$$

Eventually a Pd@Fe$_x$O NP concentration can be calculated:

$$[\mathrm{NP}] = 3.35 \times 10^{-6}\,\frac{\mathrm{mol}}{\mathrm{L}} \tag{5.12}$$

$\mathrm{Fe_xO}$ Nanoparticles

The concentration of the $\mathrm{Fe_xO}$ NPs was calculated accordingly, leading to the following values:

$$\mathrm{l} = 20\,\mathrm{nm} \tag{5.13}$$

$$\mathrm{V_O} = 3771\,\mathrm{nm}^3 \tag{5.14}$$

$$\mathrm{S_O} = 1386\,\mathrm{nm}^2 \tag{5.15}$$

$$\frac{\mathrm{S_O}}{\mathrm{S_{(111)}}} = \frac{1386\,\mathrm{nm}^2}{0.601\,\mathrm{nm}^2} = 2306 \tag{5.16}$$

$$\frac{\mathrm{V_O}}{\mathrm{V_{UC}}} = \frac{3771\,\mathrm{nm}^3}{0.578\,\mathrm{nm}^3} = 6524 \tag{5.17}$$

$$\frac{\mathrm{S_{Fe}}}{\mathrm{V_{Fe}}} = \frac{2306 \times 1.875}{6524 \times 22.65} = \frac{4324}{147769} = 0.0293 \tag{5.18}$$

$$[\mathrm{NP}] = 5.25 \times 10^{\text{-}6}\,\frac{\mathrm{mol}}{\mathrm{L}} \tag{5.19}$$

6

Synthesis of ZnO Nanoparticles and their Biomedical Application

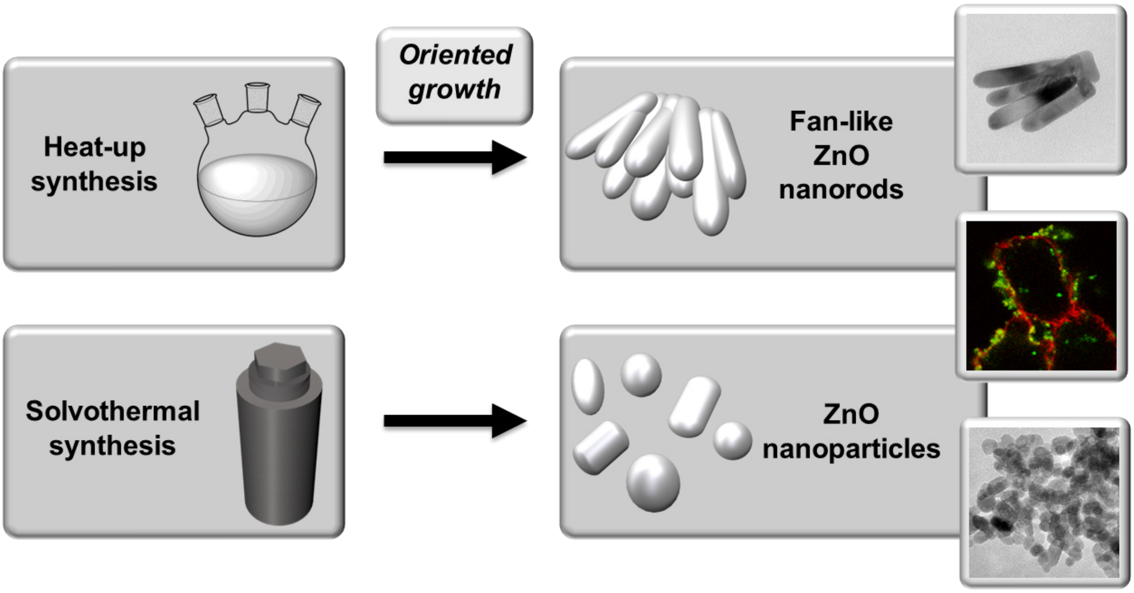

The biochemical cell experiments and the evaluation of the related data presented in this chapter were performed by M.Sc. Nadine Wiesmann, group of Prof. Dr. Jürgen Brieger, Molecular Tumorbiology, Department of Otorhinolaryngology, Head and Neck Surgery, University Medical Center Mainz as part of an interdisciplinary Max Planck Graduate Center (MPGC) cooperation. Moreover, I like to thank [redacted] *for her tremendous work in the field of zinc oxide nanoparticle synthesis accomplished during her bachelor thesis research.*[451] *Special thanks also goes to* [redacted] *of the electron microscopy facility for performing the high resolution transmission electron microscopy experiments and analysis.*

6.1 Abstract

ZnO, as a prominent group II-VI semiconductor, is widely used as additive in paints, ingredient in pharmaceutical products, UV blocker in sunscreens or conducting material in sensors. However, the increased application of ZnO has raised the awareness of possible toxic effects on human health, especially in terms of ZnO NPs with their small size and higher reactivity. At this time, the interaction of ZnO NPs with living cells is only poorly understood. Toxic effects related with the generation of reactive oxygen species (ROS), DNA damage and inflammation have been reported. We present here the synthesis of two different ZnO NP types (heat-up and solvothermal) and their subsequent functionalization with silica and fluorescence dye for the evaluation of ZnO NP cell uptake and associated toxicity. ZnO@SiO$_2$@FITC NPs were taken up into various types of cancer cells. A silica coating of > 20 nm can furthermore retard the dissolution of ZnO and the ensuing toxic effects. In contrast, pure ZnO NPs showed low cell viability after the first 3 h of incubation with A549 cells. High ionic strength as well as the early availability of large amounts of Zn^{2+} ions are of minor importance for the toxic potential within the first few hours. The low cell viability might therefore be mainly caused by attachment of the NPs to the cells or by cell uptake, inhibiting or influencing important cell functions. The long term cytotoxicity (6-27 h) is then probably more determined by the amount, biochemical character and properties of the released Zn^{2+} ions.

6.2 Introduction

ZnO is a typical group II-VI semiconductor with a band gap of 3.4 eV.[452] In nature it is found as zincite mineral in hexagonal wurtzite structure with Mn or Fe ions leading to colors from yellow to red.[453] However pure ZnO appears colorless due to the large band gap. Typically for II-VI semiconductor materials tetrahedral coordination, characteristic for covalent sp^3 hybridized bonding, is obtained. This results in the crystallization in cubic zinc blende-type or hexagonal wurtzite-type structure.[452, 454] Because of the high ionic character of the Zn-O bond cubic rock salt structure with octahedral coordination can be obtained at high pressure. However, the most stable structure-type is the wurtzite structure with the zinc blende structure only available by epitaxial growth on a cubic substrate.[452, 454, 455] The high ionic strength of the covalent Zn-O bond also causes a dipole moment in the wurtzite structure resulting in Zn terminated (001) and O terminated (00-1) layers. With {001} exhibiting the highest surface energy, the formation of ZnO nanorods with minimized {001} facets is likely.[456]

Typical applications for ZnO range from ingredients in sunscreens as UV blocker due to the semiconducting properties and the accompanied UV-absorption to ingredients in pharmaceutical pastes due to antiseptic properties.[455, 457] Further applications include the use as a white pigment in paintings,[453] heterogeneous catalyst[455] or conducting oxide material in sensors or solar cells.[454, 455] Therefore, increased release of ZnO, especially as NPs with potential reception into the respiratory system, into the environment leads to an increasing interest of researches for the investigation of potential negative effects on human health.[458] Inherent properties of ZnO such as photocorrosion[459] and low tolerance towards acidic and basic solution[460] describe potential drawbacks causing increased contact with ZnO or Zn^{2+} ions. Toxic responses to ZnO NPs have been reported so far,[461] associated with both, toxicity though ZnO NPs as well as Zn^{2+} ion related toxicity.[462, 463] The cytotoxicity of ZnO NPs is attributed to their cell uptake with the subsequent generation of reactive oxygen species (ROS) in the mitochondria of affected cells with oxidation and destruction of important cellular structures (*e.g.* cellular membrane).[464–467] Additionally, DNA damages such as DNA double strand breaks have been observed.[468, 469] Further damaging includes the intracellular release of Ca^{2+}, mitochondrial depolarization, decrease of the intracellular glutathione (GSH) antioxidant through thiol binding of Zn^{2+}, lysosomal damage, inflammation or reduced ATP production.[465, 470–472] Modification of ZnO NPs with biocompatible silica coating[473, 474] and fluorescence dye functionalization[473, 475, 476] enables to expand the current knowledge in ZnO mediated toxicity. Several studies also demonstrated, that ZnO NPs can acquire anti-cancerous activity by exhibiting selective cytotoxicity to certain types of cancer cells.[477–479] Accordingly, functionalized ZnO NPs could be interesting as a new agent in cancer therapy.

We report here the heat-up synthesis of 40-130 nm fan-like ZnO nanorods in a high boiling organic solvent (1-octadecene) through concerted classical surfactant assisted nucleation, surface reconstruction and oriented attachment. The fan-like ZnO

nanorods were subsequently coated with a silica shell for the attachment of fluorescein dye in a reverse microemulsion reaction. The functionalized ZnO@SiO$_2$@FITC NPs were internalized into A549, FaDu, HNSCCUM-02T and RMPI cancer cells. The ZnO@SiO$_2$ NPs provided a gradual dissolution kinetics of ZnO which caused a retardation of the full cytotoxic potential of the ZnO NPs for a silica shell thickness exceeding 20 nm.
5-15 nm ZnO NPs from solvothermal synthesis were used to obtain deeper insight into the various aspects influencing the toxic potential of ZnO NPs because of their small size and ligand-free surface. These NPs showed low cell viability after the first 3 h of incubation with A549 cells. It was found that high ionic strength as well as the early availability of large amounts of Zn^{2+} ions are of reduced importance for the early toxic potential of the solvothermal ZnO NPs. The low cell viability after 3 h might therefore be mainly caused by the NPs, influencing or inhibiting important cell functions by their attachment to the cells or by cell uptake. Thus, long term cytotoxicity of 6-27 h is then probably more determined by the amount, biochemical character and properties of Zn^{2+}.

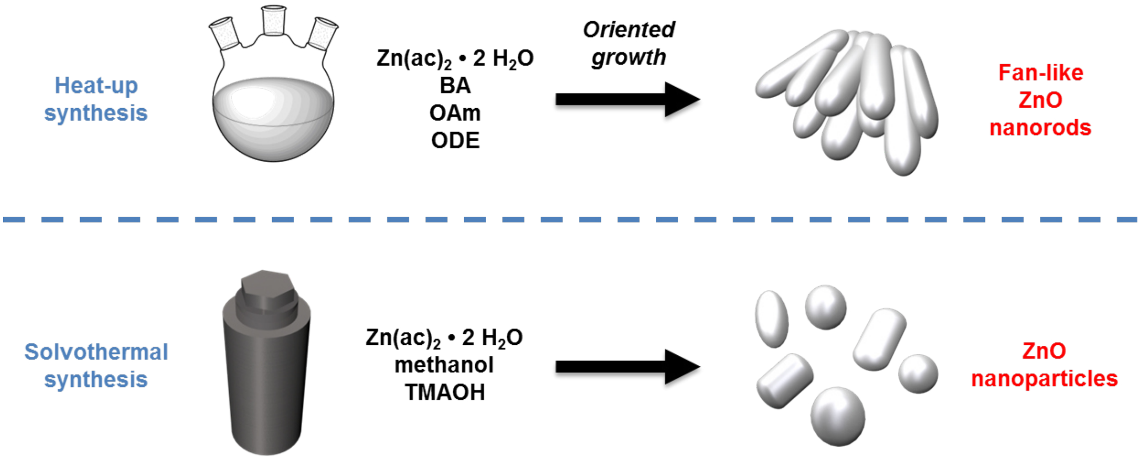

Figure 6.1: Schematic representation of the synthesis of ZnO NPs. Heat-up synthesis of fan-like ZnO nanorods and solvothermal synthesis of ZnO NPs in an autoclave reaction.

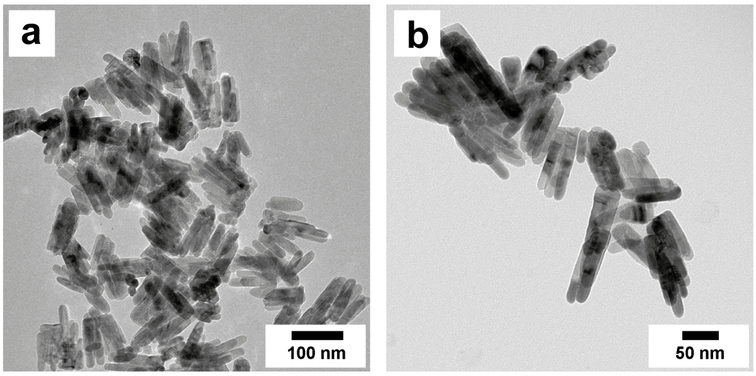

Figure 6.2: TEM images of fan-like ZnO NP bundles.

6.3 Results and Discussion

The synthesis of ZnO NPs with different morphology was carried out using two different reactions. In Figure 6.1 a schematic representation of the heat-up synthesis and solvothermal synthesis is presented. In both syntheses $Zn(ac)_2 \cdot 2\ H_2O$ is used as precursor. The heat-up synthesis was carried out in the high boiling organic solvent 1-octadecene (ODE) with oleylamine (OAm) as surfactant and benzyl alcohol (BA) for morphology control to yield fan-like ZnO nanorods. All reagents were heated to 230 °C to induce nucleation and growth. In contrast, the solvothermal synthesis is based on aqueous solvents. The Zn precursor was mixed with tetramethylammonium hydroxide (TMAOH) in methanol as solvent. Eventually, the reaction was carried out in a teflon-lined stainless steel autoclave and at 50 °C for 24 h.

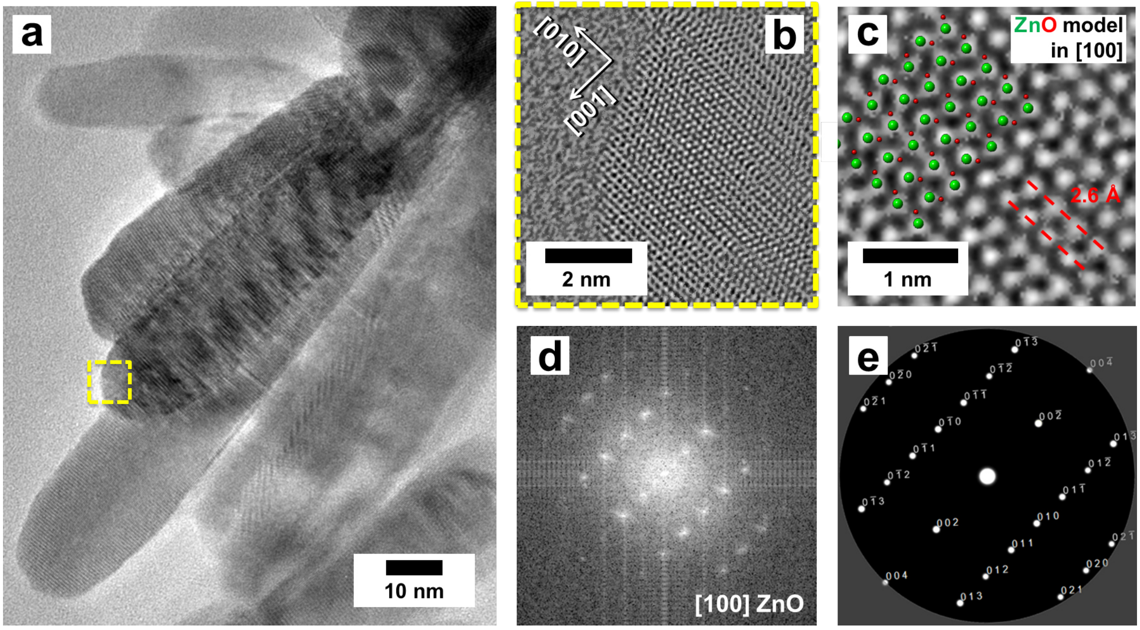

Figure 6.3: (a) TEM image of fan-like ZnO nanorods. (b) HR-TEM image of ZnO nanorod in [100] direction from marked position in (a). (c) HR-TEM defocus circle image with ZnO model in [100] direction. (d) Experimental power spectrum and (e) simulated diffraction pattern of the [100]ZnO zone axis. Experiments and data evaluation performed by Dr. Bastian Barton.

6.3.1 ZnO Nanoparticles from Heat-up Synthesis

In Figure 6.2 TEM images of the fan-like ZnO NPs resulting from heat-up synthesis are shown. The individual nanorods have sizes between approximately 40 and 130 nm and a diameter of $\sim$ 20 nm. Typically, several nanorods of different length are bundled and fanned out creating a unique morphology. The growth of the nanorod fans was best at a low heating rate of 1 °C/min and was analyzed by HR-TEM analysis (Figure 6.3). In Figure 6.3a a TEM image of a nanorod bundle is shown. Three nanorods originate from a common base and grew to different lengths. A HR-TEM image in [100] direction of the tip of a nanorod (Figure 6.3b) unveils that the nanorods grow in [001] direction as expected for nanorods in hexagonal wurtzite structure.[38] Figure 6.3c shows a defocus circle image with a model of ZnO in [100] direction and the respective atom positions of Zn and O with a plane distance of 2.6 $\AA$ between the O atoms. The experimental and simulated diffraction pattern (Figure 6.3d and e) show reflections of the [100]ZnO zone axis in harmony with the hexagonal wurtzite structure which is preferably found for ZnO due to the high bond polarity between Zn and O.[455]

Figure 6.4 displays a HR-TEM analysis of the crystal growth orientation of the nanorod bundle. Each of the three nanorods has the same [100] crystal orientation verified by the same reflections of the [100]ZnO zone axis in the accompanied power spectra. The growth direction is along the hexagonal c-axis with a small

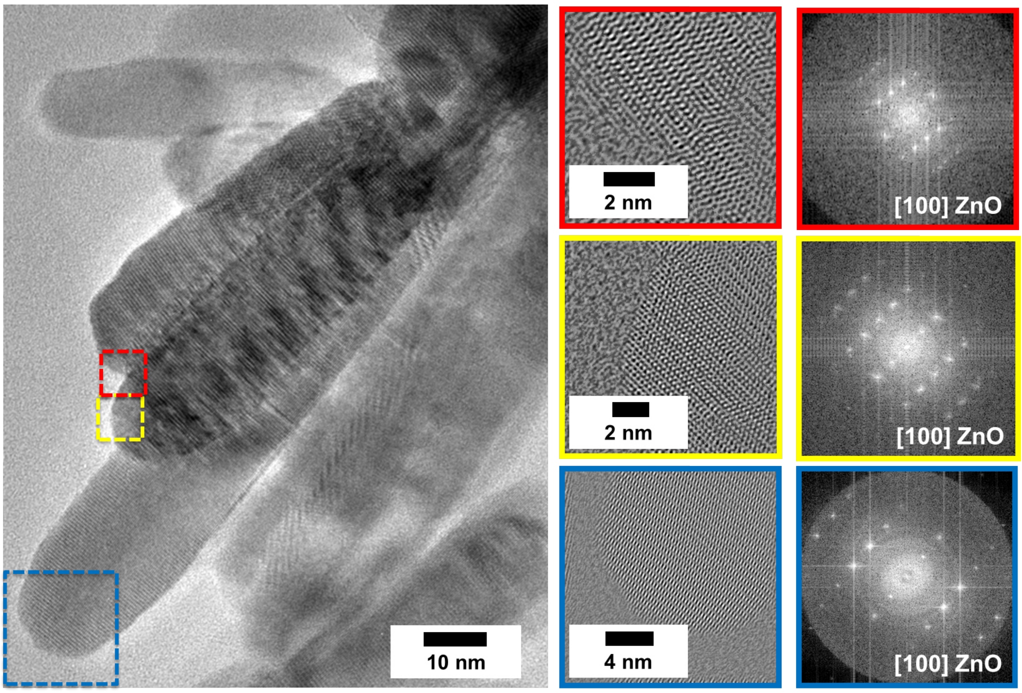

Figure 6.4: TEM image of fan-like ZnO nanorods with HR-TEM images of three different nanorod regions and their associated power spectra showing bundled rods have the same [100]ZnO crystal orientation. Experiments and data evaluation performed by Dr. Bastian Barton.

perpendicular tilt. The bundles appear to origin from a single crystal seed which was further analyzed by HR-TEM of the bundle origin (Figure 6.5). In Figure 6.5a a HR-TEM image of a ZnO nanorod in [001] direction shows the nanorod origin. Atomic modelling (Figure 6.5b) and power spectrum analysis (Figure 6.5c and d) show the [001] zone axis and reveal the hexagonal shape of the cross sections as expected from the crystal symmetry.

Ludi *et al.* investigated the mechanistic aspects of the formation and crystallization of ZnO in BA.[29, 480] They found that a bouquet- and fan-like growth to bundled nanorods can be explained by the reaction mechanism of the precursor decomposition with BA, surface reconstruction and oriented attachment. Bouquet- and fan-like ZnO nanorods emerged at 120 °C from the reaction of zinc acetylacetonate with BA. The reaction mechanism contains a nucleophilic attack of the hydroxyl function of BA on one of the carbonyl groups of the acetylacetonate which leads to a splitting of the acetylacetonate ligand and the formation of benzyl acetate and coordinated acetone in its enol form. Coordinated water releases the acetone by forming a zinc hydroxy species which can condensate to Zn-O-Zn units upon the release of water.[29, 480] Here a comparable mechanism, with the acetate ligand used in this reaction, can occur forming only benzyl acetate and the zinc hydroxy species. However, higher temperatures (also compared to the heterogeneous reaction[38]) are necessary due to the solvent and surfactant mixture of BA, OAm and ODE.

The formation of the unique morphology can be explained by two processes: (i) Adjacent particles can attach and the interface region is filled by dissolution of nearby surface species leading to a surface reconstruction and (ii) smaller building blocks can merge in an aligned manner *via* oriented attachment.[29, 481, 482] Nevertheless, oriented attachment could be apparent when interference effects in TEM images are visible, which is hardly the case for the ZnO nanorods. Also the origin from a single crystal seed and the small perpendicular tilt to the growth direction (Figures 6.4 and 6.5), which is a prerequisite for the fan out process, support classical nucleation and growth. Therefore, a third explanation has to be taken into account based on supersaturation and facet energies. In this case a faceted hexagonal shape elongated along the [001] direction is expected.[483, 484] Surfactants can direct the growth of nanocrystals due to facet specific adsorption which was demonstrated for BA based on its high polarity.[29] Additionally, surfactants can also influence oriented attachment through the promotion and direction of interparticle forces.[11, 480] They must adsorb strong enough to stabilize the nanocrystal against precipitation before attachment and on the other hand a high amount of a strong adsorbing surfactant may prevent alignment and attachment.[485, 486]

In summary, the fan-like ZnO nanorods display a concerted reaction mechanism probably uniting classical nucleation and surfactant assisted shape evolution with, in parts, non-classical oriented attachment of smaller building blocks and surface reconstruction of adjacent NPs.

6.3.2 ZnO@SiO$_2$ Nanoparticles for Studying Cell Uptake

In order to investigate the possible cell uptake of ZnO NPs into different cancer cells a silica coating strategy was chosen to provide a combined dye functionalization and NP dissolution protection. The ZnO NPs from the heat-up synthesis were coated with a 5-25 nm thick silica shell in a reverse microemulsion technique. The NPs were dispersed in cyclohexane and micelles were generated through the addition of a branched polyoxyethylene nonylphenylether (Igepal CO-520) as surfactant. By adding aqueous ammonium hydroxide solution a stable reverse microemulsion is provided. The subsequently added tetraethyl orthosilicate (TEOS) silicate precursor can be hydrolyzed at the micelle interface and ZnO NPs diffused into the micelles are coated with a silica shell. The micelles provide a controlled reaction containment enabling enhanced reaction control. Careful adjustment of the experimental procedure and reagent amounts led to an optimized amount of 150 μL ammonium hydroxide solution of pH 11.5 and 120 μL TEOS for a 2 d reaction, where 2 x 15 μL extra TEOS were added during the second reaction day. This was a reasonable agreement on feasible reaction times and minimized ZnO dissolution in the basic pH regime (*vide infra*). Discretionary, PEGTES, a trimethoxysilane functionalized polyethyleneglycol, can be added as a last reaction step to provide better long term colloidal stabilization of the ZnO@SiO$_2$ NPs.

The silica coating offers advantages in terms of biocompatibility and functionalization through the surface hydroxyl groups.[95, 102] However, some detriment need to be

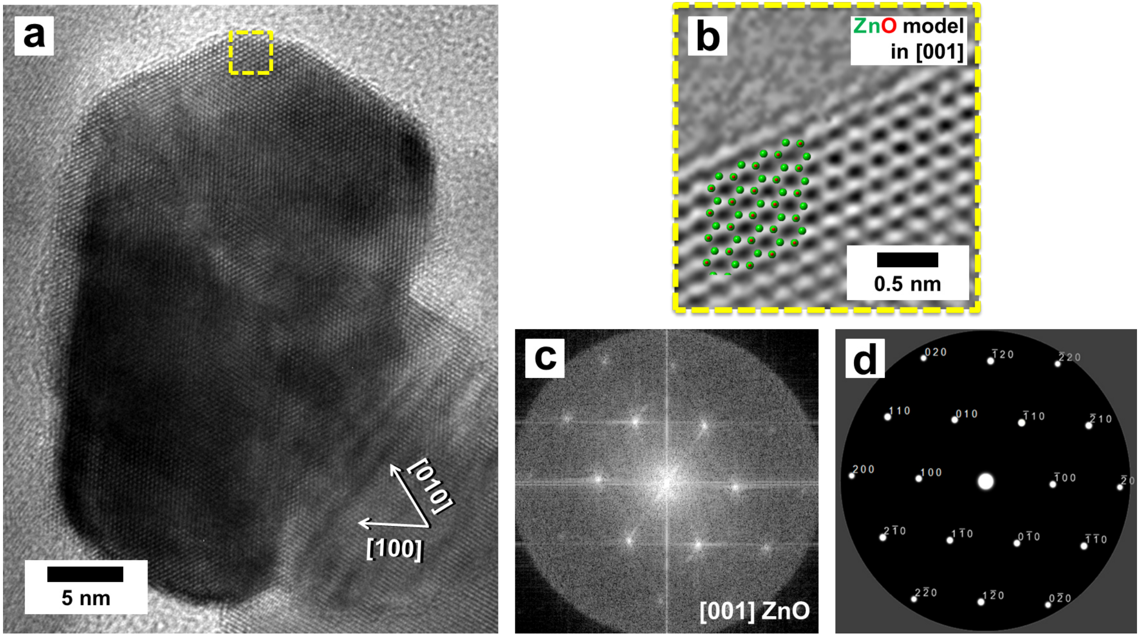

Figure 6.5: (a) Holographic HR-TEM image of a ZnO nanorod in growth direction [001]. (b) HR-TEM defocus circle image of ZnO nanorod with ZnO model in [001] direction from marked position in (a). (c) Experimental power spectrum and (d) simulated diffraction pattern of [001]ZnO zone axis. Experiments and data evaluation performed by Dr. Bastian Barton.

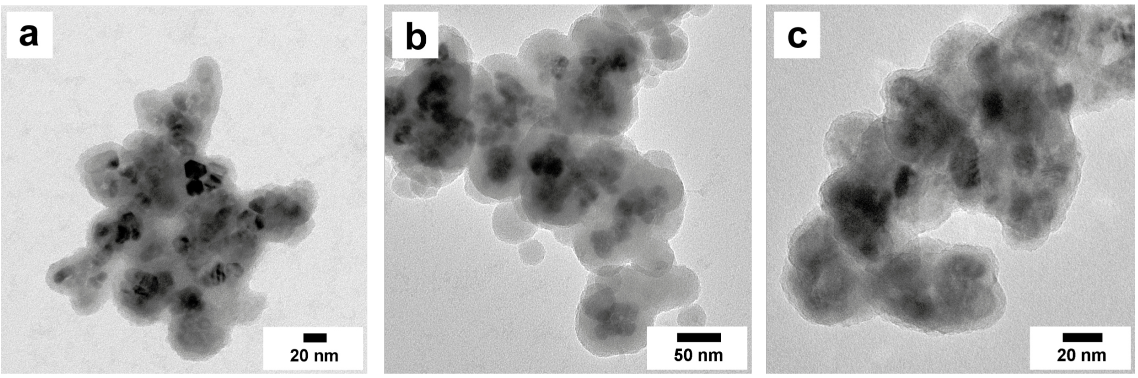

Figure 6.6: TEM images of ZnO@SiO$_2$ NPs with an average silica coating of about (a) 7.5 nm thickness (image from ref.[451]) and (b) 21 nm thickness. (c) TEM image of ZnO@SiO$_2$@FITC NPs with about 6 nm silica shell and fluorescein dye functionalization.

considered when coating ZnO NPs. Based on the formation of sol particles, which further grow into silica NPs by a hydrolysis and condensation process, the coating is usually carried out in a strong basic pH environment of concentrated ammonia solution. For preventing network formation, the basic catalysis with attack of the SiO$^-$ building units on the central Si atom of the oligomer is necessary to obtain defined NPs.[33, 101] ZnO, however, shows poor stability in both acidic and basic

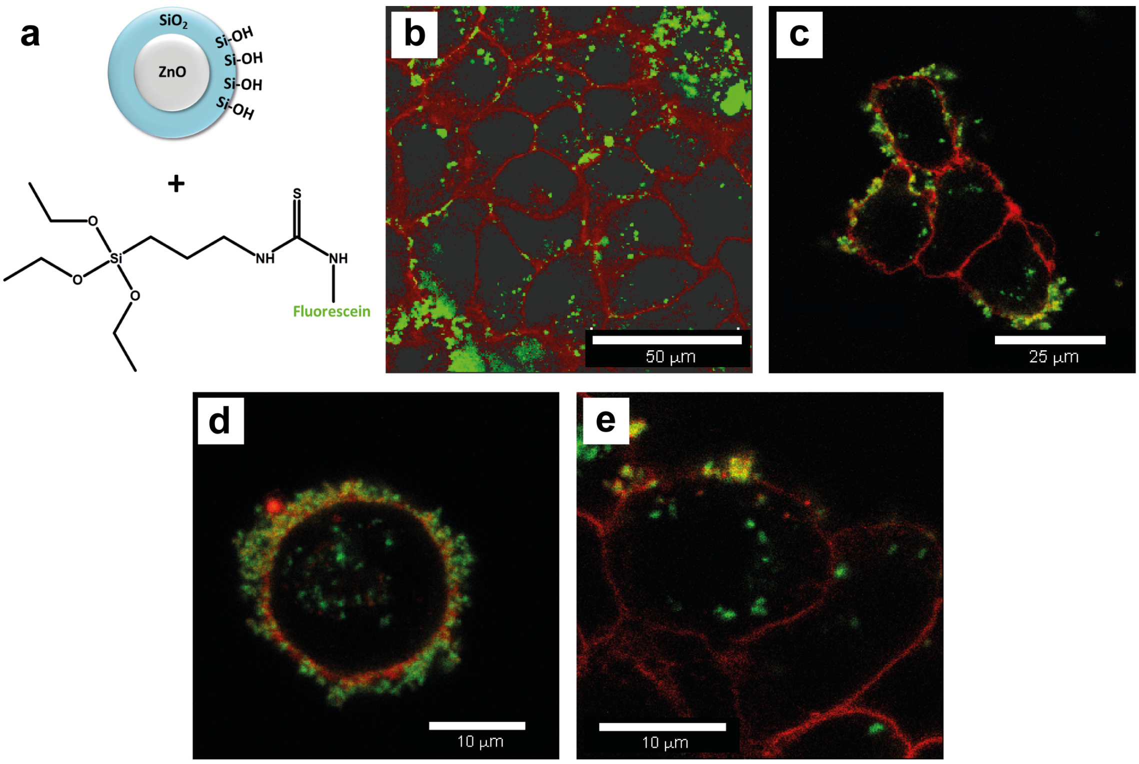

Figure 6.7: (a) Schematic representation of the condensation of surface Si-OH units with preformed APTES-FITC conjugate for covalent dye functionalization of ZnO@SiO_2 NPs. CLSM image of ZnO@SiO_2@FITC NPs (green) after cell uptake into (b) A549 lung cancer cells, (c) FaDu pharynx squamous cancer cells, (d) HNSCCUM-02T head and neck squamous cell carcinoma cancer cells and (e) RPMI-2650 nasal septum squamous cell carcinoma cancer cells. Plasma membrane stained with CellMask Orange. Experiments and data evaluation performed by M.Sc. Nadine Wiesmann.

pH environment because of the formation of $Zn(OH)_2$ with water.[453, 460] In acidic environment a $[Zn(H_2O)_6]^{2+}$ complex is formed whereas in basic environment a $[Zn(OH)_4]^{2-}$ complex is formed with high solubilities. Reducing the basic pH value reduces the dissolution of ZnO NPs during the synthesis of the silica shell but also prolongs the reaction time by a multiple. Accordingly, a reasonable pH value of 11.5 was established to address both concerns. Eventually, the reaction was carried out in a plastic containment rather than in a glass flask due to the reduced Pearson compatibility of the rather "soft" ZnO and the rather "hard" SiO_2.[133] In a non-silylated glass flask this would lead to the attachment of the hydrolyzing silica species to the glass wall rather than to the ZnO resulting in a reduced or in no silica coating. In Figure 6.6 TEM images of ZnO@SiO_2 NPs are presented which were synthesized using the *vide supra* mentioned optimized reaction conditions. In Figure 6.6a the ZnO NPs have an average silica coating of about 7.5 nm thickness, however, the shell thickness is not uniform due to agglomerated ZnO NPs during the silica synthesis. The free space between such adjacent NPs is filled with silica, thus increasing the silica thickness at these positions. Figure 6.6a displays ZnO@SiO_2 NPs where the reaction was only carried out for 1 d and no extra (2 x 15 µL) TEOS was added. In Figure 6.6b an average silica coating of about 21 nm thickness was obtained through addition of extra TEOS and 2 d reaction time. In general the ZnO NPs after silica coating show mass lost and round morphology. The concealed NPs lost their fan-like and elongated morphology almost completely due to the dissolution of the ZnO during the silica synthesis. Figure 6.6c presents ZnO@SiO_2@FITC NPs with incorporated fluorescein dye. The dye functionalization was established to monitor a possible cell uptake of the ZnO@SiO_2 NPs. For obtaining a covalent connection between dye and silica coating, an APTES-FITC conjugate was synthesized first. Using an addition reaction of the isothiocyanate functionalized fluorescein (FITC) with the amine group of (3-aminopropyl)triethoxysilane (APTES), the dye can be covalently bound to the surface Si-OH of the silica by hydrolysis and release of ethanol (Figure 6.7a). Addition of the conjugate early in the synthesis of the coating also ensures a good integration into the silica shell without perturbation of the shell (Figure 6.6c).

After functionalization with fluorescence dye, the ZnO@SiO_2@FITC NPs from Figure 6.6b with $\approx$ 21 nm silica shell were incubated with A549 lung cancer cells (Figure 6.7b), FaDu pharynx squamous cancer cells (Figure 6.7c), HNSCCUM-02T head and neck squamous cell carcinoma cancer cells (Figure 6.7d) and RPMI-2650 nasal septum squamous cell carcinoma cancer cells (Figure 6.7e). After 4 h redundant NPs were removed and the cells were monitored by confocal laser scanning microscopy (CLSM) to investigate possible cell uptake. The NPs fluoresce green and the plasma membrane was stained using CellMask Orange. All cancer cell lines show incorporated NPs. Larger NP agglomerates are often also located near the plasma membrane outside of the cells and were not taken up.

The cytotoxicity of the ZnO@SiO_2 NPs was evaluated using an Alamar Blue cell viability assay. The NPs were incubated with cells and after 4 h, 6 h and 27 h the cell viability was measured by a colorimetric read-out. In Figure 6.8a the results of the cytotoxicity measurements for 100 µg/mL ZnO@SiO_2 NPs with about 21 nm silica shell are presented. During the first observation period the viability was as high as the viability of the control cells. After 6 h the viability decreased to about 62% and after 27 h the viability was reduced to 40%, implying acute cytotoxicity. This retarded release kinetics (*vide infra*) of Zn^{2+} ions is a prerequisite to ensure a time window for the investigation of toxicity mechanisms until the full cytotoxic potential of the NPs is unleashed. However, viability assays with ZnO@SiO_2 NPs having a less thick silica thickness of about 6 nm (Figure 6.8b) unveil that only a shell thickness $>$ 20 nm provides enough protection of the ZnO NPs to effectively retard dissolution and toxic effect. It remained challenging to reproducible obtain a silica shell thickness higher than 20 nm due to the influence of various reaction parameter like pH value, amount of TEOS as well as ammonium hydroxide solution and reaction time.

For further evaluation of the ZnO@SiO_2 NPs dissolution kinetics, incubation experiments of NPs at 37 °C in Dulbecco's Modified Eagle Medium (DMEM) containing

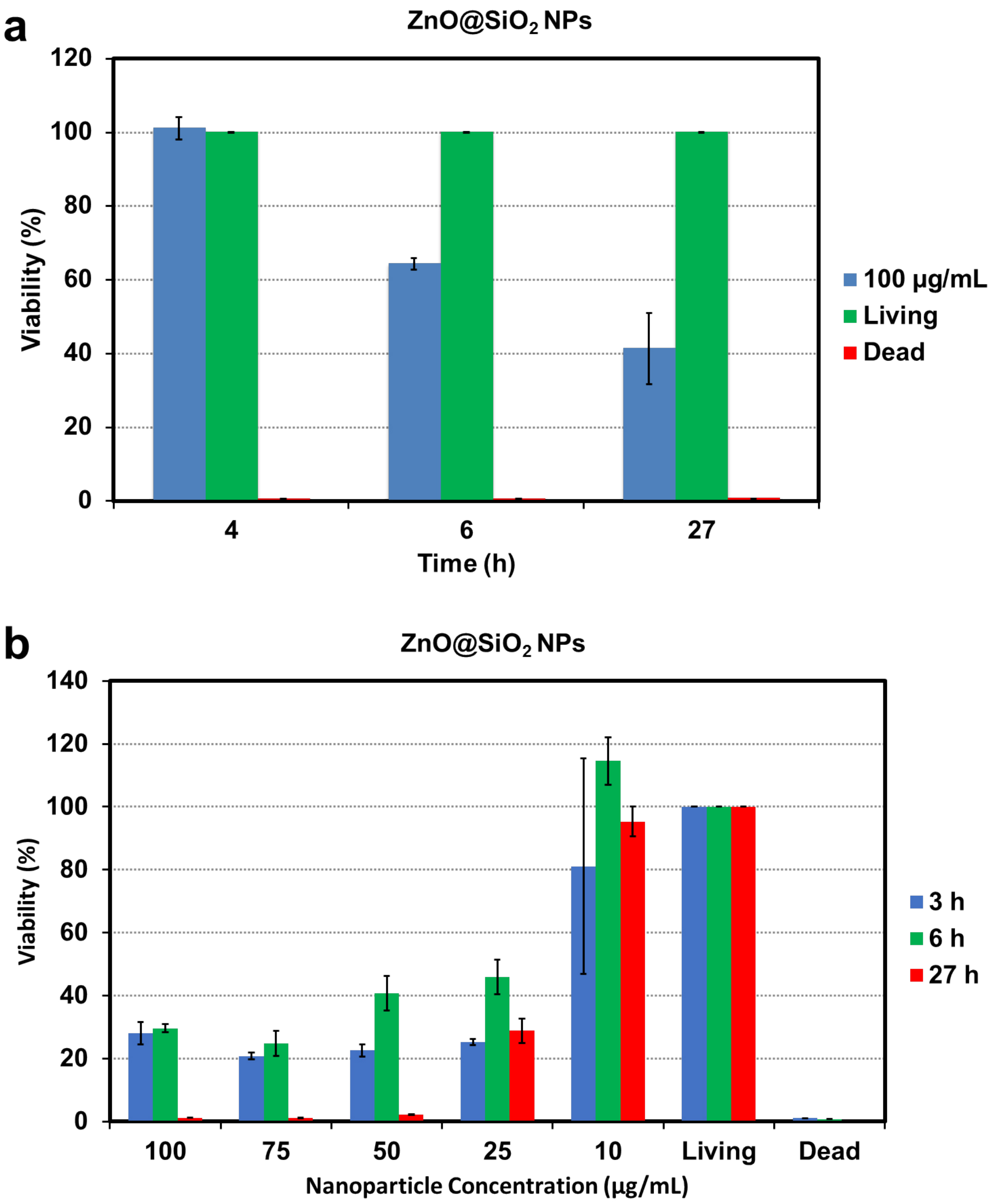

Figure 6.8: Alamar Blue cell viability assay of ZnO@SiO$_2$ NPs with about (a) 21 nm silica shell and (b) 6 nm silica shell. Experiments and data evaluation performed by M.Sc. Nadine Wiesmann.

10% of fetale calf serum (FCS) for 3 h, 6 h and 24 h were carried out and analyzed using TEM and atomic absorption spectroscopy (AAS). Figure 6.9a-d shows TEM images at the beginning (a) of the experiment and after 3 h (b), 6 h (c) and 24 h (d).

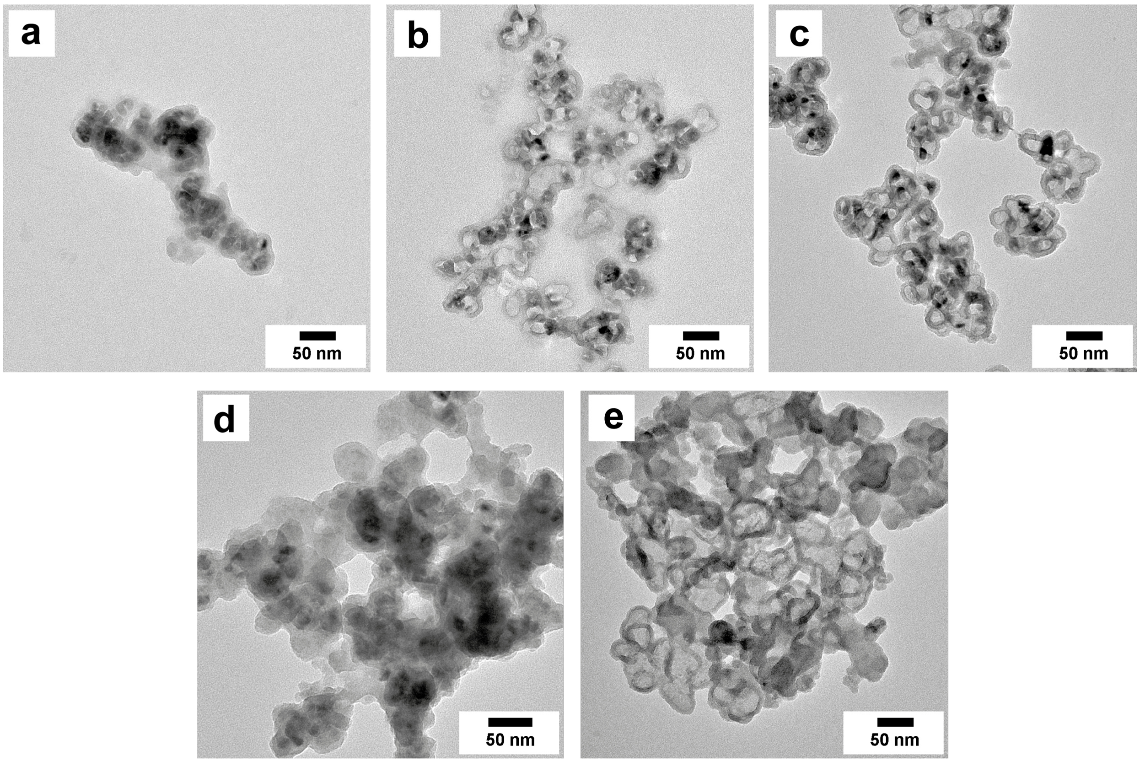

Figure 6.9: TEM images of ZnO@SiO$_2$ NPs dissolution experiments (at 37 °C in DMEM containing 10% FCS) (a) at the beginning of the experiment and after (b) 3 h, (c) 6 h and (d) 24 h. (e) Control experiment in TRIS buffer after 3 h incubation time.

At the beginning (Figure 6.9a) the silica shell of about 7.5 nm thickness is unharmed and covers the ZnO NPs complete. After 3 h (Figure 6.9b) several empty silica shells are visible which could be verified by the detection of free Zn^{2+} ions in the supernatant. After a reaction time of 6 h (Figure 6.9c) empty silica shells are again mixed with ZnO filled silica shells. At the end of the experiment after 24 h (Figure 6.9d) the silica is fused due to the beginning degradation of the coating. However, remaining ZnO is visible and Zn^{2+} ions were detected in the centrifuged residue of the NPs, demonstrating that the dissolution is not complete after 24 h.

To investigate to which extent the ionic strength, provided by the inorganic salts in the DMEM cell medium, influences the dissolution kinetics, a control experiment with 0.5 M TRIS buffer (tris(hydroxymethyl)-aminomethane), providing a high ionic strength of NaCl and KCl, was carried out. In Figure 6.9e a TEM image of ZnO@SiO$_2$ NPs after 3 h incubation in TRIS buffer is presented. The silica shells contain no ZnO NPs anymore which was verified by a low Zn^{2+} concentration in the NP residue and a high Zn^{2+} concentration in the supernatant. After 3 h the dissolution in TRIS buffer is more advanced compared to DMEM after 24 h.

Additionally, the influence of the pH value on the dissolution of the ZnO NPs was considered. The dissolution of ZnO results in the formation of Zn(OH)$_2$ and the introduction of hydroxide ions reducing the pH value. Incubation of ZnO NPs in

Milli-Q water for 24 h displayed an increase of the pH value from 6.00 to 6.67. Hence, ZnO NPs were dispersed in DMEM + FCS for 4 h under cell culture condition. The pH value increased minimal from 7.66 to 7.68 showing that the cell medium is able to buffer the hydroxide ions. Experiments without cell culture condition displayed an increased pH value of 7.92 (compared to the start value of 7.62) probably due to the decomposition of the carbonate buffer caused by the missing CO_2 atmosphere ($HCO_3^- \leftrightarrows CO_2 + OH^-$).

In summary, it was shown that ZnO NPs can be successfully coated by a silica shell to provide dye functionalization for cell uptake studies. The modified ZnO@SiO_2@FITC NPs underwent cell uptake to different cancer cell lines. A silica coating >20 nm is a prerequisite to ensure a time window for the investigation of toxicity until the full cytotoxic potential of the NPs is unleashed. ZnO NPs with a lower silica shell thickness displayed increased cytotoxicity despite of a gradual dissolution kinetics analyzed in DMEM + FCS. Hence, it is likely that the amount of Zn^{2+} released during the first hours of NP incubation in combination with cell uptake and cell adhesion is sufficient to sustainingly damage the cells if only a thin silica coating is provided. Additionally, a high ionic strength in the cell surrounding medium can accelerate the dissolution, whereas a pH value increase through the formation of hydroxide ions is successfully buffered by the cell medium under cell culture condition.

6.3.3 ZnO Nanoparticles from Solvothermal Synthesis

The solvothermal synthesis of ZnO NPs was realized by a reaction of $Zn(ac)_2 \cdot 2\ H_2O$ with tetramethylammonium hydroxide solution (TMAOH) in methanol. The aqueous based reaction allows morphology control of the ZnO NPs through the adjustment of reaction temperature and water content. After the dissolution of the $Zn(ac)_2 \cdot 2\ H_2O$ precursor in methanol, the addition of the weak base TMAOH results in the formation of $[Zn(OH)_4]^{2-}$, first in low amounts due to the water content in the reaction mixture. Next, ZnO is formed ($[Zn(OH)_4]^{2-} \leftrightarrows ZnO + 2\ OH^- + H_2O$).[484, 487] It was shown that $Zn(OH)_2$ is not directly converted to ZnO upon the release of water. To obtain a supersaturated solution for nucleation and growth the molar ratio of Zn^{2+} and OH^- should be at least 1:4 suggesting the *vide supra* mentioned reaction pathway.[488] Basic conditions with excess of hydroxide ions can lead to growth habits different from the idealized view of faceted hexagonal nanorods mentioned *vide supra*.[29, 489, 490] At RT this reaction led to the formation of rather undefined fused ZnO NPs after 24 h (Figure 6.10a). More defined NPs could be obtained at 50 °C (Figure 6.10b). The NPs are still agglomerated due to the missing surfactants and have sizes between 5 and 15 nm. An elevated temperature of 100 °C yielded 5-50 nm ZnO NPs with a more rod-like morphology (Figure 6.10c). This is caused by the expanded dissociation of TMAOH upon elevated temperatures as well as the more thermodynamic controlled reaction conditions and eventually results in a distribution of small nanorods.[487] The crystallinity of the obtained ZnO NPs was improved by heat treatment (*vide infra*). Figure 6.10d displays a TEM image

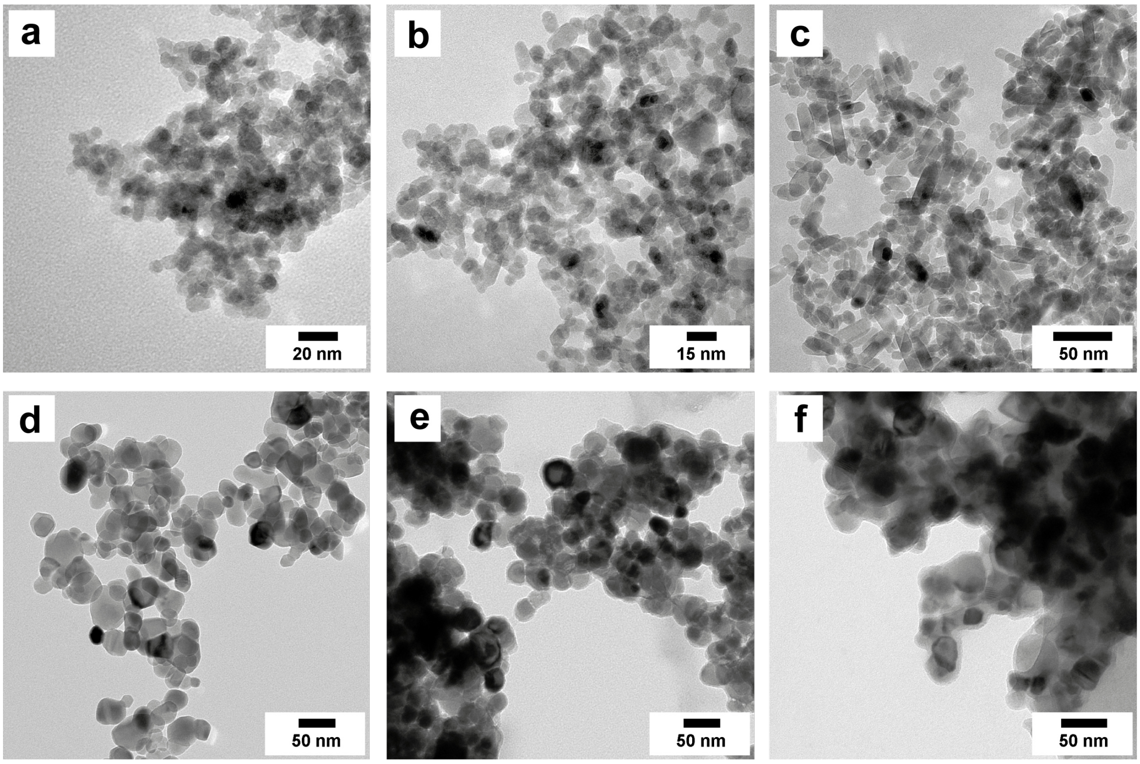

Figure 6.10: TEM images of ZnO NPs from solvothermal synthesis at (a) RT, (b) 50 °C and (c) 100 °C after 24 h reaction time. (d) TEM image of the ZnO NPs from (b) after HT to 400 °C for 3 h. (e) and (f) TEM images of the ZnO NPs from (d) after incubation in (e) DMEM + FCS and (f) DMEM + FCS + cells for 4 h.

of ZnO NPs obtained by the solvothermal synthesis at 50 °C after heat treatment at 400 °C for 3 h. The NPs show a more uniform TEM contrast pointing towards higher crystallinity and a size increase while maintaining the faceted round shape. After incubation with cell culture medium (DMEM + FCS, Figure 6.10e) and cell culture medium containing cells (Figure 6.10f) for 3 h, the ZnO NPs are still in shape, hardly dissolved and covered by a protein corona.

Prior to cytotoxicity measurements the as-synthesized and heat treated ZnO NPs were analyzed by X-ray diffraction (XRD) to evaluate the crystallinity of the NPs. In Figure 6.11 the powder diffractogram of heat-up and solvothermal ZnO NPs is compared to heat treated (HT) solvothermal ZnO NPs. The solvothermal ZnO NPs show no improved crystallinity compared to the heat-up NPs independent of the reaction temperature. Also HT at 200 °C reveals no improvement. HT at 400 °C eventually results in an improved crystallinity unveiled by a reduced width of the reflections. Accordingly the ZnO NPs heat treated at 400 °C for 3 h were chosen for further cytotoxicity experiments (*vide infra*).

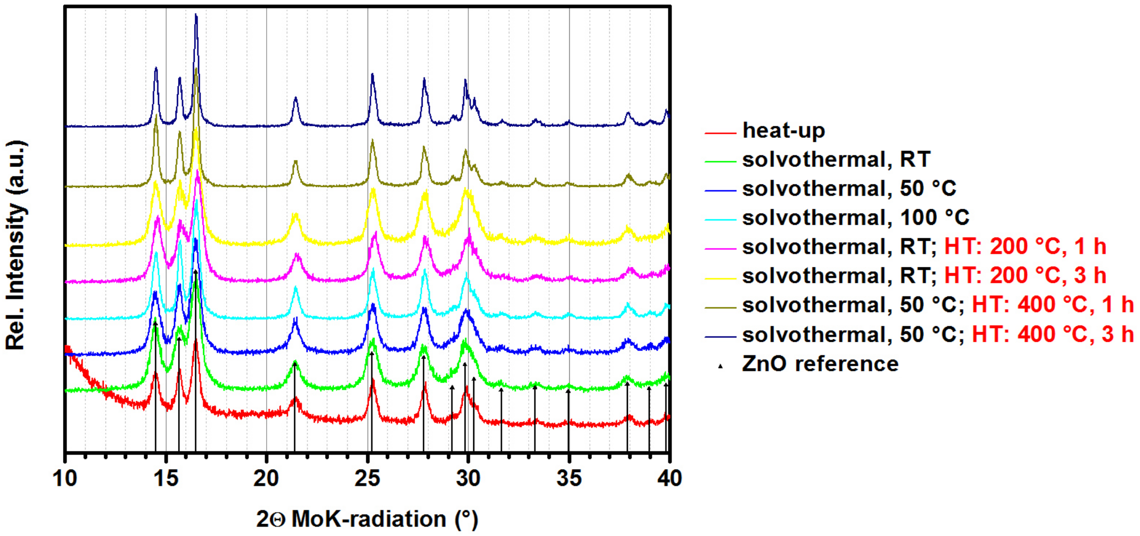

Figure 6.11: X-Ray diffraction of heat-up ZnO NPs, solvothermal ZnO NPs and solvothermal ZnO NPs after heat treatment (HT).

6.3.4 Evaluation of the Cytotoxic Potential of ZnO Nanoparticles

As investigated *vide supra*, dissolution of ZnO in ZnO@SiO_2 NPs takes place continuously during the incubation with cell medium and cytotoxicity depends on the thickness of the silica coating. It remains unclear how pure ZnO NPs without coating and organic surfactants behave in cell cytotoxicity since they show no pronounced dissolution and a protein corona (Figure 6.10e and f). Therefore, pure solvothermal (heat treated) ZnO NPs were used in cell viability assays to analyze the toxicity mechanism and potential reasons for the high cytotoxicity of ZnO due their small size and ligand-free surface. Figure 6.12a displays the results of an Alamar Blue cell viability assay of the ZnO NPs from Figure 6.10b depending on the ZnO NP concentration. Between 15 and 100 µg/mL a high cell death rate was observed already after 3 h. Longer observation periods of 6 h and 27 h resulted in no significant change in the cell toxicity. NP concentrations of 10 and 5 µg/mL showed reduced cytotoxicity within the first 3 h, but no gradual increase in cytotoxicity with increasing experimental time. AAS analysis of each ZnO concentration revealed that always a varying fraction between 40% and 96% of the desired Zn^{2+} ion concentration (which is 80.3% of the ZnO NP concentration stated in Figure 6.12, *e.g.* 16.1 µg/mL Zn^{2+} for 20 µg/mL ZnO NPs) is delivered to the cells. Hence it remains challenging to ensure the reproducible delivery of the desired Zn^{2+} ion/ZnO NP concentration. This might be due to persistent particle agglomeration which prevents an equal distribution of ZnO NPs during the preparation of the NP dispersions. A second cell viability assay (Figure 6.12b) demonstrates this. The cell viability after 3 h is significantly higher compared to the first assay in Figure 6.12a. However, it is still low for concentrations higher than 15 µg/mL. The cell viability after 6 h and 27 h is strongly reduced. The increase in cytotoxicity between 3 h and 6 h experimental time is probably due to internalized or adherent ZnO NPs dissolving.

The solvothermal ZnO NPs heat treated at 400 °C were also used for a cell viability assay. The viability for all tested NP concentrations of 100-15 µg/mL was below 40% already after 3 h. However, due to the non-reproducible delivery of the desired Zn^{2+} ion concentration, the cytotoxicity for this NPs can only be compared conditionally to the non-heat treated ZnO NP, impeding the evaluation of the crystallinity influence and heat treatment influence. The cytotoxicity of the ZnO NPs could be based on (i) rapid dissolution of ZnO NPs which releases Zn^{2+} in amounts higher than can be tolerated by the cells, (ii) uptake of ZnO NPs into the cells where they further release Zn^{2+} ions and damage cell components (*e.g.* DNA, mitochondria) and (iii) inhibition or interference of important cell functions due to NP attachment to the cells.[472] To obtain deeper insight into the toxic effect of Zn^{2+}, $ZnCl_2$ as a source for Zn^{2+} ions and $MgCl_2$ with Mg^{2+} as chemical comparable ion were used in cell viability assays. The concentration of the salts and therefore the concentration of the Zn^{2+} and Mg^{2+} ions was chosen accordingly to the concentration of Zn^{2+} ions in the ZnO NPs. $ZnCl_2$ (Figure 6.13a) displays a higher cell viability after 3 h compared to the ZnO NPs despite to the direct availability of the Zn^{2+} ions. After 6 h and 27 h the cell viability is very low for concentrations $>$ 10 µg/mL. This suggest the toxic potential of the Zn^{2+} ions evolves delayed. Also the anions to Zn^{2+} may influence the toxicity due to their chelating properties of other essential metals.[470] Cl^- showed comparatively low toxicity.[470] To exclude toxic effects provided by the high ionic strength distributed by the dissolving NPs and possibly influencing ion potentials or ion channels, Mg^{2+} ions were used in the cytotoxicity assay in the same ionic strength as Zn^{2+} ions from ZnO NPs (Figure 6.13b). Here, independent of the concentration, no toxic effects were detected.

In summary, evaluation of the cytotoxicity of solvothermal ZnO NPs is challenging because the reproducible delivery of the desired Zn^{2+} ion concentration is difficult. However, it could be demonstrated that high ionic strength as well as the direct availability of large amounts of Zn^{2+} ions are of less importance for the early toxic potential of the solvothermal ZnO NPs. Hence, the low cell viability after 3 h might be principally caused by the NPs, inhibiting or influencing important cell functions due to their attachment to the cells or due to cell uptake. Long term cytotoxicity (6-27 h) might then be determined by the biochemical character and properties of the Zn^{2+} ions as demonstrated by the strongly reduced cell viability after 6 h and 27 h for $ZnCl_2$ salt.

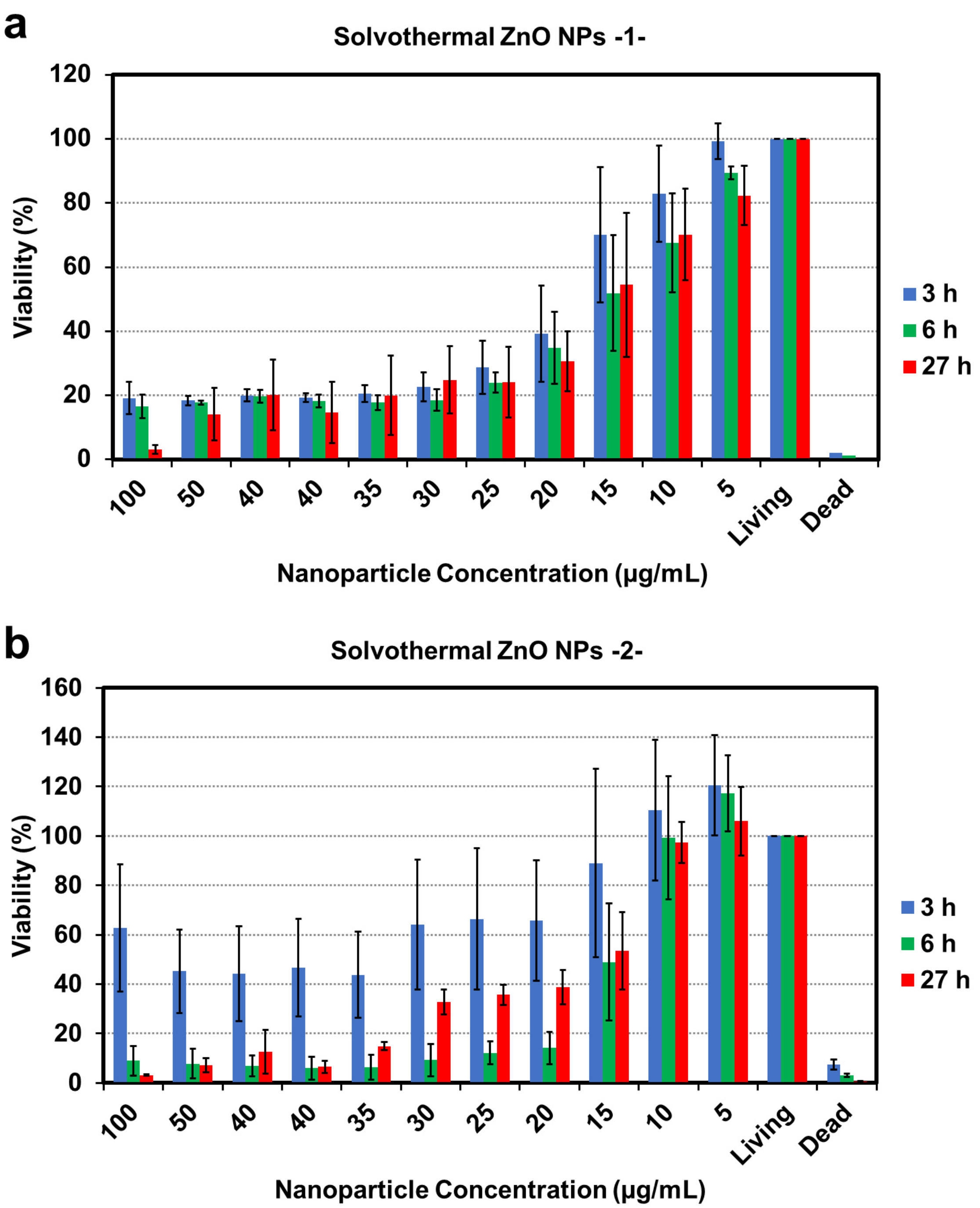

Figure 6.12: Alamar Blue cell viability assay of solvothermal ZnO NPs. The two values of 40 µg/mL result from two different concentration series used for the assay. Experiments and data evaluation performed by M.Sc. Nadine Wiesmann.

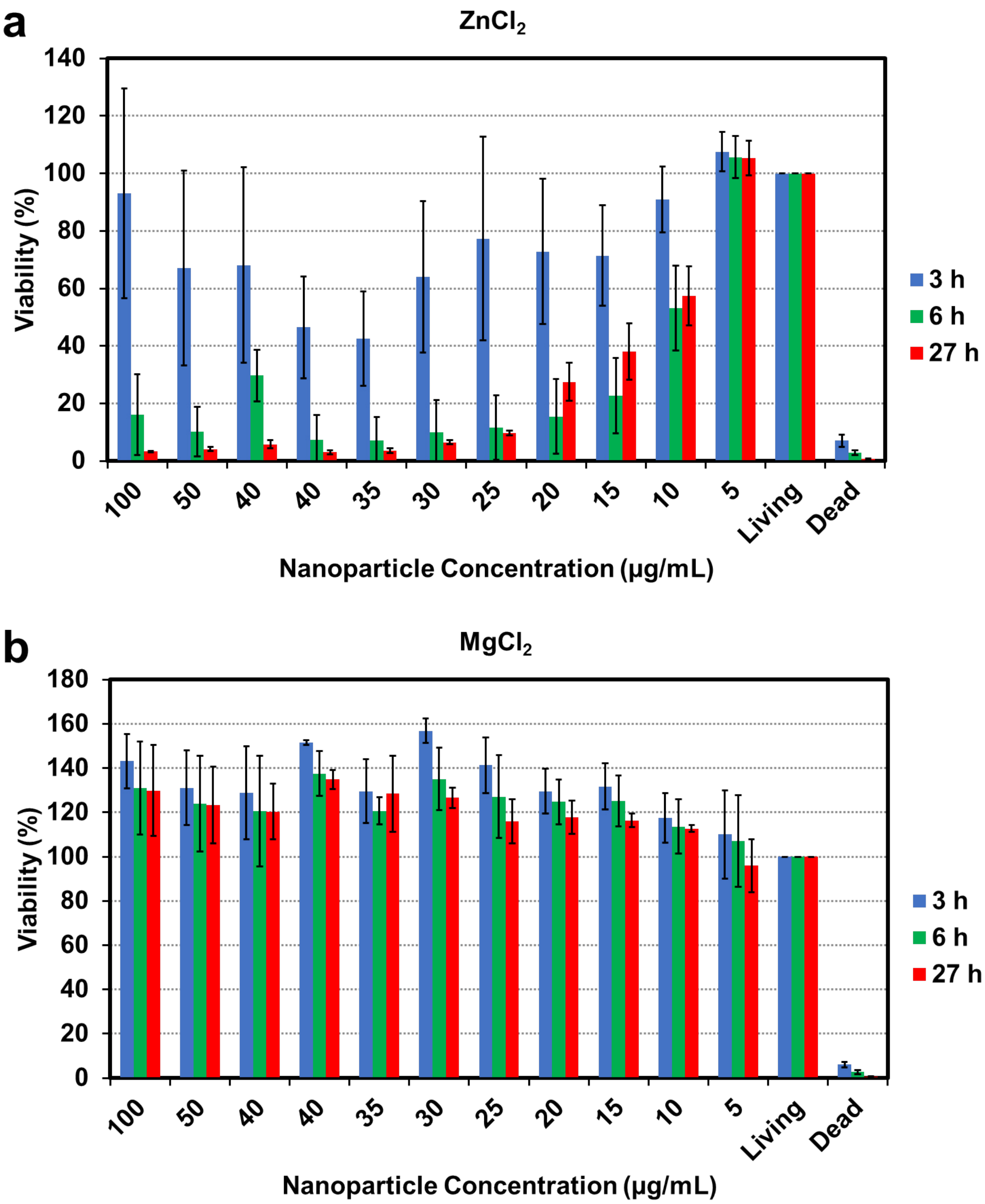

Figure 6.13: Alamar Blue cell viability assay of (a) $ZnCl_2$ and (b) $MgCl_2$ salts. The two values of 40 µg/mL result from two different concentration series used for the assay. The amounts of $ZnCl_2$ and $MgCl_2$ were prepared according to the respective amounts of Zn^{2+} in ZnO NPs. Therefore, the concentrations of $ZnCl_2$ and $MgCl_2$ are labeled as nanoparticle concentration to be comparable to the other cytotoxicity measurements. Experiments and data evaluation performed by M.Sc. Nadine Wiesmann.

6.4 Conclusion

Two different synthetic strategies for the formation of ZnO NPs were presented for the evaluation of ZnO NP cell uptake and toxicity mechanisms. Heat-up ZnO NPs were obtained by thermal decomposition of a zinc precursor in ODE, a high boiling organic solvent. BA was used to control the morphology of the ZnO NPs which yielded fan-like ZnO nanorods through concerted classical surfactant assisted nucleation, surface reconstruction and oriented attachment. The heat-up ZnO NPs were subsequently coated with silica for the attachment of fluorescein dye in a reverse microemulsion reaction. The modified ZnO@SiO$_2$@FITC NPs were internalized into A549, FaDu, HNSCCUM-02T and RMPI cancer cells. Additionally ZnO@SiO$_2$ NPs provided a gradual dissolution kinetics of ZnO which caused a retardation of the full cytotoxic potential of the ZnO NPs if the silica shell thickness is exceeding 20 nm. Smaller ZnO NPs from solvothermal synthesis with a size between 5 and 15 nm were used to obtain deeper insight into the various aspects influencing the toxic potential of ZnO NPs because of their small size and ligand-free surface. They showed low cell viability after the first 3 h of the experiment. It was found that high ionic strength as well as the direct availability of large amounts of Zn^{2+} ions are of minor importance for the high toxic potential of the solvothermal ZnO NPs in the first hours. The low cell viability after 3 h might therefore be mainly caused by the NPs, inhibiting or influencing important cell functions due to their attachment to the cells or due to cell uptake. Long term cytotoxicity of 6-27 h is then probably determined by the amount, biochemical character and properties of the released Zn^{2+} ions.

6.5 Experimental Section

Materials

Zinc(II)acetate dihydrate ($Zn(ac)_2 \cdot 2\ H_2O$, Sigma Aldrich, 98+%), benzyl alcohol (BA, Acros Organics, 99%), oleylamine (OAm, Acros Organics, 80-90%), 1-octadecene (ODE, Acros Organics, 90%), ethanol (Sigma Aldrich, *p.a.* > 99.8%), tetramethylammonium hydroxide 25 w/w in methanol (TMAOH, Acros Organics), methanol (Fisher Scientific, Analytical Reagent Grade), Igepal CO-520 (Aldrich), tetraethyl orthosilicate (TEOS, Aldrich, ≥ 99% GC), 3-[methoxy(polyethyleneoxy)propyl]trimethoxysilane 9-12 PE units (PEGTES, abcr, 90%), ammonium hydroxide solution (Sigma Aldrich, ca. 25%), cyclohexane (Fisher Scientific, Analytical Reagent Grade), fluorescein-5-isothiocyanate (FITC, Fluka, ≥ 90%), (3-aminopropyl)triethoxysilane (APTES, Aldrich, 99%) and dimethyl sulfoxide (DMSO, Alfa Aesar, HPLC grade 99.9%, Argon/Chem Seal) were used in this work.

Heat-up Synthesis of ZnO Nanoparticles

The synthesis of heat-up ZnO NPs was adapted from Tahir *et al.* with some modifications.[38] In a 100 mL three-neck round bottom flask 109.4 mg (0.5 mmol) of $Zn(ac)_2 \cdot 2\ H_2O$ (pre-annealed at 110 °C for 10 min) were dispersed in 4 mL of benzyl alcohol, 3 mL of oleylamine and 2 mL of 1-octadecene under inert gas (Ar) conditions and stirred for 5 min at RT. The mixture was heated to 120 °C at a rate of 5 °C/min and held at this temperature for 20 min. The mixture was then heated to to 230 °C with a rate of 1 °C/min and held at this temperature for 30 min. Afterwards, the mixture was slowly cooled to room temperature. The colorless product was precipitated from the mixture by adding 20 mL of ethanol. The precipitate was separated by centrifugation (9000 rpm, 10 min, RT), dispersed in cyclohexane and washed twice by adding ethanol (cyclohexane:ethanol = 1:2) and additional centrifugation (9000 rpm, 10 min, RT). Finally, the product was dispersed in cyclohexane and stored at RT.

Solvothermal Synthesis of ZnO Nanoparticles

The solvothermal synthesis of ZnO NPs was adapted from Cheng *et al.* with some modifications.[487] In a round bottom flask 1090 mg (5 mmol) of $Zn(ac)_2 \cdot 2\ H_2O$ were dissolved in 10 mL of methanol and gently shaken until no turbidity was visible anymore. Afterwards, 20 mL of tetramethylammonium hydroxide 25 w/w in methanol were slowly added at RT and the mixture was stirred for additional 20 min. The reaction mixture was subsequently transferred to a 50 mL teflon-lined stainless steel autoclave and heated at 50 °C for 24 h. The colorless precipitate was separated by centrifugation (9000 rpm, 10 min, RT) and washed twice by adding 20 mL Milli-Q water and additional centrifugation (9000 rpm, 10 min, RT). Finally, the product was dispersed in ethanol and stored at RT for long term storage or dried in air at RT for short term storage.

Synthesis of $ZnO@SiO_2$ Nanoparticles from Heat-up ZnO Nanoparticles

The synthesis of $ZnO@SiO_2$ NPs with heat-up ZnO NPs was carried out using a reverse microemulsion technique. In a 50 mL plastic tube 2 g of Igepal CO-520 and 100 µL of oleylamine were dispersed in 40 mL of cyclohexane. The mixture was ultrasonicated for 15 min. 10 mg of heat-up ZnO NPs were added and the mixture was ultrasonicated for additional 15 min. At RT 150 µL of ammonium hydroxide solution of pH 11.5 were added and the mixture was stirred for additional 10 min. The stirring speed was increased to maximum and 120 µL of TEOS were injected rapidly. The mixture was stirred over night at maximum stirring speed. In the morning and evening of the next day 15 µL of TEOS each were added and the mixture was again stirred over night at maximum stirring speed. 100 µL of PEGTES were subsequently added and the mixture was stirred for additional 4 h. The precipitate was separated by centrifugation (9000 rpm, 20 min, RT) dispersed in ethanol and washed twice by adding cyclohexane (ethanol:cyclohexane = 1:2) and additional centrifugation (9000 rpm, 20 min, RT). Finally, the product was dispersed in ethanol and stored at 8 °C.

Synthesis of APTES-FITC Conjugate

The APTES-FITC conjugate synthesis for dye functionalization of $ZnO@SiO_2$ NPs was carried out by dissolving 1.17 mg (0.003 mmol) of FITC in 0.5 mL of dry DMSO (solution 1). In a round bottom flask 2 µL (0.009 mmol) of APTES were dissolved in 0.5 mL of dry DMSO (solution 2). Afterwards, solution 1 was added to solution 2 and the mixture was stirred over night at RT under exclusion from light. The APTES-FITC conjugate can be stored at 8 °C for up to 2 d.

Synthesis of $ZnO@SiO_2@FITC$ Nanoparticles from Heat-up ZnO Nanoparticles

The synthesis of $ZnO@SiO_2@FITC$ NPs with FITC dye functionalization was performed as described above for the $ZnO@SiO_2$ NPs, but 5 µL of the prefomed APTES-FITC conjugate were added 20 min after the addition of 120 µL TEOS. The following reaction steps were carried out under exclusion from light. The product was stored dispersed in ethanol at 8 °C.

Nanoparticle Characterization

Samples for *transmission electron microscopy (TEM)* were prepared by placing a drop of dilute NP dispersion in cyclohexane on a carbon coated copper grid. TEM images

for the characterization of size and morphology were obtained using a FEI Tecnai 12 equipped with LaB_6 source at 120 kV and a twin-objective together with a Gatan US1000 CCD-camera (2kx2k pixels). High-resolution TEM data were obtained on a FEI Tecnai F30 S-TWIN TEM equipped with a field emission gun and operated at 300 kV. Atomic modelling and electron diffraction simulation were performed by Crystal Maker software.
X-ray diffraction (XRD) patterns were recorded on a Bruker AXS D8 Advance diffractometer equipped with a SolX energy dispersive detector in reflection mode using unfiltered MoKα radiation. Crystalline phases were identified according to the PDF–2 database using Bruker AXS EVA 10.0 software.
Atomic absorption spectroscopy (AAS) measurements were conducted using a Perkin Elmer 5100 ZL AA spectrometer with a Zeeman Furnace Module and a Zn hollow cathode lamp at 213.9 nm and air/acetylene mixture. For Zn^{2+} ion detection in the supernatant of an experimental sample, the sample was diluted with Milli-Q water. For Zn^{2+} ion detection in the residue of an experimental sample or for Zn^{2+} ion concentration determination, the sample was treated with aqua regia over night to dissolve any ZnO and denature any proteins, if applicable. Afterwards the sample was diluted with Mili-Q water. Samples were analyzed using the whole flame width to ensure maximum ionization and reduced matrix effects. A 3-point calibration was carried out with 9 measurements for each concentration. For each sample 9 measurements were performed. Between sample measurements the instrument was rinsed with aqua regia and Milli-Q water.
Cytotoxicity tests were carried out with the non-small cell lung cancer (NSCLC) cell line A549 which was purchased from DSMZ (German Collection of Microorganisms and Cell Cultures, Braunschweig, Germany) and whose identity was verified *via* STR analysis. All cells used in the experiments directly originate from the stocks, which were verified. Cells were maintained in DMEM/Ham's F12 (Sigma-Aldrich, St. Louis, MO) supplemented with 10% FCS (fetal calf serum; Sigma-Aldrich, St. Louis, MO) and antibiotics (100 U/ml penicillin and 100 mg/ml streptomycin) at 37 °C in 5% CO_2. For the analysis of the cellular viability after treatment with the NPs, 10.000 cells per well were seeded in a 96 well plate and were cultivated overnight for adherence. The next day, cells received fresh cell culture medium and were treated with the NP dispersions in Milli-Q water. Cells treated only with the equivalent amount of water served as control. To all wells 10% Alamar Blue (Biozol Diagnostica, Eching, Germany) were added 3 h before the desired readout point and the samples were incubated for 3 h at 37 °C under cell culture conditions. The results were obtained using a plate reader (Fluoroskan Ascent Microplate reader, Thermo Fisher Scientific GmbH, Rockford, USA; ex: 540 nm, em: 600 nm) and normalized to control cells.
Confocal laser scanning microscopy (CLSM) images were obtained with a Leica TCS-SP5 confocal laser scanning microscope. The plasma membrane of the cells was stained with CellMask Orange (Thermo Fisher Scientific GmbH, Rockford, USA).

7

Monitoring Thiol-Ligand Exchange on Au Nanoparticle Surfaces

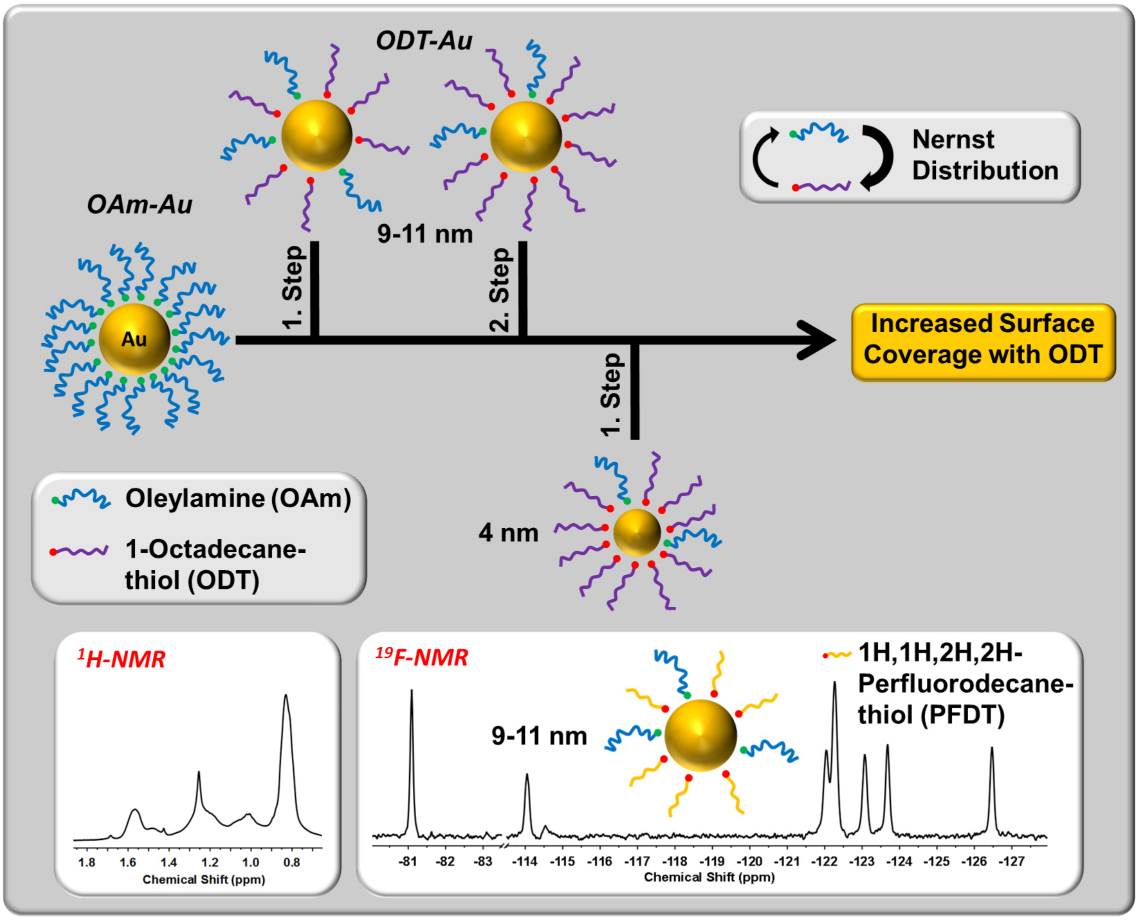

This chapter contains an adapted reproduction of Langmuir 2018, 34 (3), 1700-1710,[491] *reproduced with permission of the American Chemical Society. A detailed Authorship Statement of the publication is attached in the Appendix of this dissertation. Very special thanks goes to* [redacted] *for the excellent collaboration during this project.*

7.1 Abstract

Surface functionalization of nanoparticles (NPs) plays a crucial role in particle solubility and reactivity. It is vital for particle nucleation and growth as well as in catalysis. This raises the quest for functionalization efficiency and new approaches to probe the degree of surface coverage. We present an (*in situ*) proton nuclear magnetic resonance ^{1}H-NMR study on the ligand exchange of oleylamine (OAm) by 1-octadecanethiol (ODT) as a function of the particle size and repeated functionalization on Au NPs. Ligand exchange is an equilibrium reaction associated with Nernst distribution, which often leads to incomplete surface functionalization following "standard" literature protocols. Here, we show that the surface coverage with the ligand depends on (i) the repeated exchange reactions with large ligand excess, (ii) the size of NPs, *i.e.* the surface curvature and reactivity, and (iii) the molecular size of the ligand. As resonance shifts and extensive line broadening during and after the ligand exchange impede the evaluation of ^{1}H-NMR spectra, one- and two-dimensional ^{19}F-NMR techniques (correlation spectroscopy, COSY and diffusion ordered spectroscopy, DOSY) with 1H,1H,2H,2H-perfluorodecanthiol (PFDT) as the fluorinated thiol ligand were employed to study the reactions. The enhanced resolution associated with the spectral range of the ^{19}F nucleus allowed carrying out a site-specific study of thiol chemisorption. The widths and shifts of the resonance signals of the different fluorinated carbon moieties were correlated with the distance to the thiol anchor group. In addition, the diffusion analysis revealed that moieties closer to the NP surface are characterized by a broader diffusion coefficient distribution as well as slower diffusion.

7.2 Introduction

Many properties of nanoparticles (NPs) are dictated by the particle size, morphology and composition of the NP core.[1] In addition, the surface chemistry has a dominant effect both on the size and morphology (*i.e.* nucleation and growth behavior[492, 493]) as well as on targeted application such as catalysis. Ligand mixtures have been used for coating the NPs,[494, 495] where each ligand is supposed to confer a different property to the NPs. The organization of ligands on a NP surface by phase separation can affect the particle properties as well.[496, 497] *In situ* or post-synthetic surface functionalization strategies allow tailoring the particle toxicity[498, 499] and behavior for biosensing, in medical diagnostics and therapeutics, and electronically for optoelectronics.[500–503] Finally, particle-particle interactions through the ligand shell become important at high concentrations and lead to excluded volume effects.[504] This affects particle dynamics and microrheology[505] and plays a crucial role in NP assembly and synthesis of hybrid materials, with practical applications in drug delivery,[64] making pigments,[506] nano-clays and -composites,[507] biominerals[508] and cement industry.[509]

This raises the quest to understand the mechanism of surface functionalization and its efficiency. Several key factors for surface modification have been identified such as the dynamics of organic ligand exchange on and off the surface and temperature-dependent dynamic solvation.[21] These factor have led to different modification strategies often based on chemisorption according to Pearson's hard and soft acids bases (HSAB) principle.[133, 139] This has been demonstrated for the functionalization of Pearson-hard transition metal oxides[93, 143] with alkoxy, carboxylate or catechol ligands. For chalcogenide or noble metal particles such as CdSe or Au, the Pearson soft character makes phosphines[510] or thiols as suitable ligands for their functionalization, as demonstrated by Murray[494] and Brust.[511]

Nuclear magnetic resonance (NMR) spectroscopy is proving to be a powerful analytical tool for monitoring the NP surface chemistry[512, 513] and ligand exchange.[514–516] Its advantages are the fast and non-destructive samples analysis, identification of ligands, and the potential to monitor ligand exchange reactions, which may be viewed as nucleophilic substitution at the metal centers on the NP surface.[517, 518] The analysis of the dynamic exchange equilibrium of ligands with two-dimensional (2D) NMR techniques such as diffusion ordered spectroscopy (DOSY)[519] and nuclear Overhauser effect spectroscopy (NOESY) are particularly useful to differentiate between unbound and coordinated ligands.[517] The driving forces for ligand exchange and solubility effects can be unraveled by making use of the high sensitivity of heteronuclei such as ^{19}F. Hens and coworkers[520, 521] have investigated the binding motifs and surface chemistry of HfO_2 NPs by 2D NMR spectroscopy. They demonstrated that ligand displacement reactions can turn surfactants into reactants for nanocatalysis which overcomes the accessibility problem of catalytically active sites.[522]

Many NPs are prepared in solution using "one-pot" synthesis where a precursor is decomposed in a high boiling point solvent in the presence of a reducing agent and surfactants, typically oleic acid (OAc), oleylamine (OAm) or a mixture of both.[523] Because these surface ligands are hydrophobic the particles have to be re-functionalized at a later stage with a hydrophilic ligand, carrying a polyether backbone or a carboxylate end group.[524] Here we present a detailed study of a ligand exchange reaction where oleylamine (OAm) is replaced by 1-octadecanethiol (ODT) on 9-11 nm Au NPs. The reaction was monitored using 1D and 2D ^{1}H-NMR spectroscopy. Additionally, 1D and 2D ^{19}F-NMR spectroscopy experiments were carried out using 1H,1H,2H,2H-perfluorodecanthiol (PFDT) instead of ODT to monitor the NP-ligand interaction. Because of the inherent resolution related with the broad spectral range of the ^{19}F nucleus, the analytical scope is greatly enhanced. A site-specific evaluation of the thiol chemisorption related shift and broadening of the resonance frequencies of the different fluorinated carbon moieties was accomplished. Moreover, the width and shift of the distribution of the respective site-related diffusion coefficients could be evaluated and linked to the spatial distance to the thiol anchoring group of the ligand. Higher degrees of surface functionalization could be achieved by a second functionalization or with smaller NPs (here 2.8 nm Au NPs).

Because ligand exchange is an equilibrium reaction, the refunctionalization follows a Nernst distribution[525] and does not proceed in a single step. It is dependent on (i) the repeated ligand exchange that requires a large ligand excess, (ii) the size of the NPs, *i.e.* the curvature and reactive surface, and (iii) the length and mass of the ligand, which was studied for the two ligands ODT and PFDT. The surface coverage of the functionalized Au NPs was also traced by the shift of the surface plasmon band, thermogravimetric analysis (TGA) and Raman spectroscopy.

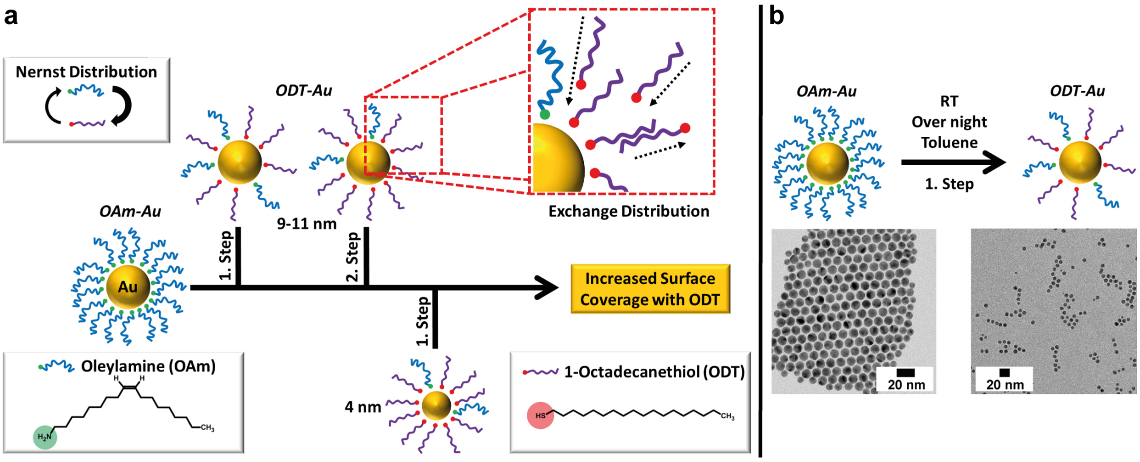

Figure 7.1: (a) Schematic representation of the (repeated) ligand exchange reaction from OAm to ODT on the Au NP surface with change of the binding moiety from nitrogen to sulfur shown for two different Au NP sizes (4 nm and 9-11 nm). (b) TEM images of functionalized OAm-Au and ODT-Au NPs.

7.3 Results and Discussions

The 9-11 nm OAm-Au NPs were functionalized with the unsaturated long-chain amine oleylamine (OAm) during the synthesis. TEM analysis (Figure 7.1) revealed the particles to have a diameter of 10.3 nm with 10% size variation. These particles were treated in an overnight ligand exchange reaction with 1-octadecanethiol (ODT) in toluene to replace the OAm surfactant. The ODT C_{18} ligand has a comparable chain length as OAm. The thiol head group allows a more tenacious d chemisorption on the Pearson soft Au surface, thereby driving the ligand exchange reaction electronically. After surface functionalization the ODT-Au NPs had a comparable diameter of 9.9 nm with approximately 10% size variation (Figure 7.1). Additionally, a second fraction of 4.4 nm ODT-Au NPs (22% standard deviation in size) emerged. This can be explained by the prolonged reaction time in unpolar toluene which supports the ligand exchange by hydrophobic interactions and also permits Ostwald ripening and fusion.[19, 362]

7.3.1 Analysis of the Initial Surface Condition by ^{1}H-NMR Spectroscopy

The formation of the OAm-Au NPs was studied by NMR spectroscopy to characterize the initial surface condition before the ligand exchange reaction. After the purification steps it is expected that the stabilizing surfactant OAm from the synthesis is still present on the NP surface. Figure 7.2a shows the ^{1}H-NMR spectra of the OAm-Au NPs (top) and the OAm ligand (for comparison) with the corresponding chemical structure (bottom). The OAm spectrum clearly shows signals for the terminal methyl group (A, t, 0.87 ppm), the α-methylene group (E, t, 2.67 ppm), the ethylene protons

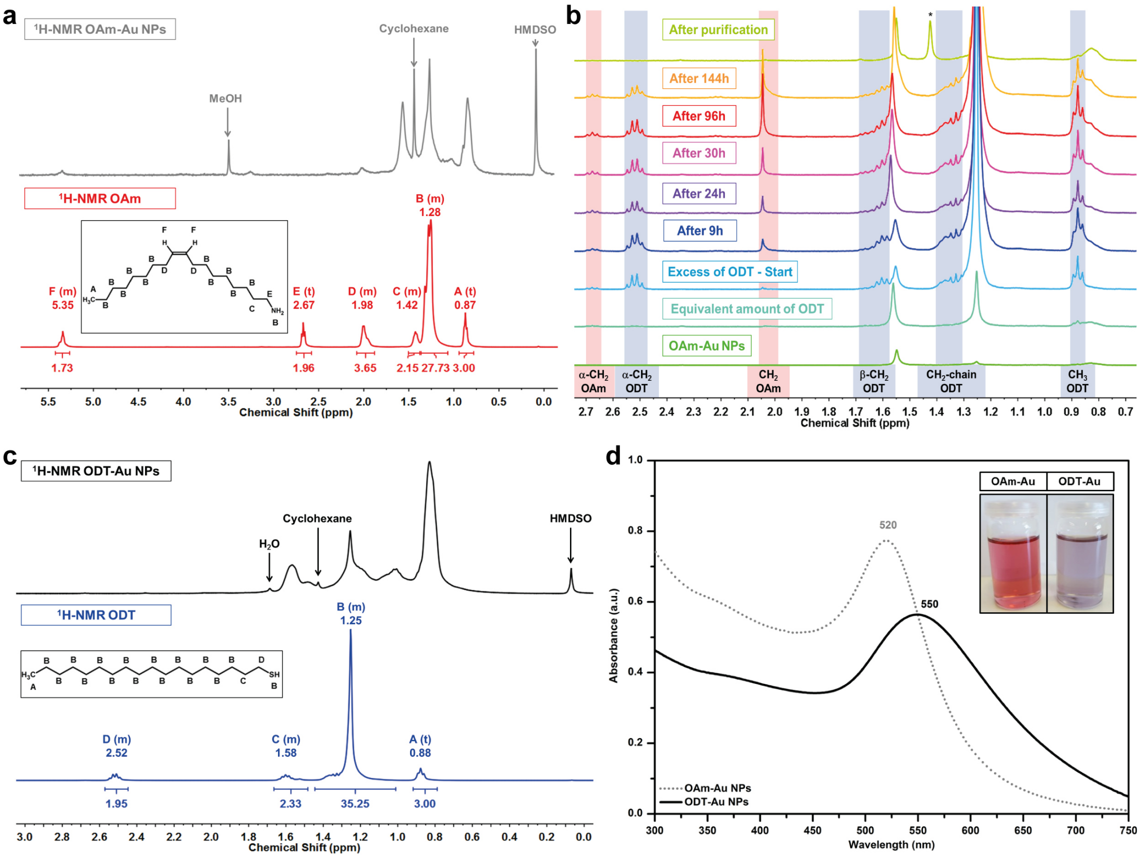

Figure 7.2: (a) ^{1}H-NMR spectra of OAm-Au NPs (top) and pure OAm ligand (bottom). HMDSO = hexamethyldisiloxane from the NMR tubing lid. (b) *In situ* ^{1}H-NMR spectra during functionalization of OAm-Au NPs with ODT. Black * marks cyclohexane from purification. NP concentration is not constant due to aliquots taken for NMR measurement. (c) ^{1}H-NMR spectra of ODT-Au NPs after functionalization (top) and pure ODT ligand (bottom). (d) UV-vis spectra of OAm-Au and ODT-Au NPs along with photographs of NPs dispersed in cyclohexane.

at 5.35 ppm (F, m) and the methylene groups adjacent to the double bond (D, m, 1.98 ppm). The methylene protons (B) of the alkyl chain as well as the amine protons are characterized by similar shielding and resonate at similar frequencies, thus giving rise to a broad signal with a maximum centered at ca. 1.28 ppm. The signals of the β-methylene protons C (m, 1.42 ppm) are shifted slightly down-field compared to the signal of the alkyl chain. In comparison, the spectrum of the OAm-Au NPs shows not only lower intensity due to the reduced ligand concentration on the NP surface but also different integrals for the respective resonances. The signals of the A, B, D, and F protons are detected at comparable chemical shifts to the free ligand. However, the peaks of the β-methylene (C) and especially the α-methylene protons (E) undergo a low field shift to 1.55 ppm and 3.25 ppm, respectively. This results from the chemisorption of the head group to the NP surface which affects the signals of the nearest methylene groups.[517, 526]

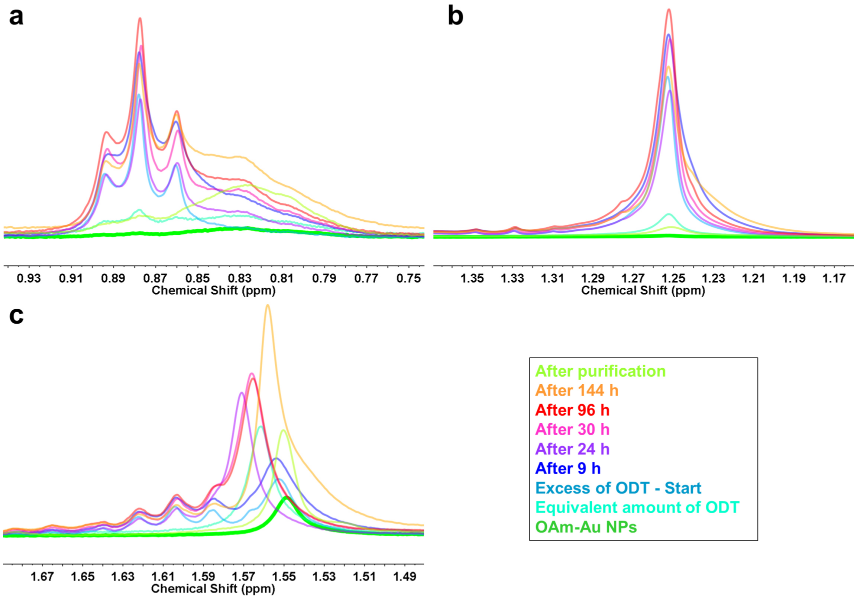

Figure 7.3: Superimposed ^{1}H-NMR spectra of signals at (a) 0.88 ppm, (b) 1.25 ppm and (c) 1.57 ppm during *in situ* ligand exchange reaction from OAm to ODT on Au NPs.

7.3.2 *In Situ* Monitoring of Surface Functionalization

Ligand exchange is an equilibrium reaction following the classical Nernst distribution where a dissolved compound is in equilibrium between two phases, *i.e.*, in this case, the ligand between the surface of the NPs and the solvent to disperse them.[525] The relation between the surface area and the reactivity of the NPs, the type of the anchor group, solubility and concentration of the ligand in the solution may have an impact on the exchange equilibrium. To gain insight into the ligand exchange process as a function of the chain length and functional head group we performed *in situ* ^{1}H-NMR spectroscopy. Figure 7.2b shows a selection of ^{1}H-NMR spectra recorded during the ligand exchange process together with the ^{1}H-NMR spectra of OAm-Au NPs before the start of the exchange process and ODT-Au NPs after purification (a detailed superimposed view of the signals at 0.88 ppm, 1.25 ppm and 1.57 ppm is given in Figure 7.3).

The ^{1}H-NMR spectrum of OAm functionalized Au NPs reveal broad signals between $\approx$ 0.8 ppm and $\approx$ 1.5 ppm related with the OAm chemisorption on the NP surface (see Figure 7.2a). The OAm capped NPs were dispersed in $CDCl_3$ using stirring under Ar atmosphere. In the next step, an equimolar amount of the ODT ligand was added. Aliquots of the reaction mixture were taken at specific reaction times, and the respective ^{1}H-NMR spectra were recorded. After 24 h no visible change occurred to the broad peaks. However, weak resonances of the free ODT ligand appeared (Figure 7.2b, emphasized in blue). This is not unexpected as the ODT ligand may be distributed between the solution phase and the NP surface, which is functionalized with the OAm ligand. The signals of the bound ODT ligand are

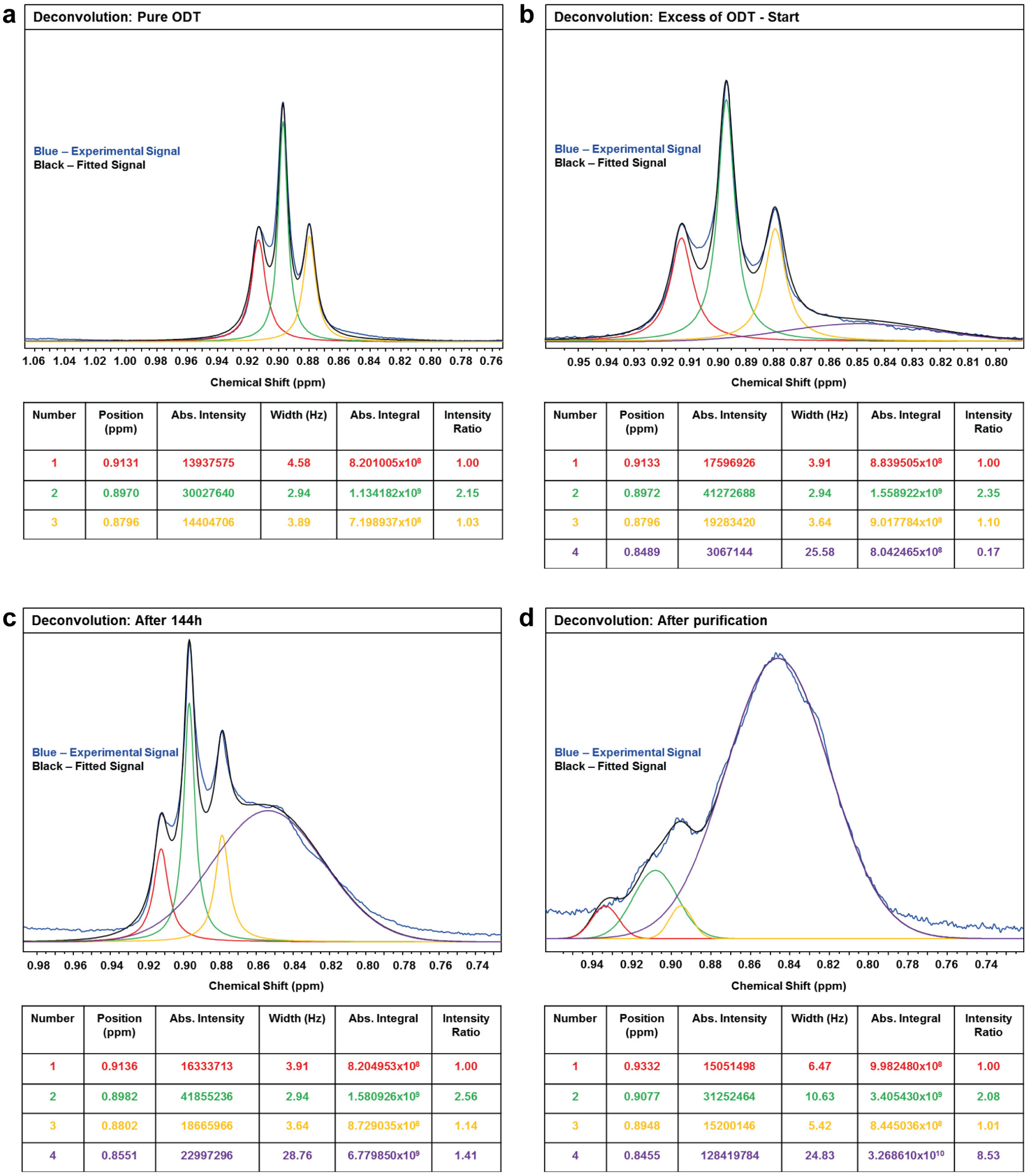

a

Number	Position (ppm)	Abs. Intensity	Width (Hz)	Abs. Integral	Intensity Ratio
1	0.9131	13937575	4.58	8.201005×10^{8}	1.00
2	0.8970	30027640	2.94	1.134182×10^{9}	2.15
3	0.8796	14404706	3.89	7.198937×10^{8}	1.03

b

Number	Position (ppm)	Abs. Intensity	Width (Hz)	Abs. Integral	Intensity Ratio
1	0.9133	17596926	3.91	8.839505×10^{8}	1.00
2	0.8972	41272688	2.94	1.558922×10^{9}	2.35
3	0.8796	19283420	3.64	9.017784×10^{8}	1.10
4	0.8489	3067144	25.58	8.042465×10^{8}	0.17

c

Number	Position (ppm)	Abs. Intensity	Width (Hz)	Abs. Integral	Intensity Ratio
1	0.9136	16333713	3.91	8.204953×10^{8}	1.00
2	0.8982	41855236	2.94	1.580926×10^{9}	2.56
3	0.8802	18665966	3.64	8.729035×10^{8}	1.14
4	0.8551	22997296	28.76	6.779850×10^{9}	1.41

d

Number	Position (ppm)	Abs. Intensity	Width (Hz)	Abs. Integral	Intensity Ratio
1	0.9332	15051498	6.47	9.982480×10^{8}	1.00
2	0.9077	31252464	10.63	3.405430×10^{9}	2.08
3	0.8948	15200146	5.42	8.445036×10^{8}	1.01
4	0.8455	128419784	24.83	3.268610×10^{10}	8.53

Figure 7.4: Deconvolution of the 0.84 ppm ^{1}H-NMR signal of the *in situ* ODT functionalization of OAm-Au NPs. (a) Deconvolution of pure ODT ligand as comparison. (b) Deconvolution at the start of the reaction after an excess of ODT was added. (c) Deconvolution after 144 h of reaction time. (d) Deconvolution after purification of the NPs and removal of excess ligands.

weak, and broadened and overlap with the dominating ^{1}H resonances of the attached OAm surface ligand.

To enhance the ligand exchange efficiency, a 15-fold excess of ODT was added. This

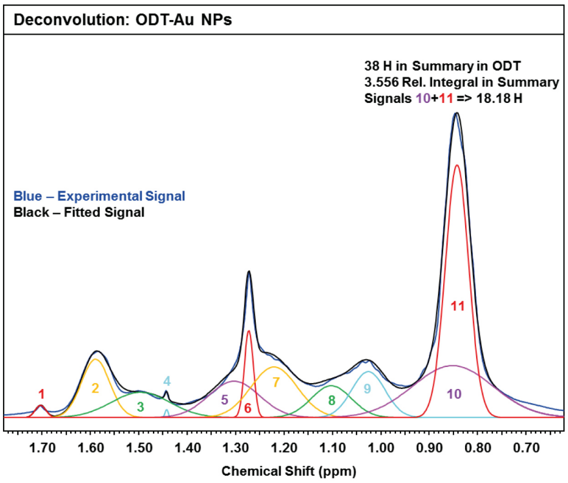

Number	Position (ppm)	Abs. Intensity	Width (Hz)	Abs. Integral	Rel. Integral	Proton Equi-valent
1 water	1.7037	12682607	10.34	1.305484×10^{9}	0.022	-
2	1.5900	59477724	27.40	1.622361×10^{10}	0.279	2.97
3	1.4972	25663638	56.91	1.453949×10^{10}	0.250	2.66
4 cyclo-hexane	1.4434	8537023	2.97	2.524093×10^{8}	0.004	-
5	1.3039	37274668	49.28	1.828635×10^{10}	0.314	3.35
6	1.2735	89093656	8.63	7.654205×10^{9}	0.131	1.40
7	1.2214	52012276	44.82	2.320706×10^{10}	0.399	4.25
8	1.1032	32689940	38.78	1.262015×10^{10}	0.217	2.31
9	1.0268	46935836	32.41	1.514525×10^{10}	0.260	2.77
10	0.8524	52890564	78.08	4.111010×10^{10}	0.706	7.52
11	0.8436	257092496	22.75	5.822849×10^{10}	1.000	10.66

Figure 7.5: Deconvolution of the ODT-Au NPs ^{1}H-NMR spectrum.

led to a higher signal intensity of the free ODT ligand (Figure 7.2b, emphasized in blue). Additionally, two new signals appeared at chemical shifts > 2 ppm (Figure 7.2b, emphasized in red). These signals (assigned to free OAm) indicate the start of the ligand exchange reaction. The intensity of these signals increased with time and with concentration of the new ligand. As the ODT ligand concentration on the NP surface increased, changes associated with ODT appeared in the ^{1}H-NMR spectrum. The broad resonance with a maximum at ca. 0.84 ppm, observed as a shoulder next to the methyl group of the free ODT (a triplet), emerged and its intensity increased with time. The initial integral ratio between both signals was 0.17, and it changed to 1.41 after 144 h reaction time (deconvolution of the 0.84 ppm signal in Figure 7.4). Similar changes were observed for the broad signals at 1.25 ppm and 1.57 ppm, as the latter one undergoing a shift as well. After the exchange reaction (6 days total reaction time of the *in situ* experiment) the particles were purified. After removing the free OAm ligand and the excess of the ODT ligand by washing the corresponding signals completely disappeared from the ^{1}H-NMR spectrum. Thus, the exchange is a function of time and ligand concentration. It is a long term process starting with the physisorption of ODT on the NP surface, followed by the conversion into chemisorbed thiolate by release of the thiol hydrogen and additional reorganization of ODT as suggested in a study of Woehrle *et al.* where broadening and shifting of resonances were monitored.[526]

For clarity the ^{1}H-NMR spectra of the ODT-Au NPs and the pure ODT ligand are presented separately in Figure 7.2c. The signals of the free ligand can be assigned to the methyl end-group (A, t, 0.88 ppm), the 15 methylene groups of the chain (B, m, 1.25 ppm), the β-methylene group (C, m, 1.58 ppm) and the α-methylene group (D, m, 2.52 ppm). The ODT-Au NPs have a different spectrum where line broadening associated with the restricted mobility of the ligands attached to the NPs was observed. A slower molecular tumbling and thus higher rotational correlation times occur owing to the larger hydrodynamic radius of the NP-ligand core-shell structure (compared to the free ligand). This reduces the transverse T_2-relaxation.[517] As the T_2-relaxation is inversely correlated with the full width at half-maximum of the signals of the resonating nuclei, signal broadening should occur for faster relaxation.[527] On the other hand, the higher rotational freedom of the free ligand results in less effective T_2-relaxation[517] and sharper signals unless there is an unfavorable motional regime. Thus, the ^{1}H resonances of the ODT-Au NPs were detected as broad peaks between 0.7 and 1.7 ppm. As the integration of this area is difficult due to the merging signals, we deconvoluted the ^{1}H spectrum (Figure 7.5). The signal centered at ≈ 0.84 ppm could be fitted with two singlets with a fwhm of ≈ 78 Hz and ≈ 23 Hz. As it possesses the highest area equivalent to ≈ 18 protons (out of 38 protons in ODT) it contains most likely some of the methylene chain protons. This probably originates from a bending of the ODT molecules and a close proximity to the NP surface due to low coverage density (see also *vide infra*). This points towards a shift of all signals because of the better chemisorption of ODT to the NPs. Especially the α- and β-methylene signals (D and C) are broadened and largely shifted or they overlap with this intense resonance as expected for thiols bound on Au NP surface.[528] Still, a full assignment of all signals of the deconvoluted spectrum remains a challenge. Changes of the chemical shift may arise from ODT adsorption to different crystallographic sites on the Au surface, from coupling of ^{1}H resonances to conduction band electrons of the metallic Au NPs, or from complex diffusion dynamics.[529]

The exchange reaction was confirmed independently by UV-vis spectroscopy. Figure 7.2d shows the UV-vis spectra of OAm-Au and ODT-Au NPs dispersed in cyclohexane. The surface plasmon resonance (SPR) of the Au NPs is centered at 520 nm. The functionalization with the thiol ligand leads to a red-shift of the maximum to 550 nm. The color change of the solution from red to purple is visible even with the naked eye. For Au NPs the maximum of the SPR linearly depends on the refractive index of the apolar solvent.[530] Therefore, we used cyclohexane for both, OAm-Au and ODT-Au NPs. Hence, the red shift can be assigned to a strong Au-S chemisorption resulting in a significant induction of charge redistribution and electron donation. Besides charge redistribution, a contribution from particle agglomeration may be possible as indicated through the width of the SPR.[530, 531]

7.3.3 2D ^{1}H-NMR Spectroscopy Shows the Presence of an Dynamic Exchange Equilibrium and Unbound Ligands

Some of the most suitable NMR techniques to study functionalization of NPs surfaces and chemical exchange are related with the introduction of the second dimension for the diffusion coefficient and the respective chemical shift. We examine here the completeness of the exchange reaction and the presence of unbound ligands on the OAm-Au and ODT-Au NPs by ^{1}H diffusion ordered spectroscopy (DOSY) (Figure 7.6a and b). In a DOSY pseudo 2D-experiment the diffusion coefficient is correlated with the chemical shift by applying a pulsed gradient field of varying strength to

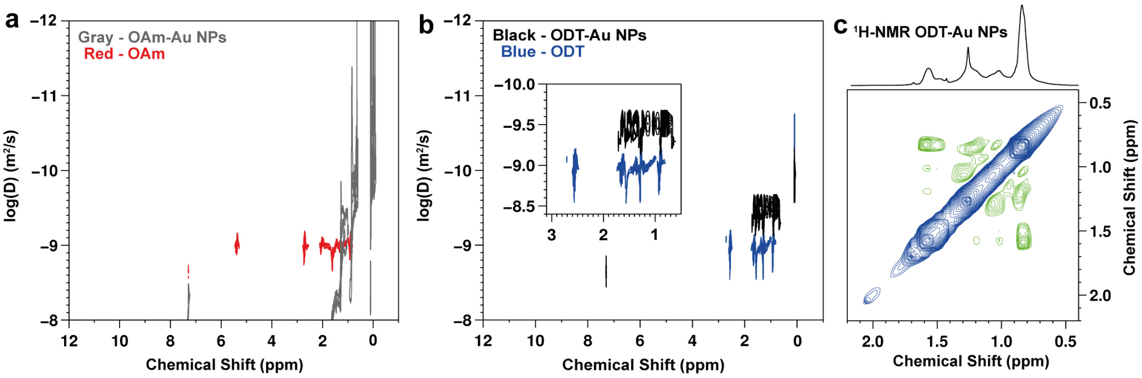

Figure 7.6: ^{1}H-DOSY-NMR spectra of (a) OAm-Au NPs along with the free OAm ligand and (b) ODT-Au NPs along with the free ODT ligand. (c) ^{1}H-NOESY-NMR spectrum of ODT-Au NPs. Blue color shows the negative phase corresponding to the chemisorbed ODT on the Au surface and green color shows the positive phase corresponding to the free ODT ligand.

obtain an exponential decay of the ^{1}H-resonance as a result of the molecules diffusing out of the excitation range.[517] A diffusion coefficient (D) of about 10^{-9} m^2/s was obtained from the diffusion analysis for the free OAm ligand, whereas the OAm-Au NPs are characterized by a significantly lower D value because of the higher molecular weight. Also a noticeable signal broadening (Figure 7.6a) resulting from the particle size and surface functionalization distributions was obtained.[147, 527] In the diffusion range of the functionalized NPs no signals for the free OAm ligand were found, confirming that no excess free OAm ligand was present. In Figure 7.6b the free ODT ligand displays a diffusion coefficient of about 10^{-9} m^2/s as well. The diffusion coefficient of the ODT-Au NPs was reduced to $10^{-9.5}$ m^2/s with a smaller distribution because of the stronger chemisorption of the sulfur compared to the amine ligands. The ^{1}H-^{1}H nuclear Overhauser effect spectroscopy (NOESY) is a powerful tool to distinguish between bound and unbound ligands. It was applied here (Figure 7.6c) to check for the existence of unbound ligand after the exchange reaction and removal of excess free ODT ligand (*vide supra*, DOSY spectra, Figure 7.6b). The nuclear Overhauser effect (NOE) can be observed when two dipolar-coupled protons relax simultaneously. This can happen *via* two different pathways: (i) Both spins can flip together in the same direction (double quantum transition, W_2) or (ii) *via* a "flip-flop" process where both spins simultaneously flip in opposite directions (zero quantum transition, W_0).[532] The dominating pathway depends on the rotational correlation time τ_c of the molecule that the protons are part of. For small molecules with high frequency motions a positive NOE is observed as τ_c is low and $\tau_c\omega_0 \ll 1$, where ω_0 is the NMR spectrometer frequency. For larger molecules in the spin diffusion limit a strong negative NOE is observed as τ_c is high and $\tau_c\omega_0 \gg 1$. The positive NOE is associated with the W_o spin cross-relaxation pathway where the positive sign is related to the positive cross-peaks in the NOESY spectrum. For negative NOE, associated with the W_2 spin cross-relaxation, the signs are equal, thus

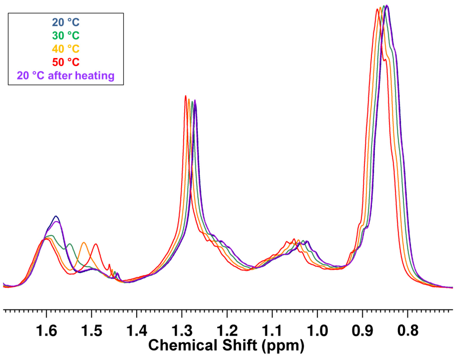

Figure 7.7: Temperature dependent ^{1}H-NMR spectra of ODT-Au NPs recorded at 20, 30, 40, and 50 °C and again after cooling to 20 °C. Signals are scaled to equal intensity.

providing both negative cross- and diagonal-peaks.[147, 517, 531, 532] The observation of cross-peaks with signs different from those of the diagonal peaks indicates the presence of unbound or free ligand. When the signs of the diagonal and cross-peaks are equal, only bound ligands are present in the system at the respective experimental conditions. By convention for small molecules the diagonal-peaks are phased negative, thus obtaining positive signs for the cross-peaks in case of a positive NOE. As observed in the NOESY spectrum (Figure 7.6c) for the ODT-Au NPs strong positive NOE cross-peaks (green) are present in addition to the diagonal signals (blue), indicating the existence of unbound ligand. This implies a dynamic exchange equilibrium for solvent-dispersed functionalized particles. The presence of excess ODT could be excluded because of the washing procedure and because no traces of free ODT could be detected in the ODT-Au NPs DOSY spectrum. The observed results could be caused by Oswald ripening associated with some release of ODT or by intermolecular interactions and exchange within ligand layers of adjacent NPs.[533] This would not lead to a release of free ODT (detectable by DOSY), but to the detection of unbound and mobile thiol in the NOESY spectrum, demonstrating the dynamic nature of the ligand coating.

7.3.4 Temperature Dependent ^{1}H-NMR Spectroscopy

To further investigate the dynamic equilibrium and the effect of molecular tumbling for the ODT-Au NPs, temperature-dependent ^{1}H-NMR spectra were recorded (Figure 7.7). The multiplet structures of the signals with $\approx$ 1.0 ppm and $\approx$ 1.2 ppm as peaks on top of a broad resonance (typical for surface bound ligands) indicate the presence of unbound ligands. The multiplet structure was better resolved upon heating to 50 °C. This suggests an enhanced ligand detachment from the NP surface in the solvent. An alternative explanation may be the presence of a larger core-shell structure with a second inverted ligand layer where the mobility of the respective surfactant molecules is enhanced.[534] At the same time the main signals at 0.83 ppm and 1.25 ppm are shifted to a lower field by 8 Hz and the full width at half maximum

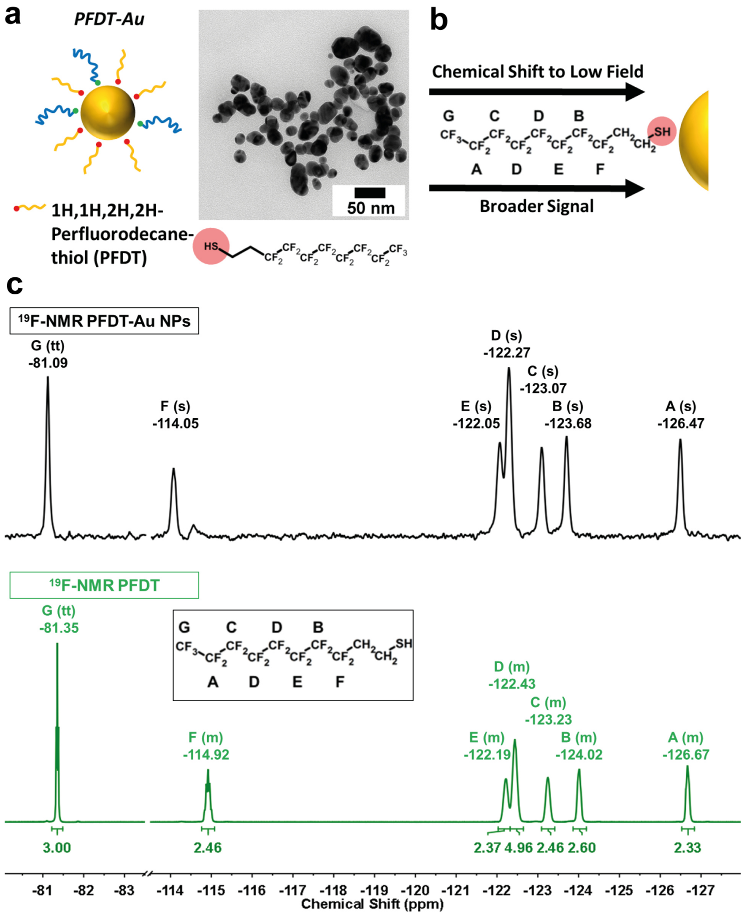

Figure 7.8: (a) Schematic representation of PFDT-Au NPs with the sulfur binding moiety along with the TEM image of functionalized Au NPs. (b) Schematic representation of the dependence of the chemical shift and signal width on the distance of the fluorinated carbon moiety to the NP surface. (c) ^{19}F-NMR spectra of PFDT-Au NPs (top) and the pure PFDT ligand (bottom).

(fwhm) for both signals is reduced by 8.2% and 14.0%, respectively. Furthermore, the signals between 1.40 ppm and 1.65 ppm are better resolved. These changes are related with faster molecular tumbling at higher temperature. The process is reversible. Cooling back to 20 °C recovers the spectrum of the ODT-Au NPs before heating.

7.3.5 ^{19}F-NMR Spectroscopy Allows the Site-Specific Evaluation of Resonance Signals and Molecular Surface Diffusion

The strong line broadening observed in the ^{1}H-NMR spectra of both, OAm-Au NPs and ODT-Au NPs may be caused macroscopically by the molecular dynamics or the magnetic susceptibility of a material. Microscopic origins may be the electronic environment of the ^{1}H nuclei and the effect of adjacent nuclear and electronic spin interactions.[535] To address this question the OAm ligand of 9-11 nm Au NPs was exchanged with 1H,1H,2H,2H-perfluorodecanthiol (PFDT). The ^{19}F core is ideally suited because its natural abundance is 100% and its relative sensitivity is close to that of ^{1}H. In addition, the molecular weight may be used to resolve the spectra of surface ligand mixtures by NMR diffusion techniques. Finally, the chemical shift range of ^{19}F is expanded compared to that of ^{1}H and therefore offers a greatly improved resolution[536] and the spectra remain simple because both ^{1}H and ^{19}F are spin 1/2 nuclei. Thus, peak splittings due to electronic interactions between neighboring nuclei are similar. Therefore, the different CF_2 moieties could be resolved individually which allowed conducting diffusion analysis with a chemical shift resolution. Still, instrumental difficulties related with the inhomogeneous excitation of the ^{19}F broad spectral range may arise for the 2D spectra.[537]

Figure 7.8a shows the schematic representation of PFDT functionalized Au NPs (PFDT-Au) including a TEM image revealing fusion of the particles due to Oswald ripening. This may be caused by reduced particle dispersability as a result of the short and heavy PFDT ligand chain. Figure 7.8b displays the changes in the chemical shift and signal width as a function of the distance to the NP surface. Figure 7.8c shows the ^{19}F-NMR spectra of the PFDT-Au NPs and the pure PFDT ligand. Only three signals of the fluorinated chain could be assigned unambiguously from the ^{19}F-NMR spectra. The terminal CF_3 group of the PFDT ligand (G, tt) resonates at -81.35 ppm, the lowest field compared to all other peaks. The signal was observed as a triplet of triplets (Figure 7.9) due to the $^{4}J_{FF}$ and $^{5}J_{FF}$ indirect coupling interactions with coupling constants of 9.9 Hz and 3.8 Hz. It is known that linear perfluorinated compounds are characterized by rather small vicinal $^{3}J_{FF}$ couplings unlike the dominating $^{4}J_{FF}$ couplings.[538] The neighboring CF_2 group (A, m) resonates typically at the highest field (-126.67 ppm) as a featureless multiplet. The signal of the CF_2 group (F) adjacent to the methylene groups[537] was the only other signal assigned from the ^{19}F spectrum. It resonates at -114.92 ppm with a resolved fine splitting structure. All other signals (B, C, D, and E) feature broad complex structures due to the contribution of several transitions associated with long range couplings between the CF_2 groups in the middle of the molecule.

As the assignment of the remaining signals was not obvious from the 1D spectrum, ^{19}F correlated spectroscopy experiments (COSY) were performed to resolve the coupling interactions (Figure 7.10a). The strong cross peaks between the CF_2 signals G and C (m, -123.23 ppm) observed in the ^{19}F-COSY spectrum of PDFT showed that C is the next nearest neighbor of G as $^{4}J_{FF}$ couplings dominate. Two additional strong correlations were detected between the C and D (m, -122.43 ppm) CF_2 groups and between the B and D (m, -124.02 ppm) CF_2 groups. Therefore C and D as well as D and B are next nearest neighbors. An additional $^{4}J_{FF}$ coupling between the signals A and D as well as the integration of signal D (4F) supported these assignments. Finally, a well resolved cross peak between the CF_2 groups F and E (m, -122.19 ppm) indicates that E is the next nearest neighbor of F. A COSY spectrum of the PFDT-Au NPs (Figure 7.10b) supported these assignments, because the $^{4}J_{FF}$ cross peaks were identical with those in the COSY spectrum of PFDT.

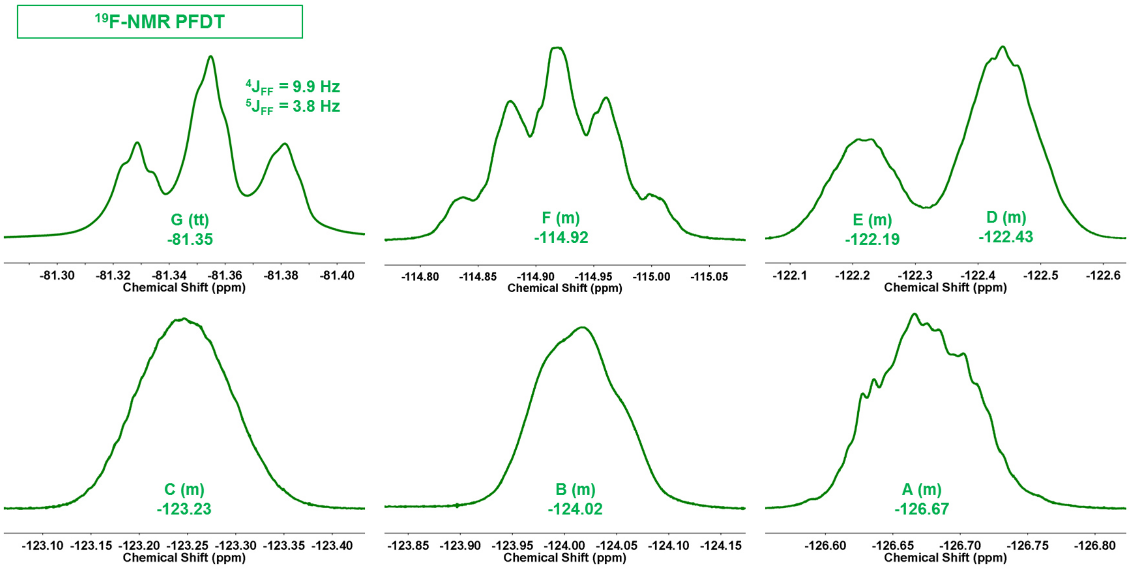

Figure 7.9: Signal analysis of the ^{19}F-NMR spectrum of PFDT ligand.

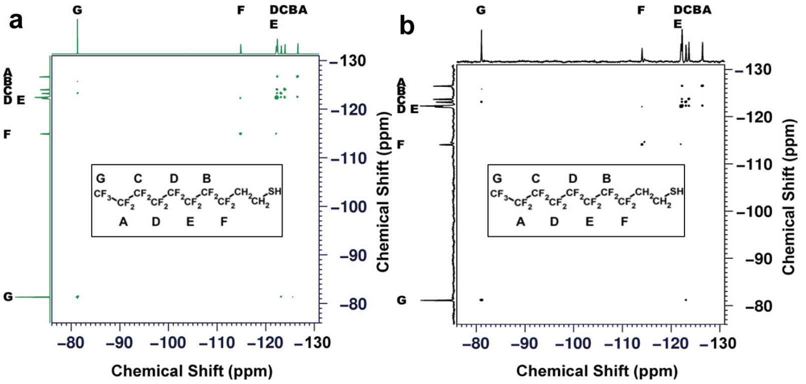

Figure 7.10: ^{19}F-^{19}F-COSY-NMR spectrum of (a) PFDT ligand and of (b) PFDT-Au NPs.

These results were compared to the ^{19}F-NMR spectrum of the PFDT-Au NPs (Figure 7.8c). The signals could be assigned in the same manner as for the free ligand. Only the tt structure of signal G (-81.09 ppm) was maintained due to line broadening resulting from the attachment of PFDT to the Au NPs. All other signals were significantly broadened. The PFDT-Au resonances are low field shifted between 52.7 Hz and 327.5 Hz. The maximum shift of 327.5 Hz was observed for signal F closest to the NP surface (Figure 7.8b).[529] Electronic interactions related to the shift of the resonance frequencies to a lower field (due to ligand coordination, *i.e.* complexation shift)[539] have only a limited effect: It is confined to the binding site and decreases along the alkyl chain. The CF_2 group closest to the anchor SH moiety has the highest shift of the resonance frequency related to the ligand-to-metal electronic donation. As a result of this interaction the electronic density is

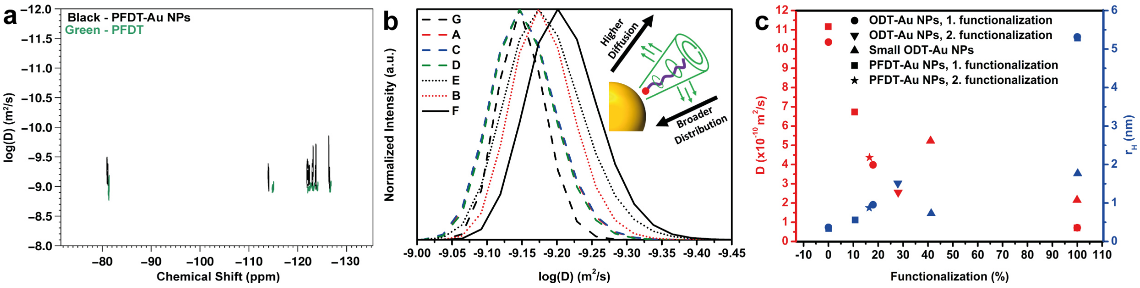

Figure 7.11: (a) ^{19}F-DOSY-NMR spectrum of PFDT-Au NPs along with the free PFDT ligand. (b) Diffusion coefficient D for each ^{19}F-signal of PFDT-Au NPs extracted from the ^{19}F-DOSY-NMR spectrum of PFDT-Au NPs in (a). Signals are scaled to equal intensity. The inset shows the dependence of D and fwhm of the D distributions from the distance to the NP surface. (c) Thiol-functionalization efficiency for different types of Au NPs with ODT and PFDT calculated from D and r_H.

redistributed and the bonds are more polarized in comparison to the free ligand.
Fluorinated ligand molecules can be spatially encoded by pulsed field gradients depending on their position on the surface. When they move after this encoding during the subsequent diffusion time, their new position can be decoded by a second gradient. The NMR signal intensity is attenuated depending on the diffusion time. The spectra resemble chromatograms in some aspects while providing NMR information that is used for signal assignment. The ^{19}F-DOSY spectra of the free PFDT ligand and the functionalized PFDT-Au NPs (measured with 100 ms diffusion time) are shown in Figure 7.11. Different from the ^{1}H-DOSY experiments, the ^{19}F signals of the bound PFDT ligand were well resolved. Therefore, the distributions of the D values for each signal in the diffusion dimension could be extracted from the DOSY spectra. They are shown in Figure 7.11b as overlay for the PFDT-Au NPs to facilitate the analysis of the spectral changes: The shift of the diffusion coefficient and the fwhm of the D distribution are related to the chemisorption of PFDT on the Au surface. A site-specific dependence of the diffusion coefficient (D) and the D distribution may explain the line broadening and the low field shift observed in the 1D ^{19}F-NMR spectrum in terms of macroscopic molecular dynamics (Figure 7.8b and c).

The maxima of the distributions, reported as log(D) values (-9.15 m^2/s to -9.20 m^2/s) for the PFDT-Au NPs, are significantly lower compared to those of the free ligand (-8.96 m^2/s). Additionally, the values for fwhm increase from 0.01 m^2/s for the free ligand to an average of 0.08 m^2/s for the bound ligand. The widths of the D distributions and the shifts of the maxima of the D distributions in Figure 7.11b are related to the distance from the NP surface: The closer a CF_2 moiety to the surface SH group the lower the D value and the higher the fwhm of the D distribution (Figure 7.11b insert). Thus, the log(D) value for the terminal CF3 group (G) is -9.15 m^2/s, whereas a log(D) value of -9.20 m^2/s was derived for the CF_2 group (F) closest to the SH group. Likewise, the fwhm of the D distributions increases in close

proximity to the NP surface: The terminal CF_3 group (G) has a value of 0.07 m^2/s compared to 0.08 m^2/s for the (F) CF_2 group adjacent to the SH anchor group.
These gradual changes most probably result from the rotational freedom of the fluorinated alkyl chains (Figure 7.11b insert). Furthermore, low diffusion times for large molecules may be associated with translations or rotations of flexible chain segments rather than with the diffusion of the whole molecules.[540, 541] Isotropic tumbling of the NPs, movements of the ligand chain with respect to the NP surface and movements of two surface bound ligands with respect to each other can contribute to T_2 relaxation and signal broadening.[542] The isotropic tumbling of the NPs is in the slow motion regime. This leads to stronger dipole-dipole (DD) couplings and chemical shift anisotropy (CSA) due to restricted chain mobility close to the thiol anchor group on the NP surface and leads to shorter T_2 relaxation times, while rotations of the alkyl chains decrease the DD couplings and increase the T_2 relaxation times. The contribution of alkyl chain movements with respect to each other is difficult to evaluate. It depends on the distance between the binding sites, the degree of surface functionalization and the motional behavior of each ligand. It may lead to shorter T_2 relaxation values for small NPs with more binding sites and a hindered ligand rotation.[542]

A DOSY experiment with a longer diffusion time (300 ms) was carried out to analyze the motional behavior of the ligand molecules and the diffusion of the functionalized NPs. Similar results were observed: The diffusion coefficients and their distributions along the fluorinated alkyl chain were retained. However, the distribution of the diffusion coefficient for the CF_2 moiety closest to the NP surface (F) was significantly broader compared to the experiment with 100 ms diffusion time. Moreover, the intensity of the F signal in the diffusion dimension was strongly reduced. The latter is related to the fact that long diffusion times eventually lead to a signal loss. This signal loss is due to dephasing of the magnetization in the transverse *xy* plane in the period between the gradient pulses. Such a process is faster for broad resonances characterized by short T_2 times.[517]

In summary, ^{19}F-DOSY-NMR spectroscopy revealed details of the PFDT ligand dynamics when bound to the Au NP surface. The broad spectral range of the ^{19}F nucleus and the improved resolution allowed a site-specific evaluation of the CF_2 and CF_3 resonance frequencies. Molecular diffusion coefficients and their distribution widths were derived for the individual chain groups. A gradual decrease of the site-specific D distributions along the alkyl chain toward the chain end was observed. The increased motional freedom toward the chain is reflected in the higher diffusion coefficients. As the motional freedom of the ligand is associated with the surface coverage density, the surface functionalization efficiency can be unraveled (*vide infra*).

7.3.6 Surface Functionalization Efficiency

Surface ligands improve colloidal stability[543] and prevent aggregation by blocking the reactive surface sites of NPs and minimizing the free energy. The degree of surface functionalization has been studied experimentally[544, 545] and theoretically.[543] We

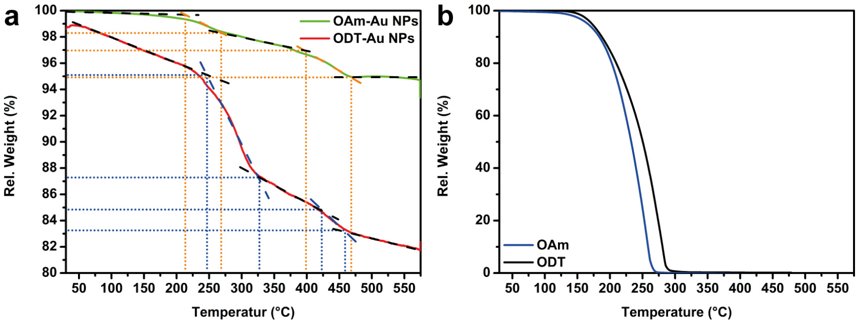

Figure 7.12: Thermogravimetric analysis of (a) OAm-Au and ODT-Au NPs and (b) pure OAm and pure ODT ligand.

used thermogravimetric analysis (TGA) to obtain quantitative information concerning the surface ligand density. Figure 7.12 shows TGA traces for OAm-Au and ODT-Au NPs up to 575 °C. Both curves are comparable as similar molecular processes occur. The slope of the ODT-Au NPs thermogram is steeper, and the resulting mass loss is more pronounced than for OAm-Au NPs (Figure 7.12a). The thermograms of the ligands reveal a complete mass loss at 270-275 °C for OAm and at 300 °C for ODT (Figure 7.12b). The pure ligands show a typical behavior for thermal decomposition with the formation of volatile compounds. The mass difference ($\approx$ 13% for the ODT-Au NPs, $\approx$ 3-4% for the OAm-Au NPs) reflects the higher affinity of the thiol ligand to the gold surface, which leads to stronger surface binding. The gradual change in the mass above 325 °C may be due to the decomposition of the Au-S surface species.

We monitored the re-functionalizations of ODT-Au NPs with different sizes and different ligands by DOSY-NMR spectroscopy to find a correlation between the hydrodynamic radius and surface functionalization. It is known that the surface coverage decreases with increasing particle size.[542] This straightforward relation may be complicated by fluctuations in the local coverage due to nanocrystal faceting, steric effects, or kinetic limitations of the capping process.[542] The dynamic equilibrium between the adsorbed and free ligands or a more complex ligand-shell system (*i.e.* formation of multilayers) is another intricacy.[534, 544, 546] The latter would be associated with an (weighted) average diffusion coefficient for the functionalized NPs and the free ligands in the fast exchange regime. Its dependence on the ratio between the bound and free ligands would lead to a shift of the D value to faster diffusion and decrease of the hydrodynamic radius.

The hydrodynamic radius (r_H) of the functionalized NPs was extracted from the Stokes-Einstein equation $D = k_B T / 6\pi\eta r_H$ (k_B, Boltzmann constant; T, absolute temperature; η, solvent viscosity) for spherical particles with the diffusion coefficient (D) obtained from the DOSY experiments.[517, 528] In a diffusion experiment the diffusion coefficient D for the ligand is related to r_H, whereas the radii of the fully functionalized NPs include the average radii of the particle core and the ligand shell.[517] The diffusion coefficients D from the DOSY experiment were obtained from

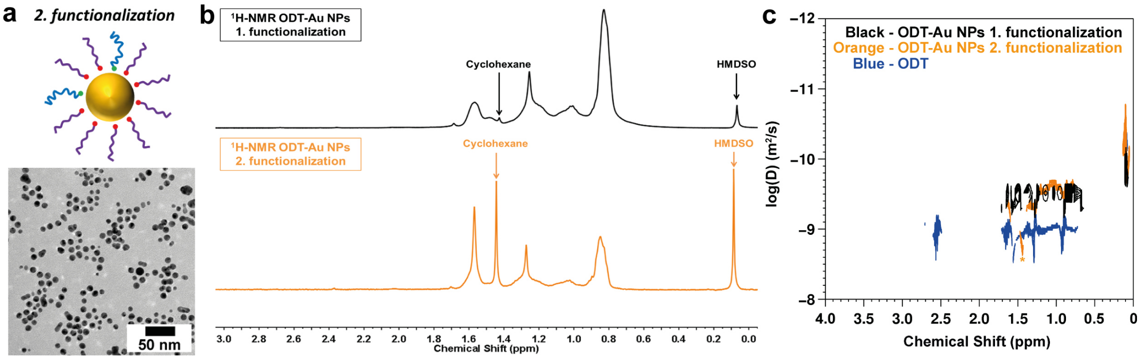

Figure 7.13: (a) Schematic representation and TEM image of ODT-Au NPs after 2. functionalization. (b) ^{1}H-NMR spectra of ODT-Au NPs after 1. (top) and 2. (bottom) functionalization. (c) ^{1}H-DOSY-NMR spectra of ODT-Au NPs after 2. functionalization along with ODT-Au NPs after 1. functionalization and free ODT ligand. Orange * marks cyclohexane from purification. HMDSO = hexamethyldisiloxane from NMR tubing lid.

a fit of the exponential decay of the signal intensity vs. the gradient field strength in consecutive experiments.

The DOSY experiment yielded a diffusion coefficient of 1.04 x 10^{-9} m^2/s for the pure ODT ligand with a hydrodynamic radius of 0.367 nm. The theoretical hydrodynamic radius $r_H = 5.317$ nm for a fully functionalized NP was calculated from the average radius of the Au NP core (4.95 nm) obtained by TEM and a single layer of the ligand shell (0.367 nm). We correlate the experimental hydrodynamic radii of the NPs with these two limiting cases to obtain an estimate of the degree of surface functionalization (Figure 7.11c). The results of the DOSY experiments and the derived values of the hydrodynamic radii are compiled in Table 7.1.

The experimental D and r_H values for the ODT-Au NPs were 3.98 x 10^{-10} m^2/s and 0.954 nm. This is compatible with a surface functionalization of ≈ 18% (Figure 7.11c). This value depends on (i) the particle size, (ii) the particle size and ligand functionalization distributions and (iii) the solubility of the ligand involved in the dynamic exchange equilibrium.[517] For comparison we conducted diffusion experiments on the same NPs for a second functionalization with ODT and for smaller ODT Au-NPs with a diameter of 2.8 nm ± 17%.

The second ODT ligand functionalization for the larger ODT-Au NPs was carried out as described above with an ≈ 600-fold excess of the free ODT ligand in toluene (Figure 7.13a). No changes were detected in the ^{1}H-NMR spectrum after the second functionalization (Figure 7.13b). The diffusion coefficient extracted from the DOSY experiment (Figure 7.13c) was 2.55 x 10^{-10} m^2/s with $r_H = 1.489$ nm. This suggests an enhanced ligand functionalization of ≈ 28% (Figure 7.11c) compared to ≈ 18% in the first step.

A 10 day long term ODT functionalization was carried out with the 9-11 nm OAm-Au NPs to investigate if the degree of surface functionalization is associated with a kinetic barrier. After this experiment the NPs were polydisperse, heavily agglomera-

Table 7.1: Extracted diffusion coefficients (D) and hydrodynamic radii (r_H) from the DOSY-NMR spectra for different ODT-Au and PFDT-Au NPs (diameter d) and the respective free ligands (ODT and PFDT).* Marked values are subject to a larger error due to particle fusion.

Compound	D	r_H	Surface coverage
	10^{-9} m^2/s	nm	%
ODT ligand	1.04	0.367	-
theoretical value for ODT-Au NPs (d = 9.9 nm)	0.071	5.317	-
ODT-Au NPs (d = 9.9 nm), 1. functionalization	0.398	0.954	18
ODT-Au NPs (d = 9.9 nm), 2. functionalization	0.255	1.489	28
theoretical value for ODT-Au NPs (d = 2.8 nm)	0.215	1.767	-
ODT-Au NPs (d = 2.8 nm)	0.523	0.726	41
PFDT ligand	1.120	0.340	-
theoretical value for PFDT-Au NPs (d = 9.9 nm)	0.072	5.290	-
PFDT-Au NPs (d = 9.9 nm), 1. functionalization*	0.675	0.563	11
PFDT-Au NPs (d = 9.9 nm), 2. functionalization*	0.436	0.871	17

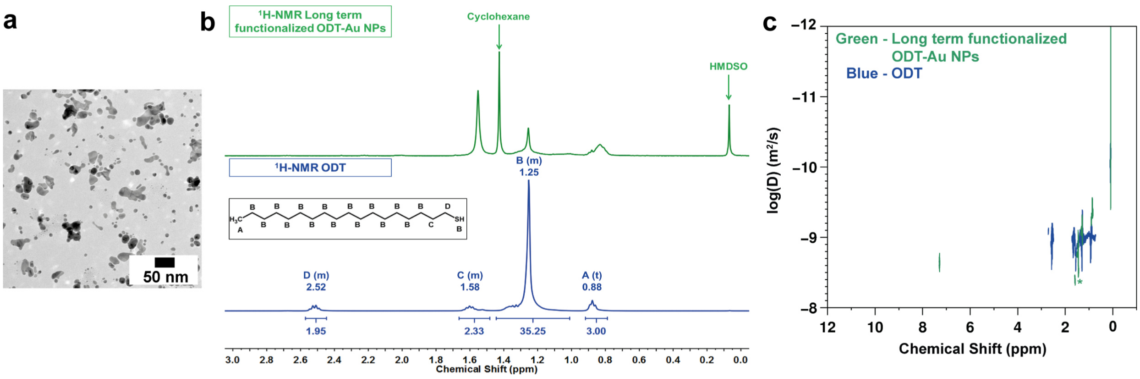

Figure 7.14: (a) TEM image of 10 days long-term ODT functionalized Au NPs. (b) ^{1}H-NMR spectra of ODT-Au NPs after 10 days long-term functionalization (top) and pure ODT ligand (bottom). (c) ^{1}H-DOSY-NMR spectra of ODT-Au NPs after 10 days long-term functionalization along with free ODT ligand. HMDSO = hexamethyldisiloxane from NMR tubing lid.

ted and fused due to Ostwald ripening and therefore no meaningful hydrodynamic radius could be derived (Figure 7.14). Thus, repeated functionalization with ODT according to the Nernst distribution is a promising technique to increase the ligand surface coverage.

Smaller Au NPs with a diameter d = 2.8 nm were functionalized with ODT *via* an exchange reaction as well (Figure 7.15a). The ^{1}H-NMR spectrum (Figure 7.15b) shows the characteristic broadening and shifts of the signals related with functionalized NPs. The diffusion coefficient extracted from the DOSY experiment (Figure 7.15c) was 5.23 x 10^{-10} m^2/s which corresponds to a hydrodynamic radius of 0.726 nm

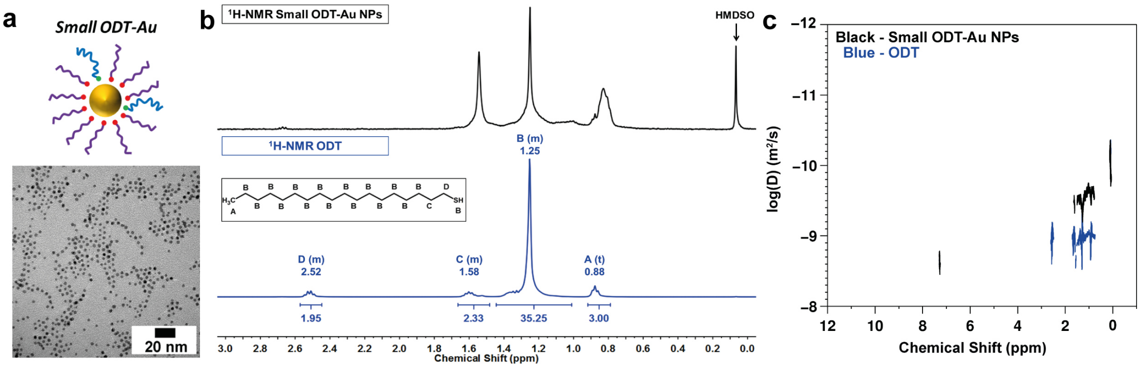

Figure 7.15: (a) Schematic representation and TEM image of ODT functionalized small Au NPs (diameter 2.8 nm ± 17%). (b) ^{1}H-NMR spectra of small ODT-Au NPs after functionalization (top) and pure ODT ligand (bottom). (c) ^{1}H-DOSY-NMR spectra of small ODT-Au NPs along with free ODT ligand. HMDSO = hexamethyldisiloxane from NMR tubing lid.

(Figure 7.11c). This confirms a functionalization of ≈ 41% because of the increased surface-to-volume ratio and the higher surface curvature. Additionally, the surface reactivity is increased through pronounced defects and step edges which emerge from the polycrystalline and multiple-twinned structure of the Au NPs.[547]

In summary, ligand replacement on the Au NP surface is a multiple exchange and does not proceed as a single step. It is an equilibrium reaction that obeys a Nernst distribution. Higher functionalization can be achieved by repeated functionalization at high ligand concentrations or by reducing the NP size. Prolonged reaction times lead to a broader distribution of the NP size due to Ostwald ripening and fusion.

7.4 Conclusion

Ligand exchange of oleylamine (OAm) to 1-octadecanethiol (ODT) on Au NPs as a function of the particle size and repeated functionalization was studied *in situ* by solution NMR. Surface dynamics and local inhomogeneities such as surface corrugation and surface defects led to signal broadening of the surface ligands on OAm-Au, ODT-Au and PFDT-Au NPs, which could be traced by ^{1}H as well as ^{19}F 1D-, 2D-diffusion-ordered (DOSY) and 2D-nuclear Overhauser effect (NOESY) spectroscopy. A site-specific evaluation of the resonance frequencies of the different CF_2 and CF_3 moieties could be given because of the resolution related with the broad spectral range of the ^{19}F nucleus. Site-related diffusion coefficients and hydrodynamic radii of the functionalized particles were derived from the corresponding DOSY spectra. Furthermore, the surface functionalization efficiency of the ODT-Au NPs was studied as a function of the particle size with smaller OAm-Au NPs and repeated functionalization. In particular, the unbound and bound or tightly bound ligands as well as the dynamics of ligand exchange in a rapid adsorption/desorption equilibrium could be distinguished by diffusion methods. Ligand exchange was found to be an equilibrium reaction associated with a Nernst distribution, which may lead to incomplete surface functionalization following "standard" literature protocols. Efficient surface coverage depends on (i) the repeated exchange reactions with large ligand excess, (ii) the size of NPs, *i.e.* the surface curvature, surface defects and reactivity, and (iii) the size of the ligand, which was studied for the two ligands ODT and PFDT. Because surface functionalization is a key prerequisite for any NP application, our results have implications for applications including controlled particle assembly, targeted delivery using NPs, or stability of particle dispersions.

7.5 Experimental Section

Materials

Hydrogen tetrachloroaurate(III) trihydrate ($HAuCl_4 \cdot 3H_2O$, Alfa Aesar, 99.99%, metals basis), oleylamine (OAm, Acros Organics, 80-90%), cyclohexane (Fisher Scientific, Analytical Reagent Grade), *tert*-butylamine borane complex (TBAB, Aldrich, 97%), 1-octadecanethiol (ODT, Alfa Aesar, 96%), 1H,1H,2H,2H-perfluorodecanethiol (PFDT, Aldrich), ethanol (Sigma-Aldrich, *p.a.*, > 99.8%), methanol (Fisher Scientific, Analytical Reagent Grade), toluene (Sigma-Aldrich, *p.a.*, > 99.7%) and $CDCl_3$ (Deutero GmbH, 99.80%) were used in this work.

Synthesis of 4 nm OAm-Au Seed Nanoparticles

The synthesis of the ca. 4 nm Au seed NPs was adapted from Peng *et al.*[547] In a 100 mL three-neck round bottom flask 84.9 mg (0.25 mmol) of $HAuCl_4 \cdot 3H_2O$ were dispersed in 10 mL of cyclohexane and 10 mL of oleylamine under inert gas (Ar) conditions and stirred for 15 min at room temperature (RT). Meanwhile, 43.5 mg (0.50 mmol) of *tert*-butylamine borane complex were dispersed in 1 mL of cyclohexane and 1 mL of OAm and ultrasonicated for 5 min. The TBAB dispersion was directly and rapidly injected into the preformed precursor solution, which turned dark red within 1-2 seconds upon injection. The mixture was stirred for 1 h at RT. The Au NPs were precipitated by adding 20 mL of methanol which contained 10 vol% of OAm and separated by centrifugation (9000 rpm, 10 min, RT). The precipitate was dispersed in cyclohexane and washed twice by adding methanol:ethanol = 1:1, which contained 10 vol% of OAm, and separated by additional centrifugation (9000 rpm, 10 min, RT). Finally, the product was dispersed in cyclohexane, flushed with Ar and stored at RT.

Synthesis of 9-11 nm OAm-Au Nanoparticles

A growth solution containing 196.9 mg (0.50 mmol) of $HAuCl_4 \cdot 3H_2O$, 10 mL of toluene and 10 mL of OAm was prepared at RT under inert gas (Ar) conditions. A dispersion of 10 mg of 4 nm OAm-Au seed NPs in 10 mL of toluene was added, and the mixture rapidly heated to 111 °C. The temperature was maintained for 2 h. The mixture was slowly cooled to RT. The precipitation and purification were identical as described above for the 4 nm OAm-Au seed NPs, but with no addition of OAm to the precipitation and washing solutions.

Thiol Functionalization of OAm-Au Nanoparticles

10 mg of 9-11 nm OAm-Au NPs were dispersed in 10 mL of toluene at RT under inert gas (Ar) conditions. Then, 1-octadecanethiol (1 mL, 3 mmol, 575 times excess) was added, and the mixture was stirred overnight at RT. A purple product was precipitated

from the mixture by adding 15 mL of methanol. The precipitate was separated by centrifugation (9000 rpm, 10 min, RT), dispersed in cyclohexane and washed twice by adding ethanol (cyclohexane:ethanol = 1:2) followed by additional centrifugation (9000 rpm, 10 min, RT). Finally, the product was dispersed in cyclohexane, flushed with Ar, and stored at RT. In the case of PFDT functionalization 0.86 mL (3 mmol) of PFDT was used instead of ODT. For *in situ* monitoring of the ligand exchange reaction, 1.8 mg of 9-11 nm OAm-Au NPs were dispersed in 3 mL of $CDCl_3$ and stirred under inert gas (Ar) conditions. Then, 4 mg of 1-octadecanethiol (15 times excess) were added, and reaction aliquots of 0.7 mL for NMR experiments were taken after the desired reaction time.

Nanoparticle Characterization

Samples for *transmission electron microscopy (TEM)* analysis were prepared by placing a drop of dilute NP dispersion in cyclohexane on a carbon coated copper grid. TEM images for the characterization of the size and morphology were obtained with a FEI Tecnai 12 using a LaB_6 source at 120 kV and a twin-objective together with a Gatan US1000 CCD-camera (2K x 2K pixels).
All *NMR spectroscopy* experiments were performed at 294 K on a Bruker Avance DRX 400 NMR spectrometer (Bruker BioSpin GmbH, Rheinstetten, Germany) operating at frequencies of 400.31 MHz for ^{1}H and 376.66 MHz for ^{19}F and equipped with a z-gradient dual channel inverse probe head with a gradient strength of 55 Gcm^{-1}. The ^{1}H spectra were referenced to the resonances of the remaining protons with $CDCl_3$, as the secondary standard to external TMS, whereas CCl_3F was used as an external reference for the ^{19}F spectra. For all ^{1}H experiments, a 30° single pulse excitation was used averaging 32 transients with a recycle delay of 1 s. The ^{19}F spectra were recorded by averaging 128 transients with 2 s recycle delay. For the 2D ^{1}H nuclear Overhauser effect spectroscopy (NOESY) 2048 data points were recorded in the direct dimension with 256 increments in the indirect dimension and 8 scans per increment in a phase sensitive mode. The mixing time was set to 1.5 s and a recycle delay of 2 s was used. The ^{19}F correlation spectroscopy (COSY) was performed using gradient pulses for coherence selection recording 1024 points in the direct dimension and 1024 increments in the indirect dimension and 48 scans per increment with 2 s recycle delay. Stimulated echo sequence with bipolar gradient pulses and a longitudinal eddy current delay was used for the diffusion ordered spectroscopy (DOSY) experiments. The gradient strength was incremented in 16 steps from 2% to 95% of the maximum gradient strength. The diffusion time and the gradient pulse length for all measured samples were 100 ms and 2.8 ms, respectively, with 10 s recycle delay. An additional ^{19}F DOSY experiment was conducted with a diffusion time of 300 ms and 2.4 ms gradient pulse length to check for possible contributions from the rotational motion and translations of the ligand chain in the measured diffusion coefficient for the NPs. After Fourier transformation and baseline correction, the diffusion dimension of the 2D DOSY spectra was processed using the Bruker Topspin 1.3 software package. The diffusion analysis was performed using the T_1/T_2

relaxation TopSpin package. Deconvolution of ^{1}H-NMR spectra was performed using Bruker 1D WIN-NMR software package.

Thermogravimetric analysis (TGA) was performed on a Perkin Elmer Pyris 6 TGA instrument under a nitrogen atmosphere (20 mL/min). The heat program was (i) 10 min at 30 °C, (ii) ramp of 10 °C/min from 30 °C to 600 °C and (iii) 30 min at 600 °C.

UV-vis spectra of NP dispersions in cyclohexane were recorded on a Cary 5G UV-vis-NIR spectrophotometer in the range of 300-750 nm.

Raman analysis was conducted on a Bruker Senterra R200-L Raman Spectrometer equipped with a 50x magnification confocal microscope and piezo stage. Measurements were performed with 20 iterations of 2 s, using a 20 mW 532 nm laser for excitation.

7.6 Appendix

The Raman spectrum of the OAm-Au and ODT-Au NPs was compared to the Raman spectrum of pure OAm and ODT (Figure 7.16). The Raman spectrum of the pure ligands displays the methyl and methylene stretching and deformation vibrations at 2800-3000 cm^{-1} and 1500-1300 cm^{-1}, respectively. ODT additionally shows the -SH stretching vibration at 2560 cm^{-1} and the CS stretching vibration at 735 cm^{-1}.[548] For both functionalized Au NPs only a broad fluorescence signal is visible between 3500 and 1700 cm^{-1}. Both NP types present a broad signal at 1600 cm^{-1} which is more pronounced for the ODT-Au NPs. Also an adjacent broad band at 1400 cm^{-1} is present for both NP types, more pronounced for ODT-Au NPs. These signals might arise from the shifted and broadened methyl and methylene deformation vibrations due to the attachment of the ligands to the NPs. The more pronounced signals in case of ODT-Au NPs might therefore emerge from better chemisorption of the thiol.[549, 550]

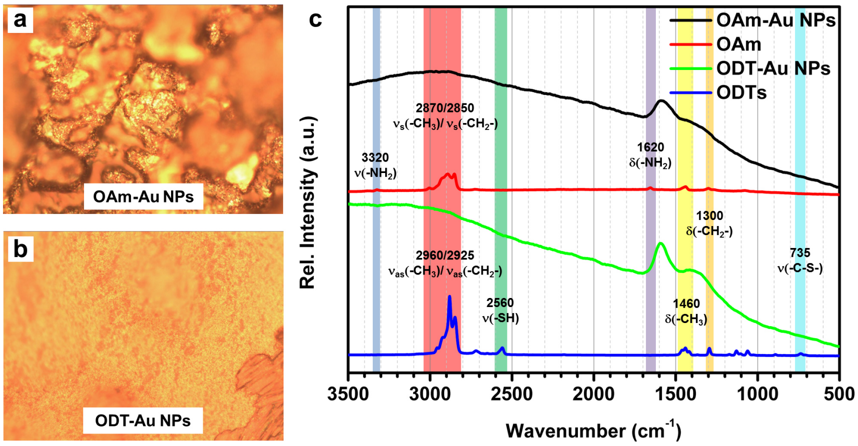

Figure 7.16: (a) Photograph of OAm-Au NPs before Raman analysis, 50x magnification. (b) Photograph of ODT-Au NPs before Raman analysis, 50x magnification. (c) Raman spectra of OAm-Au and ODT-Au NPs as well as pure OAm and ODT ligand after excitation with 532 nm laser.

8

Controlling the Morphology of Au-Pd Heterodimer Nanoparticles by Surface Ligands

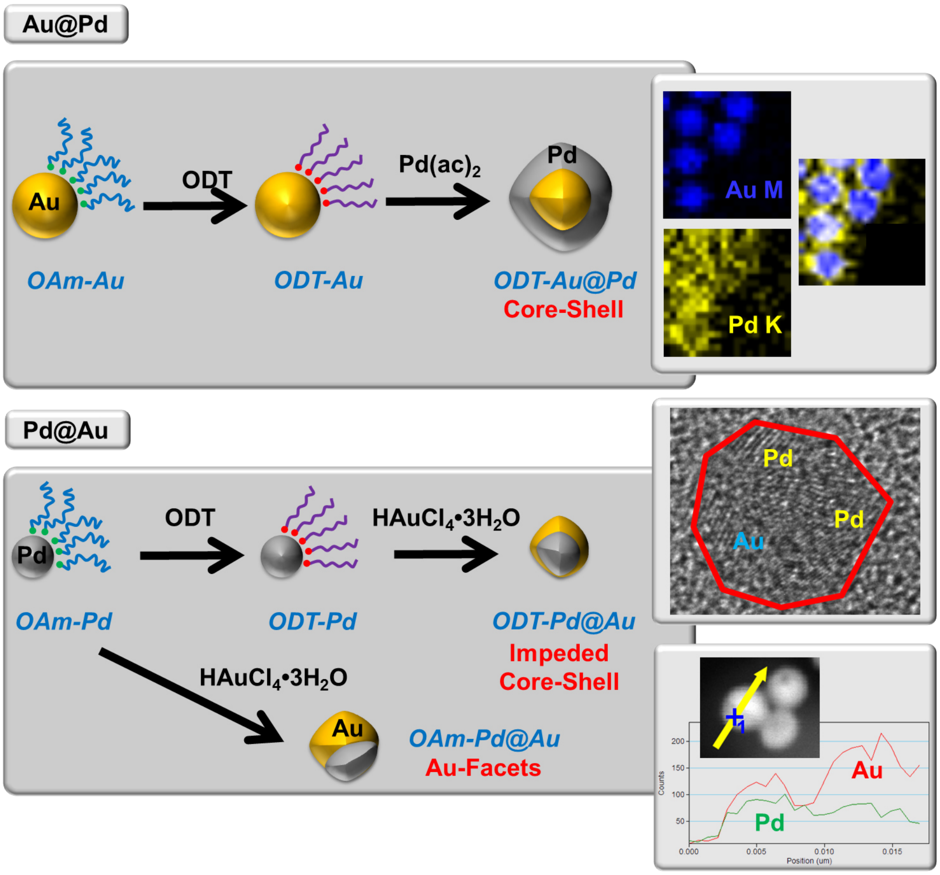

This chapter contains a manuscript for publication, submitted to the RSC Nanoscale journal. A detailed Authorship Statement of the publication is attached in the Appendix of this dissertation. Very special thanks go to the DAAD RISE students [redacted] *and* [redacted] *for their extraordinary cooperation in this project during their research stay at the University of Mainz.*

8.1 Abstract

Controlling the morphology of noble metal nanoparticles is mandatory to tune specific properties such as catalytic and optical behavior. Heterodimers consisting of two noble metals have been synthesized so far mostly in aqueous media using selective surfactants or chemical etching strategies. We report a facile synthesis for Au@Pd and Pd@Au heterodimer nanoparticles (NPs) with morphologies ranging from segregated domains (heteroparticles) to core-shell structures by applying a seed mediated growth process with Au and Pd seed nanoparticles in 1-octadecene (ODE), a high-boiling organic solvent. The as-synthesized oleylamine (OAm) functionalized Au NPs led to the formation of OAm-Au@Pd heteroparticles with a "windmill" morphology, having an Au core and Pd "blades". The multiply-twinned structure of the Au seed particles (diameter 9-11 nm) is associated with a reduced barrier for heterogeneous nucleation. This leads to island growth of bimetallic Au@Pd heteroparticles with less regular morphologies. The reaction process can be controlled by tuning the surface chemistry with organic ligands. Functionalization of Au NPs (diameter 9-11 nm) with 1-octadecanethiol (ODT) led to the formation of ODT-Au@Pd NPs with a closed Pd shell through a strong ligand-metal binding which is accompanied by a redistribution of the electron density. Experiments with varied Pd content revealed surface epitaxial growth of Pd on Au. For OAm-Pd and ODT-Pd seed particles, facetted, Au-rich domain NPs and impeded core-shell NPs were obtained, respectively. This is related to the high surface energy of the small Pd seed particles (diameter 5-7 nm). The metal distribution of all bimetallic NPs was analyzed by extended (aberration corrected) transmission electron microscopy (HR-TEM, HAADF-STEM, EDX mapping, ED). The Au and Pd NPs, as well as the ODT-Au@Pd and OAm-Pd@Au heteroparticles, catalyze the reduction of 4-nitrophenol to 4-aminophenol with borohydride. The catalytic activity is dictated by the particle structure. OAm-Au@Pd heteroparticles with facetted Au domains had the highest activity because of a mixed Au-Pd surface structure, while ODT-Au@Pd NPs, where the active Au core is covered by a Pd shell, had the lowest activity.

8.2 Introduction

Morphology-controlled aqueous syntheses of Au[551] and Pd[104] nanoparticles (NPs) by the polyol method,[31, 192] by citrate reduction[552] or by stabilization with cetyltrimethylammonium salts[24, 83] are the most established methods to explore morphology-dependent optical[190, 553] and catalytic[554, 555] applications of Au and Pd NPs. Anisotropic bimetallic particle morphologies have been obtained using water-based synthetic protocols.[88, 556, 557] An advantage of the wet chemical synthesis of Au and Pd NPs in high-boiling organic solvents is that nucleation and growth steps can be controlled individually to synthesize bimetallic Au-Pd NPs, segregated Au-Pd heterodimers or mixed alloyed NPs. These bimetallic nanoparticles are of great interest because of their enhanced catalytic activity and stability compared to the elemental counterparts.[558, 559] The synthetic repertoire for making novel nanomaterials with new and unknown properties can be greatly expanded with a variable choice of surfactants and solvents.[560–562] NPs with complex shapes have been obtained especially by seed mediated growth, because heterogeneous nucleation lowers kinetic barriers for nanocrystal formation. This leads to the formation of particles with less stable morphologies by a kinetic control of reactions.[20, 563] Additives and surfactants can play an important role for directing nanocrystal morphologies by selectively covering facets of the seed particles.[312, 564] Oleylamine, for example, was shown to have a crucial effect on the morphologies of Au and Pd NPs made by seed mediated growth.[560, 565]

Syntheses of bimetallic Au-Pd NPs with morphologies such as spherical,[566] cubic,[567] core-shell,[568, 569] octahedral,[570] and tadpole-like[571] have been explored in the past. Galvanic displacement has been a successful approach for making bimetallic NPs. For Pd NP seeds, the higher redox potential (*i.e.* the more noble character) of Au leads to an oxidation of Pd^0 to Pd^{2+}, while the applied Au^{3+} or Au^{1+} precursor is reduced to elemental Au^0.[571, 572] This approach has been used to fabricate hollow nanostructures as demonstrated by the Khashab group.[573] Ag has similarly been sacrificed in a galvanic synthesis of Au-containing bimetallic NPs.[568, 574]

Au-Pd NPs have the potential to serve as powerful catalysts due to the outstanding catalytic performance of Pd, enhanced by the admixture of Au.[575] The Au-Pd NPs, with enriched electronic environment and communication, have been found to catalyze formic acid dehydrogenation[556, 566] as well as ethanol,[573] hydrazine,[557] benzyl alcohol[576] and carbon monoxide oxidation.[577] The catalytic performance of this mixed Au-Pd system is based on the chemical similarity of Au and Pd. The lattice mismatch of approximately 5%[578] allows epitaxial growth, while alloying is equally possible.[579] Alloying effects, which may be divided into ensemble and ligand effects, can occur. Ensemble effects are related to a defined number of atoms in specific geometric orientations that are required for a successful catalytic reaction (*i.e.* a dilution of surface Pd by Au). Ligand effects describe electronic modifications through the addition of a second metal which leads in turn to heteronuclear metal-metal bonding, charge transfer and orbital re-hybridization. Both effects are affected by changes in the surface structure and catalyst composition.[558] In a simplified picture, the catalytically highly active Pd, in Au containing intermetallic NPs, is "diluted" by the less active Au. Charge is transferred from Pd to Au because of the higher electron affinity of Au. The gain of 6s and 6p electrons is partially compensated by a depletion of the Au 5d states (due to relativistic effects for Au). A similar state of affairs applies for Au-Pd alloy particles, where Pd 5s and 5p states are depleted, while 4d states are populated. The associated charge transfer from Pd to Au is responsible for the formation of isolated Pd islands, in particular because of the Pd-Pd repulsion by Coulomb effects in Pd metal, while Pd-Au interactions are reinforced.[580, 581] The d-character of late transition metals like Au and Pd is key for their chemisorption and catalytic properties. The population of Pd 4d states moves their energy away from the Fermi level, which results in a weaker surface binding of adsorbates.[582–584] Still, the perturbation of the Pd d-states by Au may alleviate the self-poisoning of Pd by reactants or products due to metal-substrate interactions and enhance the overall catalytic activity.[581] In essence, Pd-Au heteroparticles are highly relevant model systems to study phase formation and segregation at the nanoscale and their effect on the catalytic properties of Pd-Au systems.

Here we present a wet-chemical route in organic solvents to Au@Pd and Pd@Au heteroparticles with structures ranging from segregated domains (heteroparticles) to core-shell structures. The effect of surface modification of OAm-functionalized Au and Pd seeds (OAm-Au and OAm-Pd NPs) on the product particles was investigated. Therefore, ODT-functionalization of the Au and Pd seeds (ODT-Au and ODT-Pd NPs) was carried out, leading to Au-S (Pd-S) chemisorption and enhanced electronic communication through Au-S (Pd-S) electron redistribution. The functionalized Au seeds were overgrown with Pd to yield bimetallic NPs (Au-Pd) with different morphologies. In ODE solvent, ODT-Au@Pd core-shell NPs could be synthesized selectively from ODT-Au (diameter 9-11 nm) seeds. The core-shell structure of the bimetallic NPs was demonstrated by extended (aberration corrected) transmission electron microscopy (HR-TEM, HAADF-STEM, EDX mapping, ED). OAm-Pd@Au NPs, synthesized from OAm-Pd seed NPs, obtained a structure with Au facets, whereas ODT-Pd@Au NPs, synthesized from ODT-Pd seed NPs, obtained an impeded core-shell structure due to the small Pd seed particles with high surface reactivity. ODT-Au@Pd and OAm-Pd@Au NPs (as exemplary heteroparticles) as well as Au and Pd NPs (as reference) were functionalized with hydrophilic thiol-PEG surface ligands to evaluate their catalytic activity. They showed an enhanced catalytic activity for the hydrogenation of 4-nitrophenol to 4-aminophenol.

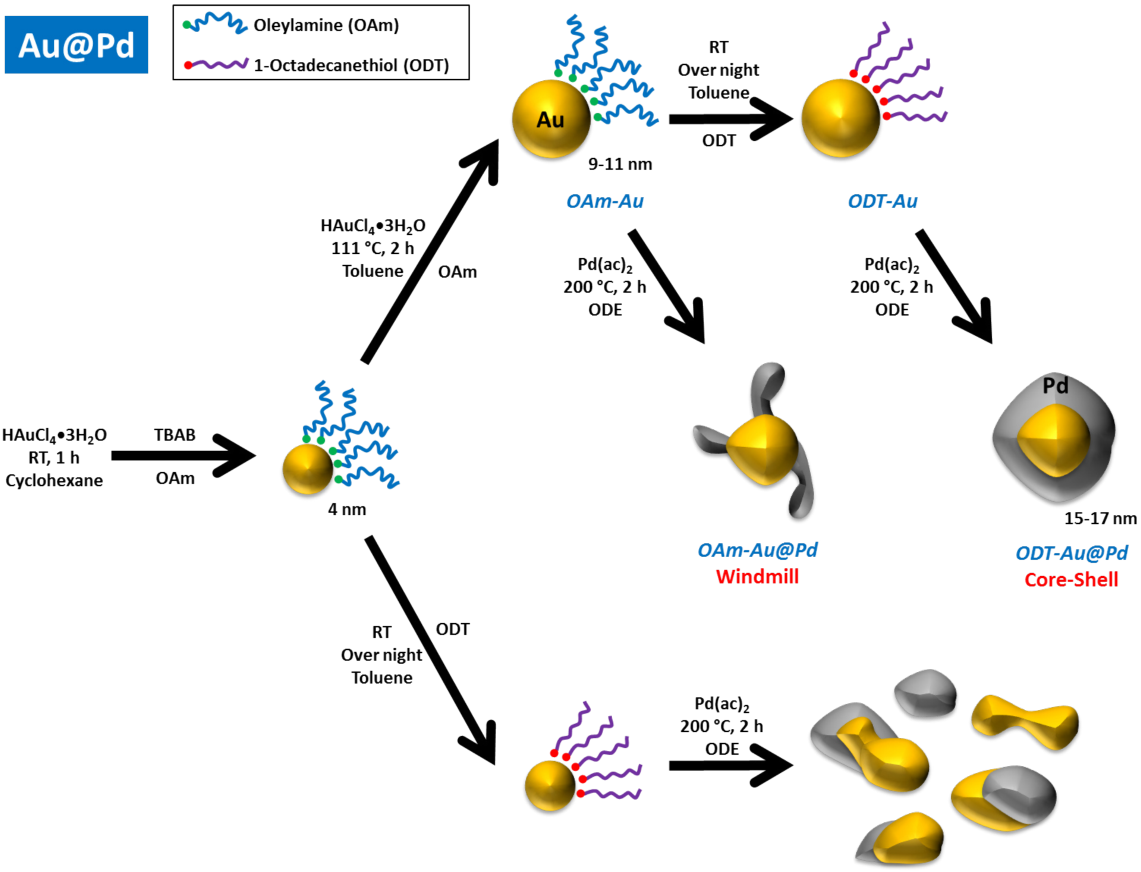

Figure 8.1: Schematic representation of 4 nm and 9-11 nm as-synthesized OAm-functionalized Au NPs, their subsequent functionalization with ODT, and their reaction with $Pd(ac)_2$ to form heterodimers.

8.3 Results and Discussion

8.3.1 Au@Pd Heterodimers

Figure 8.1 shows a schematic representation of the synthesis of OAm-Au NPs and their subsequent surface functionalization with ODT to form ODT-Au NPs. Au@Pd heterodimer NPs were synthesized by deposition of Pd^0 on the preformed OAm-Au or ODT-Au NPs. The first synthetic step resulted in Au NPs (diameter $\approx$ 4 nm) by reduction of a yellow Au^{3+} precursor in cyclohexane using OAm as a surfactant and *tert*-butylamine borane complex as reductant. The reaction mixture turned dark red immediately after adding the borane complex, indicating the formation of Au NPs. Figure 8.2a shows a TEM image of OAm functionalized Au NPs with an average size of 3.8 nm ± 11.1% (labeled 4 nm OAm-Au NPs, size distribution histogram in Figure 8.3a). In the second step, these 4 nm OAm-Au NPs were used as seeds to synthesize larger oleylamine capped Au nanoparticles (9-11 nm OAm-Au NPs). OAm is used as surfactant and reducing agent, because its reducing power is sufficient for

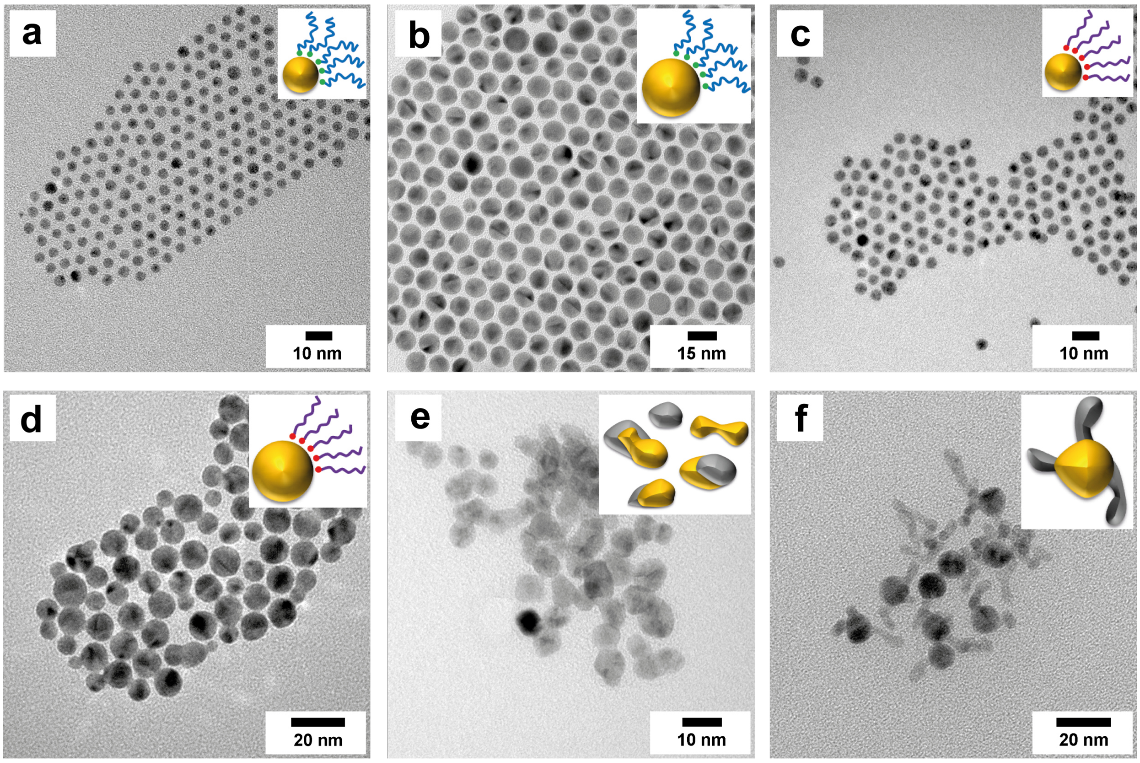

Figure 8.2: TEM images of (a) 4 nm OAm-Au NPs, (b) 9-11 nm OAm-Au NPs, (c) 4 nm ODT-Au NPs, (d) 9-11 nm ODT-Au NPs, (e) reaction of 4 nm ODT-Au NPs and (f) reaction of 9-11 nm OAm-Au NPs with $Pd(ac)_2$ to form Au-Pd heterodimers.

the formation of Au^0 when a lower energetic barrier is provided by heterogeneous nucleation.[585] Figure 8.2b shows a TEM image of the resulting OAm-Au NPs with an average size of 10.2 nm ± 8.8% (labeled 9-11 nm OAm-Au NPs, 8.3b). Both particle types were surface functionalized subsequently with ODT whose thiol anchor group can replace the OAm capping ligand because of its Pearson hardness.[133, 139, 586] Functionalization of OAm-Au NPs in toluene with excess ODT (and stirring over night at RT) yielded 4.2 nm ± 10.3% (labeled 4 nm ODT-Au NPs, Figure 8.2c, Figure 8.3c) and 9.9 nm ± 12.8% (labeled 9-11 nm ODT-Au NPs, Figure 8.2d, Figure 8.3d) ODT-Au NPs. Successful ODT-functionalization was visible even by eye inspection and could be quantified by UV-vis spectroscopy (*vide infra*) through a color change from dark red to purple. The overnight exchange reaction in a "good" solvent for both ligands was partly accompanied by Ostwald ripening, which was detectable by a broadening of the size distribution and a fusing of the NPs.[19, 362] In the next reaction step the ODT-Au NPs were used as seeds for the reduction of $Pd(ac)_2$ to form Au@Pd heterodimers. For 4 nm ODT-Au NPs, the synthesis yielded fused NPs that maintained a spherical morphology (with a significantly larger diameter), but they contained patches of Pd on the Au seeds (Figure 8.2e). The TEM contrast indicated that the particles contained Au and Pd in different extents, with compositions ranging from almost pure Au to almost pure Pd. When 9-11 nm

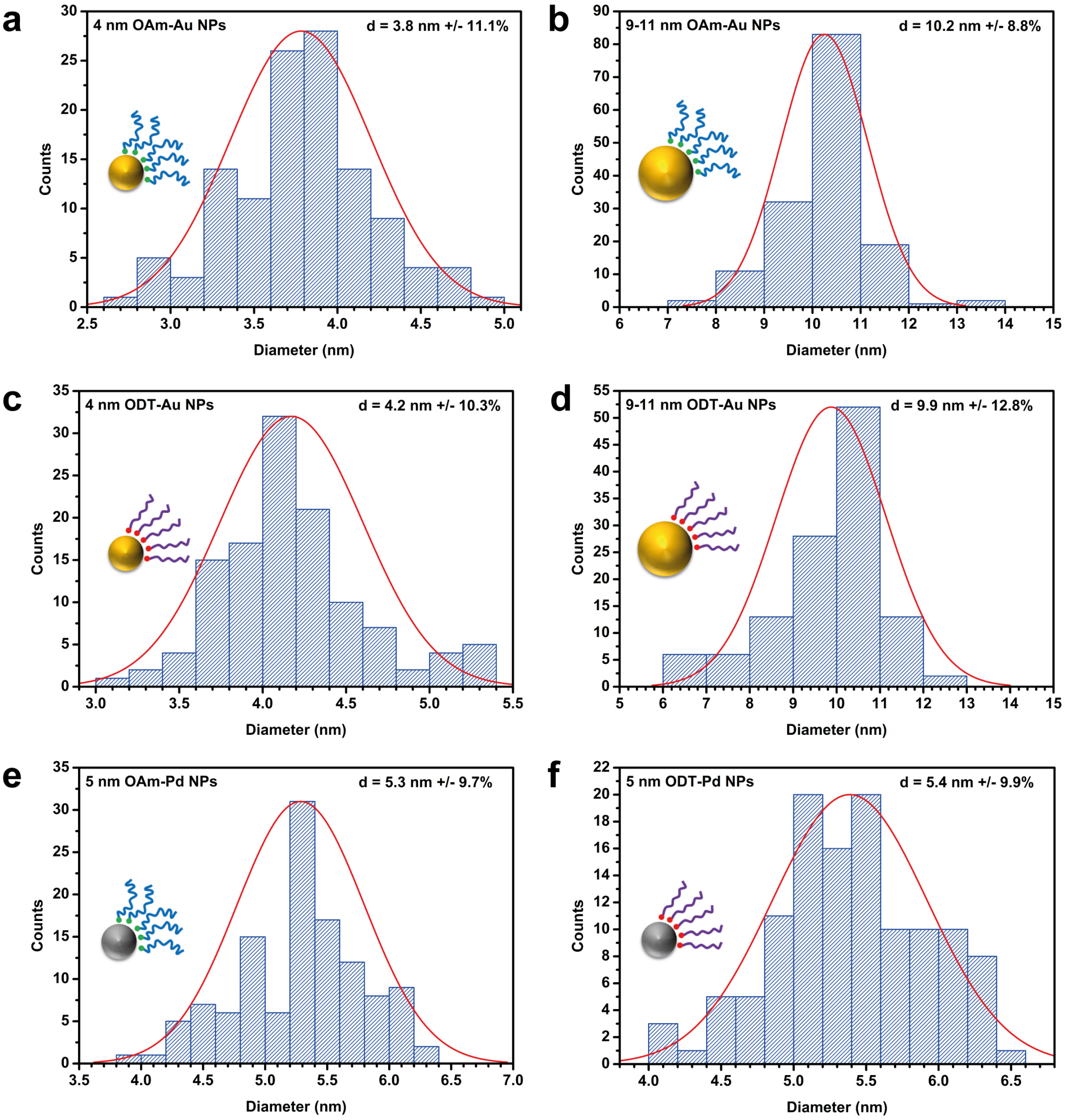

Figure 8.3: Size distribution histograms of OAm and ODT surface functionalized Au and Pd NPs.

ODT-Au NPs were used instead, ODT-Au@Pd core-shell NPs were formed with Au core and Pd shell and diameters of 15-17 nm (*vide infra*). To examine whether the formation of the core-shell NPs was related to the thiol-capped Au surface, the same experiment was carried out with 9-11 nm OAm-Au NPs. This led to the formation of particles with windmill-morphology, where 1-3 Pd "blades" were attached to an Au core. The "blades" have a rod-like morphology and a length between ≈ 5 nm and ≈ 12 nm with a varying diameter of ≈ 2-4 nm. Additionally the longer "blades" show kinks and a bended structure. The surface coverage of Pd on the Au core was incomplete (Figure 8.2f).

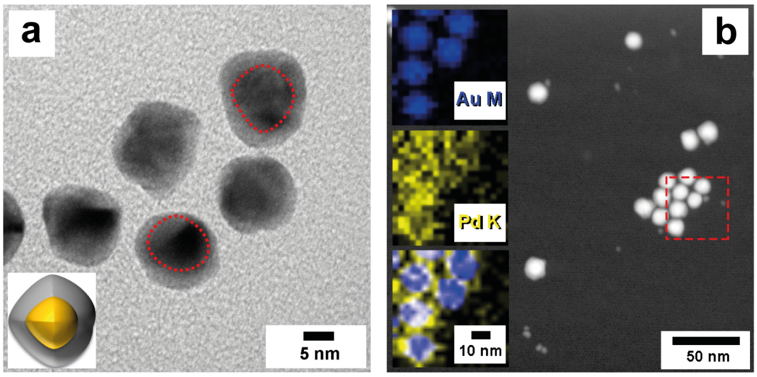

Figure 8.4: (a) TEM image of ODT-Au@Pd NPs. The circled region represents the ODT-Au core. (b) STEM-EDX mapping of ODT-Au@Pd NPs showing an Au M-shell, Pd K-shell signal and their overlay.

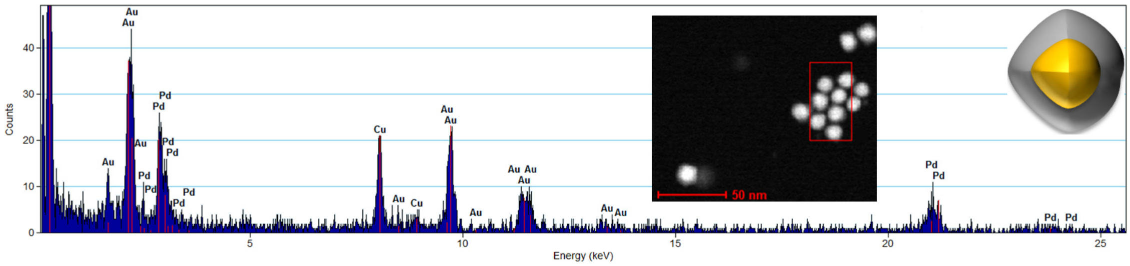

Figure 8.5: STEM image along with EDX spectrum of boxed ODT-Au@Pd NPs.

8.3.2 ODT-Au@Pd Core-Shell Nanoparticles Through Surface Modified Au Nanoparticles

As mentioned *vide supra*, the reduction of Pd^{2+} on the 9-11 nm ODT-Au NPs led to the formation of a closed Pd-shell (Figure 8.4). The diameter of the NPs is increased to $\approx$ 15.5 nm maintaining the Au core of $\approx$ 10 nm. The higher z-contrast, as indicated by the TEM image of the ODT-Au@Pd NPs (Figure 8.4a), is due to the enhanced scattering contrast of the heavier Au atoms, which is revealed only in the Au core. STEM-EDX analysis was used to verify the Au and Pd content according to Au M-shell radiation along with Pd K-shell radiation (Figure 8.5). STEM-EDX mapping (Figure 8.4b) was carried out to localize the Au and Pd content within the NP. The STEM image reveals a good distinction between Au and Pd due to the z-contrast, and it shows the Au core to be fully covered by Pd. The EDX mapping agrees, showing localized Au cores covered by a Pd shell.

The growth of the Pd shell was evaluated by TEM analysis of reaction aliquots. At 150 °C a thin but homogeneous Pd shell with lighter contrast was already visible (Figure 8.6a). After 30 min at the final reaction temperature of 200 °C, the Pd shell evolved, but it had a non-uniform morphology demonstrating that additional Pd is segregated first at spots of higher surface energy (Figure 8.6b). With increasing growth time, the shell became more uniform and almost spherical (Figure 8.6c-e). A

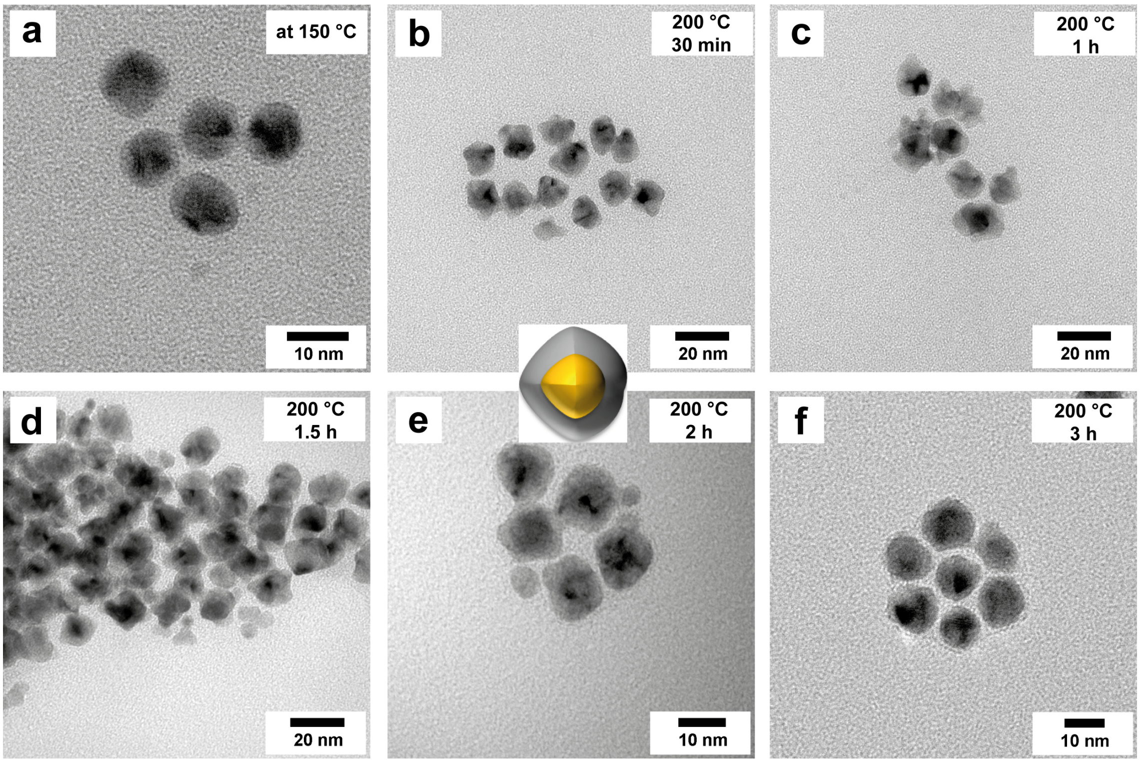

Figure 8.6: TEM images of ODT-Au@Pd NPs quenching studies at different reaction times and temperatures.

more spherical and homogeneous morphology of the NPs could be obtained when the reaction time was extended to 3 h instead of 2 h reaction time (Figure 8.6f). Well-developed Au-Pd core-shell NPs were obtained only with 9-11 nm ODT-Au NP seeds. Due to the polycrystalline and multiply-twinned structure of the as synthesized OAm-Au NPs,[547] defect sites and twin boundaries can lead to heterogeneous nucleation.[17] Twinned domains are incapable of filling the available space, leading to the formation of defects, induced strain and bond stretching.[587] This leads to high local surface energies with a strongly reduced energy barrier for heterogeneous nucleation (compared to the surface of a crystalline Au NP).[19] In the case of heterogeneous nucleation, the change of the Gibbs free surface energy can be critical for the underlying heterodimer formation process. The Gibbs free surface energy is associated with the difference between the surface energies of both components and a positive solid-solid interface term. Heterogeneous nucleation can be subdivided into island (Volmer-Weber) and layered epitaxial growth (Frank-van der Merwe). For island growth, the second component has higher energy surfaces than the first one. This leads to a negative Gibbs free surface energy, minimized overall interfacial area and domain growth. The layer-by-layer deposition for epitaxial growth is typically related to a positive Gibbs free surface energy because the surface energy of the second component is lower than that of the first. The interface term is controlled by binding strength and lattice mismatch (which is low here), leading to a small interface term. The surface energy is dictated by the exposed surface and the nature of the capping ligands.[37, 43] Hence, the properties of the surface layers and the OAm ligand coating determines the Pd overgrowth on OAm-Au NPs, leading to island growth and the formation of windmill-type NPs with Pd islands ("blades", Figure 8.2f). Pd is deposited predominantly on isolated spots of the Au NP surface, and it minimizes the interfacial area by forming elongated domains ("blades").

ODT surface functionalization alters the surface energy of the Au NPs (compared to surface functionalization with OAm). The similar Pearson hardness of S (Pearson soft) and Au (Pearson soft) leads to a strong ligand-metal binding which is accompanied by a redistribution of the electron density. The nucleation and growth of a second domain onto preformed noble metal seeds is usually controlled by the polarity of the solvent.[15, 40–42] The nucleation of a metal oxide domain onto Au seeds in a nonpolar solvent leads to a withdrawal of electron density from Au, charge transfer to the metal oxide through the interface and subsequent electron deficiency of Au, which prevents the nucleation of more than one metal oxide domain.[51] When a polar solvent is used instead, electron density can be provided to the Au seed by the solvent, allowing the formation of multiple nucleation sites and eventually the formation of core-shell NPs.[289]

Here, a comparable effect can be observed through the surface functionalization with ODT, while the solvent is maintained unpolar (ODE). The associated electron redistribution can be verified by UV-vis spectroscopy (*vide infra*). To further investigate the surface re-functionalization we carried out extensive ^{1}H and ^{19}F nuclear magnetic resonance (NMR) studies, unveiling that the re-functionalization of Au NPs with long chain organic thiols is associated with a Nernst distribution.[491] Furthermore, site-specific broadening and shifting of the resonances of the respective chain moieties was observed and could be evaluated *i.a.* by diffusion analysis. The signal broadening is caused macroscopically by the restricted mobility of the chain moieties close to the NP surface, whereas the shifting is caused microscopically by a complexation shift due to electronic interactions. The latter is a short-range effect confined to the binding site.[491] Thus, the 9-11 nm ODT-Au NPs can form a closed Pd shell through tuning the Au surface energy by electron density redistribution on the surface. In contrast, no uniform NP shape was obtained when 4 nm ODT-Au NPs were used as seeds (Figure 8.2e). The increased surface-to-volume ratio and the higher surface curvature of the small Au NPs lead to higher surface reactivity. No controlled nucleation and growth process is possible due to the presence of surface defects (*e.g.* step edges).

8.3.3 Epitaxial Growth of ODT-Au@Pd Nanoparticles by Using Different Au:Pd Ratios

In order to reveal details of the Pd nucleation and growth behavior for ODT-Au@Pd core-shell NPs, reactions with varying Au:Pd ratios were carried out. The amount of Pd^{2+} precursor was adjusted by changing the ODT-Au:Pd(ac)$_2$ ratio to 3:1 and

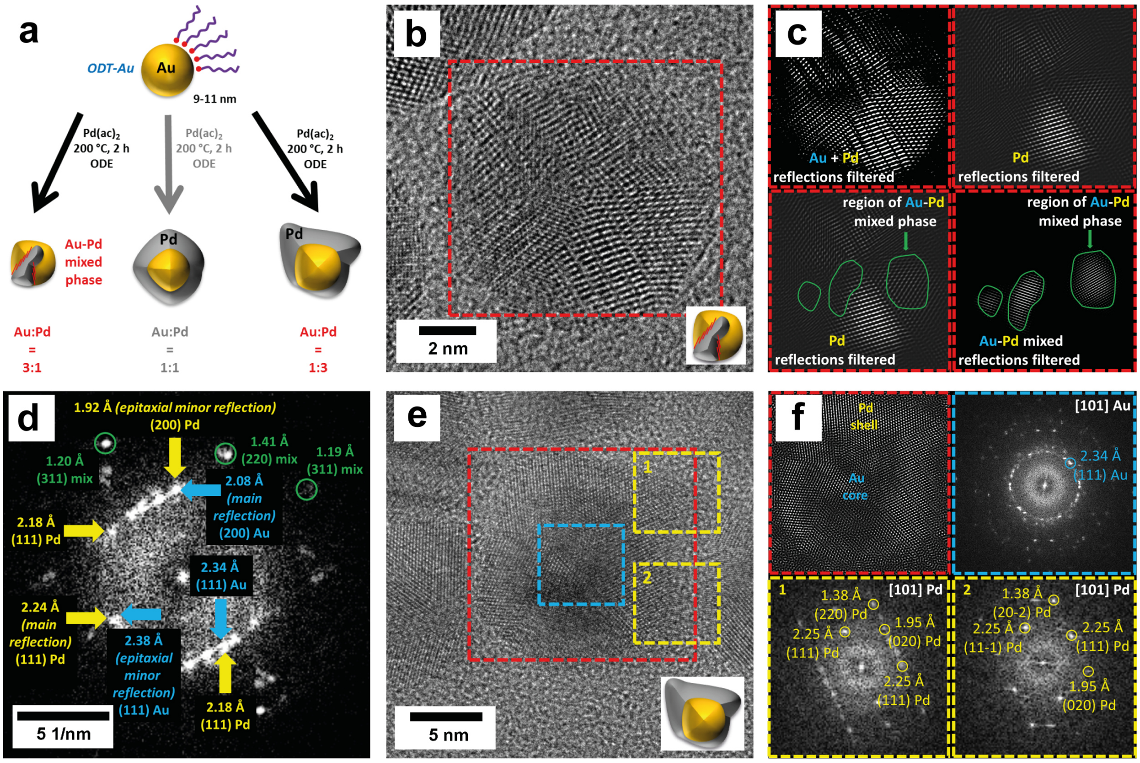

Figure 8.7: (a) Schematic representation of ODT-Au@Pd NPs with varying Au:Pd ratios. (b) Aberration corrected HR-TEM image of a ODT-Au@Pd NP with a Au:Pd ratio of 3:1. (c) Different filtered Au and Pd reflections of the red boxed region of (b). (d) Power spectrum with Au, Pd and Au-Pd mixed reflections from the NP shown in (b) revealing epitaxial growth. (e) Aberration corrected HR-TEM image of a ODT-Au@Pd NP with a Au:Pd ratio of 1:3. (f) Fourier filter along with power spectra from boxed regions in (e) showing reflections of Au and Pd as well as core-shell structure.

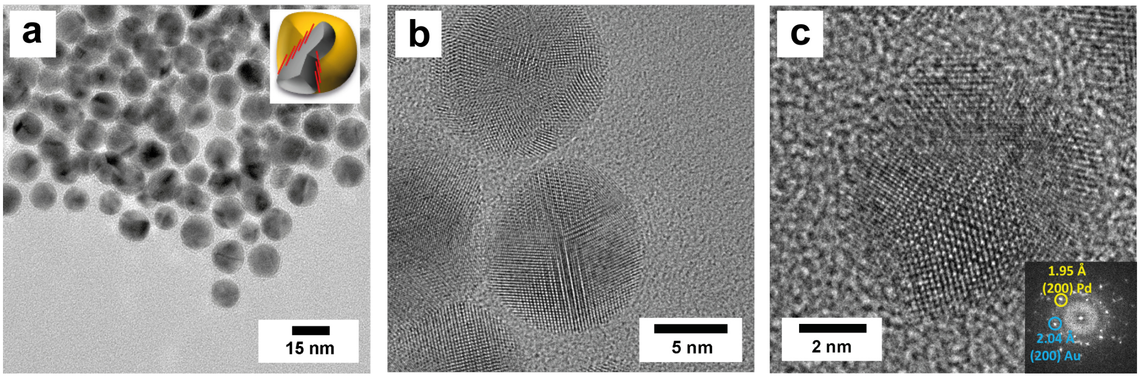

Figure 8.8: (a) TEM image of ODT-Au@Pd NPs with a Au:Pd ratio of 3:1. (b, c) Aberration corrected HR-TEM images of NPs from (a) with Au and Pd reflections marked in power spectrum (insert in c).

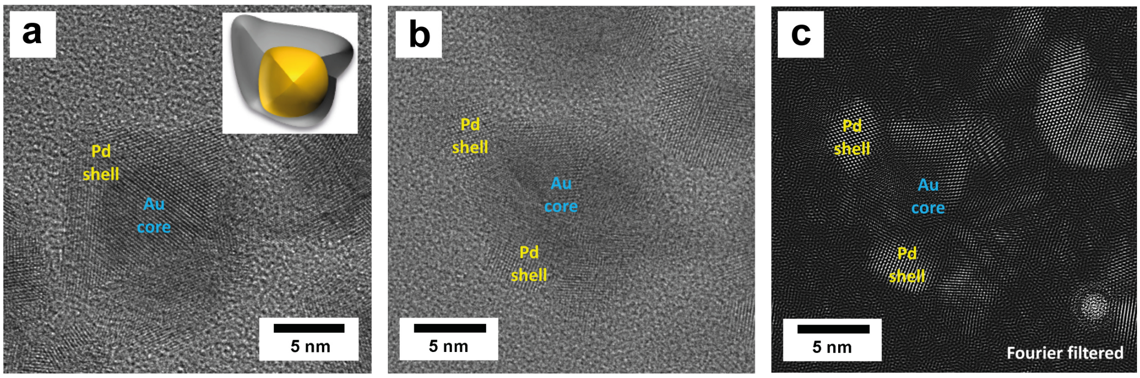

Figure 8.9: (a, b) Aberration corrected HR-TEM images of ODT-Au@Pd NPs with a Au:Pd ratio of 1:3 showing Au core and Pd shell. (c) Fourier filtered image of (b) showing accretions of Pd in the Pd shell structure.

1:3, respectively (Figure 8.7a). Figure 8.7b shows a HR-TEM image of the obtained NPs when an excess of ODT-Au seed particles was used. Spherical and facetted NPs with a size of 10.7 nm ± 16% were formed, whose diameter was slightly increased compared to the ODT-Au seed NPs (Figure 8.8). Fourier filtered images of aberration corrected HR-TEM images showed Au and Pd reflections (Figure 8.7c), indicating the presence of both metals. To obtain these filtered images, the corresponding metal reflections were selected from the power spectrum. Only the associated atom columns are shown in the filtered image. Filtered Pd reflections suggest the presence of a Au-Pd alloy phase because of the different lattice parameter. This is apparent if only these reflections are filtered (Figure 8.7c). Therefore, epitaxial growth of Pd on Au is likely and was further evaluated by electron diffraction (Figure 8.7d). Au-Pd systems are known to form intermetallic compounds and alloys of different compositions.[579] The lattice parameters adopt intermediate values between 4.0782 $\mathring{A}$ (pure Au) and 3.8790 $\mathring{A}$ (pure Pd) according to Vegard's law.[579] Electron diffraction displays a (200)Au main reflection concomitantly with a (200)Pd epitaxial minor reflection. Similar results are found for the (111)Pd main reflection. A lattice mismatch of $\approx$ 5% is tolerable, and epitaxial growth has been demonstrated for aqueous Au-Pd systems before.[569, 570, 578] Reflections of the Au-Pd mixed phase in electron diffraction (Figure 8.7d) were also detected and mark the transition of the Au to the Pd phase (Figure 8.7c). Hence, the formation of an Au-Pd intermediate mixed phase through alloying at the interface may be possible due to the elevated synthesis temperatures and short diffusion lengths.[566, 577, 581] Complete coverage of the ODT-Au core by Pd is not possible because of the reduced amount of Pd precursor used in this synthesis. Increasing the ODT-Au:Pd(ac)$_2$ ratio to 1:1 yielded the Au@Pd core-shell particles discussed before (Figure 8.4, Figure 8.7a). Increasing the amount of Pd^{2+} amount even further (1:3 ratio) led to the core-shell particles shown in Figure 8.7e through aberration corrected HR-TEM analysis with a closed Pd shell of variable thickness around an Au core. Figure 8.9 contains HR-TEM images and Fourier analyses of NPs with different shell morphologies. They show

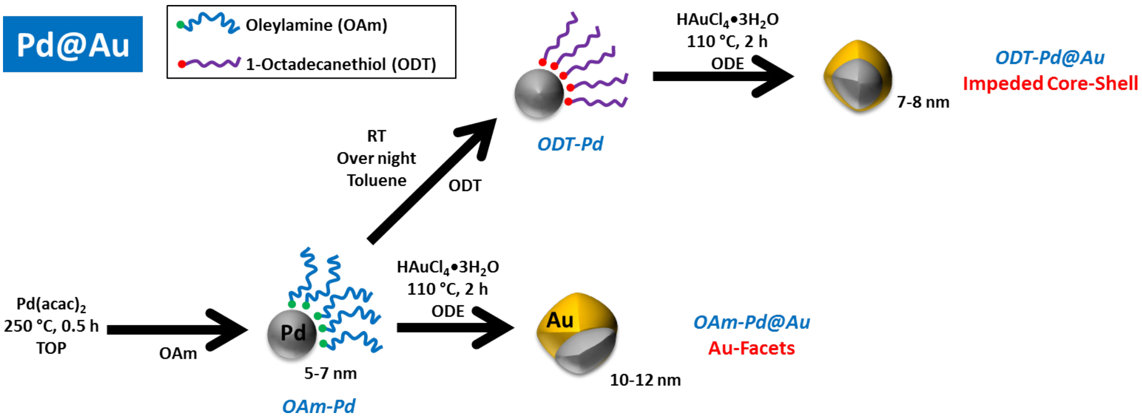

Figure 8.10: Schematic representation of as-synthesized OAm-functionalized Pd NPs with diameters of 5-7 nm, their subsequent re-functionalization with ODT and their reaction with $HAuCl_4$ to form surface functionalized Pd@Au heterodimers.

increased Pd overgrowth at different spots of the NP. This may be caused by the high Pd precursor content which leads to the deposition of additional Pd, presumably at defect sites of the shell. Analysis of the power spectra reflections (Figure 8.7f) from different regions of the NP show Au reflections for the core region and Pd reflections for different regions of the shell.

In summary, epitaxial growth of Pd onto preformed Au NP seeds to form core-shell NPs can only be obtained by post-synthetic surface functionalization of the Au NPs with ODT. Layer-by-layer deposition is facilitated by changing the surface energy with different ligands. The amount of Pd precursor determines the type and morphology of the Pd coverage. Low Pd contents lead to incomplete coverage of the Au NP, whereas Pd excess, *i.e.* ODT-Au:$Pd(ac)_2$ ratios of 1:1 and 1:3, allow core-shell formation and also Pd overgrowth.

8.3.4 Pd@Au Heterodimers

Figure 8.10 presents a scheme for the synthesis and functionalization of Pd seed NPs and Pd@Au heterodimers. First, 5-7 nm Pd seed particles were synthesized by reduction of $Pd(acac)_2$ in tri-n-octylphosphine (TOP) and OAm.[331] These OAm and TOP capped Pd NPs (Figure 8.11a, 5.3 nm ± 9.7%, Figure 8.3e) were used in a seed mediated growth reaction using ODE as solvent to form OAm-Pd@Au NPs through reduction of Au^{3+}. The preformed OAm-Pd NPs were also subject to surface functionalization with ODT (*vide supra*). After surface functionalization, the ODT-Pd NPs had a diameter of 5.4 nm ± 9.9% (Figure 8.11b, Figure 8.3f). In a subsequent reaction ODT-Pd@Au NPs were formed by Au deposition from $HAuCl_4{\cdot}3H_2O$ reduction.

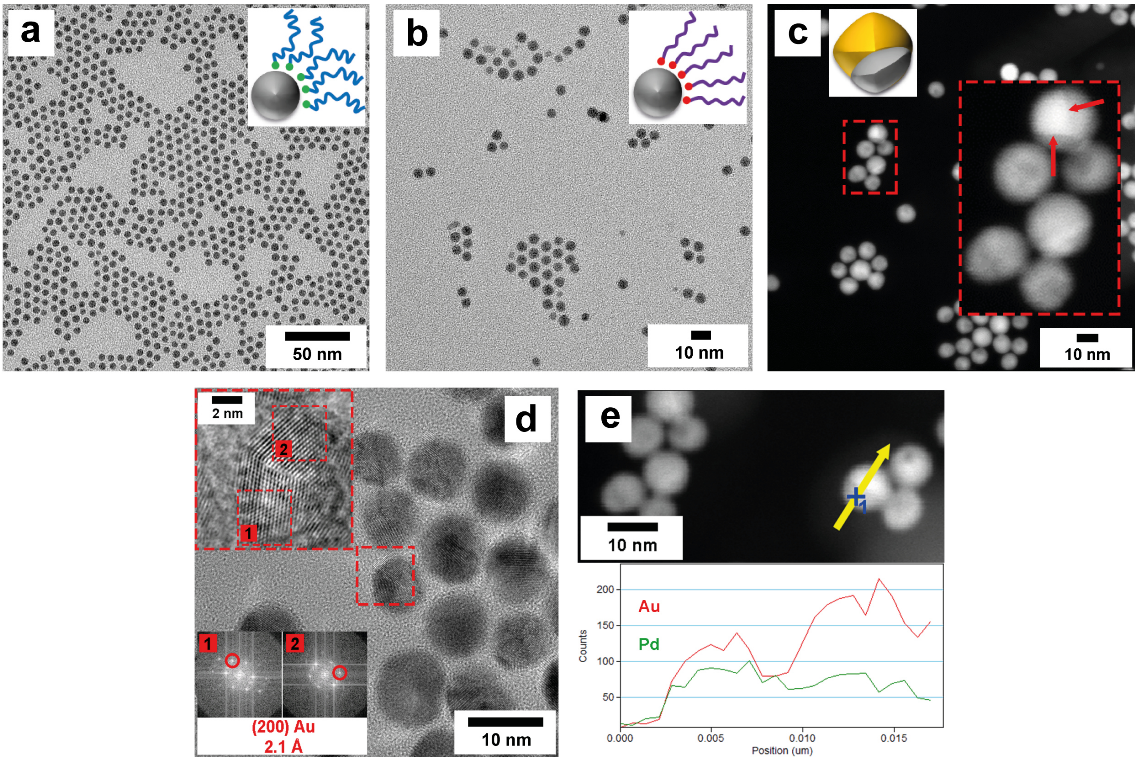

Figure 8.11: (a) TEM image of OAm-Pd NPs. (b) TEM image of ODT-Pd NPs. (c) HAADF-STEM image and (d) HR-TEM image of OAm-Pd@Au NPs showing domain boundaries of Au rich domains. (e) STEM-EDX line scan profile of an OAm-Pd@Au NP showing Au-rich domains.

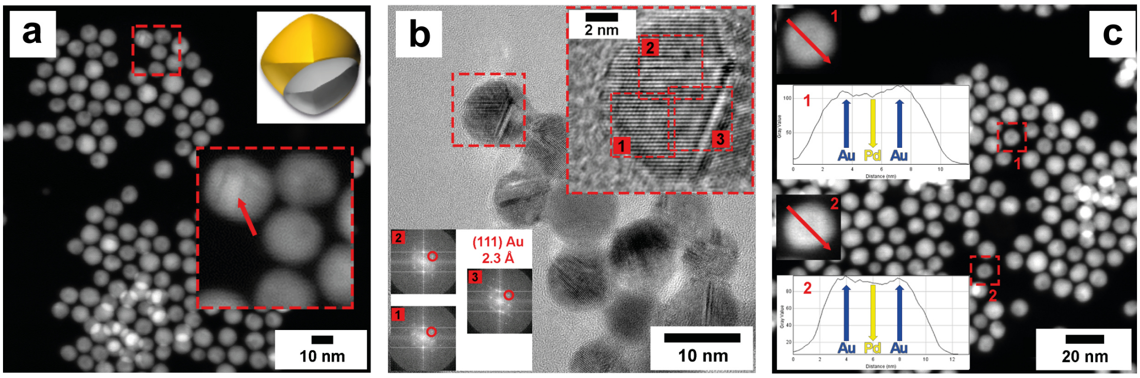

Figure 8.12: (a) HAADF-STEM image and (b) HR-TEM image of OAm-Pd@Au NPs showing domain boundaries of Au rich domains. (c) HAADF-STEM image and grey value profile for two OAm-Pd@Au NPs showing core-shell structure.

8.3.5 OAm-Pd@Au Nanoparticles With Facetted Au Overgrowth

OAm-Pd@Au NPs formed predominantly heterodimers with extended Au domains on Pd seeds (Figure 8.11c-e), where the diameter of the NPs increased to 11.1 nm

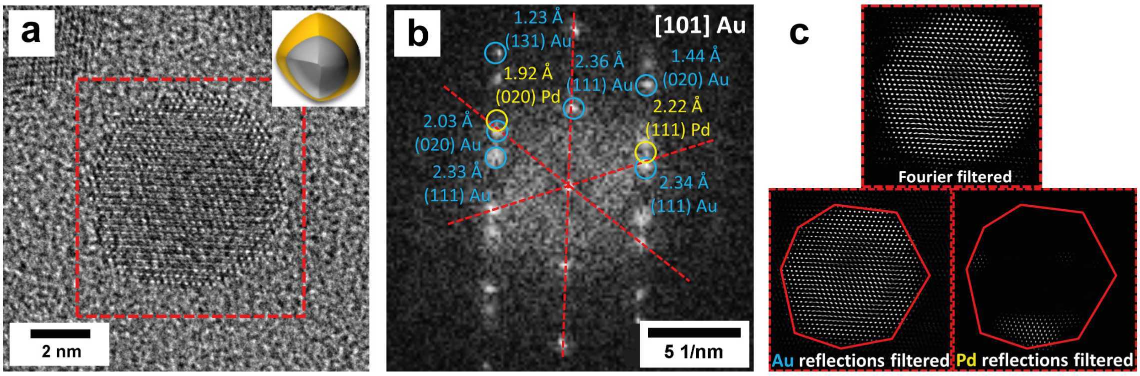

Figure 8.13: (a) Aberration corrected HR-TEM image of an ODT-Pd@Au NP. (b) Power spectrum of the [101]Au zone axis of the NP displayed in (a) showing Au and Pd reflections. (c) Fourier filter and Au and Pd reflections filter of the NP displayed in the red boxed region of (a).

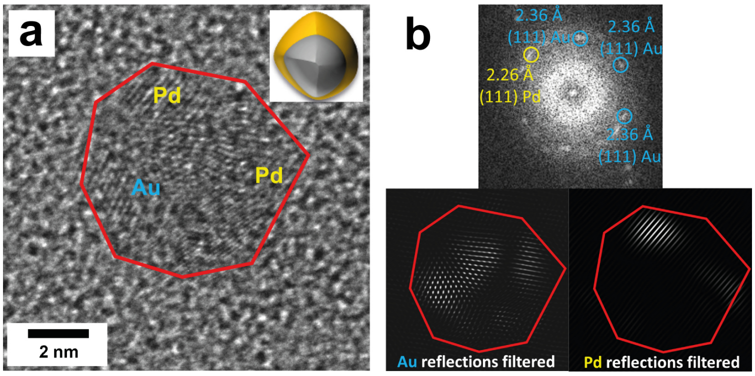

Figure 8.14: (a) Aberration corrected HR-TEM image of an ODT-Pd@Au NP with distribution of Au and Pd. (b) Power spectrum showing Au and Pd reflections of the NP displayed in (a) along with filtered Au and Pd reflections.

± 9%. HAADF-STEM was used to examine the Au-Pd distribution. Most NPs showed straight contrast boundaries and areas of high scattering contrast (Figure 8.11c arrows, Figure 8.12a arrow). HR-TEM images and power spectra analyses revealed these high scattering areas to contain adjacent Au domains (Figure 8.11d, Figure 8.12b). Figure 8.11e shows an EDX-line scan profile of an OAm-Pd@Au NP. This indicates that the Pd seed particle is covered by Au of variable thickness, generating partially dense Au domains. Still, a small fraction of the OAm-Pd@Au NPs had a core-shell structure with complete coverage with Au, as demonstrated by STEM contrast analysis (Figure 8.12c). The gray value profile of the NP is reduced at the center due to a decrease in the scattering contrast caused by the Pd core.

8.3.6 Impeded Formation of ODT-Pd@Au Core-Shell Nanoparticles

ODT-Pd NPs (Figure 8.11b) were used similarly as ODT-Au NPs in a seed mediated growth process. The results are shown in the aberration corrected HR-TEM image in Figure 8.13. After depositing the Au shell, the diameter of the ODT-Pd@Au NPs had grown to 6.8 nm ± 16%. This is an increase in size of $\approx 20\%$ compared to the diameter of 5.4 nm ± 9.9% of the ODT-Pd seeds (Figure 8.13a). Power spectrum analysis (Figure 8.13b) of the [101]Au zone axis revealed that most reflections can be attributed to Au, whereas only a few Pd reflections were detected. Filtered Au and Pd reflections from the power spectrum showed Au to be distributed around the NP. The Pd portion constitutes the bottom portion of the NP (Figure 8.13c). Studies of other NPs displayed similar results (Figure 8.14). Due to the small size, the resulting surface curvature and higher surface reactivity[362] of the ODT-Pd seeds, the formation of a uniform core-shell structure may be impeded.

8.3.7 UV-vis Spectroscopy

UV-vis spectra of OAm-Au, ODT-Au, OAm-Au@Pd and ODT-Au@Pd NPs with Au diameters of 4 nm and 9-11 nm are shown in Figure 8.15a. The surface plasmon resonance (SPR) band of the OAm-Au NPs with diameters of 9-11 nm is centered at 520 nm (while that for 4 nm OAm-Au NPs is located at 510 nm). Thiol functionalization leads to a red-shift of the maximum to 550 nm (525 nm for ODT-Au NPs with a diameter of 4 nm), where the color change of the solution from red to purple was visible even with the naked eye. For Au NPs, the maximum of the SPR linearly depends on the refractive index of the nonpolar solvent.[530] Therefore, cyclohexane was used for all experiments. The large red shift of 30 nm can be attributed to a strong Au-S chemisorption resulting in a significant charge redistribution and electron donation. Besides charge redistribution, a contribution from particle agglomeration may be possible.[530, 531] OAm-Au@Pd NPs showed a reduced SPR intensity at 512 nm, while ODT-Au@Pd NPs did not display a pronounced SPR resonance anymore. Similar results were obtained for ODT-Au@Pd NPs with different Au:Pd ratios (Figure 8.15b). These changes result from the different Pd coverage. Complete Pd coverage of ODT-Au NPs (core-shell structure) led to a SPR quenching, whereas the partial Pd coverage of the OAm-Au@Pd NPs maintained a reduced SPR.[572] The observed blue shift of the SPR maximum (520 nm to 512 nm) results from the incorporation of Pd.[567] The surface electron density is increased by electron donation from Pd to Au due to the difference of the chemical potentials.[588–590] OAm-Pd and ODT-Pd NPs showed no SPR in the UV-vis spectral range (Figure 8.15c). OAm-Pd@Au NPs showed a SPR at 514 nm due to Au domains on the Pd seeds.

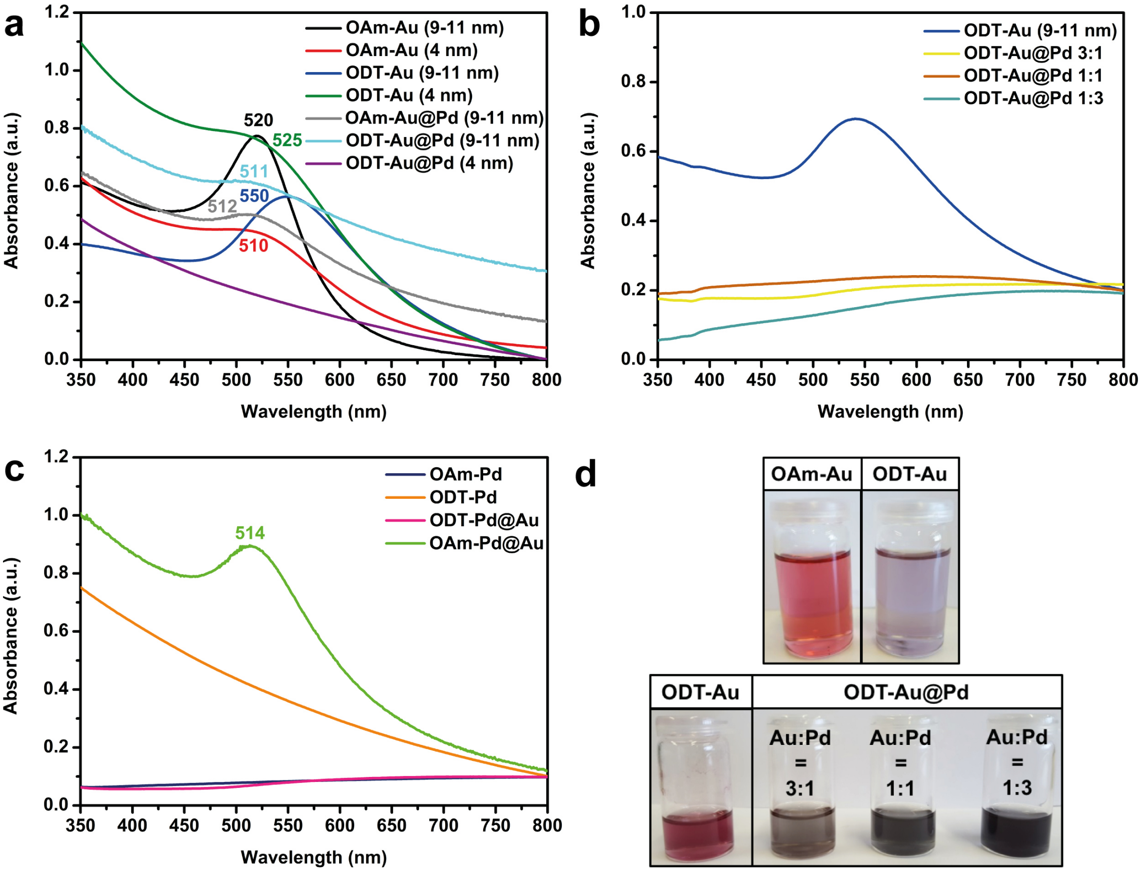

Figure 8.15: UV-vis spectra of (a) OAm-Au, ODT-Au, OAm-Au@Pd and ODT-Au@Pd NPs of 4 nm and 9-11 nm size. (b) UV-vis spectra of ODT-Au@Pd NPs with different Au:Pd ratios. (c) UV-vis spectra of OAm-Pd, ODT-Pd, ODT-Pd@Au and OAm-Pd@Au NPs. (d) Photographs of different NP dispersions of same NP concentration in cyclohexane.

8.3.8 Catalytic Activity of Au-Pd NPs Towards 4-Nitrophenol Reduction

The catalytic activity (Figure 8.16) of selected Au-Pd bimetallic NPs was studied by monitoring their ability to reduce 4-nitrophenol (4-NP) to 4-aminophenol (4-AP) with $NaBH_4$ at pH 11 in NaOH. OAm-Pd@Au and ODT-Au@Pd NPs were exemplarily used as reduction catalysts, and Au NPs with diameters of 9.2 nm and Pd NPs with diameters of 5.5 nm were used as references. OAm-Pd@Au and ODT-Au@Pd NPs are spherical with well separated Au and Pd domains. The particles have diameters of approx. 10.0 nm (OAm-Pd@Au) or an Au@Pd core-shell structure with a diameter of 11.1 nm (ODT-Au@Pd). 4-NP is a model substrate for reduction. The well-studied model reaction allows calibration of the catalytic activity properties of nanoparticles[591–594] by estimating the nanoparticle-substrate interaction.

The reduction of 4-NP to 4-AP with sodium borohydride is a model reaction that can be monitored colorimetrically by the decay of the absorption band of 4-NP

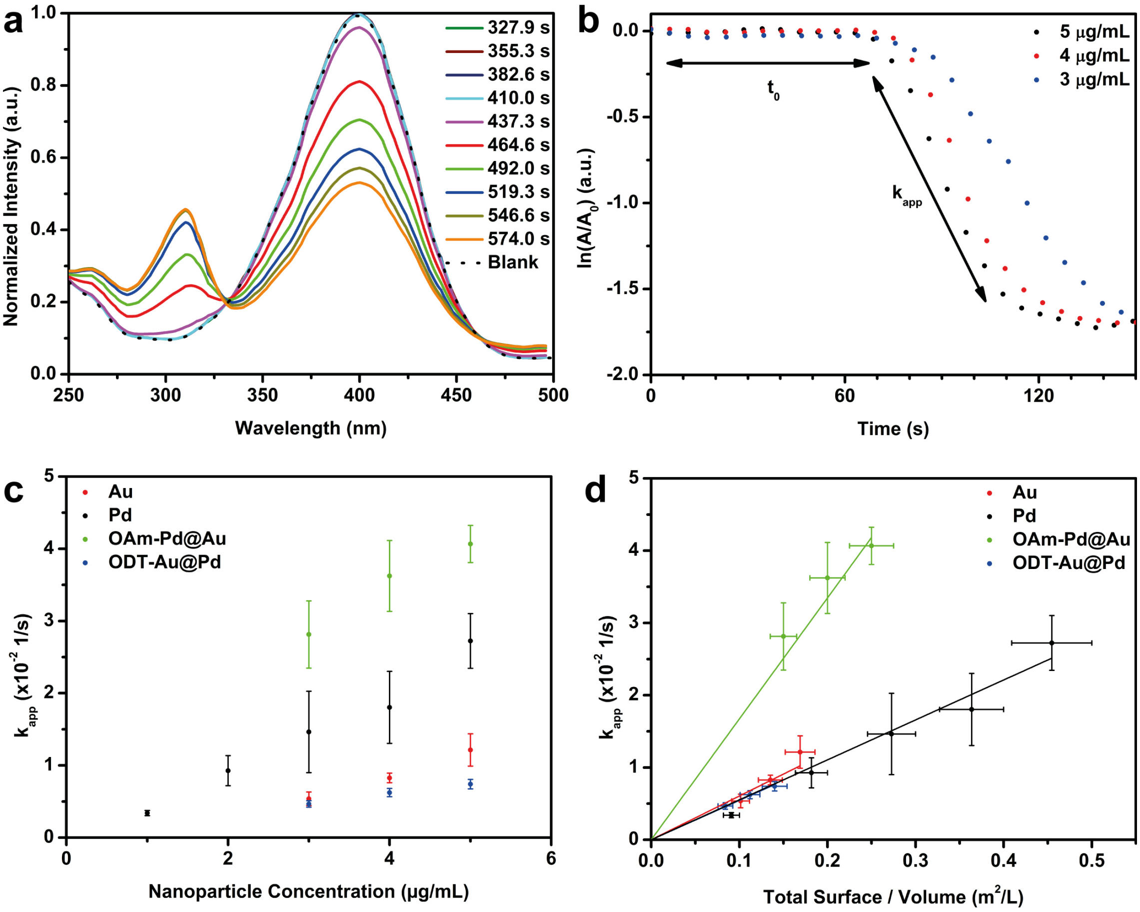

Figure 8.16: (a) Absorption spectrum of 4-NP reduction with $NaBH_4$ in presence of Au NPs. Blank marks the reaction without NPs after 10 min reaction time. (b) Time dependence of the absorption of the 4-nitrophenolate ion at 400 nm for OAm-Pd@Au NPs. t_0 marks the induction time before the reaction is started and k_{app} marks the linear region for determining the apparent reaction constant. (c) k_{app} depending on the nanoparticle concentration for the four measured NP types. (d) Linear behavior for k_{app} in dependence of the total surface to volume ratio, enabling the determination of k.

at ∼ 400 nm (Figure 8.16a), while the formation of 4-AP leads to an absorption band at ∼ 300 nm. $NaBH_4$ transfers a hydride anion onto the NP surface to form a surface-bound metal hydride species, while 4-NP chemisorbs onto the NP surface as well. The reaction follows the Langmuir-Hinshelwood mechanism which requires the concomitant adsorption of both reactants (hydride and 4-NP) to complete the reaction.[591–593] As shown in Figure 8.16a, the reaction took place within a time slot of 2-10 minutes depending on the type of NP and its concentration. The typical time dependence of the absorption of 4-NP at 400 nm is shown for the OAm-Pd@Au NPs in Figure 8.16b. t_0 marks the induction period which is typically associated with a slow adsorbate-induced surface reconstruction[595, 596] of the NPs in the presence of 4-NP.[591] It may vary for different types of NPs and concentrations from seconds to

Table 8.1: Calculated kinetic constant k for the 4-NP reduction reaction of different Au-Pd NPs and underlying nanoparticle radius r.

	r (nm)	k ($Lm^{-2}s^{-1}$)
Au	4.60	0.061 ± 0.003
Pd	2.75	0.055 ± 0.003
OAm-Pd@Au	5.00	0.167 ± 0.006
ODT-Au@Pd	5.55	0.055 ± 0.001

several minutes and it is assumed to be related to a rearrangement of single surface atoms.[597] From the linear behavior at longer reaction times, an apparent reaction constant k_{app} was derived and plotted against the NP concentration (Figure 8.16c) according to the relationship $dc_{4\text{-NP}}/dt = -k_{app} \cdot c_{4\text{-NP}}$.[591] OAm-Pd@Au NPs (with facetted Au domains) had the highest catalytic activity, followed by Pd NPs, Au NPs and core-shell ODT-Au@Pd NPs. k_{app} is proportional to the total surface area S of all metal NPs ($-k_{app} = -k \cdot S$),[591] and deviations occur for the surfaces of the four different NPs because of size differences and the associated surface/volume ratio. Plotting k_{app} against the total surface/volume ratio leads to a linear behavior for each NP type (Figure 8.16d) and a kinetic constant k for the 4-NP reduction (Table 8.1), enabling the comparison of the catalytic activity independent of the NP size. After correcting for differences in surface/volume ratio, the highest activity was found again for the OAm-Pd@Au NPs (with facetted Au domains), followed by Au NPs. ODT-Au@Pd core-shell NPs and Pd NPs had a comparable, but the lowest activity. We attribute the higher activity of the OAm-Pd@Au NPs to their mixed Au-Pd surface structure, where Au is present as large surface domains adjacent to Pd from the seed NP, supporting the catalytic reaction through electronic interaction. The high activity of the Pd NPs (with respect to the NP concentration) is related to their size. Taking into account the surface/volume ratio, Au NPs show a slightly higher activity than Pd NPs. This aids in interpreting the activity of the ODT-Au@Pd NPs containing a closed Pd shell around an Au core. The shielding of a more active Au core by a less active Pd surface shell leads to a lower catalytic activity, comparable with the activity of pure Pd NPs, because only Pd is available on the NP surface. A comparison to reported values of the kinetic constant k in the literature (Au:[598] 0.080 $Lm^{-2}s^{-1}$ and Pd:[599] 0.101 $Lm^{-2}s^{-1}$) demonstrates that our values of the Au and Pd reference NPs are lower. However, the literature values depend on the polymer carrier system.[598, 599] Taking only into account the apparent reaction constant k_{app}, our NPs show a comparable or even higher catalytic performance.[600, 601] NPs with mixed metallic surface structure show an enhanced catalytic performance compared to their monometallic counterparts,[601, 602] in agreement with our observed catalytic results.

8.4 Conclusion

Au-Pd heteroparticles were synthesized to investigate the effect of the NP structure on the catalytic activity for the reduction of 4-nitrophenol to 4-aminophenol with sodium borohydride. Au-Pd heteroparticles with different morphologies were synthesized by a seed mediated growth process in ODE, a high boiling organic solvent. Heterodimer NPs with separated Pd (Au) domains were synthesized with oleylamine capped OAm-Au (OAm-Pd) seeds. The polycrystalline and multiple-twinned structures of the seed particles have locally high surface energies. This reduces the energy barriers for heterogeneous nucleation compared to the surfaces of spherical and single crystalline NPs, inducing island growth and a concomitant reduction of the overall surface area. 1-octadecanethiol capped ODT-Au NPs were also used as seeds for the reduction of $Pd(ac)_2$ to form Au@Pd heterodimers. With 9-11 nm ODT-Au NPs, a ODT-Au@Pd core-shell NP structure (with Au core and Pd shell) with diameters of 15-17 nm was formed. The formation of the Pd shell was further investigated by varying the Au/Pd ratio. At low Pd concentrations, no closed Pd shell was formed. This allowed monitoring of the surface epitaxial growth by aberration corrected HR-TEM analysis. At high Pd concentrations, Pd shell overgrowth was observed. To examine whether the formation of the core-shell NPs was induced by the thiol-capped Au surface, the Pd overgrowth was carried out with amine-functionalized OAm-Au NPs (9-11 nm). No core-shell structures, but particles with windmill-morphology were formed, where several Pd "blades" were attached to an Au core. The surface coverage of the Au core with Pd "blades" was incomplete. For OAm-Pd and ODT-Pd seed particles, facetted, Au-rich domain NPs (OAm-Pd@Au) and impeded core-shell NPs (ODT-Pd@Au) were obtained. This is related to the high surface energy of the small Pd seed particles (diameter 5-7 nm). The highest activity in the catalytic reaction was found for the OAm-Pd@Au NPs (with facetted Au domains), followed by Au NPs and Pd NPs. The high catalytic activity of the OAm-Pd@Au NPs is attributed to the formation of a mixed Au-Pd surface structure, where Au is present as large surface domains adjacent to Pd from the seed NP. Based on their surface area, Au NPs had a higher activity than Pd NPs in the hydration. ODT-Au@Pd NPs where the more active Au core is shielded by a less active Pd surface shell had the lowest catalytic activity. The availability of well characterized Au-Pd heteroparticles with different particle structures and morphologies allows to study the effects of surfaces sites and surface morphologies on a model reduction reaction in solution close to the molecular scale.

8.5 Experimental Section

Materials

Hydrogen tetrachloroaurate(III) trihydrate ($HAuCl_4 \cdot 3H_2O$, Alfa Aesar, 99.99%), palladium(II) acetylacetonate ($Pd(acac)_2$, Acros Organics), palladium(II) acetate ($Pd(ac)_2$, Aldrich, 98%, reagent grade), oleylamine (OAm, Acros Organics, 80-90%), cyclohexane (Fisher Scientific, Analytical Reagent Grade), *tert*-butylamine borane complex (TBAB, Aldrich, 97%), tri-n-octylphosphine (TOP, abcr, 97%), 1-octadecanethiol (ODT, Alfa Aesar, 96%), 1-octadecene (ODE, Acros Organics, 90%), O-[2-(3-mercaptopropionylamino)ethyl]-O-methylpolyethyleneglycol (S-PEG, Aldrich, 5000), ethanol (Sigma-Aldrich, *p.a.*, $> 99.8\%$), methanol (Fisher Scientific, Analytical Reagent Grade), toluene (Sigma-Aldrich, *p.a.*, $> 99.7\%$), hexane (Fisher Scientific, Analytical Reagent Grade), chloroform (Aldrich, 99-99.4%), sodium borohydride ($NaBH_4$, Acros Organics, 99%), sodium hydroxide (Sigma Aldrich, *p.a.*, $> 98\%$) and 4-nitrophenol (4-NP, Fluka, $> 99.5\%$) were used in this work.

Synthesis of 4 nm OAm-Au Seed Nanoparticles

The synthesis of 4 nm Au seed NPs was adapted from Peng *et al.*[547] In a 100 mL three-neck round bottom flask, 84.9 mg (0.25 mmol) of $HAuCl_4 \cdot 3H_2O$ were dispersed in 10 mL of cyclohexane and 10 mL of oleylamine under inert gas (Ar) conditions and stirred for 15 min at room temperature (RT). Meanwhile, 43.5 mg (0.50 mmol) of *tert*-butylamine borane complex were dispersed in 1 mL of cyclohexane and 1 mL of OAm and ultrasonicated for 5 min. The TBAB dispersion was directly and rapidly injected into the preformed precursor solution, which turned dark red within 1-2 seconds upon injection. The mixture was stirred for 1 h at RT. The Au NPs were precipitated by adding 20 mL of methanol which contained 10 vol% of OAm and separated by centrifugation (9000 rpm, 10 min, RT). The precipitate was dispersed in cyclohexane and washed twice by adding a 1:1 mixture of methanol:ethanol, which contained 10 vol% of OAm, and additional centrifugation (9000 rpm, 10 min, RT). Finally, the product was dispersed in cyclohexane, flushed with Ar and stored at RT.

Synthesis of 9-11 nm OAm-Au Nanoparticles

A growth solution containing 196.9 mg (0.50 mmol) of $HAuCl_4 \cdot 3H_2O$, 10 mL of toluene and 10 mL of OAm was prepared at RT under inert gas (Ar) conditions. A dispersion of 10 mg of 4 nm OAm-Au seed NPs in 10 mL of toluene was added and the mixture was heated rapidly to 111 °C. The temperature was maintained for 2 h. Subsequently, the mixture was slowly cooled to RT. Precipitation and purification were identical as described above for the 4 nm OAm-Au seeds, but no additional OAm was added to the precipitation and washing solutions.

Synthesis of 5-7 nm OAm-Pd Nanoparticles

The synthesis of the 5-7 nm OAm-Pd seed NPs was adapted from Kim *et al.*[331] In a 100 mL three-neck round bottom flask, 100 mg of Pd(acac)$_2$ were dissolved in 1 mL of tri-n-octylphosphine under inert gas (Ar) conditions and stirred for 10 min. Subsequently, 10 mL of oleylamine were added. The mixture was heated to 250 °C at a rate of 2 °C/min and held at this temperature for 30 min. Afterwards, the mixture was slowly cooled to room temperature. A black product was precipitated from the mixture by adding 15 mL of ethanol. The precipitate was separated by centrifugation (9000 rpm, 10 min, RT), dispersed in cyclohexane and washed twice by adding ethanol (cyclohexane:ethanol = 1:2) and additional centrifugation (9000 rpm, 10 min, RT). Finally, the product was dispersed in cyclohexane, flushed with Ar and stored at RT.

1-Octadecanethiol-functionalization of OAm-Au and OAm-Pd Nanoparticles

10 mg of 4 nm OAm-Au NPs, 9-11 nm OAm-Au NPs or 5-7 nm OAm-Pd NPs were dispersed in 10 mL of toluene at RT under inert gas (Ar) conditions. 1 mL of 1-octadecanethiol (3 mmol) was added, and the mixture was stirred over night at RT. A purple (Au) or grey (Pd) product was precipitated from the mixture by adding 15 mL of methanol. The precipitate was separated by centrifugation (9000 rpm, 10 min, RT), dispersed in cyclohexane and washed twice by adding ethanol (cyclohexane:ethanol = 1:2) and additional centrifugation (9000 rpm, 10 min, RT). Finally, the product was dispersed in cyclohexane, flushed with Ar and stored at RT.

Synthesis of ODT-Au@Pd Nanoparticles

For the synthesis of heteroparticles, 10 mg of 4 nm ODT-Au NPs or 9-11 nm ODT-Au NPs were dispersed in 10 mL of 1-octadecene and 0.74 mL of OAm at RT under inert gas (Ar) conditions. Subsequently, 11.5 mg (0.05 mmol) of Pd(ac)$_2$ were added. The mixture was heated to 200 °C at a rate of 10 °C/min and held at this temperature for 2 h. Afterwards, the mixture was slowly cooled to room temperature. A black product was precipitated from the mixture by adding 15 mL of ethanol. The precipitate was separated by centrifugation (9000 rpm, 10 min, RT), dispersed in cyclohexane and washed twice by adding ethanol (cyclohexane:ethanol = 1:2) and additional centrifugation (9000 rpm, 10 min, RT). Finally, the product was dispersed in cyclohexane, flushed with Ar and stored at RT.

Synthesis of OAm-Au@Pd Nanoparticles

The synthesis was performed as described above for the ODT-Au NPs, but ODT-Au NPs were replaced by OAm-Au NPs.

Synthesis of ODT-Pd@Au nanoparticles

For the synthesis of heteroparticles 10 mg of 5-7 nm ODT-Pd NPs were dispersed in 10 mL of 1-octadecene and 0.74 mL of OAm at RT under inert gas (Ar) conditions. Subsequently, 39.5 mg (0.10 mmol) of $HAuCl_4 \cdot 3H_2O$ were added. The mixture was heated to 110 °C at a rate of 10 °C/min and held at this temperature for 2 h. Afterwards, the mixture was cooled slowly to room temperature. A black product was precipitated from the mixture by adding 15 mL of ethanol. The precipitate was separated by centrifugation (9000 rpm, 10 min, RT), dispersed in cyclohexane and washed twice by adding ethanol (cyclohexane:ethanol = 1:2) and additional centrifugation (9000 rpm, 10 min, RT). Finally, the product was dispersed in cyclohexane, flushed with Ar and stored at RT.

Synthesis of OAm-Pd@Au nanoparticles

The synthesis was performed as described above for the ODT-Pd NPs, but with OAm-Pd NPs instead of ODT-Pd NPs.

Surface functionalization of Au@Pd, Pd@Au, Au and Pd nanoparticles

A 1 mg/mL dispersion of NPs in chloroform was mixed with a 1 mg/mL solution of S-PEG in chloroform. The reaction mixture was stirred with a mechanical stirrer for 6 h at 40 °C under a gentle Ar flow. 6 mL of hexane per milligram of NPs was added, and the NPs were extracted into 1 mL of Milli-Q water per milligram of NPs using a separating funnel.

Kinetic Analysis

For the evaluation of the catalytic activity of the Au@Pd, Pd@Au, Au and Pd NPs, the NPs were dispersed in an aqueous NaOH solution (pH 11) to give 3, 4 and 5 μg/mL nanoparticle concentrations (for Pd NPs 1-5 μg/mL). Solutions of 0.1 mM 4-nitrophenol and 10 mM $NaBH_4$ were also prepared in an aqueous NaOH solution (pH 11). The solutions were always freshly prepared prior to use. Kinetic Analysis of the catalytic reduction of 4-nitrophenol was carried out on a Tecan Infinite M Pro 200 Plate Reader equipped with a UV Xenon Flash lamp. Greiner UV-Star transparent 96 well plates (300 μL) were used to monitor the reduction of 4-nitrophenol absorbance at 400 nm and the increase of 4-aminophenol absorbance at 300 nm in a time range of 10 min at 25 °C. To evaluate k_{app}, $\ln(A/A_0)$ was plotted against the time and linear fitted with eight points after expiration of the t_0 induction time. The rate constant, k, was obtained through linear fitting of k_{app} against total surface per volume (S). The total surface per volume was calculated using the radius of the NPs from TEM images and the bulk density of Au (19.3 g/cm^3) or Pd (12.0 g/cm^3), respectively. The error of the total surface per volume ratio was presumed to be 10%.

Nanoparticle Characterization

Samples for *transmission electron microscopy (TEM)* were prepared by placing a drop of dilute NP dispersion in cyclohexane on a carbon coated copper grid. TEM images for the characterization of size and morphology were obtained with a FEI Tecnai 12 using a LaB_6 source at 120 kV and a twin-objective together with a Gatan US1000 CCD-camera (2K x 2K pixels). Aberration-corrected high-resolution TEM was performed on a JEM-ARM300F instrument (Grand ARM, JEOL Co.) with double correction. The spherical aberration of the condenser and the objective lens were corrected by dodecapole correctors in the beam and the image-forming system. The TEM resolution is 0.5-0.7 *Å* depending on the resolution criterion applied. TEM images were recorded on a 4K x 4K pixel CCD array (Gatan US4000). High-resolution TEM, STEM and EDX data were obtained on a FEI Tecnai F30 S-TWIN TEM equipped with a field emission gun and operated at 300 kV.

UV-vis spectra of NP dispersions in cyclohexane were recorded on a Cary 5G UV-vis-NIR spectrophotometer in a range from 250 to 800 nm.

X-ray diffraction (XRD) patterns were recorded on a Bruker AXS D8 Advance diffractometer equipped with a SolX energy dispersive detector in reflection mode using unfiltered Mo Kα radiation. Crystalline phases were identified according to the PDF-2 database using Bruker AXS EVA version 10.0. Full profile fits (Le Bail/Pawley/ Rietveld) were performed with TOPAS Academic version 4.1 by applying the fundamental parameter approach.[347, 348]

8.6 Appendix

The Au@Pd and Pd@Au heterodimer NPs were also analyzed by X-ray powder diffraction (XRD). Figure 8.17 diplays the results of Rietveld refinements for ODT-Au@Pd NPs, OAm-Pd@Au NPs and ODT-Pd@Au NPs. For the ODT-Au@Pd NPs a bulk Au-phase of 2.3(3) wt% was found in combination with a nano Au-phase which has a refined lattice parameter of 4.064(1) *Å* (Figure 8.17a, Table 8.2). However, no Pd was detected despite of the Au-Pd core-shell structure. XRD represents a bulk analyzing method which is complicated by reflection broadening for nanocrystalline materials.[320] Additionally, the structural similarity of Au and Pd is reflected in their only slightly different lattice parameters of 4.0782 *Å* for Au and 3.8790 *Å* for Pd.[381] Therefore XRD refinement of Au next to Pd is sophisticated and not necessarily representing the nanoparticulate composition. For the OAm-Pd@Au NPs with segregated Au and Pd domains (Figure 8.17b) a nano Au-phase of 88.5(15) wt% and a nano Pd-phase of 11.5(16) wt% was refined, showing that both elements can be distinguished in the bulk phase for this NP type. The ODT-Pd@Au NPs (Figure 8.17c) display only a nano Au-phase with a slightly smaller lattice parameter of 4.063(1) *Å*, however, pointing towards some Pd admixture according to Vegards's law.[579, 581, 588]

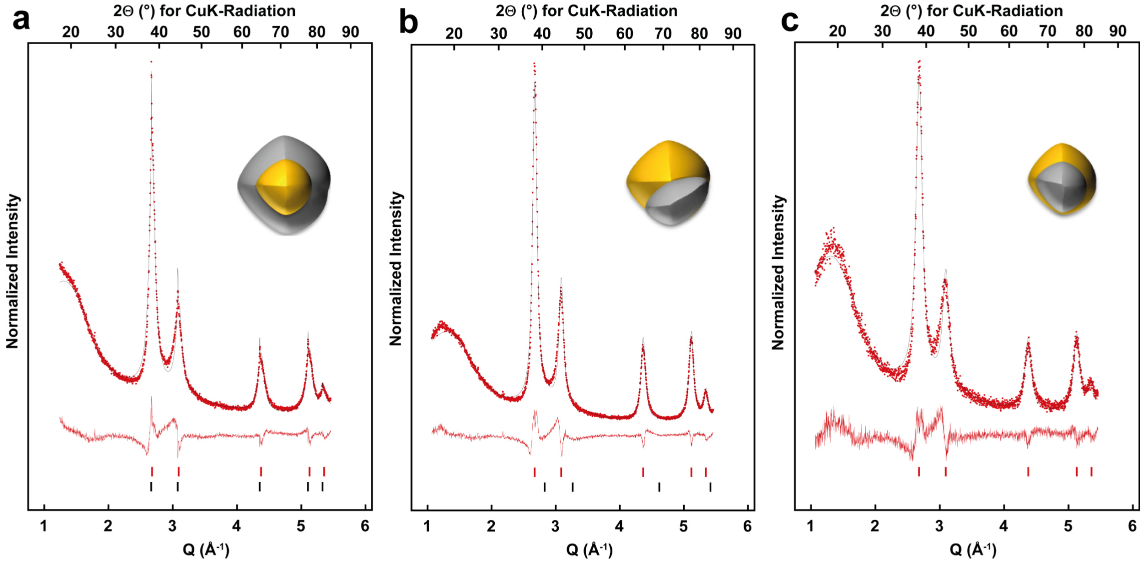

Figure 8.17: Rietveld refinements of powder XRD data for (a) ODT-Au@Pd NPs, (b) OAm-Pd@Au NPs, and (c) ODT-Pd@Au NPs. Red dots mark the experimental data, the black line corresponds to the calculated pattern, and the red line shows the difference between the experimental and calculated data. Red and black ticks mark reflections of Au and Pd, respectively. $Q = [4\pi \sin(\Theta)]/\lambda$ is the scattering vector.

Table 8.2: Additional data to the Rietveld refinement of powder XRD data. Measurement conditions: $5 \leq 2\Theta/° \leq 41.4$; $\Delta\Theta = 0.0065°$; $\Delta t = 5.14$ sec.

		ODT-Au@Pd NPs	**OAm-Pd@Au NPs**	**ODT-Pd@Au NPs**
Au-Phase (bulk)				
Cell parameter	Å	4.084(1) (lit.[381] 4.0782)	-	-
Crystallite size	nm	150.0(416)	-	-
Fraction	%wt	2.3(3)	-	-
Au-Phase (nano)				
Cell parameter	Å	4.064(1) (lit.[381] 4.0782)	4.073(1)	4.063(1)
Crystallite size	nm	5.6(1)	7.8(1)	5.3(1)
Fraction	%wt	97.7(3)	88.5(15)	100
Pd-Phase (nano)				
Cell parameter	Å	-	3.850(14) (lit.[381] 3.8790)	-
Crystallite size	nm	-	2.5(4)	-
Fraction	%wt	-	11.5(16)	-
R_{wp}		6.96	7.34	8.69
Goodness of fit (G)		3.02	3.18	1.78
Number of parameter/background		10/5	10/5	6/5

9

Conclusion and Outlook

In this thesis I have achieved to develop and examine novel inorganic nanoparticle single-, hetero- and superstructures for versatile applications ranging from enzyme mimetics and catalysis to biomedicine and diagnostics. The scientific approach started with the systematic adjustment of reaction parameters and educt composition to obtain tailor-made nanostructures with well-defined size, morphology and chemical composition. Next, a detailed chemical and physical characterization of the novel nanostructures was performed in order to authenticate the chemical composition for the aspired applications.

The nanoparticle surface, as important factor for reaction control or catalytic efficiency, was analyzed and functionalized to ensure the best application performance. To obtain the nanostructures, the noble metals Pd and Au were chosen due to their catalytic activity and tunable surface plasmon resonance and iron oxide got the attention because of the adaptable and size-dependent magnetic behavior, which enables researchers and technologists to exploit its use as contrast agent in magnetic resonance imaging or other diagnostics. Moreover, iron oxide is a promising material for peroxidase-like enzyme mimetic. The multifaceted combinations of noble metal and metal oxide nanostructures covered in this thesis, *i.e.* Pd@γ-Fe_2O_3 superparticles, Fe_xO@Fe_xO superparticles, Pd@Fe_xO heterodimer nanoparticles and Au-Pd heterodimer nanoparticles, demonstrate the opportunities of current nanoengineering to facilitate modern nanodevices with multiple application possibilities. In addition, ZnO semiconductor nanoparticles were utilized to evaluate Zn mediated cytotoxicity to cancer cells.

The first research project describes the synthesis of superparticles, which not only combine two different materials (catalytically active Pd and magnetic iron oxide) in the same nanoparticulate architecture, but also enhance the surface area and enable synergistic effects.

The project covered a two-step synthesis of Pd@γ-Fe_2O_3 superparticles by seed-mediated growth in high boiling organic solvents for a peroxidase-like enzyme mimetic. γ-Fe_2O_3 nanorods were grown on Pd nanotetrahedron and hexagonal Pd nanoplate templates. By adjusting the ratios of solvent, surfactant, and co-reductant $Fe(CO)_5$, the morphology of the Pd seed particles was varied systematically. The γ-Fe_2O_3 nanorods were grown on the preformed Pd seeds by oxidizing $Fe(CO)_5$ with trimethylamine *N*-oxide. Mössbauer spectroscopy measurements revealed that the nanorods

consist exclusively of maghemite, and a high resolution transmission electron microscopy analysis supported their epitaxial growth on the Pd surface.
The Pd@γ-Fe_2O_3 superparticles were subsequently functionalized by a hydrophilic catechol-PEG to ensure dipersibility in aqueous media. In a colorimetric assay the Pd@γ-Fe_2O_3 superparticles demonstrated an enhanced peroxidase-like catalytic activity (compared to that of isolated Fe_2O_3 nanorods) because of synergistic effects of electron transport through the Pd-γ-Fe_2O_3 interface between the Pd metal core and the γ-Fe_2O_3 nanorods. This resulted in a 10-fold higher activity of Pd@γ-Fe_2O_3 superparticles compared pure iron oxide nanorods.
We displayed the advantages of superparticles, with components interfaced *via* shared crystal faces, compared to self-assembled superstructures from small nanoparticles stabilized by van der Waals interactions. These advantages are electronic communication due to the absence of separating organic surface layers and physical stability.

The consecutive research project covered the synthetic approach for the formation of Fe_xO@Fe_xO superparticles as enhanced magnetic resonance imaging (MRI) contrast agent due to the exceptional hierarchical nanostructure. A synthesis of iron oxide flower-like and hedgehog-like superparticles based on spherical and hexagonal seed nanoparticles was performed through oxidation of $Fe(CO)_5$ precursor using trimethylamine *N*-oxide on the preformed seed nanoparticles.
The maghemite (spherical nanoparticles) and hematite (hexagonal nanoparticles) templates were decorated with maghemite iron oxide domains (spherical superparticles) and nanorods (hexagonal superparticles) based on Mössbauer spectroscopy analysis and X-Ray diffraction. While the templates determine the morphology of the superparticles, the chemistry determines the phase identity, where the hexagonal hematite seed nanoparticles were converted to maghemite during superparticle formation. The seed mediated growth process was carried out in high boiling 1-octadecene and epitaxial growth of the superparticles could be confirmed by orientation mapping, electron diffraction and high resolution transmission electron microscopy showing interfacial connections between the individual iron oxide domains and nanorods, respectively.
In addition, all particle types demonstrated low cytotoxicity and were subsequently tested for their signal enhancement potential in magnetic resonance imaging after hydrophilic catechol-PEG surface functionalization. Both superparticle types displayed contrast enhancement by increased R_1- and R_2-relaxivities compared to the template particles. The reduction of relaxation times was attributed to the higher effective superparamagnetic core radius because of the increased particle size and to the epitaxial growth relationship as well as to the anisotropy and inhomogeneity of the particle-generated magnetic field because of the unique superparticle morphology. Utmost contrast enhancement was measured for transversal relaxation, making the superparticles promising candidates for dark field imaging contrast agents.

In the third research project a protocol to synthesize Pd@Fe_xO heterodimer nanoparticles with a spherical 5 nm Pd and a faceted 25 nm iron oxide domain was developed for a catalytic hydrosilylation reaction. As starting materials Pd seed nanoparticles and an iron(III) oleate precursor was synthesized. The Pd seed nanoparticles were decorated with octahedral iron oxide domains by a seed mediated growth process based on the thermal decomposition of the iron(III) oleate precursor. The anisotropic iron oxide domains constituted of an approximately 50:50 maghemite:magnetite mixture with 65 emu/g saturation magnetization at 300 K. Afterwards the Pd@Fe_xO heterodimer nanoparticles were surface functionalized with BF_4^- to achieve a better dispersibility in polar organic media and perform catalysis.

With a proper choice of reactants and by exploring the individual properties of both domains of the heterodimer nanoparticles, a hydrophobic, macroporous and magnetic foam was synthesized that could be used for a reversible adsorption of non-polar liquids. The Pd domain provided catalytic activity in a hydrosilylation reaction of organosilicones to form the template-free foam with embedded nanoparticles. The magnetic iron oxide domain was used to move and withdraw the foam in water. Such magnetically triggered hydrophobic foams were demonstrated as potential adsorbent for oil sampling in oil wells or for separating oil from water. This presents an example of novel hybrid organic-inorganic multicomponent nanostructures connected through a solid interface and able to combine different or even incompatible properties within a single entity.

Moreover, peroxidase-like catalytic activity was demonstrated for the Pd@Fe_xO heterodimer nanoparticles. The peroxidase-like activity of the Pd@Fe_xO heterodimer nanoparticles was enhanced compared to their single material nanoparticles (*i.e.* Pd and iron oxide nanoparticles) due to electron transport across the metal-metal oxide interface and the increased surface area.

The enhanced catalytic performance of the heterodimers compared to the single material counterpart could be verified by a colorimetric assay based on the catalytic oxidation of ABTS (2,2'-azinobis(3-ethyl-benzothiazoline-6-sulfonic acid) diammonium salt) dye with H_2O_2, which leads to the formation of a $ABTS^{+\cdot}$ radical yielding a green solution. The Pd@Fe_xO heterodimer nanoparticles obtained higher Michaelis-Menten kinetic parameters (v_{max} and k_{cat}) compared to single Fe_xO nanoparticles, demonstrating a synergistic effect, charge separation and resulting electron transfer through the Pd domain and the iron oxide domain.

The influence of an increased surface area and availability of surface atoms could be addressed by a comparison of the kinetic parameters with those obtained for the enzyme mimetics of the Pd@γ-Fe_2O_3 superparticles. The concentration of surface available Fe-atoms for the Pd@Fe_xO heterodimer nanoparticles was calculated to be approximately 2.5 times higher compared to the Pd@γ-Fe_2O_3 superparticles, while the maximum reaction rate (v_{max}) was comparable. Accordingly, the superparticles showed the better catalytic performance expressed in a higher k_{cat} value. This was supported by the lower amount of superparticles necessary to obtain these values. The open structure of the superparticles with multiple nanorods available for a catalysis is probably more favorable for the substrate which is also reflected in a higher atomic absorption spectroscopy correction factor for the Pd@γ-Fe_2O_3 superparticles compared to the Pd@Fe_xO heterodimer nanoparticles, representing more surface available Fe-atoms per individual nanoparticle.

The next research project utilized ZnO nanoparticles of different synthetic strategies and morphologies for the evaluation of ZnO nanoparticle cell uptake and toxicity mechanisms. ZnO, especially in the nano-sized regime, is subject to increased environmental release due to its use in sunscreens, paints and pharmaceutical products, while toxic effects to human health have been reported, but are poorly understood so far.
First, ZnO nanoparticles were synthesized using a heat-up approach by thermal decomposition of a zinc acetate precursor in 1-octadecene. Benzyl alcohol was used to control the morphology of the ZnO nanoparticles which yielded fan-like ZnO nanorods through concerted classical surfactant assisted nucleation, surface reconstruction and oriented attachment. The ZnO nanoparticles were subsequently coated with a silica shell for the attachment of fluorescein dye in a reverse microemulsion reaction. The modified ZnO@SiO_2@FITC nanoparticles were internalized into various cancer cell types and analyzed by confocal laser scanning microscopy. Additionally, ZnO@SiO_2 nanoparticles displayed a gradual dissolution kinetics of ZnO which caused a retardation of the full cytotoxic potential of the ZnO nanoparticles if the silica shell thickness exceeds 20 nm.
Second, smaller ZnO nanoparticles with a size between 5 and 15 nm, synthesized by a hydrothermal approach, were used to obtain deeper insight into the various aspects of ZnO mediated cytotoxicity because of their small size and ligand-free surface. They showed low cell viability after the first 3 h of the experiment. We found that high ionic strength as well as the direct availability of large amounts of Zn^{2+} ions through dissolution are of minor influence for the high toxic potential of the hydrothermal ZnO nanoparticles in the first hours. The low cell viability after 3 h might therefore be mainly caused by the nanoparticles, inhibiting or influencing important cell functions due to their attachment to the cells or due to cell uptake. Long term cytotoxicity of 6-27 h is then probably determined by the amount, biochemical character and properties of the released Zn^{2+} ions.

The final two research projects covered the synthesis of Au and Pd nanoparticles and their subsequent surface modification with the long chain organic thiol 1-octadecanethiol to control and tune the morphology of Au@Pd and Pd@Au heterodimer nanostructures designed for catalytic application. For unraveling the influence of the thiol coating on the surface dynamics and reaction process, a detailed ^{1}H and ^{19}F nuclear magnetic resonance (NMR) study on 1-octadecanethiol functionalized Au nanoparticles (ODT-Au) was carried out.

We studied the ligand exchange of oleylamine (OAm) to 1-octadecanethiol (ODT) on Au nanoparticles as a function of particle size and repeated functionalization by (*in situ*) solution NMR. Furthermore, OAm-Au nanoparticles were functionalized with 1H,1H,2H,2H-perfluorodecanethiol (PFDT) to enhance the analytic scope due to the resolution advantage of ^{19}F-NMR. Surface dynamics and local inhomogeneities such as surface corrugation and surface defects led to signal broadening of the surface ligands on OAm-Au, ODT-Au and PFDT-Au nanoparticles, which could be traced by ^{1}H as well as ^{19}F, 1D-NMR, 2D-diffusion-ordered (DOSY) and 2D-nuclear Overhauser effect (NOESY) spectroscopy. A site-specific evaluation of the resonance frequencies of the different CF_2- and CF_3-moieties in PFDT-Au nanoparticles could be given because of the resolution related with the broad spectral range of the ^{19}F nucleus. Site-related diffusion coefficients and hydrodynamic radii of the functionalized particles were derived from the corresponding DOSY spectra. Thus, the width and shift of the distribution of the respective site-related diffusion coefficients could be evaluated and linked to the spatial distance to the thiol anchoring group of the ligand.

Moreover, the surface functionalization efficiency of the ODT-Au nanoparticles was studied as a function of the particle size with smaller OAm-Au nanoparticles and as a function of repeated functionalization. In particular, unbound and bound or tightly bound ligands as well as the dynamics of ligand exchange in a rapid adsorption/desorption equilibrium could be distinguished by diffusion methods.

Ligand exchange was found to be an equilibrium reaction associated with a Nernst distribution, which may lead to incomplete surface functionalization following single step reactions. Efficient surface coverage was found to depend on repeated exchange reactions with large ligand excess. In addition, the size of the nanoparticles, *i.e.* the surface curvature, surface defects and reactivity has a contribution as well as the size of the ligand. These results have implications for applications ranging from controlled particle assembly, targeted delivery using nanoparticles, or stability of particle dispersions due to surface functionalization as a key prerequisite for any nanoparticle application.

The Au@Pd and Pd@Au heterodimer nanostructures were synthesized to investigate the effect of the nanoparticle structure on the catalytic activity for the reduction of 4-nitrophenol to 4-aminophenol with sodium borohydride. Au-Pd heteroparticles with different morphologies were synthesized by a seed mediated growth process in 1-octadecene. Heterodimer nanoparticles with separated Pd (Au) domains were synthesized with oleylamine capped OAm-Au (OAm-Pd) seeds. The polycrystalline and multiple-twinned structures of the seed particles have locally high surface energies. This reduces the energy barriers for heterogeneous nucleation compared to the surfaces of spherical and single crystalline nanoparticles. As a result island growth was induced and a concomitant reduction of the overall surface area.

1-octadecanethiol capped ODT-Au nanoparticles were also used as seeds for the reduction of Pd precursor to form Au@Pd heterodimers. With 9-11 nm ODT-Au nanoparticles, a ODT-Au@Pd core-shell nanoparticle structure (with Au core and Pd shell) with diameters of 15-17 nm was formed. The formation of the Pd shell was further investigated by varying the Au/Pd ratio. At low Pd concentrations, no closed Pd shell was formed. Hence, monitoring of the surface epitaxial growth by aberration corrected high resolution transmission electron microscopy analysis was

possible. At high Pd concentrations, Pd shell overgrowth was observed.
To verify that the formation of the core-shell nanoparticles was induced by the thiol-capped Au surface, the Pd overgrowth was carried out with amine-functionalized OAm-Au nanoparticles of 9-11 nm size. No core-shell structures, but particles with windmill-morphology were formed. Several Pd "blades" were attached to an Au core and the surface coverage of the Au core with Pd "blades" was incomplete.
For OAm-Pd and ODT-Pd seed particles, facetted, Au-rich domain nanoparticles (OAm-Pd@Au) and impeded core-shell nanoparticles (ODT-Pd@Au) were obtained. This is related to the high surface energy of the small Pd seed particles with a diameter of 5-7 nm.
The catalytic activity for the reduction of 4-nitrophenol for selected heterodimer nanoparticles was subsequently evaluated in a colorimetric assay. The highest activity in the catalytic reaction was found for the OAm-Pd@Au nanoparticles (with faceted Au domains), followed by Au nanoparticles, ODT-Au@Pd core-shell nanoparticles and Pd nanoparticles. The high catalytic activity of the OAm-Pd@Au nanoparticles was attributed to the formation of a mixed Au-Pd surface structure, where Au is present as large surface domains adjacent to Pd from the seed nanoparticle and direct interaction through the interface is enabled. Based on their surface area, Au nanoparticles had a higher activity than Pd nanoparticles in the hydration. ODT-Au@Pd nanoparticles, where the more active Au core is completely shielded by a less active Pd surface shell, had a catalytic activity comparable to pure Pd nanoparticles.

Functionalized, multimaterial and hierarchical nanostructures, as presented in this thesis, are promising future candidates for applications such as in catalysis, theranostic, targeted drug delivery and multimodal imaging. For scientists it is essential to develop tailor-made tools for the fabrication of these nanodevices, since many aspects of reaction processing and reactant ratios influence the size, morphology and chemical composition of the obtained nanostructures. The complexity of the reactions increases by a multiple with every new material or surfactant added. Therefore, close examination of manifold reaction parameters is necessary to tune the nanostructures. In addition, chemical and physical characterization becomes crucial for understanding the sophisticated reaction processes and properties.
Still, the value of the novel nanostructures can only be determined by their users in engineering or medical sciences together with new methods and assays. However, at the moment little is known about the impact of multifunctional particles that display intrinsic chemical and physical asymmetry *e.g.* in biomedical applications. Current nanotechnology projects focus on functionalized superstructures with the goal to create novel functionalities. Thus, one may anticipate new phenomena associated with the exposure of human tissue to these new materials. Despite these challenges, multifunctional nanostructures provide fascinating opportunities for tailoring properties that are not possible with other types of materials or therapeutics.
These opportunities and challenges are fueling the enthusiasm of researchers!

10
Appendix

10.1 Autorship Statements

Bio-Nano: Theranostic At Cellular Level

Manuscript Title:

Bio-Nano: Theranostic At Cellular Level (in the book "The Role of Particulate Nature in Pharmaceuticals" by Editor Henk Merkus to be published in the Springer Series "Advances in the Pharmaceutical Sciences")

All persons who meet authorship criteria are listed as authors, and all authors certify that they have participated sufficiently in the work to take public responsibility for the content, including participation in the concept, design, analysis, writing, or revision of the manuscript. Furthermore, each author certifies that this material or similar material has not been and will not be submitted to or published in any other publication before its appearance in the in the Springer book "The Role of Particulate Nature in Pharmaceuticals".

Authorship contributions:

Please indicate the specific contributions made by each author (list the authors' initials followed by their surnames). The name of each author must appear at least once in each of the three categories below. The * marks the first author(s).

Category 1:

Conception and design of study: M. Kluenker*, S. Kurch, M. N. Tahir, W. Tremel

Acquisition of data: Not applicable

Analysis and/or interpretation of data: Not applicable

Category 2:

Drafting the manuscript: M. Kluenker* (the part written by M. Kluenker is used in this thesis), S. Kurch, W. Tremel

Revising the manuscript critically for important intellectual content: M. Kluenker*, S. Kurch, M. N. Tahir, W. Tremel

Category 3:

Approval of the version of the manuscript to be published (the names of all authors must be listed): M. Kluenker*, S. Kurch, M. N. Tahir, W. Tremel

Acknowledgments:

All persons who have made substantial contributions to the work reported in the manuscript (*e.g.*, technical help, writing and editing assistance, general support), but who do not meet the criteria for authorship, are named in the Acknowledgments. If we have not included Acknowledgments, then that indicates that we have not received substantial contributions from non-authors.

The authors acknowledge the contribution of Editor Henk Merkus in the revision process of the manuscript.

Pd@Fe_2O_3 Superparticles

Manuscript Title:

Pd@Fe_2O_3 Superparticles with Enhanced Peroxidase Activity by Solution Phase Epitaxial Growth[93] (ACS Chemistry of Materials 2017, 29 (3), 1134-1146, published online December 23, 2016, reproduced with permission of the American Chemical Society, August 14, 2017)

All persons who meet authorship criteria are listed as authors, and all authors certify that they have participated sufficiently in the work to take public responsibility for the content, including participation in the concept, design, analysis, writing, or revision of the manuscript. Furthermore, each author certifies that this material or similar material has not been and will not be submitted to or published in any other publication before its appearance in the ACS Chemistry of Materials journal.

Authorship contributions:

Please indicate the specific contributions made by each author (list the authors' initials followed by their surnames). The name of each author must appear at least once in each of the three categories below. The * marks the first author(s).

Category 1:

Conception and design of study: M. Kluenker*, M. N. Tahir, R. Ragg, K. Korschelt, W. Tremel

Acquisition of data: M. Kluenker* (synthesis and functionalization of nanoparticles, SQUID magnetic measurements, catalytic experiments, transmission electron microscopy, development of the novel calculation method for activities normalized to one active site), M. N. Tahir (synthesis assistance, high resolution transmission electron microscopy, Mössbauer spectroscopy), R. Ragg (development of the novel calculation method for activities normalized to one active site), K. Korschelt (development of the novel calculation method for activities normalized to one active site), P. Simon (high resolution transmission electron microscopy), T. E. Gorelik (high resolution transmission electron microscopy), B. Barton (high resolution transmission electron microscopy), S. I. Shylin (Mössbauer spectroscopy), M. Panthöfer (X-Ray diffraction and Rietveld refinement), J. Herzberger (polymer synthesis), H. Frey (polymer synthesis), V. Ksenofontov (Mössbauer spectroscopy), A. Möller (Mössbauer spectroscopy), U. Kolb (high resolution transmission electron microscopy), J. Grin (high resolution transmission electron microscopy)

Analysis and/or interpretation of data: M. Kluenker*, M. N. Tahir, R. Ragg, K. Korschelt, P. Simon, T. E. Gorelik, B. Barton, S. I. Shylin, M. Panthöfer, J. Herzberger, V. Ksenofontov, W. Tremel

Category 2:

Drafting the manuscript: M. Kluenker*, M. N. Tahir, T. E. Gorelik, W. Tremel

Revising the manuscript critically for important intellectual content: M. Kluenker*, M. N. Tahir, R. Ragg, K. Korschelt, P. Simon, T. E. Gorelik, B. Barton, S. I. Shylin, M. Panthöfer, J. Herzberger, H. Frey, V. Ksenofontov, A. Möller, U. Kolb, J. Grin, W. Tremel

Category 3:

Approval of the version of the manuscript to be published (the names of all authors must be listed): M. Kluenker*, M. N. Tahir, R. Ragg, K. Korschelt, P. Simon, T. E. Gorelik, B. Barton, S. I. Shylin, M. Panthöfer, J. Herzberger, H. Frey, V. Ksenofontov, A. Möller, U. Kolb, J. Grin, W. Tremel

Acknowledgments:

All persons who have made substantial contributions to the work reported in the manuscript (*e.g.*, technical help, writing and editing assistance, general support), but who do not meet the criteria for authorship, are named in the Acknowledgments. If we have not included Acknowledgments, then that indicates that we have not received substantial contributions from non-authors.

This publication is based on the research project about Pd-iron oxide superparticles, which was started during the research for my diploma thesis[603] and extended and finished during the research for this thesis.

Fe_xO Superparticles

Manuscript Title:

Iron Oxide Superparticles with Enhanced MRI Performance by Solution Phase Epitaxial Growth (submitted to ACS Chemistry of Materials)

All persons who meet authorship criteria are listed as authors, and all authors certify that they have participated sufficiently in the work to take public responsibility for the content, including participation in the concept, design, analysis, writing, or revision of the manuscript. Furthermore, each author certifies that this material or similar material has not been and will not be submitted to or published in any other publication before its appearance in the ACS Chemistry of Materials journal.

Authorship contributions:

Please indicate the specific contributions made by each author (list the authors' initials followed by their surnames). The name of each author must appear at least once in each of the three categories below. The * marks the first author(s).

Category 1:

Conception and design of study: M. Kluenker*, M. N. Tahir*, W. Tremel

Acquisition of data: M. Kluenker* (synthesis and functionalization of nanoparticles, SQUID magnetic measurements, magnetic resonance imaging experiments, transmission electron microscopy), M. N. Tahir* (synthesis assistance, SQUID magnetic measurements), R. Dören (synthesis of nanoparticles), M. Deuker (functionalization of nanoparticles), P. Komforth (synthesis of nanoparticles), S. Plana-Ruiz (high resolution transmission electron microscopy), B. Barton (high resolution transmission electron microscopy), S. I. Shylin (Mössbauer spectroscopy), V. Ksenofontov (Mössbauer spectroscopy), M. Panthöfer (X-Ray diffraction and Rietveld refinement), N. Wiesmann (cytotoxicity measurements), J. Herzberger (polymer synthesis), A. Möller (Mössbauer spectroscopy), H. Frey (polymer synthesis), J. Brieger (cytotoxicity measurements), U. Kolb (high resolution transmission electron microscopy)

Analysis and/or interpretation of data: M. Kluenker*, M. N. Tahir*, S. Plana-Ruiz, B. Barton, S. I. Shylin, V. Ksenofontov, M. Panthöfer, N. Wiesmann, J. Herzberger, A. Möller, U. Kolb, W. Tremel

Category 2:

Drafting the manuscript: M. Kluenker*, M. N. Tahir*, W. Tremel

Revising the manuscript critically for important intellectual content: M. Kluenker*, M. N. Tahir*, R. Dören, M. Deuker, P. Komforth, S. Plana-Ruiz, B. Barton, S. I. Shylin, V. Ksenofontov, M. Panthöfer, N. Wiesmann, J. Herzberger, A. Möller, H. Frey, J. Brieger, U. Kolb, W. Tremel

Category 3:

Approval of the version of the manuscript to be published (the names of all authors must be listed): M. Kluenker*, M. N. Tahir*, R. Dören, M. Deuker, P. Komforth, S. Plana-Ruiz, B. Barton, S. I. Shylin, V. Ksenofontov, M. Panthöfer, N. Wiesmann, J. Herzberger, A. Möller, H. Frey, J. Brieger, U. Kolb, W. Tremel

Acknowledgments:

All persons who have made substantial contributions to the work reported in the manuscript (*e.g.*, technical help, writing and editing assistance, general support), but who do not meet the criteria for authorship, are named in the Acknowledgments. If we have not included Acknowledgments, then that indicates that we have not received substantial contributions from non-authors.

The authors thank Dr. Peter Blümler, Department of Physics, Johannes Gutenberg-University Mainz, Germany for the support during the magnetic resonance measurements and the possibility to use the affiliated MRI instrument.

B.Sc. Rene Dören,[350] B.Sc. Mareike Deuker,[351] and B.Sc. Patric Komforth[352] participated in this project during their bachelor thesis research.

Fe_xO Heterodimer Nanoparticles

Manuscript Title:

From Single Molecules to Nanostructured Functional Materials: Formation of a Magnetic Foam Catalyzed by Pd@Fe_xO Heterodimers[378] (ACS Applied Nano Materials 2017, DOI: 10.1021/acsanm.7b00051, published online December 7, 2017, reproduced with permission of the American Chemical Society, December 14, 2017)

All persons who meet authorship criteria are listed as authors, and all authors certify that they have participated sufficiently in the work to take public responsibility for the content, including participation in the concept, design, analysis, writing, or revision of the manuscript. Furthermore, each author certifies that this material or similar material has not been and will not be submitted to or published in any other publication before its appearance in the ACS Applied Nano Materials journal.

Authorship contributions:

Please indicate the specific contributions made by each author (list the authors' initials followed by their surnames). The name of each author must appear at least once in each of the three categories below. The * marks the first author(s).

Category 1:

Conception and design of study: M. N. Tahir*, M. Kluenker*, F. Natalio, W. Tremel

Acquisition of data: M. Kluenker* (synthesis and functionalization of nanoparticles, SQUID magnetic measurements, catalytic experiments, transmission electron microscopy, infrared spectroscopy), M. N. Tahir* (synthesis assistance, thermogravimetric analysis), B. Barton (high resolution transmission electron microscopy), K. Korschelt (assistance in catalytic experiments), S. I. Shylin (Mössbauer spectroscopy), M. Panthöfer (X-Ray diffraction and Rietveld refinement), V. Ksenofontov (Mössbauer spectroscopy), A. Möller (Mössbauer spectroscopy), U. Kolb (high resolution transmission electron microscopy)

Analysis and/or interpretation of data: M. Kluenker*, M. N. Tahir*, B. Barton, K. Korschelt, S. I. Shylin, M. Panthöfer, V. Ksenofontov, A. Möller, W. Tremel

Category 2:

Drafting the manuscript: M. Kluenker*, M. N. Tahir*, W. Tremel

Revising the manuscript critically for important intellectual content: M. Kluenker*,

M. N. Tahir*, F. Natalio, B. Barton, K. Korschelt, S. I. Shylin, M. Panthöfer, V. Ksenofontov, A. Möller, U. Kolb, W. Tremel

Category 3:

Approval of the version of the manuscript to be published (the names of all authors must be listed): M. N. Tahir*, M. Kluenker*, F. Natalio, B. Barton, K. Korschelt, S. I. Shylin, M. Panthöfer, V. Ksenofontov, A. Möller, U. Kolb, W. Tremel

Acknowledgments:

All persons who have made substantial contributions to the work reported in the manuscript (*e.g.*, technical help, writing and editing assistance, general support), but who do not meet the criteria for authorship, are named in the Acknowledgments. If we have not included Acknowledgments, then that indicates that we have not received substantial contributions from non-authors.

The authors acknowledge the collaboration of B.Sc. Nabil Boui, who synthesized the Fe_xO nanoparticles comparison sample (Figure 4.9) during his bachelor thesis research.[401]

Thiol-Ligand Exchange on Au Nanoparticle Surfaces

Manuscript Title:

Monitoring Thiol-Ligand Exchange on Au Nanoparticle Surfaces[491] (ACS Langmuir 2018, 34 (3), 1700-1710, published online January 8, 2018, reproduced with permission of the American Chemical Society, January 17, 2018)

All persons who meet authorship criteria are listed as authors, and all authors certify that they have participated sufficiently in the work to take public responsibility for the content, including participation in the concept, design, analysis, writing, or revision of the manuscript. Furthermore, each author certifies that this material or similar material has not been and will not be submitted to or published in any other publication before its appearance in the ACS Langmuir journal.

Authorship contributions:

Please indicate the specific contributions made by each author (list the authors' initials followed by their surnames). The name of each author must appear at least once in each of the three categories below. The * marks the first author(s).

Category 1:

Conception and design of study: M. Kluenker*, M. Mondeshki*, M. N. Tahir, W. Tremel

Acquisition of data: M. Kluenker* (synthesis and functionalization of nanoparticles, nuclear magnetic resonance spectroscopy, UV-vis spectroscopy, Raman spectroscopy, transmission electron microscopy), M. Mondeshki* (nuclear magnetic resonance spectroscopy), M. N. Tahir (thermogravimetric analysis)

Analysis and/or interpretation of data: M. Kluenker*, M. Mondeshki*

Category 2:

Drafting the manuscript: M. Kluenker*, M. Mondeshki*, W. Tremel

Revising the manuscript critically for important intellectual content: M. Kluenker*, M. Mondeshki*, M. N. Tahir, W. Tremel

Category 3:

Approval of the version of the manuscript to be published (the names of all authors must be listed): M. Kluenker*, M. Mondeshki*, M. N. Tahir, W. Tremel

Acknowledgments:

All persons who have made substantial contributions to the work reported in the manuscript (*e.g.*, technical help, writing and editing assistance, general support), but who do not meet the criteria for authorship, are named in the Acknowledgments. If we have not included Acknowledgments, then that indicates that we have not received substantial contributions from non-authors.

Au-Pd Heterodimer Nanoparticles

Manuscript Title:

Controlling the Morphology of Au-Pd Heterodimer Nanoparticles by Surface Ligands (submitted to RSC Nanoscale)

All persons who meet authorship criteria are listed as authors, and all authors certify that they have participated sufficiently in the work to take public responsibility for the content, including participation in the concept, design, analysis, writing, or revision of the manuscript. Furthermore, each author certifies that this material or similar material has not been and will not be submitted to or published in any other publication before its appearance in the RSC Nanoscale journal.

Authorship contributions:

Please indicate the specific contributions made by each author (list the authors' initials followed by their surnames). The name of each author must appear at least once in each of the three categories below. The * marks the first author(s).

Category 1:

Conception and design of study: M. Kluenker*, M. N. Tahir, W. Tremel

Acquisition of data: M. Kluenker* (synthesis and functionalization of nanoparticles, catalytic experiments, UV-vis spectroscopy, transmission electron microscopy), B. M. Connolly (synthesis and functionalization of nanoparticles), D. M. Marolf (synthesis and functionalization of nanoparticles), K. Korschelt (assistance in catalytic experiments), P. Simon (high resolution transmission electron microscopy), U. Köhler (high resolution transmission electron microscopy), B. Barton (high resolution transmission electron microscopy), M. Panthöfer (X-Ray diffraction and Rietveld refinement), U. Kolb (high resolution transmission electron microscopy)

Analysis and/or interpretation of data: M. Kluenker*, B. M. Connolly, D. M. Marolf, M. N. Tahir, K. Korschelt, P. Simon, U. Köhler, B. Barton, M. Panthöfer, W. Tremel

Category 2:

Drafting the manuscript: M. Kluenker*, M. N. Tahir, W. Tremel

Revising the manuscript critically for important intellectual content: M. Kluenker*, B. M. Connolly, D. M. Marolf, M. N. Tahir, K. Korschelt, P. Simon, U. Köhler, B. Barton, M. Panthöfer, U. Kolb, W. Tremel

Category 3:

Approval of the version of the manuscript to be published (the names of all authors must be listed): M. Kluenker*, B. M. Connolly, D. M. Marolf, M. N. Tahir, K. Korschelt, P. Simon, U. Köhler, B. Barton, M. Panthöfer, U. Kolb, W. Tremel

Acknowledgments:

All persons who have made substantial contributions to the work reported in the manuscript (*e.g.*, technical help, writing and editing assistance, general support), but who do not meet the criteria for authorship, are named in the Acknowledgments. If we have not included Acknowledgments, then that indicates that we have not received substantial contributions from non-authors.

Bethany M. Connolly and David M. Marolf were supported through scholarships of the German Academic Exchange Service (DAAD) in their program Research Internships in Science and Engineering (RISE).

10.2 General Acknowledgments

The research presented in this thesis was supported by the Max Planck Graduate Center (MPGC) through scholarships to Martin Klünker, Karsten Korschelt, Nadine Wiesmann and Ruben Ragg.

We acknowledge support through the SFB 1066 "Nanodimensionale polymere Therapeutika für die Tumortherapie".

The facilities of the Electron Microscopy Center in Mainz (EZMZ) were supported by the State Excellence Cluster CINEMA.

Bibliography

[1] M. C. Daniel, D. Astruc, *Chem. Rev.* **2004**, *104*, 293–346.

[2] M. Faraday, *Philos. Trans. R. Soc. London* **1857**, *147*, 145–181.

[3] W. Ostwald, *Z. Phys. Chem.* **1900**, *34*, 495–503.

[4] J. Turkevich, P. C. Stevenson, J. Hillier, *Discuss. Faraday Soc.* **1951**, *11*, 55–75.

[5] V. K. LaMer, R. R. H. Dinegar, *J. Am. Chem. Soc.* **1950**, *72*, 4847–4854.

[6] V. K. LaMer, *Ind. Eng. Chem.* **1952**, *44*, 1270–1277.

[7] J. Park, J. Joo, S. G. Kwon, Y. Jang, T. Hyeon, *Angew. Chem.* **2007**, *119*, 4714–4745.

[8] M. Grzelczak, J. Pérez-Juste, P. Mulvaney, L. M. Liz-Marzán, *Chem. Soc. Rev.* **2008**, *37*, 1783–1791.

[9] R. Ferrando, J. Jellinek, R. L. Johnston, *Chem. Rev.* **2008**, *108*, 845–910.

[10] P.-G. De Gennes, *Angew. Chem. Int. Ed.* **1992**, *31*, 842–845.

[11] T. Wang, X. Wang, D. LaMontagne, Z. Wang, Z. Wang, Y. C. Cao, *J. Am. Chem. Soc.* **2012**, *134*, 18225–18228.

[12] T. Wang, J. Zhuang, J. Lynch, O. Chen, Z. Wang, X. Wang, D. LaMontagne, H. Wu, Z. Wang, Y. C. Cao, *Science* **2012**, *338*, 358–363.

[13] A. Burns, H. Ow, U. Wiesner, *Chem. Soc. Rev.* **2006**, *35*, 1028–1042.

[14] F. Hoffmann, M. Cornelius, J. Morell, M. Fröba, *Angew. Chem. Int. Ed.* **2006**, *45*, 3216–3251.

[15] I. Schick, S. Lorenz, D. Gehrig, A. M. Schilmann, H. Bauer, M. Panthöfer, K. Fischer, D. Strand, F. Laquai, W. Tremel, *J. Am. Chem. Soc.* **2014**, *136*, 2473–2483.

[16] M. R. Buck, J. F. Bondi, R. E. Schaak, *Nat. Chem.* **2012**, *4*, 37–44.

[17] Y. Wang, J. He, C. Liu, W. H. Chong, H. Chen, *Angew. Chem. Int. Ed.* **2014**, *53*, 2–32.

[18] N. T. K. Thanh, N. Maclean, S. Mahiddine, *Chem. Rev.* **2014**, *3*, 7610–7630.

[19] S. G. Kwon, T. Hyeon, *Small* **2011**, *7*, 2685–2702.

[20] Y. Xia, Y. Xiong, B. Lim, S. E. Skrabalak, *Angew. Chem. Int. Ed.* **2009**, *48*, 60–103.

[21] Y. Yin, A. P. Alivisatos, *Nature* **2005**, *437*, 664–670.

[22] J. J. De Yoreo, P. U. P. A. Gilbert, N. A. J. M. Sommerdijk, R. L. Penn, S. Whitelam, D. Joester, H. Zhang, J. D. Rimer, A. Navrotsky, J. F. Banfield, A. F. Wallace, F. M. Michel, F. C. Meldrum, H. Colfen, P. M. Dove, *Science* **2015**, *349*, 6247/1–6247/9.

[23] Y. W. Jun, J. S. Choi, J. Cheon, *Angew. Chem. Int. Ed.* **2006**, *45*, 3414–3439.

[24] J. Zhang, M. R. Langille, M. L. Personick, K. Zhang, S. Li, C. A. Mirkin, *J. Am. Chem. Soc.* **2010**, *132*, 14012–14014.

[25] A. R. Tao, S. Habas, P. Yang, *Small* **2008**, *4*, 310–325.

[26] P. D. Cozzoli, T. Pellegrino, L. Manna, *Chem. Soc. Rev.* **2006**, *35*, 1195–1208.

[27] J. Yang, L. L. Chng, X. Yang, X. Chen, J. Y. Ying, *Chem. Commun.* **2014**, *50*, 1141–1143.

[28] H.-J. Yang, S.-Y. He, H.-Y. Tuan, *Langmuir* **2014**, *30*, 602–610.

[29] B. Ludi, M. J. Süess, I. A. Werner, M. Niederberger, *Nanoscale* **2012**, *4*, 1982–1995.

[30] A. P. Alivisatos, *Science* **2000**, *289*, 736–737.

[31] Y. Sun, Y. Xia, *Science* **2002**, *298*, 2176–2180.

[32] E. Ye, M. D. Regulacio, S.-Y. Zhang, X. J. Loh, M.-Y. Han, *Chem. Soc. Rev.* **2015**, *44*, 6001–6017.

[33] J. E. Lofgreen, G. A. Ozin, *Chem. Soc. Rev.* **2014**, *43*, 911–933.

[34] M. T. Sheldon, P. E. Trudeau, T. Mokari, L. W. Wang, A. Paul Alivisatos, *Nano Lett.* **2009**, *9*, 3676–3682.

[35] Y. Sun, J. J. Foley, S. Peng, Z. Li, S. K. Gray, *Nano Lett.* **2013**, *13*, 3958–3964.

[36] D. Steiner, T. Mokari, U. Banin, O. Millo, *Phys. Rev. Lett.* **2005**, *95*, 056805/1–056805/4.

[37] L. Carbone, P. D. Cozzoli, *Nano Today* **2010**, *5*, 449–493.

[38] M. N. Tahir, F. Natalio, M. A. Cambaz, M. Panthofer, R. Branscheid, U. Kolb, W. Tremel, *Nanoscale* **2013**, *5*, 9944–9949.

[39] S. Khanal, G. Casillas, N. Bhattarai, J. J. Velázquez-Salazar, U. Santiago, A. Ponce, S. Mejía-Rosales, M. José-Yacamán, *Langmuir* **2013**, *29*, 9231–9239.

[40] I. Schick, D. Gehrig, M. Montigny, B. Balke, M. Panthöfer, A. Henkel, F. Laquai, W. Tremel, *Chem. Mater.* **2015**, *27*, 4877–4884.

[41] T. D. Schladt, M. I. Shukoor, K. Schneider, M. N. Tahir, F. Natalio, I. Ament, J. Becker, F. D. Jochum, S. Weber, O. Köhler, P. Theato, L. M. Schreiber, C. Sönnichsen, H. C. Schröder, W. E. G. Müller, W. Tremel, *Angew. Chem.* **2010**, *122*, 4068–4072.

[42] T. Schladt, T. Graf, O. Köhler, H. Bauer, M. Dietzsch, J. Mertins, R. Branscheid, U. Kolb, W. Tremel, *Chem. Mater.* **2012**, *24*, 525–535.

[43] I. V. Markov, *Crystal Growth for Beginners: Fundamentals of Nucleation, Crystal Growth and Epitaxy*, World Scientific, Singapore, **2003**.

[44] C. Wang, C. Xu, H. Zeng, S. Sun, *Adv. Mater.* **2009**, *21*, 3045–3052.

[45] X. Zhang, Y. L. Chen, R.-S. Liu, D. P. Tsai, *Reports Prog. Phys.* **2013**, *76*, 046401/1–046401/41.

[46] W. Shi, H. Zeng, Y. Sahoo, T. Y. Ohulchanskyy, *Nano Lett.* **2006**, *6*, 875–881.

[47] Y. H. Jang, Y. J. Jang, S. T. Kochuveedu, M. Byun, Z. Lin, D. H. Kim, *Nanoscale* **2014**, *6*, 1823–1832.

[48] H. J. Yun, H. Lee, N. D. Kim, D. M. Lee, S. Yu, J. Yi, *ACS Nano* **2011**, *5*, 4084–4090.

[49] Z. W. Seh, S. Liu, M. Low, S. Y. Zhang, Z. Liu, A. Mlayah, M. Y. Han, *Adv. Mater.* **2012**, *24*, 2310–2314.

[50] E. Roduner, *Chem. Soc. Rev.* **2014**, *2*, 8226–8239.

[51] H. Yu, M. Chen, P. M. Rice, S. X. Wang, R. L. White, S. Sun, *Nano Lett.* **2005**, *5*, 379–382.

[52] H. Zeng, S. Sun, *Adv. Funct. Mater.* **2008**, *18*, 391–400.

[53] J. Cheon, J. H. Lee, *Acc. Chem. Res.* **2008**, *41*, 1630–1640.

[54] L. Zhang, Y.-H. Dou, H.-C. Gu, *J. Colloid Interface Sci.* **2006**, *297*, 660–664.

[55] V. Subramanian, E. E. Wolf, P. V. Kamat, *J. Am. Chem. Soc.* **2004**, *126*, 4943–4950.

[56] S. T. Kochuveedu, Y. H. Jang, D. H. Kim, *Chem. Soc. Rev.* **2013**, *42*, 8467–8493.

[57] Y. S. Chen, H. Choi, P. V. Kamat, *J. Am. Chem. Soc.* **2013**, *135*, 8822–8825.

[58] C. Wang, H. Daimon, S. Sun, *Nano Lett.* **2009**, *9*, 1493–1496.

[59] P. Li, Z. Wei, T. Wu, Q. Peng, Y. Li, *J. Am. Chem. Soc.* **2011**, *133*, 5660–5663.

[60] W. Shi, Y. Sahoo, H. Zeng, Y. Ding, M. T. Swihart, P. N. Prasad, *Adv. Mater.* **2006**, *18*, 1889–1894.

[61] C. Li, L. Sun, Y. Sun, T. Teranishi, *Chem. Mater.* **2013**, *25*, 2580–2590.

[62] S. Pradhan, D. Ghosh, S. Chen, *ACS Appl. Mater. Interfaces* **2009**, *1*, 2060–2065.

[63] L. Landgraf, P. Ernst, I. Schick, O. Köhler, H. Oehring, W. Tremel, I. Hilger, *Biomaterials* **2014**, *35*, 6986–6997.

[64] L. Landgraf, C. Christner, W. Storck, I. Schick, I. Krumbein, H. Dähring, K. Haedicke, K. Heinz-Herrmann, U. Teichgräber, J. R. Reichenbach, W. Tremel, S. Tenzer, I. Hilger, *Biomaterials* **2015**, *68*, 77–88.

[65] K. Cheng, M. Yang, R. Zhang, C. Qin, X. Su, Z. Cheng, *ACS Nano* **2014**, *8*, 9884–9896.

[66] N. Glaser, D. J. Adams, A. Bo, G. Krausch, *Langmuir* **2006**, *22*, 5227–5229.

[67] L.-C. Cheng, J.-H. Huang, H. M. Chen, T.-C. Lai, K.-Y. Yang, R.-S. Liu, M. Hsiao, C.-H. Chen, L.-J. Her, D. P. Tsai, *J. Mater. Chem.* **2012**, *22*, 2244–2253.

[68] Y. Yu, K. Sun, Y. Tian, X.-Z. Li, M. J. Kramer, D. J. Sellmyer, J. E. Shield, S. Sun, *Nano Lett.* **2013**, *13*, 4975–4979.

[69] J. Zhuang, H. Wu, Y. Yang, Y. C. Cao, *J. Am. Chem. Soc.* **2007**, *129*, 14166–14167.

[70] J. Zhuang, A. D. Shaller, J. Lynch, H. Wu, O. Chen, A. D. Q. Li, Y. C. Cao, *J. Am. Chem. Soc.* **2009**, *131*, 6084–6085.

[71] A. Courty, A. Mermet, P. A. Albouy, E. Duval, M. P. Pileni, *Nat. Mater.* **2005**, *4*, 395–398.

[72] A. Courty, A.-I. Henry, N. Goubet, M.-P. Pileni, *Nat. Mater.* **2007**, *6*, 900–907.

[73] A. Dong, Y. Jiao, D. J. Milliron, *ACS Nano* **2013**, *7*, 10978–10984.

[74] M. Han, X. Gao, J. Z. Su, S. Nie, *Nat. Biotechnol.* **2001**, *19*, 631–635.

[75] E. Ozbay, *Science* **2006**, *311*, 189–194.

[76] S. Sun, *Science* **2000**, *287*, 1989–1992.

[77] J. Zhuang, H. Wu, Y. Yang, Y. C. Cao, *Angew. Chem. Int. Ed.* **2008**, *47*, 2208–2212.

[78] R. Costi, A. E. Saunders, U. Banin, *Angew. Chem. Int. Ed.* **2010**, *49*, 4878–4897.

[79] A. Boal, F. Ilhan, J. DeRouchey, T. Thurn-Albrecht, T. Russell, V. Rotello, *Nature* **2000**, *404*, 746–748.

[80] M. M. Maye, J. Luo, I. I. S. Lim, L. Han, N. N. Kariuki, D. Rabinovich, T. Liu, C. J. Zhong, *J. Am. Chem. Soc.* **2003**, *125*, 9906–9907.

[81] T. Wang, D. LaMontagne, J. Lynch, J. Zhuang, Y. C. Cao, *Chem. Soc. Rev.* **2013**, *42*, 2804–2823.

[82] J. Huang, M. Guo, H. Ke, C. Zong, B. Ren, G. Liu, H. Shen, Y. Ma, X. Wang, H. Zhang, Z. Deng, H. Chen, Z. Zhang, *Adv. Mater.* **2015**, *27*, 5049–5056.

[83] Y. T. Chu, K. Chanda, P. H. Lin, M. H. Huang, *Langmuir* **2012**, *28*, 11258–11264.

[84] X. Sun, S. Guo, C.-S. Chung, W. Zhu, S. Sun, *Adv. Mater.* **2013**, *25*, 132–136.

[85] J. L. Elechiguerra, J. Reyes-Gasga, M. J. Yacaman, *J. Mater. Chem.* **2006**, *16*, 3906–3919.

[86] G. Wulff, *Z. Kristallog.* **1901**, *34*, 449–449.

[87] T. Herricks, J. Chen, Y. Xia, *Nano Lett.* **2004**, *4*, 2367–2371.

[88] R. G. Weiner, S. E. Skrabalak, *Angew. Chem. Int. Ed.* **2015**, *54*, 1181–1184.

[89] Z. Li, W. Li, P. H. C. Camargo, Y. Xia, *Angew. Chem. Int. Ed.* **2008**, *47*, 9653–9656.

[90] M. J. Mulvihill, X. Y. Ling, J. Henzie, P. Yang, *J. Am. Chem. Soc.* **2010**, *132*, 268–274.

[91] L. Ma, C. Wang, M. Gong, L. Liao, R. Long, J. Wang, D. Wu, W. Zhong, M. J. Kim, Y. Chen, Y. Xie, Y. Xiong, *ACS Nano* **2012**, *6*, 9797–9806.

[92] M. N. Tahir, J. Herzberger, F. Natalio, O. Koehler, R. Branscheid, E. Mugnaioli, V. Ksenofontov, M. Panthoefer, U. Kolb, H. Frey, W. Tremel, *Nanoscale* **2016**, *8*, 9548–9555.

[93] M. Kluenker, M. N. Tahir, R. Ragg, K. Korschelt, P. Simon, T. E. Gorelik, B. Barton, S. I. Shylin, M. Panthoefer, J. Herzberger, H. Frey, V. Ksenofontov, A. Möller, U. Kolb, Y. Grin, W. Tremel, *Chem. Mater.* **2017**, *29*, 1134–1146.

[94] R. G. Chaudhuri, S. Paria, *Chem. Rev.* **2012**, *112*, 2373–2433.

[95] D. Knopp, D. Tang, R. Niessner, *Anal. Chim. Acta* **2009**, *647*, 14–30.

[96] C. Graf, D. L. J. Vossen, A. Imhof, A. van Blaaderen, *Langmuir* **2003**, *19*, 6693–6700.

[97] N. Jana, C. Earhart, J. Ying, *Chem. Mater.* **2007**, *5*, 5074–5082.

[98] Y. Lu, Y. Yin, Z.-y. Li, Y. Xia, *Nano Lett.* **2002**, *2*, 785–788.

[99] W. Stöber, A. Fink, E. Bohn, *J. Colloid Interface Sci.* **1968**, *26*, 62–69.

[100] F. Di Renzo, F. Testa, J. Chen, H. Cambon, A. Galarneau, D. Plee, F. Fajula, *Microporous Mesoporous Mater.* **1999**, *28*, 437–446.

[101] C. Brinker, W. Scherer, *The Physics and Chemistry of Sol-Gel Processing*, Academic Press, San Diego, **1990**.

[102] S.-H. Wu, C.-Y. Mou, H.-P. Lin, *Chem. Soc. Rev.* **2013**, *42*, 3862–3875.

[103] J. W. Hu, J. F. Li, B. Ren, D. Y. Wu, S. G. Sun, Z. Q. Tian, *J. Phys. Chem. C* **2007**, *111*, 1105–1112.

[104] W. Niu, W. Zhang, S. Firdoz, X. Lu, *Chem. Mater.* **2014**, *26*, 2180–2186.

[105] X. Huang, S. Tang, X. Mu, Y. Dai, G. Chen, Z. Zhou, F. Ruan, Z. Yang, N. Zheng, *Nat. Nanotechnol.* **2011**, *6*, 28–32.

[106] C. Loo, A. Lin, L. Hirsch, M.-H. Lee, J. Barton, N. Halas, J. West, R. Drezek, *Technol. Cancer Res. Treat.* **2004**, *3*, 33–40.

[107] H. Zeng, J. Li, J. P. Liu, Z. L. Wang, S. Sun, *Nature* **2002**, *420*, 395–398.

[108] J. P. Zimmer, S.-W. Kim, S. Ohnishi, E. Tanaka, J. V. Frangioni, M. G. Bawendi, *J. Am. Chem. Soc.* **2006**, *128*, 2526–2527.

[109] L. Spanhel, M. Haase, H. Weller, A. Henglein, *J. Am. Chem. Soc.* **1987**, *109*, 5649–5655.

[110] W. U. Huynh, J. J. Dittmer, A. P. Alivisatos, *Science* **2002**, *295*, 2425–2427.

[111] R. Hong, N. Fischer, *Chem. Mater.* **2005**, *13*, 4617–4621.

[112] B. P. Lee, J. L. Dalsin, P. B. Messersmith, *Biomacromolecules* **2002**, *3*, 1038–1047.

[113] A. Thomas, H. Bauer, A. M. Schilmann, K. Fischer, W. Tremel, H. Frey, *Macromolecules* **2014**, *47*, 4557–4566.

[114] V. S. Wilms, H. Bauer, C. Tonhauser, A. M. Schilmann, M. C. Müller, W. Tremel, H. Frey, *Biomacromolecules* **2013**, *14*, 193–199.

[115] C. C. Berry, S. Wells, S. Charles, A. S. G. Curtis, *Biomaterials* **2003**, *24*, 4551–4557.

[116] M. Ballauff, Y. Lu, *Polymer* **2007**, *48*, 1815–1823.

[117] J. Qin, S. Laurent, Y. S. Jo, A. Roch, M. Mikhaylova, Z. M. Bhujwalla, R. N. Müller, M. Muhammed, *Adv. Mater.* **2007**, *19*, 1874–1878.

[118] R. De Palma, S. Peeters, M. J. Van Bael, H. Van den Rul, K. Bonroy, W. Laureyn, J. Mullens, G. Borghs, G. Maes, *Chem. Mater.* **2007**, *19*, 1821–1831.

[119] T. Sun, Y. S. Zhang, B. Pang, D. C. Hyun, M. Yang, Y. Xia, *Angew. Chem.* **2014**, *126*, 2–51.

[120] M. Bruchez Jr., M. Moronne, P. Gin, S. Weiss, A. P. Alivisatos, *Science* **1998**, *281*, 2013–2016.

[121] W. C. W. Chan, S. Nie, *Science* **1998**, *281*, 2016–2018.

[122] X. Michalet, F. F. Pinaud, L. A. Bentolila, J. M. Tsay, S. Doose, J. J. Li, G. Sundaresan, A. M. Wu, S. S. Gambhir, S. Weiss, *Science* **2008**, *538*, 538–544.

[123] T. D. Schladt, K. Schneider, H. Schild, W. Tremel, *Dalt. Trans.* **2011**, *40*, 6315–6343.

[124] J. Kim, H. H. S. Kim, N. Lee, T. Kim, H. H. S. Kim, T. Yu, I. C. Song, W. K. Moon, T. Hyeon, *Angew. Chem. Int. Ed.* **2008**, *47*, 8438–8441.

[125] Y.-W. Jun, J.-H. Lee, J. Cheon, *Angew. Chem. Int. Ed.* **2008**, *47*, 5122–5135.

[126] S. Gomez-Grana, F. Hubert, *Langmuir* **2011**, *28*, 1453–1459.

[127] B. Dubertret, P. Skourides, D. J. Norris, V. Noireaux, A. H. Brivanlou, A. Libchaber, *Science* **2002**, *298*, 1759–1762.

[128] X. Gao, Y. Cui, R. M. Levenson, L. W. K. Chung, S. Nie, *Nat. Biotechnol.* **2004**, *22*, 969–976.

[129] J. Qin, Y. S. Jo, M. Muhammed, *Angew. Chem. Int. Ed.* **2009**, *48*, 7845–7849.

[130] F. Osaki, T. Kanamori, S. Sando, T. Sera, Y. Aoyama, *J. Am. Chem. Soc.* **2004**, *126*, 6520–6521.

[131] W. W. Yu, E. Chang, J. C. Falkner, J. Zhang, a. M. Al-Somali, C. M. Sayes, J. Johns, R. Drezek, V. L. Colvin, *J. Am. Chem. Soc.* **2007**, *129*, 2871–2879.

[132] K. Knop, R. Hoogenboom, D. Fischer, U. S. Schubert, *Angew. Chem. Int. Ed.* **2010**, *49*, 6288–6308.

[133] R. G. Pearson, *J. Am. Chem. Soc.* **1963**, *85*, 3533–3539.

[134] T. Xia, M. Kovochich, M. Liong, H. Meng, S. Kabehie, S. George, J. I. Zink, A. E. Nel, *ACS Nano* **2009**, *3*, 3273–3286.

[135] D. R. Radu, C.-Y. Lai, K. Jeftinija, E. W. Rowe, S. Jeftinija, V. S. Lin, *J. Am. Chem. Soc.* **2004**, *126*, 13216–13217.

[136] S. W. Kim, S. Kim, J. B. Tracy, A. Jasanoff, M. G. Bawendi, *J. Am. Chem. Soc.* **2005**, *127*, 4556–4557.

[137] M. S. Nikolic, M. Krack, V. Aleksandrovic, A. Kornowski, S. Förster, H. Weller, *Angew. Chem.* **2006**, *118*, 6727–6731.

[138] K. Cheng, N. A. Frey, S. Sun, S. Peng, K. Cheng, S. Sun, *Chem. Soc. Rev.* **2009**, *38*, 2532–2542.

[139] J. K. Sahoo, M. N. Tahir, A. Yella, T. D. Schladt, E. Mugnaoli, U. Kolb, W. Tremel, *Angew. Chem. Int. Ed.* **2010**, *49*, 7578–7582.

[140] H. T. Uyeda, I. L. Medintz, J. K. Jaiswal, S. M. Simon, H. Mattoussi, *J. Am. Chem. Soc.* **2005**, *127*, 3870–3878.

[141] L. Josephson, C.-H. Tung, A. Moore, R. Weissleder, *Bioconjug. Chem.* **1999**, *10*, 186–191.

[142] M. Yang, J. Li, P. R. Chen, *Chem. Soc. Rev.* **2014**, *43*, 6511–6526.

[143] R. Ragg, F. Natalio, M. N. Tahir, H. Janssen, A. Kashyap, D. Strand, S. Strand, W. Tremel, *ACS Nano* **2014**, *8*, 5182–5189.

[144] R. Ragg, A. M. Schilmann, K. Korschelt, C. Wieseotte, M. Kluenker, M. Viel, L. Völker, S. Preiß, J. Herzberger, H. Frey, K. Heinze, P. Blümler, M. N. Tahir, F. Natalio, W. Tremel, *J. Mater. Chem. B* **2016**, *4*, 7423–7428.

[145] V. Amendola, S. Scaramuzza, L. Litti, M. Meneghetti, G. Zuccolotto, A. Rosato, E. Nicolato, P. Marzola, G. Fracasso, C. Anselmi, M. Pinto, M. Colombatti, *Small* **2014**, *10*, 2476–2486.

[146] C. A. Traina, J. Schwartz, *Langmuir* **2007**, *23*, 9158–9161.

[147] D. Q. Vo, E. J. Kim, S. Kim, *J. Colloid Interface Sci.* **2009**, *337*, 75–80.

[148] J. K. Sahoo, M. N. Tahir, A. Yella, T. D. Schladt, E. Mugnaoli, U. Kolb, W. Tremel, *Angew. Chem.* **2010**, *122*, 7741–7745.

[149] M. D. Shultz, J. Ulises Reveles, S. N. Khanna, E. E. Carpenter, *J. Am. Chem. Soc.* **2007**, *129*, 2482–2487.

[150] S. Zürcher, D. Wäckerlin, Y. Bethuel, B. Malisova, M. Textor, S. Tosatti, K. Gademann, *J. Am. Chem. Soc.* **2006**, *128*, 1064–1065.

[151] U. Tromsdorf, PhD thesis, Dissertation, University of Hamburg, **2010**.

[152] Z. Zhao, Z. Zhou, J. Bao, Z. Wang, J. Hu, X. Chi, K. Ni, R. Wang, X. Chen, Z. Chen, J. Gao, *Nat. Commun.* **2013**, *4*, 2266/1–2266/7.

[153] J.-H. Lee, Y.-M. Huh, Y.-w. Jun, J.-w. Seo, J.-t. Jang, H.-T. Song, S. Kim, E.-J. Cho, H.-G. Yoon, J.-S. Suh, J. Cheon, *Nat. Med.* **2007**, *13*, 95–99.

[154] D. Yoo, J. H. Lee, T. H. Shin, J. Cheon, *Acc. Chem. Res.* **2011**, *44*, 863–874.

[155] A. Senyei, K. Widder, G. Czerlinski, *J. Appl. Phys.* **1978**, *49*, 3578–3583.

[156] C. Sun, J. S. H. J. Lee, M. Zhang, *Adv. Drug Deliv. Rev.* **2008**, *60*, 1252–1265.

[157] R. Weissleder, D. D. Stark, B. L. Engelstad, B. a. Bacon, D. L. White, P. Jacobs, J. Lewis, *Am. J. Roentgenol.* **1989**, *152*, 167–173.

[158] E. M. Haacke, R. W. Brown, M. R. Thomson, R. Venkatesan, *Magnetic Resonance Imaging - Physical Principles and Sequence Design*, John Wiley & Sons, New York, **1999**.

[159] D. G. Mitchell, M. S. Cohen, *MRI Principles*, Elsevier Saunders, Philadelphia, **2004**.

[160] M. P. Morales, S. V. Verdangure, M. I. Montero, C. J. Serna, A. Roig, L. Casas, B. Martinez, F. Sandiumenge, *Chem. Mater.* **1999**, *11*, 3058–3064.

[161] X. Sun, A. Klapper, Y. Su, K. Nemkovski, A. Wildes, H. Bauer, O. Köhler, A. Schilmann, W. Tremel, O. Petracic, T. Brückel, *Phys. Rev. B* **2017**, *95*, 134427/1–134427/8.

[162] Y.-W. Jun, Y.-M. Huh, J.-S. Choi, J.-H. Lee, H.-T. Song, S. Kim, S. Yoon, K.-S. Kim, J.-S. Shin, J.-S. Suh, J. Cheon, *J. Am. Chem. Soc.* **2005**, *127*, 5732–5733.

[163] M. I. Shliomis, A. F. Pshenichnikov, K. I. Morozov, I. Y. Shurubor, *J. Magn. Magn. Mater.* **1990**, *85*, 40–46.

[164] S. Tong, S. Hou, Z. Zheng, J. Zhou, G. Bao, *Nano Lett.* **2010**, *10*, 4607–4613.

[165] S. H. Noh, W. Na, J. T. Jang, J. H. Lee, E. J. Lee, S. H. Moon, Y. Lim, J. S. Shin, J. Cheon, *Nano Lett.* **2012**, *12*, 3716–3721.

[166] N. Lee, H. Kim, S. H. Choi, M. Park, D. Kim, H.-C. Kim, Y. Choi, S. Lin, B. H. Kim, H. S. Jung, H. Kim, K. S. Park, W. K. Moon, T. Hyeon, *Proc. Natl. Acad. Sci.* **2011**, *108*, 2662–2667.

[167] R. A. McCurrie, *Ferromagnetic Materials: Structure and Properties*, Academic Press, San Diego, **1994**.

[168] J.-T. Jang, H. Nah, J.-H. Lee, S. H. Moon, M. G. Kim, J. Cheon, *Angew. Chem. Int. Ed.* **2009**, *48*, 1234–1238.

[169] Y. Yang, X. Liu, Y. Lv, T. S. Herng, X. Xu, W. Xia, T. Zhang, J. Fang, W. Xiao, J. Ding, *Adv. Funct. Mater.* **2015**, *25*, 812–820.

[170] S. Mornet, S. Vasseur, F. Grasset, E. Duguet, *J. Mater. Chem.* **2004**, *14*, 2161–2175.

[171] J.-P. Fortin, C. Wilhelm, J. Servais, C. Menager, J.-C. Bacri, F. Gazeau, *J. Am. Chem. Soc.* **2007**, *129*, 2628–2635.

[172] J.-H. Lee, J.-T. Jang, J.-S. Choi, S. H. Moon, S.-H. Noh, J.-W. Kim, J.-G. Kim, I.-S. Kim, K. I. Park, J. Cheon, *Nat. Nanotechnol.* **2011**, *6*, 418–422.

[173] R. Rosensweig, *J. Magn. Magn. Mater.* **2002**, *252*, 370–374.

[174] C. Martinez-Boubeta, K. Simeonidis, A. Makridis, M. Angelakeris, O. Iglesias, P. Guardia, A. Cabot, L. Yedra, S. Estradé, F. Peiró, Z. Saghi, P. A. Midgley, I. Conde-Leborán, D. Serantes, D. Baldomir, *Sci. Rep.* **2013**, *3*, 1652/1–1652/8.

[175] A. Walter, C. Billotey, A. Garofalo, C. Ulhaq-Bouillet, Corinne Lefèvre, J. Taleb, S. Laurent, L. V. Elst, R. N. Muller, D. Felder-Flesch, S. Begin-Colin, *Chem. Mater.* **2014**, *26*, 5252–5264.

[176] L. Lartigue, P. Hugounenq, D. Alloyeau, S. P. Clarke, M. Lévy, J. C. Bacri, R. Bazzi, D. F. Brougham, C. Wilhelm, F. Gazeau, *ACS Nano* **2012**, *6*, 10935–10949.

[177] L. Zhang, Y. Chen, Z. Li, L. Li, P. Saint-Cricq, C. Li, J. Lin, C. Wang, Z. Su, J. I. Zink, *Angew. Chem. Int. Ed.* **2016**, *55*, 2118–2121.

[178] W. Fang, S. Tang, P. Liu, X. Fang, J. Gong, N. Zheng, *Small* **2012**, *8*, 3816–3822.

[179] Y. Liu, K. Ai, L. Lu, *Acc. Chem. Res.* **2012**, *45*, 1817–1827.

[180] S. Yu, A. Watson, *Chem. Rev.* **1999**, *99*, 2353–2377.

[181] D. Pan, E. Roessl, J. P. Schlomka, S. D. Caruthers, A. Senpan, M. J. Scott, J. S. Allen, H. Zhang, G. Hu, P. J. Gaffney, E. T. Choi, V. Rasche, S. A. Wickline, R. Proksa, G. M. Lanza, *Angew. Chem. Int. Ed.* **2010**, *49*, 9635–9639.

[182] D. Kim, S. Park, J. H. Lee, Y. Y. Jeong, S. Jon, *J. Am. Chem. Soc.* **2007**, *129*, 7661–7665.

[183] H. Shi, Z. Wang, C. Huang, X. Gu, T. Jia, A. Zhang, Z. Wu, L. Zhu, X. Luo, X. Zhao, N. Jia, F. Miao, *Small* **2016**, *12*, 3995–4006.

[184] H. Sun, Q. Yuan, B. Zhang, K. Ai, P. Zhang, L. Lu, *Nanoscale* **2011**, *3*, 1990–1996.

[185] K. Ai, Y. Liu, J. Liu, Q. Yuan, Y. He, L. Lu, *Adv. Mater.* **2011**, *23*, 4886–4891.

[186] Y. Liu, K. Ai, J. Liu, Q. Yuan, Y. He, L. Lu, *Angew. Chem. Int. Ed.* **2012**, *51*, 1437–1442.

[187] L. Guo, D. D. Yan, D. Yang, Y. Li, W. Xiaodong, O. Zalewski, B. Yan, W. Lu, *ACS Nano* **2015**, *8*, 5670–5681.

[188] Y. Hu, Y. Yang, H. Wang, H. Du, *ACS Nano* **2015**, *9*, 8744–8754.

[189] Z. Kang, X. Yan, L. Zhao, Q. Liao, K. Zhao, H. Du, X. Zhang, X. Zhang, Y. Zhang, *Nano Res.* **2015**, *8*, 1–11.

[190] S. Tang, M. Chen, N. Zheng, *Small* **2014**, *10*, 3139–3144.

[191] S. Shi, Y. Huang, X. Chen, J. Weng, N. Zheng, *ACS Appl. Mater. Interfaces* **2015**, *7*, 14369–14375.

[192] S. Tang, M. Chen, N. Zheng, *Nano Res.* **2014**, *8*, 165–174.

[193] M. G. Bawendi, M. L. Steigerwald, L. E. Brus, *Annu. Rev. Phys. Chem.* **1990**, *41*, 477–496.

[194] P. Alivisatos, *Nat. Biotechnol.* **2004**, *22*, 47–52.

[195] W. C. W. Chan, D. J. Maxwell, X. Gao, R. E. Bailey, M. Han, S. Nie, *Curr. Opin. Biotechnol.* **2002**, *13*, 40–46.

[196] G. Wang, X. Wang, J. Liu, X. Sun, *Chem. Eur. J.* **2012**, *18*, 5361–5366.

[197] G. Chen, J. Wang, C. Wu, C. Z. Li, H. Jiang, X. Wang, *Langmuir* **2012**, *28*, 12393–12399.

[198] C. Wang, Y. Xu, C. Deng, Z. Liu, R. Wang, H. Zhao, *RSC Adv.* **2016**, *6*, 113115–113122.

[199] K. D. Wegner, N. Hildebrandt, *Chem. Soc. Rev.* **2015**, *44*, 4792–4834.

[200] W. R. Algar, D. E. Prasuhn, M. H. Stewart, T. L. Jennings, J. B. Blanco-Canosa, P. E. Dawson, I. L. Medintz, *Bioconjug. Chem.* **2011**, *22*, 825–858.

[201] J. M. Klostranec, Q. Xiang, G. A. Farcas, J. A. Lee, A. Rhee, E. I. Laffert, S. D. Perrault, K. C. Kain, W. C. W. Chan, *Nano Lett.* **2007**, *7*, 2812–2818.

[202] A. P. Alivisatos, *Science* **1996**, *271*, 933–937.

[203] W. R. Algar, K. Susumu, J. B. Delehanty, I. L. Medintz, *Anal. Chem.* **2011**, *83*, 8826–8837.

[204] C. A. Leatherdale, W.-K. Woo, F. V. Mikulec, M. G. Bawendi, *J. Phys. Chem. B* **2002**, *106*, 7619–7622.

[205] D. R. Larson, W. R. Zipfel, R. M. Williams, S. W. Clark, M. P. Bruchez, F. W. Wise, W. W. Webb, *Science* **2003**, *300*, 1434–1436.

[206] M. Wu, Z. Lin, O. S. Wolfbeis, *Anal. Biochem.* **2003**, *320*, 129–135.

[207] V. Biju, T. Itoh, M. Ishikawa, *Chem. Soc. Rev.* **2010**, *39*, 3031–3056.

[208] M. M. C. Cheng, G. Cuda, Y. L. Bunimovich, M. Gaspari, J. R. Heath, H. D. Hill, C. A. Mirkin, A. J. Nijdam, R. Terracciano, T. Thundat, M. Ferrari, *Curr. Opin. Chem. Biol.* **2006**, *10*, 11–19.

[209] F. Zhang, E. Lees, F. Amin, P. Rivera-Gil, F. Yang, P. Mulvaney, W. J. Parak, *Small* **2011**, *7*, 3113–3127.

[210] K. Susumu, H. T. Uyeda, I. L. Medintz, T. Pons, J. B. Delehanty, H. Mattoussi, *J. Am. Chem. Soc.* **2007**, *129*, 13987–13996.

[211] M. Pumera, *Chem. Commun.* **2011**, *47*, 5671–5680.

[212] S. Giri, E. A. Sykes, T. L. Jennings, W. C. W. Chan, *ACS Nano* **2011**, *5*, 1580–1587.

[213] V. Bagalkot, L. Zhang, E. Levy-Nissenbaum, S. Jon, P. W. Kantoff, R. Langer, O. C. Farokhzad, *Nano Lett.* **2007**, *7*, 3065–3070.

[214] W. J. Parak, R. Boudreau, M. Le Gros, D. Gerion, D. Zanchet, C. M. Micheel, S. C. Williams, A. P. Alivisatos, C. Larabell, *Adv. Mater.* **2002**, *14*, 882–885.

[215] S. Le Gac, I. Vermes, A. D. Van Den Berg, *Nano Lett.* **2006**, *6*, 1863–1869.

[216] Y. Zhang, J. M. Liu, X. P. Yan, *Anal. Chem.* **2013**, *85*, 228–234.

[217] M. Bottrill, M. Green, *Chem. Commun.* **2011**, *47*, 7039–7050.

[218] H. Kobayashi, Y. Hama, Y. Koyama, T. Barrett, C. A. S. Regino, Y. Urano, P. L. Choyke, *Nano Lett.* **2007**, *7*, 1711–1716.

[219] W. Cai, K. Chen, Z.-B. Li, S. S. Gambhir, X. Chen, *J. Nucl. Med.* **2007**, *48*, 1862–1870.

[220] J. Ding, Y. Wang, M. Ma, Y. Zhang, S. Lu, Y. Jiang, C. Qi, S. Luo, G. Dong, S. Wen, Y. An, N. Gu, *Biomaterials* **2013**, *34*, 209–216.

[221] M. Jakob, H. Levanon, P. V. Kamat, *Nano Lett.* **2003**, *3*, 353–358.

[222] Y. J. Jang, D. H. Kim, *Chem. Eur. J.* **2011**, *17*, 540–545.

[223] Y. Tian, T. Tatsuma, *J. Am. Chem. Soc.* **2005**, *127*, 7632–7637.

[224] C. G. Silva, R. Juárez, T. Marino, R. Molinari, H. García, *J. Am. Chem. Soc.* **2011**, *133*, 595–602.

[225] A. Furube, L. Du, K. Hara, R. Katoh, M. Tachiya, *J. Am. Chem. Soc.* **2007**, *129*, 14852–14853.

[226] S. Linic, P. Christopher, D. B. Ingram, *Nat. Mater.* **2011**, *10*, 911–921.

[227] P. Christopher, H. Xin, A. Marimuthu, S. Linic, *Nat. Mater.* **2012**, *11*, 1044–1050.

[228] M. D. L. Ruiz Peralta, U. Pal, R. S. Zeferino, *ACS Appl. Mater. Interfaces* **2012**, *4*, 4807–4816.

[229] Y. Zheng, L. Zheng, Y. Zhan, X. Lin, Q. Zheng, K. Wei, *Inorg. Chem.* **2007**, *46*, 6980–6986.

[230] Y. Zheng, C. Chen, Y. Zhan, X. Lin, Q. Zheng, K. Wei, J. Zhu, *J. Phys. Chem. C* **2008**, *112*, 10773–10777.

[231] C. Gu, C. Cheng, H. Huang, T. Wong, N. Wang, T. Y. Zhang, *Cryst. Growth Des.* **2009**, *9*, 3278–3285.

[232] W. Kaim, B. Schwederski, *Bioanorganische Chemie*, Springer, Wiesbaden, **2005**.

[233] H. Wei, E. Wang, *Chem. Soc. Rev.* **2013**, *42*, 6060–6093.

[234] M. N. Tahir, R. André, J. K. Sahoo, F. D. Jochum, P. Theato, F. Natalio, R. Berger, R. Branscheid, U. Kolb, W. Tremel, *Nanoscale* **2011**, *3*, 3907–3914.

[235] R. Breslow, L. E. Overman, *J. Am. Chem. Soc.* **1970**, *92*, 1075–1077.

[236] L. Gao, J. Zhuang, L. Nie, J. Zhang, Y. Zhang, N. Gu, T. Wang, J. Feng, D. Yang, S. Perrett, X. Yan, *Nat. Nanotechnol.* **2007**, *2*, 577–583.

[237] H. B. Dunford, J. S. Stillman, *Coord. Chem. Rev.* **1976**, *19*, 187–251.

[238] N. C. Veitch, *Phytochemistry* **2004**, *65*, 249–259.

[239] J. H. Dawson, *Science* **1988**, *240*, 433–439.

[240] X. Liu, Q. Wang, H. Zhao, L. Zhang, Y. Su, Y. Lv, *Analyst* **2012**, *137*, 4552–4558.

[241] C. Zheng, A.-X. Zheng, B. Liu, X.-L. Zhang, Y. He, J. Li, H.-H. Yang, G. Chen, *Chem. Commun.* **2014**, *50*, 13103–13106.

[242] R. Andre, F. Natalio, M. Humanes, J. Leppin, K. Heinze, R. Wever, H.-C. Schröder, W. E. G. Müller, W. Tremel, *Adv. Funct. Mater.* **2011**, *21*, 501–509.

[243] M. López-Lázaro, *Cancer Lett.* **2007**, *252*, 1–8.

[244] H. B. Dunford, *Peroxidases and Catalases: Biochemistry Biophysics, Biotechnology and Physiology*, John Wiley & Sons, Hoboken, **2010**.

[245] H. Fenton, *J. Chem. Soc. Trans.* **1894**, *65*, 899–910.

[246] K. Fan, C. Cao, Y. Pan, D. Lu, D. Yang, J. Feng, L. Song, M. Liang, X. Yan, *Nat. Nanotechnol.* **2012**, *7*, 459–464.

[247] D. Duan, K. Fan, D. Zhang, S. Tan, M. Liang, Y. Liu, J. Zhang, P. Zhang, W. Liu, X. Qiu, G. P. Kobinger, G. Fu Gao, X. Yan, *Biosens. Bioelectron.* **2015**, *74*, 134–141.

[248] H. Wei, E. Wang, *Anal. Chem.* **2008**, *80*, 2250–2254.

[249] K. Qu, P. Shi, J. Ren, X. Qu, *Chem. Eur. J.* **2014**, *20*, 7501–7506.

[250] Z. Chen, J. J. Yin, Y. T. Zhou, Y. Zhang, L. Song, M. Song, S. Hu, N. Gu, *ACS Nano* **2012**, *6*, 4001–4012.

[251] I. Celardo, J. Z. Pedersen, E. Traversa, L. Ghibelli, *Nanoscale* **2011**, *3*, 1411–1420.

[252] K. Herget, P. Hubach, S. Pusch, P. Deglmann, H. Götz, T. E. Gorelik, I. A. Gural'skiy, F. Pfitzner, T. Link, S. Schenk, M. Panthöfer, V. Ksenofontov, U. Kolb, T. Opatz, R. André, W. Tremel, *Adv. Mater.* **2016**, *29*, 1603823/1–1603823/8.

[253] M. R. N. Murthy, T. J. Reid, A. Sicignano, N. Tanaka, M. G. Rossmann, *The Structure of Beef Liver Catalase - The Biological Chemistry of Iron - A Look at the Metabolism of Iron and Its Subsequent Uses in Living Organisms*, Springer Netherlands, Dordrecht, **1982**, pp. 439–458.

[254] J. M. McCord, B. B. Keele, I. Fridovich, *Proc. Natl. Acad. Sci.* **1971**, *68*, 1024–1027.

[255] A. Amano, S. Shizukuishi, H. Tamagawa, K. Iwakura, S. Tsunasawa, A. Tsunemitsu, *J. Bacteriol.* **1990**, *172*, 1457–1463.

[256] D. L. Piddington, F. C. Fang, T. Laessig, M. Cooper, I. M. Orme, N. A. Buchmeier, A. M. Cooper, *Infect. Immun.* **2001**, *69*, 4980–4987.

[257] F. S. Archibald, I. Fridovich, *J. Bacteriol* **1981**, *146*, 928–936.

[258] K. Barnese, E. B. Gralla, D. E. Cabelli, J. S. Valentine, *J. Am. Chem. Soc.* **2008**, *130*, 4604–4606.

[259] A. Karakoti, S. Singh, J. M. Dowding, S. Seal, W. T. Self, *Chem. Soc. Rev.* **2010**, *39*, 4422–4432.

[260] R. W. Tarnuzzer, J. Colon, S. Patil, S. Seal, *Nano Lett.* **2005**, *5*, 2573–2577.

[261] C. Korsvik, S. Patil, S. Seal, W. T. Self, *Chem. Commun.* **2007**, *10*, 1056–1058.

[262] T. Pirmohamed, J. M. Dowding, S. Singh, B. Wasserman, E. Heckert, A. S. Karakoti, J. E. S. King, S. Seal, W. T. Self, *Chem. Commun.* **2010**, *46*, 2736–2738.

[263] C. K. Kim, T. Kim, I. Y. Choi, M. Soh, D. Kim, Y. J. Kim, H. Jang, H. S. Yang, J. Y. Kim, H. K. Park, S. P. Park, S. Park, T. Yu, B. W. Yoon, S. H. Lee, T. Hyeon, *Angew. Chem. Int. Ed.* **2012**, *51*, 11039–11043.

[264] F. Natalio, R. André, A. F. Hartog, B. Stoll, K. P. Jochum, R. Wever, W. Tremel, *Nat. Nanotechnol.* **2012**, *7*, 530–535.

[265] R. Ragg, M. N. Tahir, W. Tremel, *Eur. J. Inorg. Chem.* **2016**, *13*, 1906–1915.

[266] S. A. Borchardt, E. J. Allain, J. J. Michels, G. W. Stearns, R. F. Kelly, W. F. McCoy, *Appl. Environ. Microbiol.* **2001**, *67*, 3174–3179.

[267] A. Rosenhahn, S. Schilp, H. J. Kreuzer, M. Grunze, *Phys. Chem. Chem. Phys.* **2010**, *12*, 4275–4286.

[268] Z. Hasan, R. Renirie, R. Kerkman, H. J. Ruijssenaars, A. F. Hartog, R. Wever, *J. Biol. Chem.* **2006**, *281*, 9738–9744.

[269] H. S. Soedjak, J. V. Walker, A. Butler, *Biochemistry* **1995**, *34*, 12689–12696.

[270] G. Schwarz, R. R. Mendel, M. W. Ribbe, *Nature* **2009**, *460*, 839–847.

[271] R. M. Garrett, J. L. Johnson, T. N. Graf, A. Feigenbaum, K. V. Rajagopalan, *Proc. Natl. Acad. Sci.* **1998**, *95*, 6394–6398.

[272] J. L. Johnson, K. V. Rajagopalan, S. K. Wadman, *Adv. Exp. Med. Biol.* **1993**, *338*, 373–378.

[273] J. S. Modica-Napolitano, J. R. Aprille, *Adv. Drug Deliv. Rev.* **2001**, *49*, 63–70.

[274] H. J. Fan, P. Werner, M. Zacharias, *Small* **2006**, *2*, 700–717.

[275] Y. Xia, P. Yang, Y. Sun, Y. Wu, B. Mayers, B. Gates, Y. Yin, F. Kim, H. Yan, *Adv. Mater.* **2003**, *15*, 353–389.

[276] P. Nagpal, N. C. Lindquist, S.-H. Oh, D. J. Norris, *Science* **2009**, *325*, 594–598.

[277] A. Yella, M. N. Tahir, S. Meuer, R. Zentel, R. Berger, M. Panthöfer, W. Tremel, *J. Am. Chem. Soc.* **2009**, *131*, 17566–17575.

[278] J. A. Enterkin, K. R. Poeppelmeier, L. D. Marks, *Nano Lett.* **2011**, *11*, 993–997.

[279] F. R. Fan, Y. Ding, D. Y. Liu, Z. Q. Tian, L. W. Zhong, *J. Am. Chem. Soc.* **2009**, *131*, 12036–12037.

[280] A. Figuerola, A. Fiore, R. Di Corato, A. Falqui, C. Giannini, E. Micotti, A. Lascialfari, M. Corti, R. Cingolani, T. Pellegrino, P. D. Cozzoli, L. Manna, *J. Am. Chem. Soc.* **2008**, *130*, 1477–1487.

[281] Y. Yoo, K. Seo, S. Han, K. S. K. Varadwaj, H. Y. Kim, J. H. Ryu, H. M. Lee, J. P. Ahn, H. Ihee, B. Kim, *Nano Lett.* **2010**, *10*, 432–438.

[282] R. K. Joshi, J. J. Schneider, *Chem. Soc. Rev.* **2012**, *41*, 5285–5312.

[283] G. Koster, M. Huijben, *Epitaxial Growth of Complex Metal Oxides*, Woodhead Publishing Series in Electronic and Optical Materials, **2015**.

[284] J. Junquera, P. Ghosez, *Nature* **2003**, *422*, 506–509.

[285] D. Seo, I. Y. Choong, J. Jung, H. Song, *J. Am. Chem. Soc.* **2008**, *130*, 2940–2941.

[286] B. Lim, M. Jiang, P. H. C. Camargo, E. C. Cho, J. Tao, X. Lu, Y. Zhu, Y. Xia, *Science* **2009**, *324*, 1302–1305.

[287] B. T. Sneed, C. N. Brodsky, C. H. Kuo, L. K. Lamontagne, Y. Jiang, Y. Wang, F. Tao, W. Huang, C. K. Tsung, *J. Am. Chem. Soc.* **2013**, *135*, 14691–14700.

[288] M. Casavola, R. Buonsanti, G. Caputo, P. D. Cozzoli, *Eur. J. Inorg. Chem.* **2008**, 837–854.

[289] I. Schick, S. Lorenz, D. Gehrig, S. Tenzer, W. Storck, K. Fischer, D. Strand, F. F. Laquai, W. Tremel, *Beilstein J. Nanotechnol.* **2014**, *5*, 2346–2362.

[290] Y. L. Lyubarskaya, A. A. Shestopalov, *ACS Appl. Mater. Interfaces* **2013**, *5*, 7323–7329.

[291] Y. Yamada, C.-K. Tsung, W. Huang, Z. Huo, S. E. Habas, T. Soejima, C. E. Aliaga, G. a. Somorjai, P. Yang, *Nat. Chem.* **2011**, *3*, 372–376.

[292] H. Zhao, M. Zhou, L. Wen, Y. Lei, *Nano Energy* **2015**, *13*, 790–813.

[293] L. Li, X. Chen, Y. Wu, D. Wang, Q. Peng, G. Zhou, Y. Li, *Angew. Chem. Int. Ed.* **2013**, *52*, 11049–11053.

[294] J. K. Sahoo, M. N. Tahir, F. Hoshyargar, B. Nakhjavan, R. Branscheid, U. Kolb, W. Tremel, *Angew. Chem. Int. Ed.* **2011**, *50*, 12271–12275.

[295] Y. Song, R. M. Dorin, R. M. Garcia, Y. B. Jiang, H. Wang, P. Li, Y. Qiu, F. Van Swol, J. E. Miller, J. A. Shelnutt, *J. Am. Chem. Soc.* **2008**, *130*, 12602–12603.

[296] X. Huang, Y. Li, Y. Chen, H. Zhou, X. Duan, Y. Huang, *Angew. Chem. Int. Ed.* **2013**, *52*, 6063–6067.

[297] X. Huang, S. S. Li, Y. Huang, S. Wu, X. Zhou, S. S. Li, C. L. Gan, F. Boey, C. a. Mirkin, H. Zhang, *Nat. Commun.* **2011**, *2*, 292/1–292/6.

[298] J. Niu, D. Wang, H. Qin, X. Xiong, P. Tan, Y. Li, R. Liu, X. Lu, J. Wu, T. Zhang, W. Ni, J. Jin, *Nat. Commun.* **2014**, *5*, 3313/1–3313/7.

[299] Y. Xiong, J. M. McLellan, J. Chen, Y. Yin, Z.-Y. Li, Y. Xia, *J. Am. Chem. Soc.* **2005**, *127*, 17118–17127.

[300] Y. Xiong, A. R. Siekkinen, J. Wang, Y. Yin, M. J. Kim, Y. Xia, *J. Mater. Chem.* **2007**, *17*, 2600–2602.

[301] Z. Liu, H. Zhou, Y. S. Lim, J. H. Song, L. Piao, S. H. Kim, *Langmuir* **2012**, *28*, 9244–9249.

[302] J. E. Millstone, S. Park, K. L. Shuford, L. Qin, G. C. Schatz, C. A. Mirkin, *J. Am. Chem. Soc.* **2005**, *127*, 5312–5313.

[303] X. Huang, H. Li, S. Li, S. Wu, F. Boey, J. Ma, H. Zhang, *Angew. Chem. Int. Ed.* **2011**, *50*, 12245–12248.

[304] B. Lim, J. Wang, P. H. C. Camargo, M. Jiang, M. J. Kim, Y. Xia, *Nano Lett.* **2008**, *8*, 2535–2540.

[305] H. Yoo, J. E. Millstone, S. Li, J. W. Jang, W. Wei, W. Jinsong, G. C. Schatz, C. A. Mirkin, *Nano Lett.* **2009**, *9*, 3038–3041.

[306] J. S. Duchene, W. Niu, J. M. Abendroth, Q. Sun, W. Zhao, F. Huo, W. D. Wei, *Chem. Mater.* **2013**, *25*, 1392–1399.

[307] S. S. Shankar, A. Rai, B. Ankamwar, A. Singh, A. Ahmad, M. Sastry, *Nat. Mater.* **2004**, *3*, 482–488.

[308] J. Xie, J. Y. Lee, D. I. C. Wang, Y. P. Ting, *ACS Nano* **2007**, *1*, 429–439.

[309] S. P. Chandran, M. Chaudhary, R. Pasricha, A. Ahmad, M. Sastry, *Biotechnol. Prog.* **2006**, *22*, 577–583.

[310] J. Xie, J. Y. Lee, D. I. C. Wang, Y. P. Ting, *Small* **2007**, *3*, 672–682.

[311] C. Tan, H. Zhang, *Nat. Commun.* **2015**, *6*, 7873.

[312] J. Zhang, C. Feng, Y. Deng, L. Liu, *Chem. Mater.* **2014**, *26*, 1213–1218.

[313] H. Li, G. Chen, H. Yang, X. Wang, J. Liang, P. Liu, M. Chen, N. Zheng, *Angew. Chem. Int. Ed.* **2013**, *52*, 8368–8372.

[314] Y. Dai, X. Mu, Y. Tan, K. Lin, Z. Yang, N. Zheng, G. Fu, *J. Am. Chem. Soc.* **2012**, *134*, 7073–7080.

[315] X. Yin, X. Liu, Y.-T. Pan, K. a. Walsh, H. Yang, *Nano Lett.* **2014**, *14*, 7188–7194.

[316] Y. Li, Y. Yan, Y. Li, H. Zhang, D. Li, D. Yang, *CrystEngComm* **2015**, *17*, 1833–1838.

[317] J. T. Weiss, J. C. Dawson, K. G. Macleod, W. Rybski, C. Fraser, C. Torres-Sánchez, E. E. Patton, M. Bradley, N. O. Carragher, A. Unciti-Broceta, *Nat. Commun.* **2014**, *5*, 3277/1–3277/9.

[318] R. M. Yusop, A. Unciti-Broceta, E. M. V. Johansson, R. M. Sánchez-Martín, M. Bradley, *Nat. Chem.* **2011**, *3*, 239–243.

[319] H. Kura, M. Takahashi, T. Ogawa, *J. Phys. Chem. C* **2010**, *114*, 5835–5838.

[320] C. Weidenthaler, *Nanoscale* **2011**, *3*, 792–810.

[321] G. Salazar-Alvarez, J. Sort, A. Uheida, M. Muhammed, S. Surinach, M. D. Baro, J. Nogues, *J. Mater. Chem.* **2007**, *17*, 322–328.

[322] U. Gonser, *Topics in Applied Physics: Mössbauer Spectroscopy*, Springer, Berlin, **1975**.

[323] J. A. Ramos Guivar, A. Bustamante, J. Flores, M. Mejía Santillan, A. M. Osorio, A. I. Martínez, L. De Los Santos Valladares, C. H. W. Barnes, *Hyperfine Interact.* **2014**, *224*, 89–97.

[324] A. Gedikoqlu, *Scr. Metall.* **1983**, *17*, 45–48.

[325] I. S. Lyubutin, C. R. Lin, Y. V. Korzhetskiy, T. V. Dmitrieva, R. K. Chiang, *J. Appl. Phys.* **2009**, *106*, 034311/1–034311/6.

[326] S. L. Zhang, J. R. Zhang, *Phys. status solidi b* **1994**, *182*, 421–427.

[327] X. D. Dai, Y. Kong, J. H. Li, B. X. Liu, *J. Phys. Condens. Matter* **2006**, *18*, 4527–4542.

[328] R. Davis, H. P. Schultz, *J. Org. Chem.* **1962**, *27*, 854–857.

[329] T. T. Trinh, R. Sato, M. Sakamoto, Y. Fujiyoshi, M. Haruta, H. Kurata, T. Teranishi, *Nanoscale* **2015**, *7*, 12435–12444.

[330] S. Chikazumi, *Physics of Magnetism*, Wiley, New York, **1964**.

[331] S.-W. Kim, J. Park, Y. Jang, Y. Chung, S. Hwang, T. Hyeon, Y. W. Kim, *Nano Lett.* **2003**, *3*, 1289–1291.

[332] N. Wang, L. Zhu, M. Wang, D. Wang, H. Tang, *Ultrason. Sonochem.* **2010**, *17*, 78–83.

[333] B. R. E. Childs, W. G. Bardsley, *Biochem. J.* **1975**, *145*, 93–103.

[334] H. Gallati, *Clin. Chem. Lab. Med.* **1979**, *17*, 1–8.

[335] H. Ikemoto, Q. Chi, J. Ulstrup, *J. Phys. Chem. C* **2010**, *114*, 16174–16180.

[336] F. Yu, Y. Huang, A. J. Cole, V. C. Yang, *Biomaterials* **2009**, *30*, 4716–4722.

[337] A. C. Patel, S. Li, J. M. Yuan, Y. Wei, *Nano Lett.* **2006**, *6*, 1042–1046.

[338] Y. Liu, F. Yu, *Nanotechnology* **2011**, *22*, 145704/1–145704/8.

[339] I. H. Segel, *Enzyme Kinetics: Behavior and Analysis of Rapid Equilibrium and Steady-State Enzyme Systems*, Wiley, New York, **1993**.

[340] S. M. Yusuf, J. M. De Teresa, M. D. Mukadam, J. Kohlbrecher, M. R. Ibarra, J. Arbiol, P. Sharma, S. K. Kulshreshtha, *Phys. Rev. B* **2006**, *74*, 224428/1–224428/11.

[341] B. Liu, J. Liu, *Nanoscale* **2015**, *7*, 13831–13835.

[342] Y. Nangia, B. Kumar, J. Kaushal, C. R. Suri, *Anal. Chim. Acta* **2012**, *751*, 140–145.

[343] X. Xia, J. Zhang, N. Lu, M. J. Kim, K. Ghale, Y. Xu, E. Mckenzie, *ACS Nano* **2015**, *9*, 9994–10004.

[344] T. Ishikawa, E. Matijevic, *Langmuir* **1988**, *4*, 26–31.

[345] Y. Wei, S. Han, D. a. Walker, S. C. Warren, B. A. Grzybowski, *Chem. Sci.* **2012**, *3*, 1090–1094.

[346] Y. Xia, T. D. Nguyen, M. Yang, B. Lee, A. Santos, P. Podsiadlo, Z. Tang, S. C. Glotzer, N. a. Kotov, *Nat. Nanotechnol.* **2011**, *6*, 580–587.

[347] A. Coelho, TOPAS Academic V 4.1, **2007**.

[348] R. W. Cheary, A. Coelho, *J. Appl. Crystallogr.* **1992**, *25*, 109–121.

[349] K. Lagarec, D. G. Rancourt, *Nucl. Instrum. Methods Phys. Res. Sect. B* **1997**, *129*, 266–280.

[350] R. Dören, *Kolloidale Superpartikel basierend auf Eisenoxid – Synthese und Charakterisierung*, Bachelor Thesis, Johannes Gutenberg-Universität Mainz, **2015**.

[351] M. Deuker, *Kolloidale Eisenoxid-Nanopartikel als künstliche Nanoenzyme*, Bachelor Thesis, Johannes Gutenberg-Universität Mainz, **2016**.

[352] P. Komforth, *"Bottom-up" Synthese dreidimensional organisierter Eisenoxid Nanomaterialien in hochsiedenden Lösemitteln*, Bachelor Thesis, Johannes Gutenberg-Universität Mainz, **2016**.

[353] A.-H. Lu, E. L. Salabas, F. Schüth, *Angew. Chem. Int. Ed.* **2007**, *46*, 1222–1244.

[354] T. Lam, P. Pouliot, P. K. Avti, F. Lesage, A. K. Kakkar, *Adv. Colloid Interface Sci.* **2013**, *199-200*, 95–113.

[355] C. Xu, S. Sun, *Adv. Drug Deliv. Rev.* **2013**, *65*, 732–743.

[356] T.-H. Shin, Y. Choi, S. Kim, J. Cheon, *Chem. Soc. Rev.* **2015**, *44*, 4501–4516.

[357] Y. Hu, Y. Liu, Y. Sun, *Adv. Funct. Mater.* **2015**, *25*, 1638–1647.

[358] A. Ahniyaz, Y. Sakamoto, L. Bergström, *Proc. Natl. Acad. Sci.* **2007**, *104*, 17570–17574.

[359] A. A. Gunawan, B. D. Chernomordik, D. S. Plemmons, D. D. Deng, E. S. Aydil, K. A. Mkhoyan, *Chem. Mater.* **2014**, *26*, 3328–3333.

[360] B. Nakhjavan, M. N. Tahir, M. Panthöfer, H. Gao, T. Gasi, V. Ksenofontov, R. Branscheid, S. Weber, U. Kolb, L. M. Schreiber, W. Tremel, *Chem. Commun.* **2011**, *47*, 8898–8900.

[361] B. Nakhjavan, M. N. Tahir, F. Natalio, M. Panthöfer, H. Gao, M. Dietzsch, R. Andre, T. Gasi, V. Ksenofontov, R. Branscheid, U. Kolb, W. Tremel, *Nanoscale* **2012**, *4*, 4571–4577.

[362] H. Goesmann, C. Feldmann, *Angew. Chem. Int. Ed.* **2010**, *49*, 1362–1395.

[363] C. L. Choi, A. P. Alivisatos, *Annu. Rev. Phys. Chem.* **2010**, *61*, 369–389.

[364] I. Gur, N. A. Fromer, M. L. Geier, A. P. Alivisatos, *Science* **2005**, *310*, 462–465.

[365] S. Sun, H. Zeng, *J. Am. Chem. Soc.* **2002**, 8204–8205.

[366] F. Jiang, X. Li, Y. Zhu, Z. Tang, *Phys. B Condens. Matter* **2014**, *443*, 1–5.

[367] H. S. Dehsari, M. Heidari, A. H. Ribeiro, W. Tremel, G. Jakob, D. Donadio, R. Potestio, K. Asadi, *Chem. Mater.* **2017**, *29*, 9648–9656.

[368] P. Daniel, S. I. Shylin, H. Lu, M. N. Tahir, M. Panthofer, T. Weidner, A. Moller, V. Ksenofontov, W. Tremel, *J. Mater. Chem. C* **2018**, *6*, 326–333.

[369] C. N. R. Rao, J. Gopalakrishnan, *New Directions in Solid State Chemistry*, 2nd, Cambridge University Press, Cambridge, **2008**.

[370] R. M. Cornell, U. Schwertmann, *The Iron Oxides*, 2nd, Wiley VCH, Weinheim, **2003**.

[371] H.-G. Liao, D. Zherebetskyy, H. Xin, C. Czarnik, P. Ercius, H. Elmlund, M. Pan, L.-W. Wang, H. Zheng, *Science* **2014**, *345*, 916–919.

[372] C. Yang, J. Wu, Y. Hou, *Chem. Commun.* **2011**, *47*, 5130–5141.

[373] Z. Zhou, X. Zhu, D. Wu, Q. Chen, D. Huang, C. Sun, J. Xin, K. Ni, J. Gao, *Chem. Mater.* **2015**, *27*, 3505–3515.

[374] N. N. Greenwood, T. Gibb, *Mössbauer Spectroscopy*, Chapman and Hall, London, **1971**.

[375] L. Bronstein, X. Huang, J. Retrum, A. Schmucker, M. Pink, B. D. Stein, B. Dragnea, *Chem. Mater.* **2007**, *19*, 3624–3632.

[376] S. Palchoudhury, W. An, Y. Xu, Y. Qin, Z. Zhang, N. Chopra, R. A. Holler, C. H. Turner, Y. Bao, *Nano Lett.* **2011**, *11*, 1141–1146.

[377] S. G. Kwon, Y. Piao, J. G. J. Park, S. Angappane, Y. Jo, N. M. Hwang, J. G. J. Park, T. Hyeon, *J. Am. Chem. Soc.* **2007**, *129*, 12571–12584.

[378] M. N. Tahir, M. Kluenker, F. Natalio, B. Barton, K. Korschelt, S. I. Shylin, M. Panthöfer, V. Ksenofontov, A. Möller, U. Kolb, W. Tremel, *ACS Appl. Nano Mater.* **2017**, DOI: 10.1021/acsanm.7b00051.

[379] L. Chen, X. Yang, J. Chen, J. Liu, H. Wu, H. Zhan, C. Liang, M. Wu, *Inorg. Chem.* **2010**, *49*, 8411–8420.

[380] T. Ruskov, T. Tomov, S. Georgiev, *Phys. status solidi* **1976**, *37*, 295–302.

[381] D. R. Lide, *CRC Handbook of Chemistry and Physics*, CRC-Press, **2003**, 84th Edition, CRC Press.

[382] K. Woo, J. Hong, S. Choi, H.-W. Lee, J.-P. Ahn, C. S. Kim, S. W. Lee, *Chem. Mater.* **2004**, *16*, 2814–2818.

[383] J. B. Goodenough, *Phys. Rev.* **1955**, *100*, 564–573.

[384] J. B. Goodenough, *J. Phys. Chem. Solids* **1958**, *6*, 287–297.

[385] J. Kanamori, *J. Phys. Chem. Solids* **1959**, *10*, 87–98.

[386] F. Morin, *Phys. Rev.* **1950**, *78*, 819–820.

[387] C. G. Shull, W. A. Strauser, E. O. Wollan, *Phys. Rev.* **1951**, *83*, 333–345.

[388] S. B. Wang, Y. L. Min, S. H. Yu, *J. Phys. Chem. C* **2007**, *111*, 3551–3554.

[389] F. Jiao, A. Harrison, J.-C. Jumas, A. V. Chadwick, W. Kockelmann, P. G. Bruce, *J. Am. Chem. Soc.* **2006**, *128*, 5468–5474.

[390] I. E. Dzialoshinskii, *Sov. Phys. JETP* **1957**, *5*, 1259–1272.

[391] T. Moriya, *Phys. Rev.* **1960**, *120*, 91–98.

[392] R. Nathans, S. J. Pickart, H. A. Alperin, P. J. Brown, *Phys. Rev.* **1964**, *136*, A1641–A1647.

[393] P. J. Besser, A. H. Morrish, C. W. Searle, *Phys. Rev.* **1967**, *153*, 632–640.

[394] S. Foner, S. J. Williamson, *J. Appl. Phys.* **1965**, *36*, 1154–1156.

[395] J. Park, K. An, Y. Hwang, J.-G. Park, H.-J. Noh, J.-Y. Kim, J.-H. Park, N.-M. Hwang, T. Hyeon, *Nat. Mater.* **2004**, *3*, 891–895.

[396] U. Kolb, T. Gorelik, C. Kübel, M. T. Otten, D. Hubert, *Ultramicroscopy* **2007**, *107*, 507–513.

[397] U. Kolb, E. Mugnaioli, T. E. Gorelik, *Cryst. Res. Technol.* **2011**, *46*, 542–554.

[398] E. F. Rauch, J. Portillo, S. Nicolopoulos, D. Bultreys, S. Rouvimov, P. Moeck, *Z. Kristallog.* **2010**, *225*, 103–109.

[399] J. Portillo, E. F. Rauch, S. Nicolopoulos, M. Gemmi, D. Bultreys, *Mater. Sci. Forum* **2010**, *644*, 1–7.

[400] A. Coelho, TOPAS Academic V 6.0, **2016**.

[401] N. Boui, *Synthese von Pd-Fe2O3 Heteropartikeln*, Bachelor Thesis, Johannes Gutenberg-Universität Mainz, **2015**.

[402] A. Balanta, C. Godard, C. Claver, *Chem. Soc. Rev.* **2011**, *40*, 4973–4985.

[403] Y. Ito, H. Ohta, Y. M. A. Yamada, T. Enoki, Y. Uozumi, *Chem. Commun.* **2014**, *50*, 12123–12126.

[404] J. J. Topczewski, P. J. Cabrera, N. I. Saper, M. S. Sanford, *Nature* **2016**, *531*, 220–224.

[405] M. R. Decan, S. Impellizzeri, M. L. Marin, J. C. Scaiano, *Nat. Commun.* **2014**, *5*, 4612/1–4612/8.

[406] L. Wang, Y. Zhu, J.-Q. Wang, F. Liu, J. Huang, X. Meng, J.-M. Basset, Y. Han, F.-S. Xiao, *Nat. Commun.* **2015**, *6*, 6957/1–6957/8.

[407] X. Qi, M. R. Axet, K. Philippot, P. Lecante, P. Serp, *Dalton Trans.* **2014**, *2*, 9283–9295.

[408] R. Ciriminna, V. Pandarus, G. Gingras, F. Béland, M. Pagliaro, *ACS Sustainable Chem. Eng.* **2013**, *1*, 249–253.

[409] M. C. Hong, M. C. Choi, Y. W. Chang, Y. Lee, J. Kim, H. Rhee, *Adv. Synth. Catal.* **2012**, *354*, 1257–1263.

[410] H. Zhang, T. Watanabe, M. Okumura, M. Haruta, N. Toshima, *Nat. Mater.* **2011**, *11*, 49–52.

[411] M. J. Sweetman, S. J. P. McInnes, R. B. Vasani, T. Guinan, A. Blencowe, N. H. Voelcker, *Chem. Commun.* **2015**, *51*, 10640–10643.

[412] K. S. Egorova, V. P. Ananikov, *Angew. Chem. Int. Ed.* **2016**, *55*, 12150–12162.

[413] S. Wooh, Y.-G. Lee, M. N. Tahir, D. Song, M. Meister, F. Laquai, W. Tremel, J. Bisquert, Y. S. Kang, K. Char, *J. Mater. Chem. A* **2013**, *1*, 12627–12634.

[414] T. C. Lee, M. Alarcón-Correa, C. Miksch, K. Hahn, J. G. Gibbs, P. Fischer, *Nano Lett.* **2014**, *14*, 2407–2412.

[415] L. Zhang, H. Jing, G. Boisvert, J. Z. He, H. Wang, *ACS Nano* **2012**, *6*, 3514–3527.

[416] C. Xu, J. Xie, D. Ho, C. Wang, N. Kohler, E. G. Walsh, J. R. Morgan, Y. E. Chin, S. Sun, *Angew. Chem. Int. Ed.* **2008**, *47*, 173–176.

[417] S. Najafishirtari, P. Guardia, A. Scarpellini, M. Prato, S. Marras, L. Manna, M. Colombo, *J. Catal.* **2016**, *338*, 115–123.

[418] N. Sakuma, T. Ohshima, T. Shoji, Y. Suzuki, R. Sato, A. Wachi, A. Kato, Y. Kawai, A. Manabe, T. Teranishi, *ACS Nano* **2011**, *5*, 2806–2814.

[419] J. Zhang, X. Zheng, F. Wu, B. Yan, S. Zhou, S. Qu, J. Weng, *ACS Macro Lett.* **2016**, *5*, 1317–1321.

[420] M. Lattuada, T. A. Hatton, *Nano Today* **2011**, *6*, 286–308.

[421] S. Ogasawara, S. Kato, *J. Am. Chem. Soc.* **2010**, *132*, 4608–4613.

[422] A. Dumas, P. Couvreur, *Chem. Sci.* **2015**, *6*, 2153–2157.

[423] A. Y. Nikitin, P. Alonso-González, S. Vélez, S. Mastel, A. Centeno, A. Pesquera, A. Zurutuza, F. Casanova, L. E. Hueso, F. H. L. Koppens, R. Hillenbrand, *Nat. Photonics* **2016**, *10*, 239–243.

[424] D. Wang, C. Deraedt, J. Ruiz, D. Astruc, *Acc. Chem. Res.* **2015**, *48*, 1871–1880.

[425] V. Polshettiwar, R. Luque, A. Fihri, H. Zhu, M. Bouhrara, J. M. Basset, *Chem. Rev.* **2011**, *111*, 3036–3075.

[426] C. W. Lim, I. S. Lee, *Nano Today* **2010**, *5*, 412–434.

[427] X. L. Wu, T. Wen, H. L. Guo, S. Yang, X. Wang, A. W. Xu, *ACS Nano* **2013**, *7*, 3589–3597.

[428] Z. Wang, X. Yang, Z. Cheng, Y. Liu, L. Shao, L. Jiang, *Mater. Horiz.* **2017**, *4*, 701–708.

[429] Y. Q. Zhang, X. B. Yang, Z. X. Wang, J. Long, L. Shao, *J. Mater. Chem. A* **2017**, *5*, 7316–7325.

[430] Y. Lu, J. D. Miller, *J. Colloid Interface Sci.* **2002**, *256*, 41–52.

[431] H. B. Abrahamson, H. C. Lukaski, *J. Inorg. Biochem.* **1994**, *54*, 115–130.

[432] L. Bao, W.-L. Low, J. Jiang, J. Y. Ying, *J. Mater. Chem.* **2012**, *22*, 7117–7120.

[433] F. Söderlind, H. Pedersen, R. M. Petoral, P. O. Käll, K. Uvdal, *J. Colloid Interface Sci.* **2005**, *288*, 140–148.

[434] R. Hufschmid, H. Arami, R. M. Ferguson, M. Gonzales, E. Teeman, L. N. Brush, N. D. Browning, K. M. Krishnan, *Nanoscale* **2015**, *7*, 11142–11154.

[435] E. J. W. Verwey, *Nature* **1939**, *144*, 327–328.

[436] I. Bernal-Villamil, S. Gallego, *J. Physics. Condens. Matter* **2014**, *27*, 1–8.

[437] G. K. Rozenberg, M. P. Pasternak, W. M. Xu, Y. Amiel, M. Hanfland, M. Amboage, R. D. Taylor, R. Jeanloz, *Phys. Rev. Lett.* **2006**, *96*, 1–4.

[438] M. P. Pasternak, W. M. Xu, G. K. Rozenberg, R. D. Taylor, R. Jeanloz, *J. Magn. Magn. Mater.* **2003**, *265*, 107–112.

[439] W. Jones, J. M. Thomas, R. K. Thorpe, M. J. Tricker, *Appl. Surf. Sci.* **1978**, *1*, 388–407.

[440] S. Bedanta, W. Kleemann, *J. Phys. D. Appl. Phys.* **2009**, *42*, 1–28.

[441] T. Yang, C. Shen, Z. Li, H. Zhang, C. Xiao, S. Chen, Z. Xu, D. Shi, J. Li, H. Gao, *J. Phys. Chem. B* **2005**, *109*, 23233–23236.

[442] R. D. Zysler, D. Fiorani, A. M. Testa, *J. Magn. Magn. Mater.* **2001**, *224*, 5–11.

[443] C. Cannas, A. Ardu, A. Musinu, D. Peddis, G. Piccaluga, *Chem. Mater.* **2008**, *20*, 6364–6371.

[444] A. F. Gross, M. R. Diehl, K. C. Beverly, E. K. Richman, S. H. Tolbert, *J. Phys. Chem. B* **2003**, *107*, 5475–5482.

[445] J. Lu, X. Jiao, D. Chen, W. Li, *J. Phys. Chem. C* **2009**, *113*, 4012–4017.

[446] D. H. Han, J. P. Wang, H. L. Luo, *J. Magn. Magn. Mater.* **1994**, *136*, 176–182.

[447] H. G. O. Becker, W. Berger, G. Domschke, E. Fanghänel, *Organikum*, Wiley-VCH, **2001**, 21. Auflage, Wiley–VCH.

[448] S. H. Lee, W. S. Jahng, K. H. Park, N. Kim, W. J. Joo, D. H. Choi, *Macromol. Res.* **2003**, *11*, 431–436.

[449] D. Cai, A. Neyer, R. Kuckuk, H. M. Heise, *J. Mol. Struct.* **2010**, *976*, 274–281.

[450] A. Dong, X. Ye, J. Chen, Y. Kang, T. Gordon, J. M. Kikkawa, C. B. Murray, *J. Am. Chem. Soc.* **2011**, *133*, 998–1006.

[451] M. Machtakova, *Synthese, Charakterisierung und Funktionalisierung von ZnO-Nanopartikeln für die biomedizinische Anwendung*, Bachelor Thesis, Johannes Gutenberg-Universität Mainz, **2016**.

[452] C. F. Klingshirn, *ChemPhysChem* **2007**, *8*, 782–803.

[453] A. F. Holleman, E. Wiberg, N. Wiberg, *Lehrbuch der Anorganischen Chemie*, 102nd, Walter de Gruyter and Co., Berlin, **2007**.

[454] Ü. Özgür, Y. I. Alivov, C. Liu, A. Teke, M. A. Reshchikov, S. Dogan, V. Avrutin, S. J. Cho, H. Morkoc, *J. Appl. Phys.* **2005**, *98*, 1–103.

[455] C. F. Klingshirn, A. Waag, A. Hoffmann, J. Geurts, *Zinc Oxide: From Fundermental Properties Towards Novel Applications*, Springer, Heidelberg, **2010**.

[456] C. Wöll, *Prog. Surf. Sci.* **2007**, *82*, 55–120.

[457] N. Jones, B. Ray, K. T. Ranjit, A. C. Manna, *FEMS Microbiol. Lett.* **2008**, *279*, 71–76.

[458] F. Gottschalk, T. Sondere, R. Schols, B. Nowack, *Environ. Sci. Technol.* **2009**, *43*, 9216–9222.

[459] Y. Li, W. Xie, X. Hu, G. Shen, X. Zhou, Y. Xiang, X. Zhao, P. Fang, *Langmuir* **2010**, *26*, 591–597.

[460] A. A. Khodja, T. Sehili, J.-F. Pilichowski, P. Boule, *J. Photochem. Photobiol. A Chem.* **2001**, *141*, 231–239.

[461] I. L. Hsiao, Y. J. Huang, *Chem. Res. Toxicol.* **2011**, *24*, 303–313.

[462] L. Hao, L. Chen, J. Hao, N. Zhong, *Ecotoxicol. Environ. Saf.* **2013**, *91*, 52–60.

[463] Y. Xie, N. G. Williams, A. Tolic, W. B. Chrisler, J. G. Teeguarden, B. L. Maddux, J. G. Pounds, A. Laskin, G. Orr, *Toxicol. Sci.* **2012**, *125*, 450–461.

[464] Y. Y. Kao, Y. M. Chiung, Y. C. Chen, T. J. Cheng, P. S. Liu, *Toxicol. Sci.* **2012**, *125*, 462–472.

[465] T. Xia, M. Kovochich, M. Liong, L. Mädler, B. Gilbert, H. Shi, J. I. Yeh, J. I. Zink, A. E. Nel, *ACS Nano* **2008**, *2*, 2121–2134.

[466] R. M. C. Ignacio, C.-S. Kim, S.-K. Kim, *Mol. Cell. Toxicol.* **2014**, *10*, 237–244.

[467] A. Sirelkhatim, S. Mahmud, A. Seeni, N. H. M. Kaus, L. C. Ann, S. K. M. Bakhori, H. Hasan, D. Mohamad, *Nano-Micro Lett.* **2015**, *7*, 219–242.

[468] V. Sharma, R. K. Shukla, N. Saxena, D. Parmar, M. Das, A. Dhawan, *Toxicol. Lett.* **2009**, *185*, 211–218.

[469] S. Hackenberg, A. Scherzed, A. Technau, M. Kessler, K. Froelich, C. Ginzkey, C. Koehler, M. Burghartz, R. Hagen, N. Kleinsasser, *Toxicol. Vitr.* **2011**, *25*, 657–663.

[470] S. Pavlica, F. Gaunitz, R. Gebhardt, *Toxicol. Vitr.* **2009**, *23*, 653–659.

[471] A. E. Nel, L. Mädler, D. Velegol, T. Xia, E. M. V. Hoek, P. Somasundaran, F. Klaessig, V. Castranova, M. Thompson, *Nat. Mater.* **2009**, *8*, 543–557.

[472] J. Heim, E. Felder, M. N. Tahir, A. Kaltbeitzel, U. R. Heinrich, C. Brochhausen, V. Mailänder, W. Tremel, J. Brieger, *Nanoscale* **2015**, *7*, 8931–8938.

[473] M. Susewind, A.-M. Schilmann, J. Heim, A. Henkel, T. Link, K. Fischer, D. Strand, U. Kolb, M. N. Tahir, J. Brieger, W. Tremel, *J. Mater. Chem. B* **2015**, *3*, 1813–1822.

[474] V. B. Kumar, A. Gedanken, P. Paik, *ChemPhysChem* **2013**, *14*, 3215–3220.

[475] H. Wang, D. Wingett, M. H. Engelhard, K. Feris, K. M. Reddy, P. Turner, J. Layne, C. Hanley, J. Bell, D. Tenne, C. Wang, A. Punnoose, *J. Mater. Sci. Mater. Med.* **2009**, *20*, 11–22.

[476] J. Zhang, A. Thurber, D. A. Tenne, J. W. Rasmussen, D. Wingett, C. Hanna, A. Punnoose, *Adv. Funct. Mater.* **2010**, *20*, 4358–4363.

[477] G. Bisht, S. Rayamajhi, *Nanobiomedicine* **2016**, *3*, 9/1–9/11.

[478] J. Gupta, P. Bhargava, D. Bahadur, *J. Mater. Chem. B* **2015**, *3*, 1968–1978.

[479] J. W. Rasmussen, E. Martinez, P. Louka, D. G. Wingett, *Expert Opin. Drug Deliv.* **2010**, *7*, 1063–1077.

[480] B. Ludi, M. Niederberger, *Dalton Trans.* **2013**, *42*, 12554–12568.

[481] J. Zhang, F. Huang, Z. Lin, *Nanoscale* **2010**, *2*, 18–34.

[482] C. J. Dalmaschio, C. Ribeiro, E. R. Leite, *Nanoscale* **2010**, *2*, 2336–2345.

[483] R. A. Laudise, A. A. Ballman, *J. Phys. Chem.* **1960**, *64*, 688–691.

[484] W. J. Li, E. W. Shi, W. Z. Zhong, Z. W. Yin, *J. Cryst. Growth* **1999**, *203*, 186–196.

[485] Z. Tang, N. A. Kotov, M. Giersig, *Science* **2002**, *297*, 237–240.

[486] A. Narayanaswamy, H. Xu, N. Pradhan, X. Peng, *Angew. Chem. Int. Ed.* **2006**, *45*, 5361–5364.

[487] B. Cheng, Shi, J. M. Russell-Tanner, L. Zhang, E. T. Samulski, *Inorg. Chem.* **2006**, *45*, 1208–1214.

[488] B. Liu, H. C. Zeng, *Langmuir* **2004**, *20*, 4196–4204.

[489] L. N. Dem'yanets, D. V. Kostomarov, I. P. Kuz'mina, *Inorg. Mater.* **2002**, *38*, 124–131.

[490] X. Zhao, C. Sun, Y. Si, M. Liu, D. Xue, *Mod. Phys. Lett. B* **2009**, *23*, 3809–3815.

[491] M. Kluenker, M. Mondeshki, M. N. Tahir, W. Tremel, *Langmuir* **2018**, *34*, 1700–1710.

[492] M. Personick, C. Mirkin, *J. Am. Chem. Soc.* **2013**, *135*, 18238–18247.

[493] X. Lu, M. Rycenga, S. E. Skrabalak, B. Wiley, Y. Xia, *Annu. Rev. Phys. Chem.* **2009**, *60*, 167–192.

[494] A. C. Templeton, W. P. Wuelfing, R. W. Murray, *Acc. Chem. Res.* **2000**, *33*, 27–36.

[495] A. Stewart, S. E. J. Bell, *Chem. Commun.* **2011**, *47*, 4523–4525.

[496] C. Singh, P. K. Ghorai, M. A. Horsch, A. M. Jackson, R. G. Larson, F. Stellacci, S. C. Glotzer, *Phys. Rev. Lett.* **2007**, *99*, 1–4.

[497] O. Uzun, Y. Hu, A. Verma, S. Chen, A. Centrone, F. Stellacci, *Chem. Commun.* **2008**, *2*, 196–198.

[498] C. M. Goodman, C. D. McCusker, T. Yilmaz, V. M. Rotello, *Bioconjug. Chem.* **2004**, *15*, 897–900.

[499] M. P. Murphy, *Biochim. Biophys. Acta - Bioenerg.* **2008**, *1777*, 1028–1031.

[500] K. A. Willets, R. P. Van Duyne, *Annu. Rev. Phys. Chem.* **2007**, *58*, 267–297.

[501] J. R. McBride, T. J. Pennycook, S. J. Pennycook, S. J. Rosenthal, *ACS Nano* **2013**, *7*, 8358–8365.

[502] A. J. Wilson, K. A. Willets, *WIREs Nanomed. Nanobiotechnol.* **2013**, *5*, 180–189.

[503] K. A. Willets, A. J. Wilson, V. Sundaresan, P. B. Joshi, *Chem. Rev.* **2017**, *117*, 7538–7582.

[504] L. Onsager, *Ann. New York Acad. Sci.* **1949**, *51*, 627–659.

[505] R. Poling-Skutvik, K. I. S. Mongcopa, A. Faraone, S. Narayanan, J. C. Conrad, R. Krishnamoorti, *Macromolecules* **2016**, *49*, 6568–6577.

[506] S. Jadhav, R. Bongiovanni, D. Marchisio, D. Fontana, C. Egger, *Pigment Resin Technol.* **2014**, *43*, 219–227.

[507] D. A. Kunz, J. Schmid, P. Feicht, J. Erath, A. Fery, J. Breu, *ACS Nano* **2013**, *7*, 4275–4280.

[508] F. Natalio, T. P. Corrales, M. Panthofer, D. Schollmeyer, I. Lieberwirth, W. E. G. Muller, M. Kappl, H.-J. Butt, W. Tremel, *Science* **2013**, *339*, 1298–1302.

[509] A. Picker, L. Nicoleau, A. Nonat, C. Labbez, H. Cölfen, *Adv. Mater.* **2014**, *26*, 1135–1140.

[510] E. Rafter, T. Gutmann, F. Löw, G. Buntkowsky, K. Philippot, B. Chaudret, P. W. N. M. van Leeuwen, *Catal. Sci. Technol.* **2013**, *3*, 595–599.

[511] M. Brust, M. Walker, D. Bethell, D. J. Schiffrin, R. Whyman, *Chem. Commun.* **1994**, *0*, 801–802.

[512] R. Graf, M. R. Hansen, D. Hinderberger, K. Muennemann, H. W. Spiess, *Phys. Chem. Chem. Phys.* **2014**, *16*, 9700–9712.

[513] L. A. Straasø, Q. Saleem, M. R. Hansen, *A Toolbox of Solid-State NMR Experiments for the Characterization of Soft Organic Nanomaterials - Annual Reports on NMR Spectroscopy, Vol. 88*, (Ed.: G. A. Webb), Academic Press, **2016**, pp. 307–383.

[514] X. Liu, M. Yu, H. Kim, M. Mameli, F. Stellacci, *Nat. Commun.* **2012**, *3*, 1–9.

[515] B. Fritzinger, R. K. Capek, K. Lambert, J. C. Martins, Z. Hens, *J. Am. Chem. Soc.* **2010**, *132*, 10195–10201.

[516] A. Badia, L. Cuccia, L. Demers, F. Morin, R. B. Lennox, *J. Am. Chem. Soc.* **1997**, *119*, 2682–2692.

[517] Z. Hens, J. C. Martins, *Chem. Mater.* **2013**, *25*, 1211–1221.

[518] A. M. Smith, K. A. Johnston, S. E. Crawford, L. E. Marbella, J. E. Millstone, *Analyst* **2017**, *142*, 11–29.

[519] T. Gutmann, E. Bonnefille, H. Breitzke, P.-J. Debouttière, K. Philippot, R. Poteau, G. Buntkowsky, B. Chaudret, *Phys. Chem. Chem. Phys.* **2013**, *15*, 17383–17394.

[520] J. De Roo, F. Van Den Broeck, K. De Keukeleere, J. C. Martins, I. Van Driessche, H. Zeger, *J. Am. Chem. Soc.* **2014**, *136*, 9650–9657.

[521] J. De Roo, Y. Justo, K. De Keukeleere, F. Van den Broeck, J. C. Martins, I. Van Driessche, Z. Hens, *Angew. Chem. Int. Ed.* **2015**, *54*, 6488–6491.

[522] J. De Roo, I. Van Driessche, J. C. Martins, Z. Hens, *Nat. Mater.* **2016**, *15*, 1–6.

[523] T. D. Schladt, T. Graf, W. Tremel, *Chem. Mater.* **2009**, *21*, 3183–3190.

[524] M. Bartz, J. Küther, G. Nelles, N. Weber, R. Seshadri, W. Tremel, *J. Mater. Chem.* **1999**, *9*, 1121–1125.

[525] W. Nernst, *Z. Phys. Chem.* **1891**, *8*, 110–139.

[526] G. H. Woehrle, L. O. Brown, J. E. Hutchison, *J. Am. Chem. Soc.* **2005**, *127*, 2172–2183.

[527] A. M. Smith, L. E. Marbella, K. A. Johnston, M. J. Hartmann, S. E. Crawford, L. M. Kozycz, D. S. Seferos, J. E. Millstone, *Anal. Chem.* **2015**, *87*, 2771–2778.

[528] G. Canzi, A. A. Mrse, P. Kubiak, *J. Phys. Chem. C* **2011**, *115*, 7972–7978.

[529] A. Badia, L. Demers, L. Dickinson, F. G. Morin, R. B. Lennox, L. Reven, *J. Am. Chem. Soc.* **1997**, *119*, 11104–11105.

[530] S. K. Ghosh, S. Nath, S. Kundu, *J. Phys. Chem. B* **2004**, *108*, 13963–13971.

[531] P. Zhang, T. K. Sham, *Phys. Rev. Lett.* **2003**, *90*, 245502/1–245502/4.

[532] G. Morris, J. Emsley, *Multidimensional NMR methods for the solution state*, Wiley, New York, **2010**, pp. 233–244.

[533] G. Salassa, A. Sels, F. Mancin, T. Bürgi, *ACS Nano* **2017**, *11*, 12609–12614.

[534] A. Abraham, E. Mihaliuk, B. Kumar, J. Legleiter, T. Gullion, *J. Phys. Chem. C* **2010**, *114*, 18109–18114.

[535] L. E. Marbella, J. E. Millstone, *Chem. Mater.* **2015**, *27*, 2721–2739.

[536] A. Dass, R. Guo, J. B. Tracy, R. Balasubramanian, A. D. Douglas, R. W. Murray, *Langmuir* **2008**, *24*, 310–315.

[537] W. R. Dolbier, *Guide to Fluorine NMR for Organic Chemists*, Wiley, New York, **2009**.

[538] A. A. Ribeiro, *J. Fluor. Chem.* **1997**, *83*, 61–66.

[539] I. Cano, M. A. Huertos, A. M. Chapman, G. Buntkowsky, T. Gutmann, P. B. Groszewicz, P. W. N. M. Van Leeuwen, *J. Am. Chem. Soc.* **2015**, *137*, 7718–7727.

[540] B. Antalek, *Concepts Magn. Reson.* **2002**, *14*, 225–258.

[541] C. Vericat, M. E. Vela, G. Benitez, P. Carro, R. C. Salvarezza, *Chem. Soc. Rev.* **2010**, *39*, 1805–1834.

[542] J. R. Sachleben, E. W. Wooten, L. Emsley, A. Pines, V. L. Colvin, A. P. Alivisatos, *Chem. Phys. Lett.* **1992**, *198*, 431–436.

[543] R. J. B. Kalescky, W. Shinoda, P. B. Moore, S. O. Nielsen, *Langmuir* **2009**, *25*, 1352–1359.

[544] R. R. Knauf, J. C. Lennox, J. L. Dempsey, *Chem. Mater.* **2016**, *28*, 4762–4770.

[545] I. Chambrier, C. Banerjee, S. Remiro-Buenamañana, Y. Chao, A. N. Cammidge, M. Bochmann, *Inorg. Chem.* **2015**, *54*, 7368–7380.

[546] J. C. Love, L. A. Estroff, J. K. Kriebel, R. G. Nuzzo, G. M. Whitesides, *Chem. Rev.* **2005**, *105*, 1103–1169.

[547] S. Peng, Y. Lee, C. Wang, H. Yin, S. Dai, S. Sun, *Nano Res.* **2008**, *1*, 229–234.

[548] Y. Chen, L. Wu, Y. Chen, N. Bi, X. Zheng, H. Qi, M. Qin, X. Liao, H. Zhang, Y. Tian, *Microchim. Acta* **2012**, *177*, 341–348.

[549] B. Varnholt, P. Oulevey, S. Luber, C. Kumara, A. Dass, T. Bürgi, *J. Phys. Chem. C* **2014**, *118*, 9604–9611.

[550] A. Kudelski, *J. Raman Spectrosc.* **2003**, *34*, 853–862.

[551] F. Kim, S. Connor, H. Song, T. Kuykendall, P. Yang, *Angew. Chem. Int. Ed.* **2004**, *43*, 3673–3677.

[552] M. Wuithschick, A. Birnbaum, S. Witte, M. Sztucki, U. Vainio, N. Pinna, K. Rademann, F. Emmerling, R. Kraehnert, J. Polte, *ACS Nano* **2015**, *9*, 7052–7071.

[553] R. Leary, A. Kumar, P. Straney, S. Collins, R. Dunin-Borkowski, P. Midgley, J. Millstone, E. Ringe, *J. Phys. Chem.* **2016**, *120*, 20843–20851.

[554] J. Wei, X. Chen, S. Shi, S. Mo, N. Zheng, *Nanoscale* **2015**, *7*, 19018–19026.

[555] R. Zhao, G. Fu, T. Zhou, Y. Chen, X. Zhu, Y. Tang, T. Lu, *Nanoscale* **2014**, *6*, 2776–2781.

[556] X. Gu, Z.-H. Lu, H.-L. Jiang, T. Akita, Q. Xu, *J. Am. Chem. Soc.* **2011**, *133*, 11822–11825.

[557] S. Dutta, C. Ray, S. Mallick, S. Sarkar, A. Roy, T. Pal, *RSC Adv.* **2015**, *5*, 51690–51700.

[558] C. W. Yi, K. Luo, T. Wei, D. W. Goodman, *J. Phys. Chem. B* **2005**, *109*, 18535–18540.

[559] F. Maroun, F. Ozanam, O. M. Magnussen, R. J. Behm, *Science* **2001**, *293*, 1811–1814.

[560] Z. Niu, Q. Peng, M. Gong, H. Rong, Y. Li, *Angew. Chem. Int. Ed.* **2011**, *50*, 6315–6319.

[561] M. Kuno, J. K. Lee, B. O. Dabbousi, F. V. Mikulec, M. G. Bawendi, *J. Chem. Phys.* **1997**, *106*, 9869–9882.

[562] H. Lee, S. E. Habas, S. Kweskin, D. Butcher, G. A. Somorjai, P. Yang, *Angew. Chem. Int. Ed.* **2006**, *45*, 7824–7828.

[563] Y. Xia, K. D. Gilroy, H.-C. Peng, X. Xia, *Angew. Chem. Int. Ed.* **2016**, *56*, 60–95.

[564] T. H. Ha, H.-J. Koo, B. H. Chung, *J. Phys. Chem. C* **2007**, *111*, 1–8.

[565] Y. Ma, J. Zeng, W. Li, M. McKiernan, Z. Xie, Y. Xia, *Adv. Mater.* **2010**, *22*, 1930–1934.

[566] Ö. Metin, X. Sun, S. Sun, *Nanoscale* **2013**, *5*, 910–912.

[567] B. Lim, H. Kobayashi, T. Yu, J. Wang, M. J. Kim, Z. Y. Li, M. Rycenga, Y. Xia, *J. Am. Chem. Soc.* **2010**, *132*, 2506–2507.

[568] D. Chen, C. Li, H. Liu, F. Ye, J. Yang, *Nature* **2015**, *5*, 11949/1–11949/9.

[569] H. M. Song, D. H. Anjum, N. M. Khashab, *RSC Adv.* **2012**, *2*, 3621–3624.

[570] F.-R. Fan, D.-Y. Liu, Y.-F. Wu, S. Duan, Z.-X. Xie, Z.-Y. Jiang, *J. Am. Chem. Soc.* **2008**, *130*, 6949–6951.

[571] P. H. C. Camargo, Y. Xiong, L. Ji, J. M. Zuo, Y. Xia, *J. Am. Chem. Soc.* **2007**, *129*, 15452–15453.

[572] N. Toshima, T. Yonezawa, *New J. Chem.* **1998**, *22*, 1179–1201.

[573] H. M. Song, D. H. Anjum, R. Sougrat, M. N. Hedhili, N. M. Khashab, *J. Mater. Chem.* **2012**, *22*, 25003–25010.

[574] H. Liu, J. Qu, Y. Chen, J. Li, F. Ye, J. Y. Lee, J. Yang, *J. Am. Chem. Soc.* **2012**, *134*, 11602–11610.

[575] I. Saldan, Y. Semenyuk, I. Marchuk, O. Reshetnyak, *J. Mater. Sci.* **2015**, *50*, 2337–2354.

[576] A. M. Henning, J. Watt, P. J. Miedziak, S. Cheong, M. Santonastaso, M. Song, Y. Takeda, A. I. Kirkland, S. H. Taylor, R. D. Tilley, *Angew. Chem. Int. Ed.* **2013**, *52*, 1477–1480.

[577] J. Xu, T. White, P. Li, C. He, J. Yu, W. Yuan, Y. F. Han, *J. Am. Chem. Soc.* **2010**, *132*, 10398–10406.

[578] Y. Ding, F. Fan, Z. Tian, Z. L. Z. Wang, *J. Am. Chem. Soc.* **2010**, *16*, 12480–12486.

[579] H. Okamoto, T. B. Massalski, *Bull. Alloy Phase Diagrams* **1985**, *6*, 229–235.

[580] J. A. Rodriguez, *Surf. Sci. Rep.* **1996**, *24*, 223–287.

[581] F. Gao, D. W. Goodman, *Chem. Soc. Rev.* **2012**, *41*, 8009–8020.

[582] P. Liu, J. K. Nørskov, *Phys. Chem. Chem. Phys.* **2001**, *3*, 3814–3818.

[583] Y. Baer, P. F. Hedén, J. Hedman, M. Kiasson, C. Nordling, K. Siegbahn, *Solid State Commun.* **1970**, *8*, 517–519.

[584] R. Hoffmann, *Rev. Mod. Phys.* **1988**, *60*, 601–628.

[585] S. Mourdikoudis, L. Liz-Marzan, *Chem. Mater.* **2013**, *25*, 1465–1476.

[586] P. Liu, R. Qin, G. Fu, N. Zheng, *J. Am. Chem. Soc.* **2017**, *139*, 2122–2131.

[587] C. Lofton, W. Sigmund, *Adv. Funct. Mater.* **2005**, *15*, 1197–1208.

[588] D. Jana, A. Dandapat, G. De, *J. Phys. Chem. C* **2009**, *113*, 9101–9107.

[589] A. Sárkány, O. Geszti, G. Sáfrán, *Appl. Catal. A Gen.* **2008**, *350*, 157–163.

[590] D. Mei, E. W. Hansen, M. Neurock, *J. Phys. Chem. B* **2003**, *107*, 798–810.

[591] S. Wunder, F. Polzer, Y. Lu, Y. Mei, M. Ballauff, *J. Phys. Chem. C* **2010**, *114*, 8814–8820.

[592] S. Wunder, Y. Lu, M. Albrecht, M. Ballauff, *ACS Catal.* **2011**, *1*, 908–916.

[593] S. Wu, J. Dzubiella, J. Kaiser, M. Drechsler, X. Guo, M. Ballauff, Y. Lu, *Angew. Chem.* **2012**, *124*, 2272–2276.

[594] S. Gu, S. Wunder, Y. Lu, M. Ballauff, R. Fenger, K. Rademann, B. Jaquet, A. Zaccone, *J. Phys. Chem. C* **2014**, *118*, 18618–18625.

[595] G. A. Somorjai, J. Y. Park, *Angew. Chem. Int. Ed.* **2008**, *47*, 9212–9228.

[596] P. Jungwirth, *Faraday Discuss.* **2008**, *141*, 9–30.

[597] X. Zhou, W. Xu, G. Liu, D. Panda, P. Chen, *J. Am. Chem. Soc.* **2010**, *132*, 138–146.

[598] J. Cao, S. Mei, H. Jia, A. Ott, M. Ballauff, Y. Lu, *Langmuir* **2015**, *31*, 9483–9491.

[599] Y. Mei, Y. Lu, F. Polzer, M. Ballauff, M. Drechsler, *Chem. Mater.* **2007**, *19*, 1062–1069.

[600] M. T. Islam, J. E. Padilla, N. Dominguez, D. C. Alvarado, M. S. Alam, P. Cooke, M. M. J. Tecklenburg, J. C. Noveron, *RSC Adv.* **2016**, *6*, 91185–91191.

[601] J. Zhang, G. Chen, D. Guay, M. Chaker, D. Ma, *Nanoscale* **2014**, *6*, 2125–2130.

[602] S. Gu, Y. Lu, J. Kaiser, M. Albrecht, M. Ballauff, *Phys. Chem. Chem. Phys.* **2015**, *17*, 28137–28143.

[603] M. Kluenker, *Synthese und Charakterisierung von kolloidalen Pd@Fe2O3-Superpartikeln aus Pd-Nanopartikeln und gamma-Fe2O3-Nanostäbchen*, Diploma Thesis, Johannes Gutenberg-Universität Mainz, **2014**.

List of Figures

List of Tables